Synthesis of Metal Oxides with Controllable Morphology and Surface Charge and Their Composites for Gas Sensor Application

	Tohoku University
URL	http://hdl.handle.net/10097/00131198

博士学位論文

Synthesis of Metal Oxides with Controllable Morphology and Surface Charge and Their Composites for Gas Sensor Application

形態と表面電荷を制御可能な金属酸化物の合 成と
それらの複合材料におけるガスセンサーへ の応用

A Thesis

Submitted for the Degree of

DOCTOR OF PHILOSOPHY (Ph.D.)

By:

Angga Hermawan (B7GD3501)

Supervisor: Prof. Shu Yin

東北大学環境科学研究科
先端環境創成学専攻
応用環境学コース
August 2020

MOTIVATION

"Whoever follows a path in pursuit of knowledge, Allah makes his way easy to paradise." (A Hadith narrated by Imaam Al Bukhari)

"When a man dies all his deeds comes to an end except for three: an ongoing charity, beneficial knowledge and a righteous son who prays for him." (A Hadith narrated by Imaam Al Bukhari)

Acknowledgement

In the name of Allah, the most grateful and the most merciful.

First of all, I would like to express my deepest and sincere gratitude to my academic advisor, Prof. Shu Yin for his exceptional guidance, patience, supports and encouragements. His broad knowledge and valuable advice have been helping me to finish my doctoral thesis. I am deeply grateful to Assist. Prof. Yusuke Asakura and Assist. Prof. Takuya Hasegawa for his worthwhile suggestions, interests, and discussions in this research.

I wish to extend my warmest thanks to my past and currents colleagues in Environmental Inorganic Material Chemistry Laboratory: Ms. Shio Komatsuda, Mr. Masahito Hatsukano, Mr. Yuto Anada, Dr. Zhizuan Zhao, Dr. Jimin Fan, Dr. Honghong Chang, Mr. Mikihiko Kobayashi, Mr. Yuto Anada, Dr. Anung Riapanitra, Ms. Chiaki Noda, Ms. Misuzu Nakamura, Ms. Yukiho Nishimura, Mr. Zhangyong Gu, Ms. Jinweng Wang, Ms. Mayu Otomo, Ms. Amiko Miyake, Mr. Biao Zhang, Mr. Ardiansyah Taufik, Ms. Jingdi Cao, Mr. Tingru Chen, Ms. Tomoyo Akahira, Ms. Nonoko Suzuki, Ms. Zijing Wang, Mr. Peng Sun, Mr. Namiki Uchiyama, Ms. Tetsuhiro Onodera, Mr. Hanyu Liu, Mr. Iimura and Mr. Yasuo Hangai for their cooperation, assists and friendly atmosphere.

I owe my thousands thanks to all of my Indonesian fellows in Indonesian Student Association in Sendai (PPI Sendai), without their presence, my life in Sendai have certainly been
less interesting.

I acknowledge the Ministry of Education, Culture, Sport, Science and Technology (MEXT) for providing the scholarship during my master study through the IELP Programs. Last but not the least, my greatest appreciation is reserved for my wife, Raras for her uninterruptedly prayer. She has been my inspiration and motivation to put my best effort for writing this thesis. I express my greatest love to my family for their sincere pray and motivations.
Without them, it would seem impossible for me to finish this work.

Angga Hermawan

August 2020

2

Declaration Statement

1. I declare that this doctoral thesis was composed by myself, that the work contained herein is my own except where explicitly stated otherwise in the text, and that this work has not been submitted for any other degree or processional qualification except as specified. Parts of this work have been published in *Ceram. Int.*, 45 (2019) 15435-15444, *J. Mater. Sci. Tech.* (2020), ACS Appl. Nano Mater. (2020) and *Inorg. Chem. Front.* (2020). Part of this works are under submission and/or under preparation of full publication in an international peer-review journal.

2. The density functional theory (DFT) calculation presented in this thesis was obtained in an experiment carried out by Mr. Adie Tri Hanindyo and Mr. Erland Rachmad Ramadhan in Japan Advanced Institute of Science and Technology (JAIST), Ishikawa, Japan. The analysis of DFT data was written by me with their supervision.

I am aware of and understand the university's policy on plagiarism and I certify that this thesis is my own work, expect where indicated by referencing, and the work presented in it has not been submitted in support of another degree or qualification from this or any other university or institute of learning.

Abstract

Rapid globalization of industrial activities has led to the increase of released pollutants in the form of the gaseous and liquid state into our environment. The gaseous pollutants (CO_2, CH_4, NO_x, CO, SO_2, VOCs, etc.) which are produced from the combustion of fossil fuels, not only has become a major contributor to global warming and climate change, but also human respiratory problems. For example, volatile organic compounds (VOCs) and nitrogen oxides (NO_x) induced by recent situations, including rapid industrialization, massive fuel combustion and utilization of chemical in many household products. In particular, VOCs are quickly evaporated at relatively low temperatures and therefore VOCs amount in the atmosphere can gradually increase over time making our environment and other living creatures endangered. Among various harmful VOCs, gaseous toluene (C_7H_8) is poisonous for both humans and the environment produced from paints, thinners, adhesives, cleaning agents, leather tanning processes. On the other side, NO_x is a major residue from fuel burning from automotive and industrial. Both gases are eventually near to our daily life. Moreover, long and intense exposure to these gases can potentially harm the human body through inhalation. Therefore, VOCs and NO_x should be immediately detected.

To detect toxic gases, semiconducting metal oxides material (SMOX) is one of the most explored compounds for chemiresistive gas sensors application. Because of their low cost and versatility of development, ease of use, wide range of observable gases/possible fields of use, they have drawn much interest in the field of gas sensing under atmospheric conditions. These materials exhibited exceptional sensing performances as compared to other types of sensors, e.g. catalytic-type and electrochemical-type gas sensors. However, they have some drawbacks such as their low sensitivity and selectivity to distinguish the toluene with other gases.
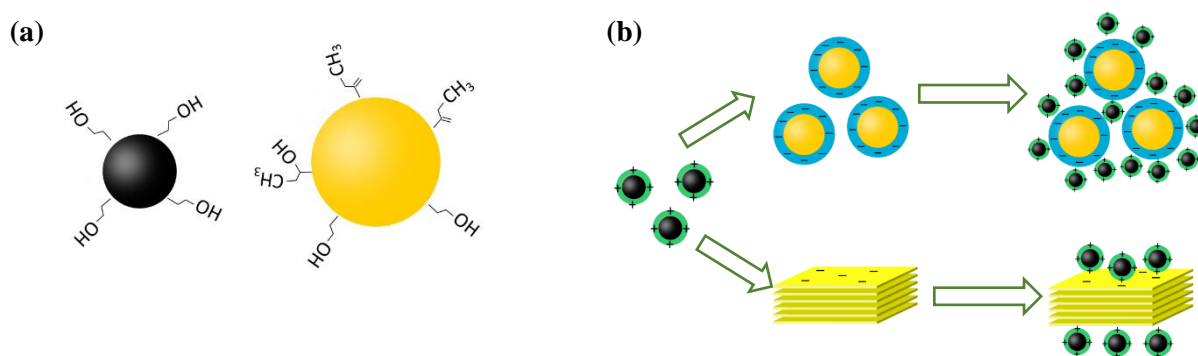
Fig. 1 (a) Organic molecules functionalization-induced unique surface charge,

(b) electrostatic self-assembly process.

In the present thesis, we successfully improved the SMOX gas sensing properties by (i) Precise control of morphology and facet, (ii) Fabrication of heterostructure p-n junction and (iii) Hybridization with 2D $Ti_3C_2T_x$ MXene with metallic phase materials to introduce a Schottky Junction. The unique approach of this thesis is we have been able to combine two materials by harnessing their organic molecules functionalization-induced effective surface charge (Fig. 1 (a)). This approach enables the preparation of hybrid structures (p-n junction or Schottky M-S contact) at room temperature without damaging the structures and original properties may be preserved (Fig. 1 (b)). This is so-called electrostatic self-assembly method.

A facile solvothermal synthesis in an ethanol/acetic acid mixtures so-called "water controlled-release solvothermal process (WCRSP)" has been successfully utilized for fabrication of SnO_2 with a controllable hierarchical spherical size and micro-/mesoporosity. The obtained SnO_2 spheres exhibited a particle size in the range of 0.6 –1.6 μm, a pore size of about 1.4–1.9
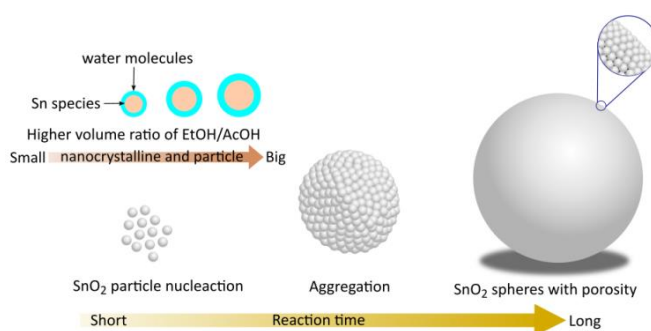

Fig. 2 The formation mechanism of SnO_2 spheres with mesoporous structure.

nm, and effective surface charge depending on the volume ratio of acetic acid to ethanol in the reaction mixture, and the spheres were constructed by nanoscale particles (**Fig. 2**). Due to its micro-/mesoporous structure, the SnO_2 spheres exhibited large specific surface areas over 100 m^2/g. When 10 vol. % of acetic acid at 200 ^{o}C for 20 h was used for the reaction, the obtained SnO_2 possessed a high specific surface area of 145 m^2/g (SnO_2_10). The gas sensing property of SnO_2_10 without an additional noble metal co-catalyst exhibited a large toluene sensing response (R_a/R_g) of 20.2 at 400 ^{o}C, which was about 6 times higher and acceptable selectivity compared to those of other samples. The study found that the sensing performance in the SnO_2 hierarchical spheres was influenced by several factors *e.g.* particle morphology, pore size and specific surface area rather than only a single parameter. Therefore, a precise control of those influencing parameters may lead to the optimum sensing property.

This method can also be applied to control the facet of metal oxides/hydroxides since it is an efficient approach to boost their gas sensing performance. Herein, we demonstrate the
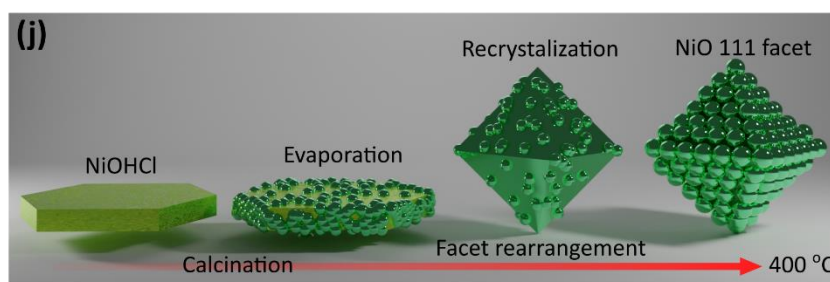
Fig. 3 The transformation mechanism of octahedral morphology NiO with 111 facet from a hexagonal morphology NiOHCl

successful synthesis of NiO with a dominantly (111) facet from the transformation of NiOHCl with a layered structure synthesized by WCSRP (**Fig. 3**). Among other crystal facets, NiO-Octa (111) exhibited the best NOx gas sensing response (16.5 %) to 300 pp b level and deNOx photocatalytic ability over 50% under UV irradiation. The DFT calculation revealed that the abundance of Ni atoms on the clean (111) surface layer allows the favorable adsorption of N adatoms, forming the Ni-N bond. The charge transfer took place from NiO to NO orbital has proven to be a cause of bond weakening and stretching from 1.1692 Å to 1.2231 Å, leading to NO_x molecular decomposition, consistent with the experimental results.

A uniformly CuO nanoparticles decorated SnO_2 ($SnO_2@CuO$) is successfully prepared by electrostatic self-assembly, taking the benefit from opposed surface charges of a positively charged CuO and a negatively charged SnO_2. The surface charge of oxides is tunable, depending on the solvent used during solvothermal treatment. The toluene response ($R_{toluene} = R_a/R_g$) and selectivity ($S = R_{toluene}/R_{othergas}$) of CuO/$SnO_2$ based material toward the exposure of 75 ppm toluene had reached to such high as 540 and 5, respectively due to the p-n heterojunction p-type CuO/n-type SnO_2 (**Fig. 4**). The response/recovery times were 100/36 s. We found that CuO NPs was reduced to Cu metal NPs in high exposure of toluene concentration, forming metal-semiconductor (M-S) contact to greatly improve toluene response. The limit of detection of $SnO_2@CuO$ can reach to around 1 ppm.
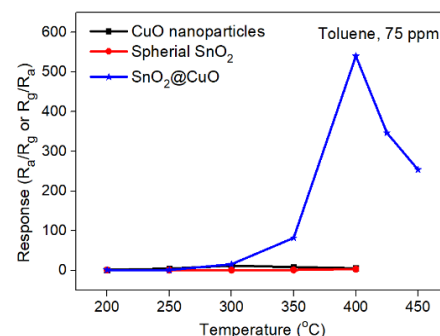
Fig. 4 Gas sensing performance of $SnO_2@CuO$

We have successfully coupled CuO with 2D $Ti_3C_2T_x$ MXene. MXenes is a new family of 2D materials which offers more exceptional performances for energy storage, sensor, photocatalyst, functional flexible devices than other 2D materials. To date, the novel functionality of hybrid containing MXene and metal oxides starts being explored. As shown in **Fig.**
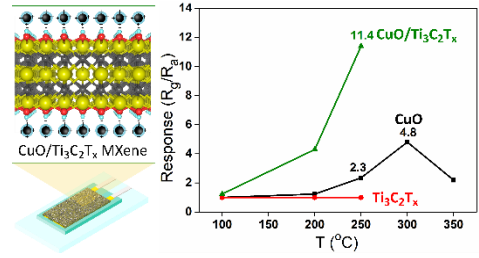

Fig. 5 Gas sensing performance of CuO/$Ti_3C_2T_x$

5, the CuO/$Ti_3C_2T_x$ MXene exhibited the improved toluene gas sensing response (R_g/R_a) of 11.4, which is nearly 5 times higher than that of the pristine CuO nanoparticles (2.3) to 50 ppm of toluene. Due to the different work function (Φ), the Schottky junction was established at the interface of CuO/$Ti_3C_2T_x$ MXene, acting as hole trapping region (HTR) at $Ti_3C_2T_x$ MXene side. Compared to other hybrid 2D materials such as MoS_2 and rGO, which have possessed a higher work function, the CuO/$Ti_3C_2T_x$ MXene maintained better toluene sensing performance. Thus, the work function is critical for designing a high sensing performance of hybrid metal oxides/2D materials. The sensor showed fast responses (270 s) and recovery times (10 s) due to the high conductivity of the metallic phase in $Ti_3C_2T_x$ MXene. Such excellent performance showed promising applications for VOCs gas sensing.

Table of Content

CHAPTER 1

General Introduction

1.1 Environmental gaseous pollutants

Progressive human and industrial activities have brought severe environmental downgrade besides their bringing to the economic cycle, well-being, wealthiness and human prosperity.[1,2] Air quality worsening, one of the serious environmental issues caused by automotive engine and industrial exhaust gases has become an utmost concern for scientists, engineers, and environmentalists due to their effect on human health and surrounding eco-systems. Although the air quality in certain countries has improved in recent years due to the implementation of COP 21 (Paris Agreement) under the United Nations Framework Convention on Climate Change (UNFCCC) in late 2015. This framework aims to reduce carbon and greenhouse emission to a certain level and accelerate the sustainable development goals (SGDs) set by the United Nation.

Air pollution emissions includes carbon monoxide (CO), Nitrogen monoxide (NO), sulfur dioxides (SO_2), volatile organic compounds (VOCs), ozone (O_3)and many more are released from certain activities of human being such as the burning of non-renewable fossil fuels, thermal power plants or automobile combustions, and industrial activities-induced by-product gases. These harmful gases affect the respiratory and nervous systems in long-term exposure as illustrated in **Scheme 1.** Evidence of health risk exists associated with the air pollution such as low birth weight, increased infant and perinatal mortality, tuberculosis, cataract, and so on. Air pollution can be found in indoor or outdoor environments.

In particular, VOCs generated by recent situations including rapid industrialization, massive fuels combustion and utilization of chemical in many household products[3–5] should be immediately detected because VOCs can potentially harm the human body through inhalation in the long-term exposure.[4,6] Since VOCs are quickly evaporated at relatively low temperature, VOCs amount in the atmosphere can gradually increase over time making our environment and other living creatures endangered.[4,7–9] Moreover, some VOCs are tasteless, colorless, odorless and exist in a very low concentration, making them more difficult to be detected by human sense. In all variety of harmful VOCs, toluene gas (C_7H_8) is a toxic gas and a cause of health problem in nervous systems including dizziness, headache, and unconsciousness to induce a permanent speech, hearing, and vision loss for the repeated exposure. It mostly comes from paints, thinners, adhesives, cleaning agents, leather tanning processes.[10,11] Therefore, rapid

detection of these dangerous gas is of great importance to reduce health risk from its exposure and monitoring its concentration in the indoor and outdoor environment.

Scheme 1. Air pollution source (Ref : https://www.idt.com/jp/en/application/iot-building-technology/outdoor-air-quality-sensor-oaq)

Another example of harmful gases beside VOCs is nitrogen oxides NO_x. They are deadly atmospheric contaminants produced from hydrocarbons combustion processes such as vehicle engines or power plants which usually occur at high temperature.[12–14] Not to mention electrical generation from non-renewable fuels, the massive use of vehicles, especially in the metropolitan city, has made the condition is getting worse by the time.[15] A number of studies suggested that NO_2 is a source for asthma or asthma symptoms.[16]

In this regard, there is an urgent need for the sensitive, robust, and fast detection of these severe gases, quantitively, to overcome human sense limitation and protect the larger community. Gas sensor device is a promising way to sense unseen gas threat. Moreover, it is predicted in the future that gas sensor devices can be fully integrated into a flexible, wearable, and smart system into our body making it very attractive to control the exposure of harmful pollutants to our body. It is also a great promise to monitor our health problem through biomarkers such as from breath or skin. Gas sensor device is formed by two main elements: Electrode device and sensing material. This thesis will mainly present the later element, that is gas sensing material.

1.2 Gas sensing materials, working principle and influencing factor

1.2.1 Semiconducting Metal Oxides (SMOX) gas sensing material

Semiconductor metal oxides material, or well-known as SMOX, is one of the most explored compounds for chemiresistive gas sensors application. Because of their low cost and versatility of development, ease of use, wide range of observable gases/possible fields of use, they have drawn much interest in the field of gas sensing under atmospheric conditions. These materials exhibited exceptional sensing performances as compared to other types of sensors, e.g. catalytic-type and electrochemical-type gas sensors (**Fig. 1.1**).[17] The detection of the gases can be determined by the change of resistance (Ω) conductance (Ω^{-1}), capacitance (F), work function (Φ), optical properties, or the release of energy during gas-phase solid reaction. Numerous SMOX have been utilized to identify dangerous and poisonous gases. In general, there are two primary categories of semiconductor metal oxide sensors, namely n-type, the majority charge carrier of which is an electron (for example SnO_2, ZnO, TiO_2, WO_3, $W_{18}O_{49}$, Fe_2O_3, Ga_2O_3, In_2O_3, and many more) and p-type, the majority charge carrier of which is a hole (such as NiO, CuO, CoO, Cr_2O_3, Mn_3O_4 and a few others). The first group is being widely investigated to explore their novel functionality for detecting the unwanted gases. In contrary, relatively little exposure has been given to the latter group, and relevant work into the manufacture of these chemiresistors is only in the preliminary stages of production. **Table 1.1**
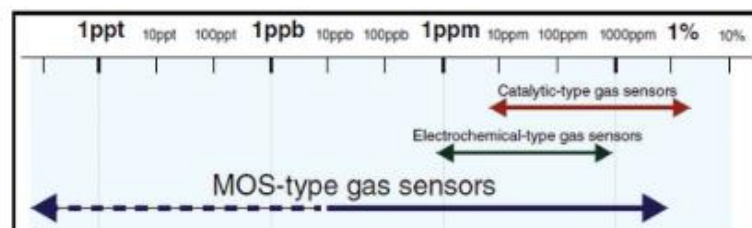
Fig. 1.1 Gas concentration range of some common gas sensor.
Reprinted with permission from Royal Chemical Society.[17]

summarized previous works on detecting VOCs gas based on SMOX material. Due to the very abundance work on this material, we have focused on the materials of which related to the present thesis.

Table 1.1 A brief summary of some SMOX-based gas sensing materials

Sensor Materials	Group	Morphological structures	Target gas	Operating temperature	Ref.
SnO_2	n-type (E_g = 3.6 eV)	Nanoparticles, Nanotubes, Nanowires, Hierarchical porous structures, Thin film, spherical, cubic, etc.	Cl_2, NO_2, H_2, CO, Benzene, Toluene, Ethylene, Xylene, Ethanol, Formaldehyde, etc.	RT-400	[18–25]
CuO	p-type (E_g = 1.2 eV)	Nanoparticles Nanorods, Nanosheets, Thin Film, Urchin-like, Nanowires, Hollow spheres, etc.	Ethanol, H_2, H_2S, NH_3, etc.	RT-300	[26–33]
NiO	p-type (E_g = 3.6-4.0 eV)	Nanoflowers, Nanotubes, Thin Film, Nanowires, Hollow spheres, Hierarchical structures	Ethanol, Butanol, HCHO, NH_3, CO, etc.	RT-400	[34–44]

Although, SMOX-based sensor obviously exhibited excellent gas sensing performance, it comes with limitation as well. Although SMOX shows an excellent gas sensing response, in practical, SMOX is sensitive to not only single target gas, but also other gases and moistures which could lead to the poor selectivity. SMOX could not bear the harsh environment and thus their long-term durability still lacks. To realize the robust gas sensing materials, some approaches are attempted by scientists. The improvement method based on gas sensing working prince is discussed in the following description.

1.2.2 Gas sensing working principle

Prior to the explanation on how the gas sensing properties of certain material can be improved, it is crucial to discuss the sensing mechanism of chemiresistive SMOX-based gas sensors. Although exceptionally long history, there are still several debates among the researchers on the exact fundamental mechanism that causes a response if SMOX is exposed to target gas. However, in general, the accumulation of electrons in adsorbed molecules and the band bending caused by these charged molecules is responsible for an alteration in conductivity of the SMOX. The recent gas sensing mechanism proposed by Ji and co-workers,[17] the adsorption models, the bulk resistance mechanism, and the gas diffusion control mechanism can provide sufficient explanation on physical phenomena such as bend bending, the formation of electron depletion layers (EDLs)/Hole Accumulation Layers (HALs), and grain boundary barrier change. Thus, this present thesis will emphasize these gas sensing mechanisms parameter.

The adsorption model is proposed because the physical or chemical adsorption/desorption on the gas sensing materials has caused the alteration in a sensor resistance, leading to the change in charge carrier concentration. At first, we took an example of n-type SnO_2, as a common gas sensing material, to explain the adsorption model. The work from Li and the team,[45] where they prepared hierarchical SnO_2 nanostructures from assembled nanosheets, has theoretically proposed the oxygen vacancy formation at high temperatures in a reducing environment (Eq. 1.1).

$$O_o = V_o + 2e + \frac{1}{2}O_2(g) \qquad\qquad (Eq.\,1.1)$$
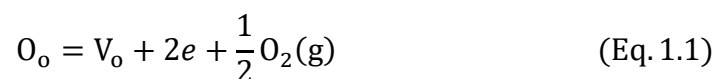
Where O_o represents O atom in O site and V_o represents oxygen vacancy. **Fig. 1.2** shows an atomic model of SnO_2 (left side) and their corresponding band structure (right side). Left side of **Fig. 1.2 (a)** displays a nonstoichiometric SnO_2 surface with oxygen vacancies, where the pre-existed oxygen vacancies filled donor states which positions below the conduction band edge and thus there is a pre-existed energy barriers (X_1) (right side of **Fig. 1.2 (a)**). During the air injection process, the oxygen molecules were adsorbed on the SnO_2 surface by inhabiting the pre-existed oxygen vacancies. Then, they capture the electrons near the conduction band leading to the formation of oxygen ions. Ionic oxygen species are temperature-dependent, means that the oxygen ion species at certain working temperature is specific. The temperature dependency of oxygen dissociation is shown below. (Eqs. 1.2 – 1.5).

$$O_{2(gas)} \rightarrow O_{2(ads)} \quad\quad\quad \text{(Eq. 1.2)}$$

$$O_{2(ads)} + e^- \rightarrow O_2^-{}_{(ads)} \; (< 150 \; ^\circ C) \quad\quad\quad \text{(Eq. 1.3)}$$

$$O_2^-{}_{(ads)} + e^- \rightarrow 2O^-{}_{(ads)} \; (150 \; ^\circ C–400 \; ^\circ C) \quad\quad\quad \text{(Eq. 1.4)}$$

$$O^-{}_{(ads)} + e^- \rightarrow O^{2-}{}_{(ads)} \; (> 400 \; ^\circ C) \quad\quad\quad \text{(Eq. 1.5)}$$
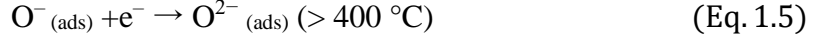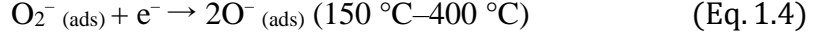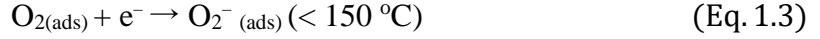
Due to the trapping of electrons at the conduction band, a typical formation of electron depletion layers (EDLs) occurred. This also caused in the change of band structure of SnO_2. In short, the energy barriers (X_2) were formed, the Fermi energy went down and oppositely, conduction band moved upwards (**Fig. 1.2 (b)**).[46] Accordingly, the sensor resistance became higher since the electron's mobility was blocked by the EDLs. In the case of ethanol enters as a sensing gas, it undertakes a redox reaction with oxygen ions, as described in Eq. 1-6. This removal of oxygen ions by the reaction of ethanol from the surfaces caused the thinner size of
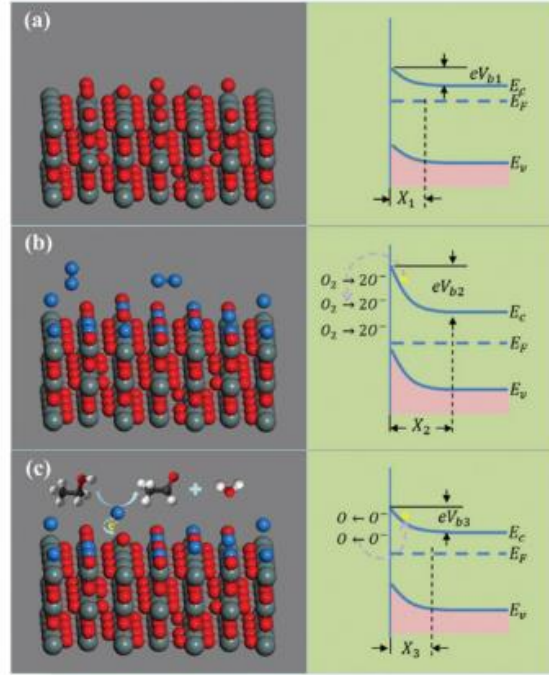
Fig. 1.2 (a–c) Schematic illustration and the corresponding energy band diagram of (a) nonstoichiometric SnO_2 surface with oxygen vacancies, (b) partially repopulated SnO_2 with adsorbed oxygen and (c) reaction between C_2H_5OH and pre-adsorbed oxygen atoms. The gray, red, blue, black and white balls represent Sn, O, adsorbed O, C and H, respectively. Reproduced from reference[45]

EDLs to decrease the potential barrier (X_3), move Fermi level upwards and conduction band edge downwards, resulting in the decrement of sensor resistance.

$$C_5H_2OH_{(gas)} + 10.5\ O^{2-}_{(ads)} \rightarrow 5\ CO_{2\ (gas)} + 1.5\ H_2O_{(gas)} + 21\ e^- \qquad \text{(Eq. 1.6)}$$
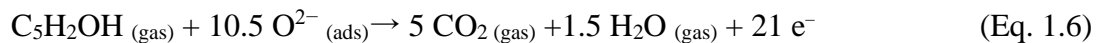
The above adsorption/desorption mechanism mainly discussed the interaction between oxygen species with analyte gas, without involving a direct contact between semiconductor surface with analyte gas. Although oxygen undergoes chemical adsorption/desorption, such mechanism is unsatisfactory to explain some interesting phenomenon at which a formation of by-product material can be found after the exposure of testing gas. This alone is a clear indication that not only oxygen species which interacted with SMOX surface, but also the testing gas itself. For example. Xiao et al. [47] prepared mesoporous SnO_2 for the H_2S gas detection. They interpreted the gas sensing mechanism by the oxygen adsorption models that adsorbed onto the grain of SnO_2 (**Fig. 1.3**). EDLs formed and covered the grains, leading to the depleted region at the grain boundary and increment of gas sensor resistance. When 50 ppm of H_2S was injected, the ionosorption oxygen was actively interact with the H_2S gas, shrinking the depletion layer thickness and decreasing the sensor resistance. This process is a normal oxygen adsorption/desorption. However, they noticed the formation of SnS_2 compound after the gas sensing evaluation as confirmed by the existence S 2p core level spectra in XPS scan. Thus, the H_2S would eventually have direct interaction with SnO_2 surface only after a complete removal of adsorbed oxygen ion species, but H_2S flow still proceeded. The formation of SnS_2 was described in Eq. 1.7

$$H_2S + SnO_2 \rightarrow SnS_2 + H_2O \qquad \text{(Eq. 1.7)}$$
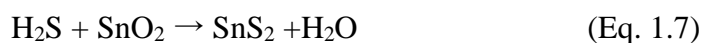
SnS_2 is a well-known material for solar cell application due to its low band gap to effectively harvest the solar energy by adsorbing the wide range infrared spectrum. SnS_2 exhibited higher conductivity than SnO_2, and therefore its presence during the H_2S exposure can further decrease the resistance, leading to the higher sensitivity of SnO_2-based sensor.
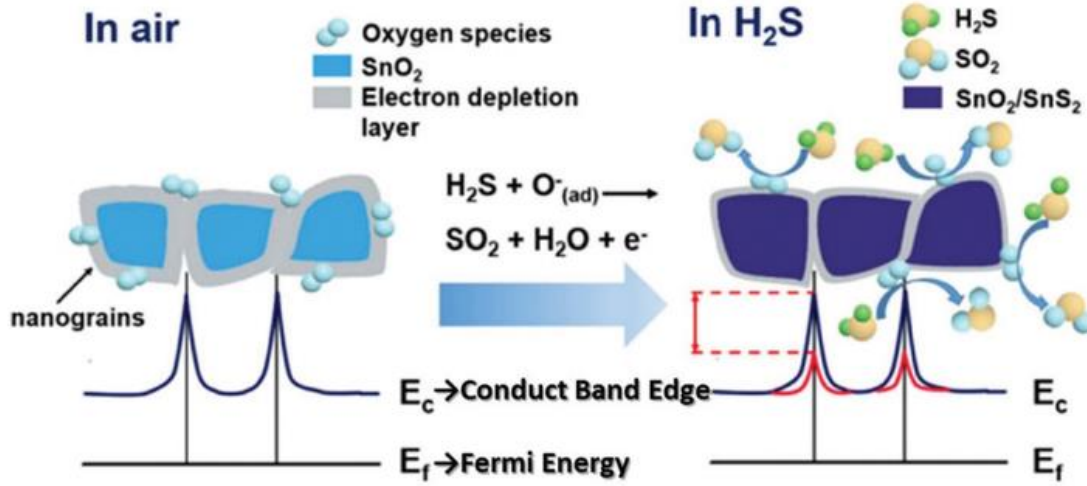
Fig. 1.3 Schematic diagram of the H$_2$S-sensing mechanism of sensors based on mesoporous SnO$_2$. Reproduced with permission from Ref. [47]

The systematic concept of adsorption models in n-type SMOX, including both oxygen and chemical adsorption, is also applicable for its counterpart, namely p-type SMOX. Yakhmi et. al synthesized CuO thin film to detect various gases such as Cl$_2$, H$_2$S, NH$_3$, CH$_4$, CO and NO. It was found that the CuO thin film-based sensor exhibited a reasonable response (R_g/R_a) of 37.7 to 10 ppm H$_2$S at 200 ^{o}C.[48] It also shows a remarkable selectivity when it was exposed to other hazardous gases as mentioned above. They believe that the gas sensing mechanism of p-type CuO thin film sensor was similar to that of any n-type SMOX exposed in H$_2$S, that is involving oxygen and chemical adsorption. When CuO is exposed to certain temperatures, CuO surface absorbs oxygen from air and created HALs, resulting in a low resistance value. Then, upon the flow of H$_2$S at low concentration (<500 ppb), adsorbed oxygens on the CuO surface reacted with H$_2$S, releasing electrons (Eq. 1.8). Then, it recombined with holes in VB caused an increase in sensor resistance. However, when high concentrated H$_2$S (>50 ppm) were flown, the chemical oxidation of H$_2$S occurred (Eq. 1.9). Subsequently, CuS layer formed and covered the entire CuO grains surface. CuS itself exhibit a metallic properties that enhances the connectivity between CuO interparticles, resulting a huge decrease in film resistance. The whole oxygen and chemical adsorption process were schematically illustrated in **Fig. 1.4.**

$$H_2S_{(g)}+3O_2^{-}{}_{(ads)} \rightarrow 2H_2O_{(g)}+2SO_{2(g)}+3e^{-} \qquad \text{(Eq. 1.8)}$$

$$H_2S_{(g)}+CuO_{(s)} \rightarrow CuS_{(s)}+H_2O_{(g)} \qquad \text{(Eq. 1.9)}$$
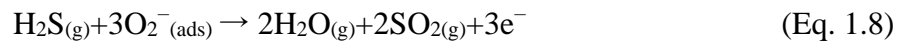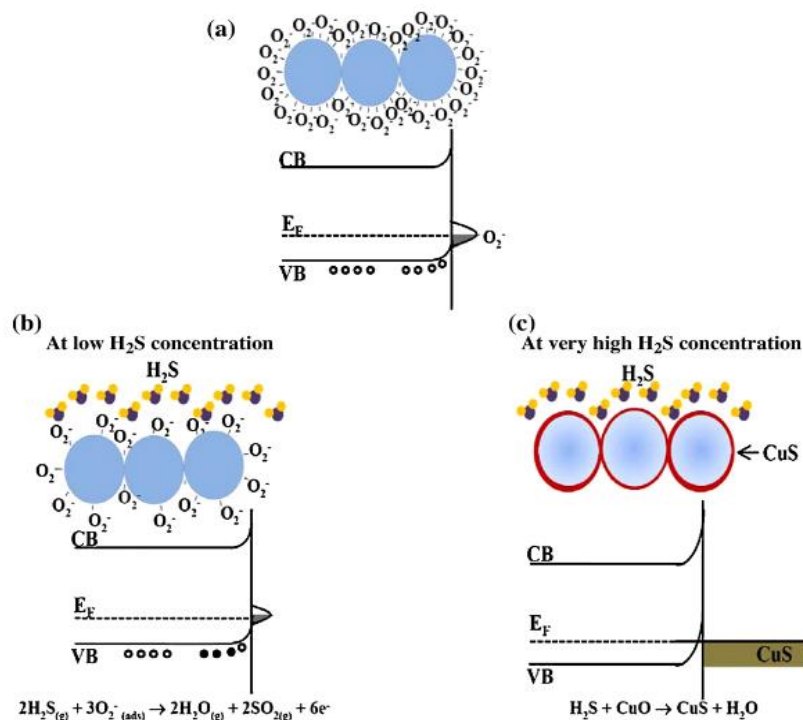
Fig. 1.4 Schematics and band diagrams showing various stages before and after the CuO films were exposed to H2S gas of different concentrations. (a) In air, (2) in low H2S concentration and (3) in high H2S concentration. Reproduced from ref. [48] copyright Elsevier (2010).

1.2.3 Influencing factor on the improved gas sensing properties

For many decades, a lot of researchers worldwide have put their efforts to explore critical factors affecting gas sensing properties of semiconducting metal oxides SMOX, and the best way to explain how their performances can be enhanced is that by using a comprehensive gas sensing mechanism. According to the discussion in the previous section, the gas sensing mechanism can be improved by increasing the oxygen chemisorbed species and target gas molecules adsorption. Herein we discuss influencing factors which can effectively alter the gas sensing properties.

1.2.3.1 Morphological control

The sensitivity of the SMOX-based sensor can be increased significantly by changing their particle size and morphological structures, as have been reported by many publications .[49] It is reasonable because the size of particle determines the core-shell structures of depleted regions, namely Electron Depletion layers (EDLs) and Hole Accumulation Layers (HALs) for n-type and p-type SMOX, respectively, as illustrated in **Fig. 1.5**.[34,50] While the morphological

structures govern the configuration of their assembly and interparticle contact.[51–56] Both depleted regions are formed because of electrons drawing from the valence band of SMOX. However, they have opposite behaviors. EDLs, due to the high density of electrons, it has a high resistance. Consequently, n-type SMOX exhibited a high resistance in air atmosphere. HALs, in opposite, possessed a low resistance in the ambient atmosphere due to the accumulation of hole. The gas sensing response of SMOX, hypothetically, is depleted region dependent. The response will dramatically increase if SMOX particles is smaller than twice thickness of EDLs.[50,51,57] As also illustrated in **Fig. 1.6**, three different models regarding the relation between particle size (D) and charge depletion layers thickness (L) can be explained. The L is formed around the surface due to oxygen ions adsorption and the size of L is expected to be 3 nm for standard SnO_2 nanostructured materials.[58–60] If the D much larger than 2L (D>>2L), the conductivity is governed by the inner mobile charge carriers and electrical resistivity depends largely on the height of potential barrier. If the D is larger or comparable to 2L (D ≥ 2L), there is a formation of interparticle space-charge layers, inhibiting the conduction channel within each particle. Therefore, the electrical resistivity not only depends on particle boundary, but also the space-charge contact on the particle neck and so it is so sensitive to charge reactions. When D is smaller than 2L (D<2L), the depleted layers dominates the particles and thus the bands are nearly flat in whole structures. The electrical resistivity is

(a) n-type oxide semiconductors

Semiconducting core (low resistance)

Electron depletion layer (high resistance)

(b) p-type oxide semiconductors

Insulating core (high resistance)

Hole accumluation layer (low resistance)
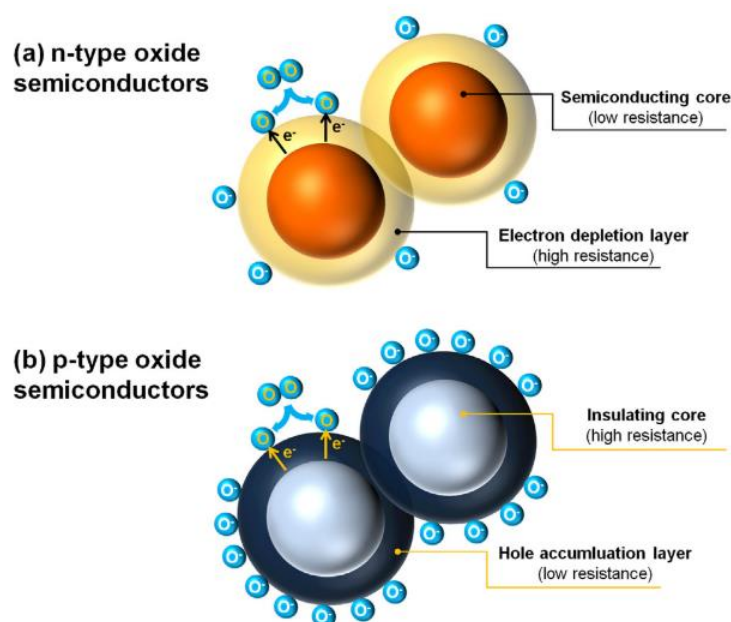
Fig. 1.5. Formation of electronic core–shell structures in (a) n-type and (b) p-type oxide semiconductors. Reprinted with permission from Ref.[34]

controlled by the interparticle resistivity. Even only a few charges is transferred from the surface reactions can cause a significant changing in the electrical resistivity.[61]

The effect of morphology and particle size variation of n-type (SnO$_2$ and ZnO) and p-type (CuO and NiO) on their gas sensing properties gathered from the literatures is summarized in **Table 1.2**. The table informs how the morphology can greatly tune the sensing responses.
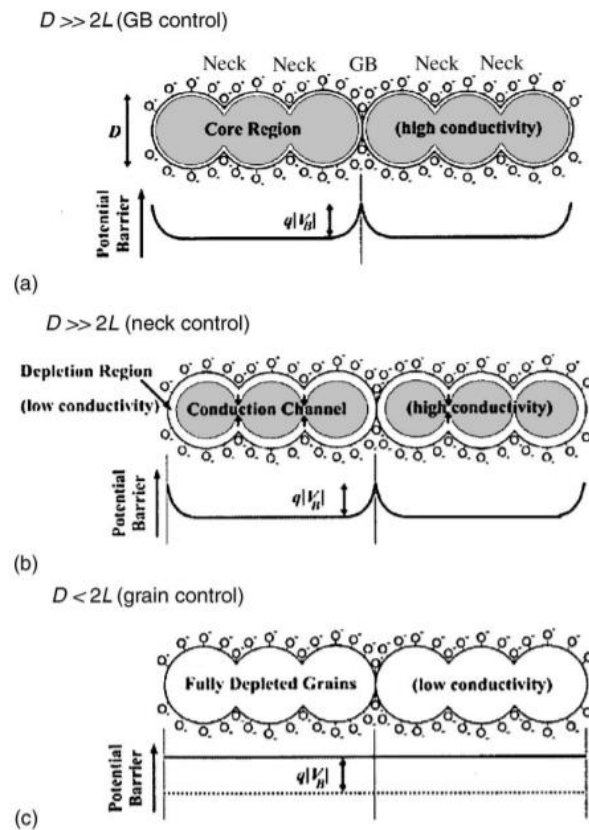
Fig. 1.6 Schematic model of the effect of the crystallite size on the sensitivity of metal-oxide gas sensors: (a) D >> 2L; (b) D ≥ 2L; (c) D < 2L.(D: particle size , L: charge depletion layers thickness) Reprinted from reference. [61]

Mostly, they attributed the enhanced gas sensing properties to the high specific surface area, interparticle contact and porous structures. Nevertheless, the relationship between morphological design and their gas sensing performance still remains difficult because different materials, although they have the same morphology, will exhibit different gas sensing properties.

Table 1.2 Morphology-dependent gas sensing properties of semiconducting metal oxide-based sensing materials

Sensor Materials	Morphology	Target gas	Working Temperature (^oC)	Response (R_g/R_a) or (R_a/R_g)	Refs.
SnO_2	Hierarchical NSs	Acetone	500	$R_{shuttle-shaped} = 60$ $R_{cone-shaped} = 175$ $R_{rod-shaped} = 32$	[62]
SnO_2	Flower-like Sheet-like Nanoparticles	CO	250	$R_{flower-like} = 71.5$ $R_{sheet-like} = 17.7$ $R_{nanoparticles} = 16.3$	[63]
ZnO	Nanorods Nanoparticles	NO_2	100	$R_{nanorods} = 34.8$ $R_{nanoparticle} = 1.02$	[64]
ZnO	Nanorods Needle-like Pencil-like	NO_2	80-400	$R_{nanorods} = 624$ $R_{needle-like} = 44.8$ $R_{pencil-like} = 206$	[65]
CuO	Hierarchical NSs	H_2	200	$R_{Hierarchical} = 5.8$ $R_{Nanorods} = 3.4$	[66]
CuO	Hierarchical NSs	H_2S	190	$R_{Hierarchical} = 4.5$ $R_{Solid\ spheres} = 3.2$	[67]
NiO	Nanotubes	Ethanol	250	$R_{Nanotubes} = 4.2$ $R_{Nanofibers} = 1.4$	[68]
NiO	Hollow Spheres	1-Butanol	350	$R_{Hollow\ spheres} = 2.55$ $R_{Nanoparticles} = 1.73$	[69]

NSs = Nanostructures

R_a = Resistance in Air

R_g = Resistance in gas

1.2.3.2 Exposed facets design

Gas adsorption/desorption during the sensing process mostly occurs on the surface of materials, and due to the fact that different exposed surface facet exhibit different surface adsorption-desorption abilities, gas sensing performances, in many cases, are largely affected by surface nature of the material. High-energy facets tend to show more excellent gas sensing properties because of higher surface energy and stronger interaction with analytes. In the reported literatures, the influence of exposed facets is always accompanied by first-principle calculation, besides the experimental work to gain a more comprehensive understanding about the surface nature and how they interact with the gas molecules. Therefore, a precise and facile design of a highly active surface facets is getting more popular in the gas sensing field.

We can take ZnO, a common and well-known gas sensing material, as a representative to observe crystal facet-dependent gas sensing properties. In one report,[70] porous ZnO nanosheets with two well-defined facets were successfully synthesized, namely (0001) and (10$\bar{1}$0). They were used to detect ethanol vapors. **Fig. 1.7** (a) illustrates crystal facet in ZnO porous nanosheet. The gas sensing results depicted in **Fig. 1.7** (b-f) clearly shows the ZnO with (0001) surface facet exhibited a better ethanol sensing properties than ZnO with (10$\bar{1}$0) surface facet, at all operating temperatures. Not only its superior sensitivity, (0001) surface facet was found to be more selective than that of (10$\bar{1}$0) surface facet. They proposed that the (0001) surface facet exhibited a large amount of oxygen vacancy as well as unpaired dangling bonds, contributing much in gas molecular adsorption favorability, so that the gas sensing properties improved.

Fig. 1.8 (a) shows a crystal structure of hexagonal ZnO with both (0001) and (10$\bar{1}$0) crystal facets. It is obvious that on the surface of (0001) facet, two dangling bonds in 2-fold coordinated sites and one dangling bond in 3-fold are existed. On the other hands, only one dangling bond in 3-fold coordinated sites can be found in (10$\bar{1}$0) crystal facet. ZnO nanosheet with dominantly (0001)-exposed facet should be able to adsorb more ionized oxygen species and gas molecules greatly, leading to the better sensing performance than ZnO with dominantly (10$\bar{1}$0)-exposed facet.

The influence of facet can also be clarified by DFT calculation. Fig. **Fig. 1.8** (b-f) display a model of O_2 adsorption on the (0001) and (10$\bar{1}$0) crystal facets. From the calculation, adsorption energies (ΔE_{ads}) when O_2 is added were -1.0665 eV and -0.5233 eV for (0001) and

$(10\bar{1}0)$-exposed crystal facet, respectively. It indicates that O₂ easily be adsorbed on the (0001) than $(10\bar{1}0)$ facet. It tracks well with the experimental evidence.
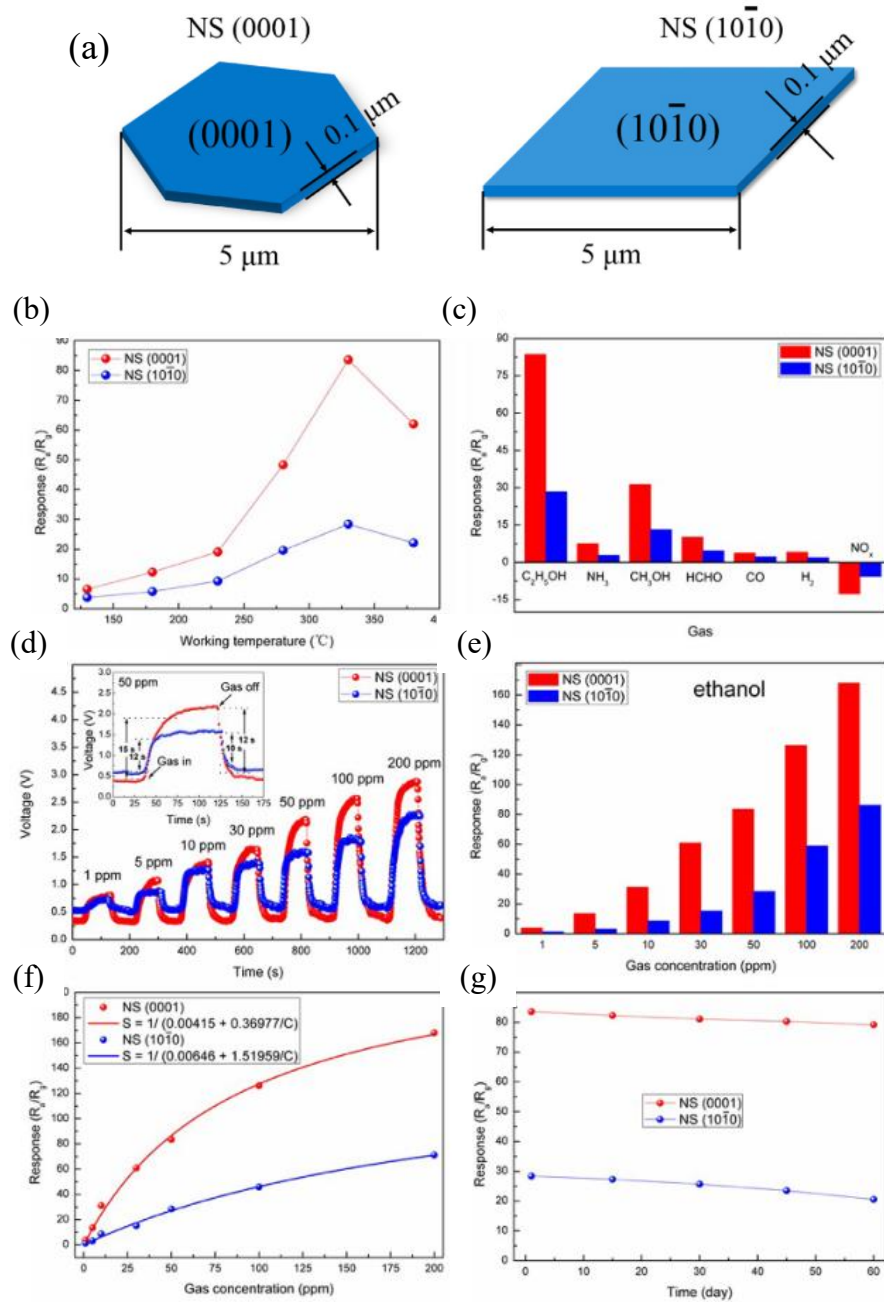
Fig. 1.7 (a) Schematic diagram of the crystal faces in ZnO nanosheets (b-f) gas sensing properties of ZnO nanosheets with (0001) and $(10\bar{1}0)$ facets to ethanol. Reproduced from reference.[70]
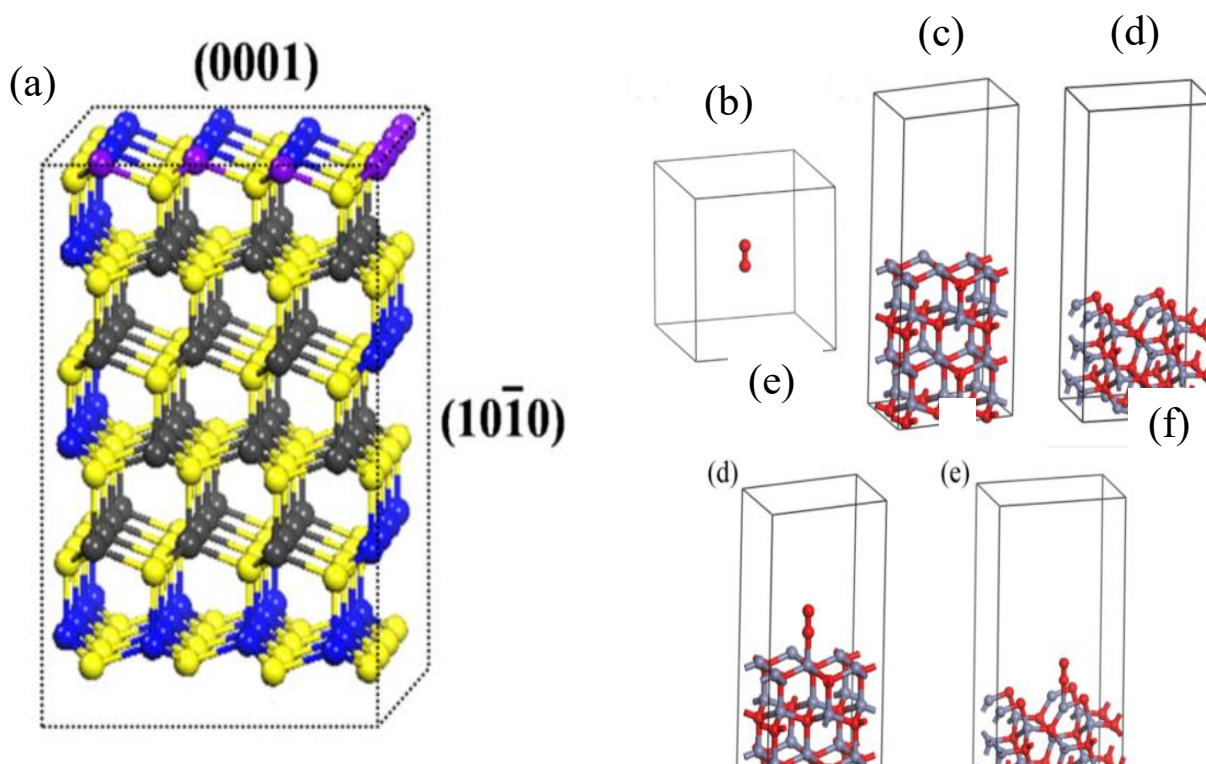
Fig. 1.8 (a) Atomic model of hexagonal wurtzite ZnO (b-f) oxygen adsorption model on the (0001) and (10$\bar{1}$0) exposed facets. Reproduced from reference. [70]

1.2.3.3 Surface functionalization *via* noble metal decoration

The noble metals surface-functionalized metal oxide semiconductors (MOS) can greatly boost the catalytic chemical reaction occurred at the surface. In this sense, the gas sensing performance can be also escalated because the greater reaction between ionized oxygen species and gas analytes. These following are most used noble metals: Au, Ag, Pt and Pd. Although there are several contributions of these metal precious for improving the gas sensing performance include the reduction of activation energy and Schottky barrier band depletion, the most critical role of the noble metal-loaded MOS is to introduce a spillover effect.[71] The spillover phenomenon is explained by an improved oxygen molecules dissociation into oxygen ionic species, usually forming a weak bond between oxygen molecule and noble metal. As shown in **Fig 1.9 (a-c)**, the dissociation of oxygen molecules was accelerated due to the high catalytic reaction. The electron amount and mobility were also increased, leading to not only high sensitivity but also faster response and recovery speed to allow a faster gas detection (**Fig 1.9 (d)**). This approach is also known as electronic sensitization. In some cases,

functionalization of noble metals also reduces the optimum working temperature due to the low potential barrier. This strategy, although shows a promising performance, potentially increases the cost of sensor device fabrication or poisoning, unless we can keep the performance high with a low amount of these noble metals.
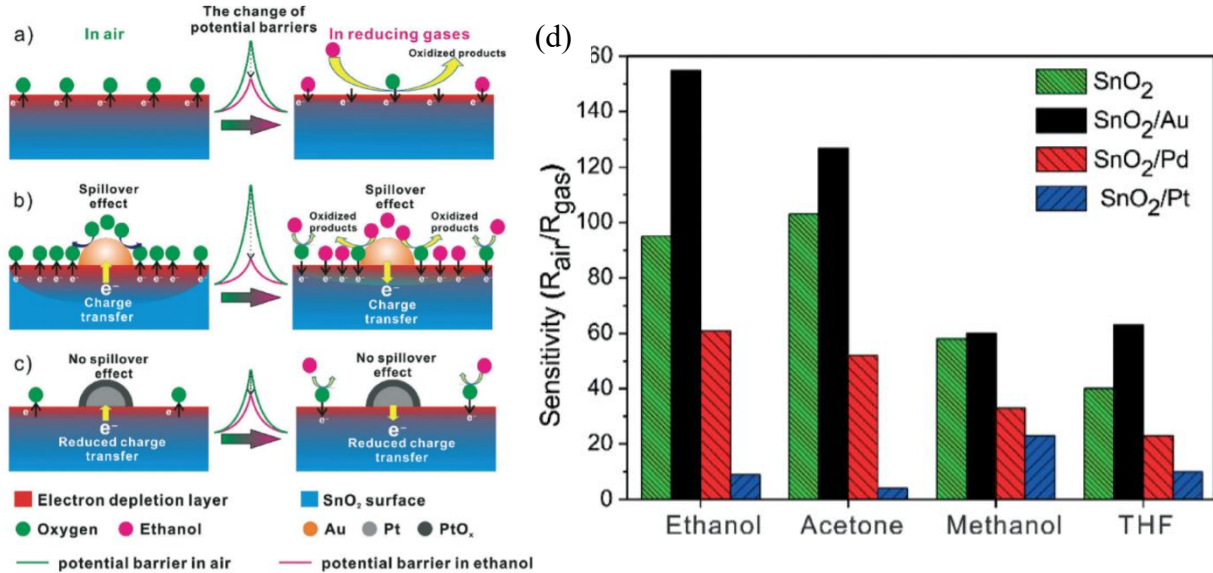
Fig. 1.9 (a-c) Schematic diagram illustrating the sensitization mechanism of noble metal-functionalized metal oxides and (d) their gas sensing performance. Reproduced from reference.[71]

1.2.3.4 Atomic Doping

Gas sensing mechanism involves heavily on the oxygen adsorption by taking electron near the valence band. Therefore, increasing charge carrier concentration can effectively improve the gas sensing performance of metal oxide semiconductor (MOS), because will be more oxygen species are adsorbed and the higher response can be expected. In fact, introducing an atomic doping into MOS crystal, in many cases, increased the charge carrier concentration. The addition of atomic doping also changes the particle size, porosity, specific surface area and crystal defect. Besides, band structures such as band gap and Fermi energy level will also be altered compared to pre-doping MOS. Normally, metal heteroatoms were used as atomic doping to replace a certain amount of metal in MOS crystal lattice.

DFT *ab initio* calculation is a conventional approach to elucidate the influence of metal doping on the band structure engineering and gas sensing properties and mechanism. Xue *et al.*[72] synthesized a flower-like SnO_2 doped by Pt nanoparticles. It is different with that Pt-decoration strategies, because in this case, Pt has been incorporated into SnO_2 crystal structures. They found that Pt-doped flower-like SnO_2 not only give a significant improvement to the sensitivity, but also reduce the optimum working temperature, stability and selectivity compared to that of pristine SnO_2 sensors. DFT calculation revealed that there are four sites (Sn_{5C}, Sn_{6C}, O_b and O_p) on which CH_4 molecules be adsorbed (**Fig. 1.10** (a)). Moreover, the adsorption energy of methane after Pt doping reduced greatly. As shown in **Fig. 1.10** (b)), the adsorption energy different of CH_4 (with H_3CH as a model) at the Op site is 4 times higher than in other sites and other models, revealing the H_3CH adsorption model doped with O_p adsorption
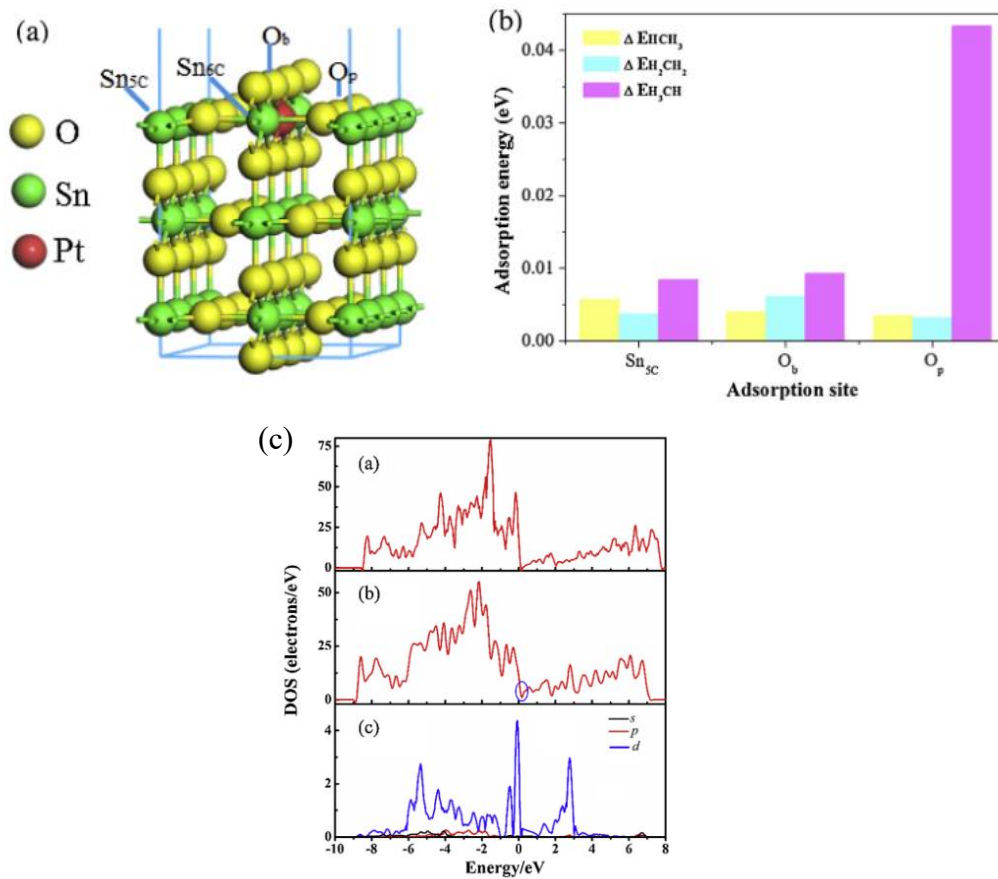
Fig. 1.10 (a) The computational model of Pt-doped SnO_2, with the atoms of Pt doping, (b) The absolute values of the adsorption energy reduction after doping of three methane adsorption models of Sn_{5c}, O_b and O_p. (c) Density of states for undoped (top) and Pt-doped SnO_2(110) surfaces (mid), and partial density of states of Pt (bottom). Reference [72]

sites on Pt surface is more conducive to methane adsorption. As we discussed in previous part, the metal doping changes the band structure. **Fig. 1.10** (c) shows total density of states of the

pristine and Pt-doped flower-like SnO_2. After Pt doping, a new electrons state emerged around the Fermi level, which is attributed to 5d states of Pt. Thereafter, the electrical resistance would be lower, promoting the fast transfer of electrons and minimized the required energy for electron excitation. Besides Pt, other metals doping with lower costs such as Ce, Ni, Al, etc., can be used to enhance the gas sensing properties of metal oxide semiconductor (MOS), as listed in **Table 1.4**. The examples of such atomic doping approach, in conclusion, is an attractive strategy that can be further explored in the future.

Table. 1.4 Metal-doped metal oxide semiconductor gas sensing materials

Material	Dopant	Morphology	Target gas (concentration)	Sensitivity (R_a/R_g) or (R_g/R_a)	Refs.
SnO_2	Ce	Nanoparticles	Acetone (50 ppm)	33.4 (undoped) 50.5 (doped)	[73]
SnO_2	Pt	Flower-like	Methane (500 ppm)	1.26 (undoped) 1.98 (doped)	[72]
SnO_2	Ni	Nanoparticles	Acetone (100 ppm)	137 (undoped) 169 (doped)	[74]
ZnO	Al	Nanoparticles	CO (50 ppm)	3 (undoped) 6.1 (doped)	[75]
ZnO	Fe	Porous Nanosheet	Ethanol (500 ppm)	10.4 (undoped) 52.3 (doped)	[76]
CuO	Cr	Nanorod	NO_2 (100 ppm)	7.5 (undoped) 134.2 (doped)	[77]
CuO	Mn	Nanoflakes	Ethanol (500 ppm)	3.9 (undoped) 8.0 (doped)	[78]

1.2.3.5 Heterojunction structures construction

With all respect to the above-mentioned approaches, build a heterojunction structure by combining two or more MOS materials is a promising strategy, since each component give complementarily advantages to subsidize their drawbacks and eventually lead to the improvement of sensing properties. Examples of its advantages include increased catalytic reaction, formation of depleted regions, adsorption site abundant, and band structures

alteration.[79] These reasons make the heterojunction structures an ideal approach if we consider the gas sensing mechanism. Based on the type of metal oxides, the hetero-contact can be classified into three cases, those are p-n heterojunction, n-n heterojunction and p-p heterojunction **(Fig. 1.11)**.[80]

In a p-n heterojunction, due to their charge carrier density (N_d) characteristic, electrons flow from the n-type to the p-type, while holes move in back directions, that is from the p-type to the n-type until the fermi energy level is equalized. Therefore, an expansion of the depleted region at the interface of heterojunction will occur and electrical resistance would subsequently increase in the ambient air or when oxygen species adsorption. During the materials is under
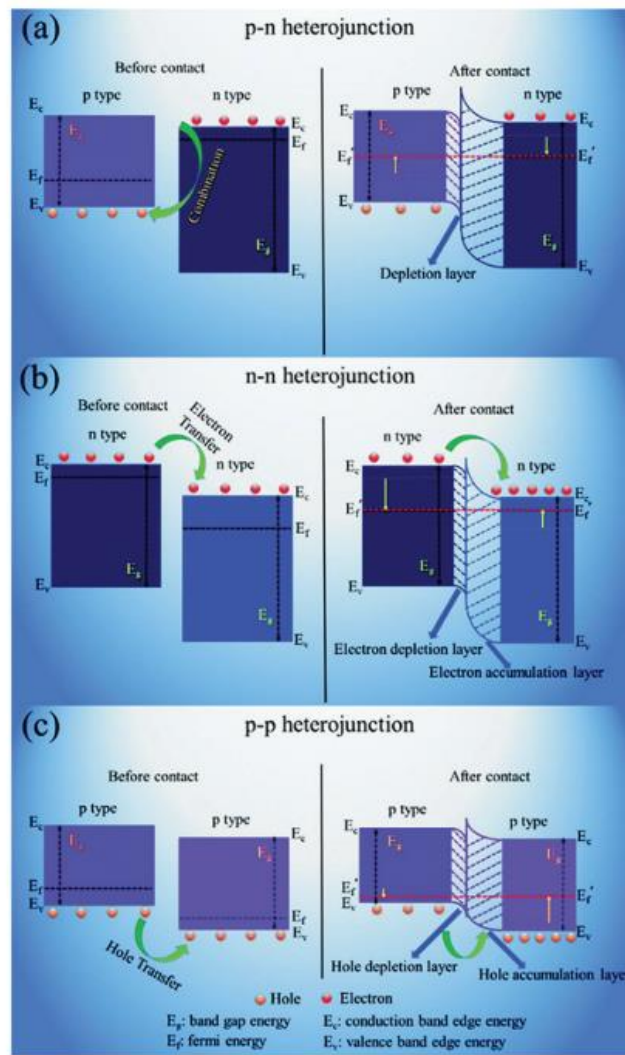
Fig. 1.11 Schematic illustrations of the energy band structures at hetero- junction interfaces of different types of heterojunctions: (a) p–n, (b) n–n and (c) p–p. [80]

the exposure of a reducing gas, the oxygen species on the surface reacts with the target gas and forced the electrons back to the conduction band of n-type and holes back to the p-type SMOX.

This process causes a decrease in overall electrical resistivity of the p-n heterostructures due to reducing of the interface barrier. When the reducing gas flow is stopped and the air is flown, the potential barrier will again be established. In the case of both n-n and p-p heterojunction, they are built because of the work function difference between two or more SMOX. To balance the charge carrier in the n-n and p-p heterojunction, the charge carrier flow occurs, and flow direction depends on the work function and charge carrier density. The existence of p-p and n-n heterojunction, of course, can provide more gas adsorption and better gas sensing performance compared to a single component.

In addition to above discussion, the metal oxides can also be combined with metallic phase materials to build the so-called Schottky and Ohmic junction for enhancing the gas sensing properties. Before their contact, metal and SMOX are electrically neutral with their respective work function level, φm (metallic work function) supposed to be higher than that of
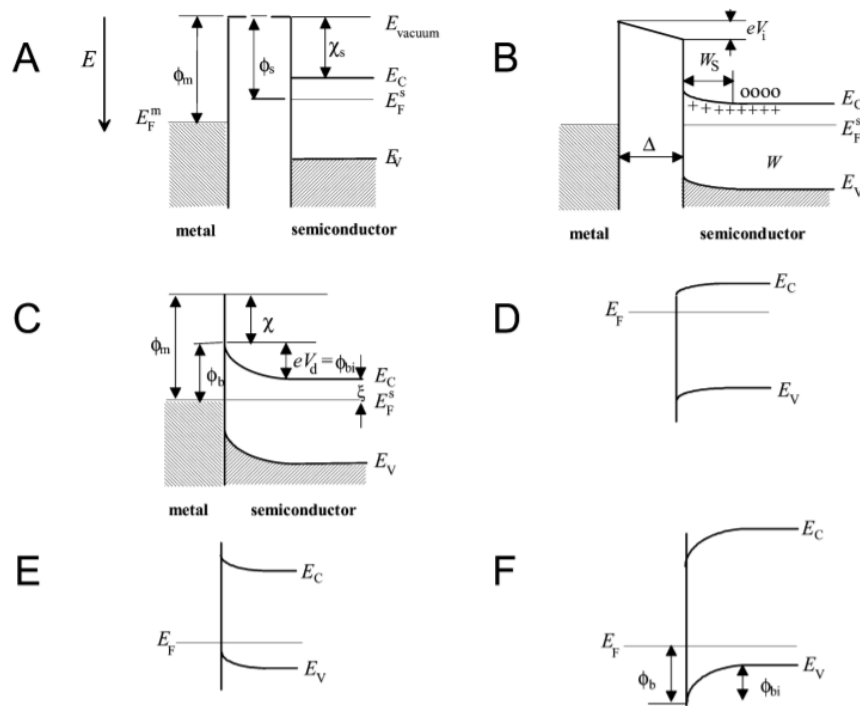
Fig. 1.12 Formation of a barrier between a metal and a semiconductor: (A) neutral and isolated; (B) electrically connected; (C) in perfect n-type Schottky contact ($\varphi m > \varphi s$); (D) n-type ohmic contact ($\varphi m < \varphi s$); (E) p-type ohmic contact ($\varphi m > \varphi s$); (F) p-type Schottky contact ($\varphi m < \varphi s$). o denotes electron in conduction band; + denotes donor ion.

φs (n-type semiconductor work function), as displayed in **Fig. 1.12 A**. When they are in electrically contact, the electron transfer from semiconductor into metal. This causes an excessive electrons on the metal and formation a depleted zone with a certain thickness (W_S)

in the near surface of semiconductor (**Fig. 1.12 B**). This also cause a formation of an interface dipole and production an internal electric field which is directed from the semiconductor to the metallic phase material. When they are in physical contact, the gradient of potential barrier in the depletion layer governs the electric resistivity which induce a well-known band-bending. The band-bending direction and type of contact largely depend on the work function position and type of semiconductor. In the case of n-type, if the work function of metal is higher than that of semiconductor ($\varphi m > \varphi s$), the Schottky contact should be build (**Fig. 1.12 C**). In fact, otherwise, the contact is biased so that electrons flow from the semiconductor to the metal. They encounter no barrier due to the $\varphi m < \varphi s$. It is called by ohmic contact (**Fig. 1.12 D**). In a p-type, an ohmic contact, in contrary, is built when $\varphi m > \varphi s$ as shown in **Fig. 1.12 E** and Schottky junction is formed if the φm falls behind φs ($\varphi m < \varphi s$) as shown in **Fig. 1.12 F**.

To get better understanding on how these heterojunction improve the gas sensing properties, one representative study is taken. Na *et al.*[81] synthesized Mn_3O_4-decorated ZnO NBs for the detection of ethanol gas. The gas sensing properties of Mn_3O_4-decorated ZnO were compared to the pristine ZnO NBs or Mn_3O_4 NWs. **Fig. 1.13** shows that both ZnO NBs and Mn_3O_4-decorated ZnO NBs behave like n-type semiconductor response. Meanwhile the ZnO−$ZnMn_2O_4$ core−shell NCs or Mn_3O_4 NWs showed p-type gas sensing behaviors. To note, both $ZnMn_2O_4$ and Mn_3O_4 are p-type semiconductors. This result indicates that the conduction and chemoresistive variation in are dominated by continuous p-type $ZnMn_2O_4$ shell layers. As we can see, the response of Mn_3O_4-decorated ZnO NBs exceeded the pristine ZnO NBs and Mn_3O_4 NWs. These results clearly demonstrate that gas response selectivity can be enhanced or tuned by the configurational design of radial p−n junctions in heterostructures.

Fig. 1.13. Sensing transients to 100 ppm C_2H_5OH at 400 °C: (a) ZnO NBs, (b) Mn_3O_4-decorated ZnO NBs, (c) ZnO−$ZnMn_2O_4$ NCs, and (d) Mn_3O_4 NWs. Reproduced from reference[81]. Copyright American Chemical Society (2012).
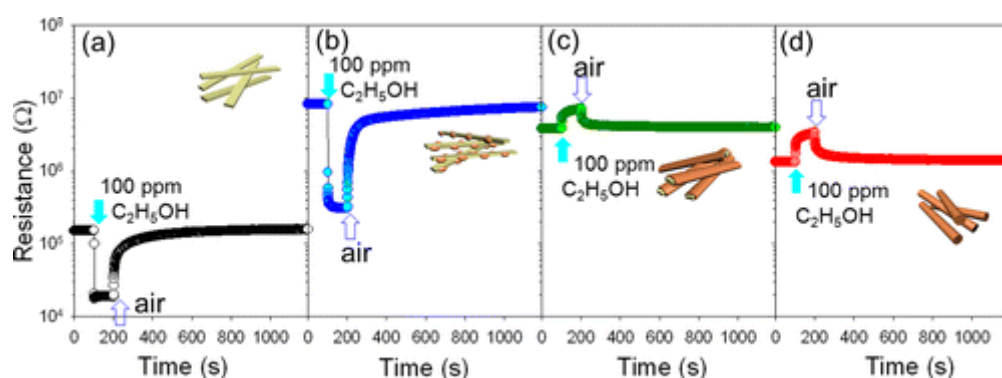
In fact, the SMOX can also be combined with polymeric or organic semiconductors resulting a heterostructures. However, the corresponding discussion is beyond the thesis scope.

1.3 Principle of non-hydrolytic synthesis of metal oxide semiconductor

In general, semiconducting metal oxides can be synthesized by physical and chemical method.[82,83] Physical methods consisted of pulsed laser deposition (PLD), physical or chemical vapor deposition (PVD or CVD), spray pyrolysis, etc., and chemical method or commonly well-known as wet-chemical method comprised of precipitation, sol–gel, reverse micelle, thermal decomposition, solvothermal, hydrothermal, microwave-assisted and flow reactor synthesis. Although physical method can produce a nearly perfect crystalline and amorphous SMOX nanostructures, due to its overly complex and expensive apparatus and time-consuming, it is not a favorable method, or it cannot be conducted by every scientist. Wet chemical approach can be an alternative synthetic method to fabricate nanostructured SMOX. Hydrothermal and solvothermal approaches are gaining popularity among other counterparts due to their controllability in the synthetic parameters, leading to the controllability of properties of the obtained materials.[84–90] In a particular, hydrothermal method or some scientists call as "aqueous approach" is defined as the conversion of a precursor solution into a solid-state material by using water as a solvent. The precursors or the starting materials can be either metals salts such as chlorides, sulfates, nitrates or metal organic such as metal alkoxides. Due to the use of waters, the inorganic solids obtained from this process, are generally owing low amount of organic impurities and good surface accessibility.[91–93] However, the morphological feature such as particle size and shape, cannot be easily controlled due to the fast polymerization or hydrolysis reaction. It is still possible to control their morphology by using surfactants, but once again, the morphology cannot be easily predicted since one surfactant is capable to shape a well-defined morphology of metal oxide but may not be work to other metal oxides.[94] Meanwhile, its counterpart, solvothermal treatment or well-known as non-aqueous approach, the transformation of starting materials solution is induced in an organic or mixed organics solvents with the exclusion of water. The wide range of precursors is available not limited to metal salts and alkoxides but also acetates and acetylacetonates.[95] The organic solvents act as an oxygen source during the transformation process and can influence the size, shape, sometime facet-selective, porosity and inorganic composition or crystal structures.[96] Although the excellent control over crystal size of inorganic solids with

narrow size distribution and low agglomeration can be obtained, the large amount of organic impurities existed on the surface in addition to the potential toxicity of the solvents itself. A comparative literature of benefits and disbenefits of aqueous and non-aqueous method is listed in **Table. 1.5**. Another interesting feature of non-aqueous approach is the yield higher than 80% which make this approach economically preferable. From the scientific point of view, the absence of surfactant can simplify the chemical reaction pathway. As previously discussed, excellent control of the particle size and shaping down to nanometer scale are an important factor in improving the gas sensing properties, the synthesis process to produce metal oxide materials in this thesis will be based on non-aqueous approach. We will further discuss how the choice of solvent largely influences their crystal shape and size in detail.

Table 1.5 Benefits and disbenefits of Aqueous and Non-aqueous solvent approach[88]

	Hydrothermal (Aqueous)	**Solvothermal (Non-Aqueous)**
Benefits	Low amount of organic impurities	Excellent control over crystal size
	Nontoxic solvents	Narrow size distribution
	Simple, robust and widely applicable synthesis	Low agglomeration formation
	Good accessibility of the nanoparticles surface	Good redispersibility
Disbenefits	Less control over crystallite size and shape	Large amount of organic impurities
	Broader size distribution	Toxicity of solvents
	Agglomeration tendency	Restricted accessibility of the nanoparticle surface
	Restricted redispersibility	Complex reaction mixture

There are numerous reports on the synthesis of inorganic solids nanomaterials using nonaqueous process and the number are rapidly growing in a recent year, this alone indicates the potentiality of the process a versatile alternative to aqueous method.[88,97–102] Based on these studies, the chemical pathway can be summarized into 5 major reactions (**Fig. 1.14**), accompanied by an example for each reaction. Alkyl halide elimination (reaction 1) is the polymerization reaction between metal salts and metal alkoxides under the use of alcohol
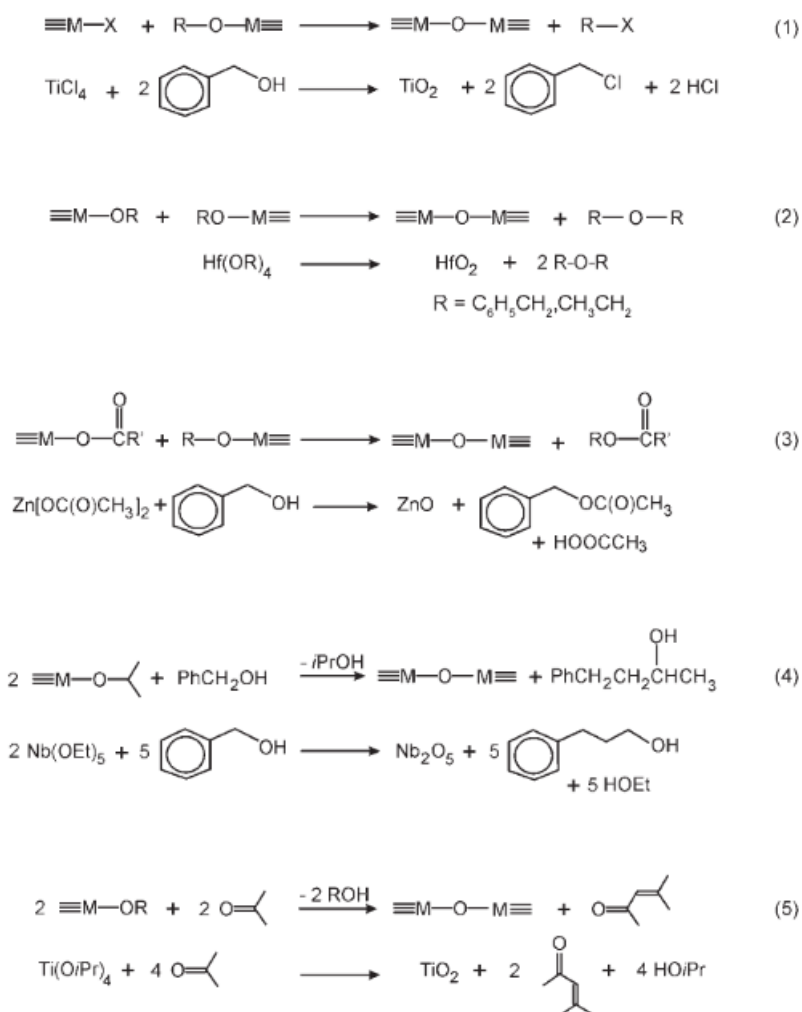
Fig. 1.14. Selected condensation steps in nonaqueous sol–gel processes together with one example. 1) Alkyl halide elimination, 2) ether elimination, 3) ester elimination, 4) C-C bond formation between benzylic alcohols and alkoxides, 5) aldol-like condensation reactions. [88]

solvent. One of example is the condensation between TiCl$_4$ and benzyl alcohol resulting in an TiO$_2$ anatase nanostructures.[103] Ether elimination (reaction 2) occurs when two metal oxides condensates with the release of organic ether. The mechanism worked for the synthesis of HfO$_2$ nanoparticles.[104] Ester elimination process (reaction 3) is the reaction between metal carboxylate and metal alkoxides or between metal carboxylates and alcohols solvents,

exemplified by the synthesis of ZnO nanoparticles which involves the reaction between zinc acetate and benzyl alcohol.[105] These first three routes are the most common reactions in nonaqueous method. C-C bond formation (reaction 4) is induced by the excellent catalytic activity of the metal centers in the alkoxy groups, as proven by the case of formation of Nb_2O_5 nanoparticles from $Nb(OEt)_5$ in or BaTiO3 nanoparticles from $Ti(iOPr)_4$ and Ba metal in benzyl alcohol solvent.[106,107] Aldol condensation (reaction 5) involves the use of ketones as solvents and two carbonyl compounds with the release of water molecules. The well-known example is the formation of TiO_2 in acetone solvent.[108]

As we can see from the above examples, almost all metal oxides, either binary or ternary system can be successfully obtained with a well-defined nanostructure. **Fig. 1.15** shows TEM observation of some representative of metal oxides prepared by nonaqueous approaches.[109] Well-dispersed nanostructured ranging from 2-5 nm was formed in the case of CeO_2, ZrO_2, HfO_2, SnO_2-doped In_2O_3, $BaTiO_3$, and Fe_3O_4.

However, the critical drawback rises in this approach is that the existence of organic compound in the form of surface functional groups in the obtained nano-oxide particles. This can diminish the accessibility of the surface, that is a very critical issues when the metal oxides are applied as gas sensing materials which relies so much on the surface reaction. In fact, the surface functional groups come from excess organics solvent can give a different in the effective surface charges depends on the attached organic molecules. Therefore, in this point of view, the particular drawback can potentially be turned into benefits when we would like to combine two or more metal oxides. Ideally, two oxides with different surface charge (one negative and one positive), if they are self-assembled, the interface contacts should be very intimate due to electrostatic force. The interface contact is also a very crucial factor in designing an oxide nanocomposite-based gas sensing material.
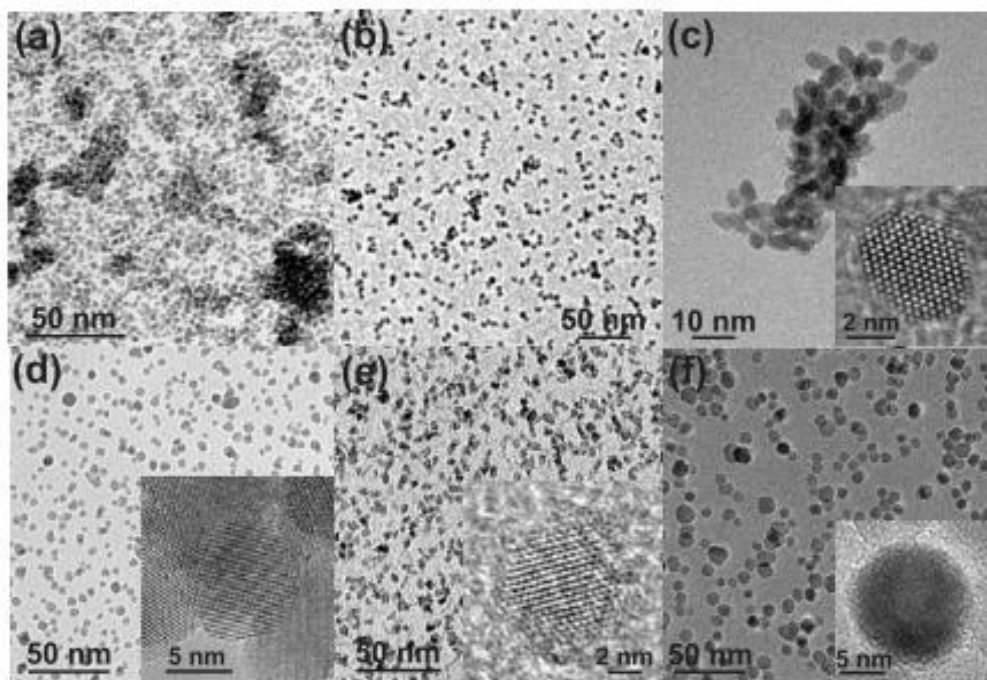
Fig. 1.15 TEM overview images of various metal oxide nanoparticles obtained from halide-free precursors in benzyl alcohol: (a) CeO_2, (b) ZrO_2, (c) HfO_2, (d) SnO_2-doped In_2O_3, (e) $BaTiO_3$, and (f) Fe_3O_4. [109]

1.4 Effective Surface charge

The effective surface charge and adsorption properties of the metal oxides nanostructure are two common parameters to be measured in surface chemistry. They are probed by means of (surface enhanced Raman spectroscopy (SERS) and Fourier transform infrared (FTIR) spectroscopy) and microscopic (scanning tunneling microscopy (STM) and atomic force microscopy (AFM)). One study [110] showed the detection of TMA^+ and $ClO4^-$ in the TiO_2 particles by using surface titration by internal reflection spectroscopy (STIRS). They suspected the remained charge impurities originated from tetramethylammonium hydroxide [TMAOH] and tetramethylammonium perchlorate [TMAP] used in the synthesis. To quantitively measure the exact value of the surface charge on the metal oxides material, zeta potential measurement is a very versatile method.[111] The relation between zeta potential of oxide nanoparticles and electronegativity of a metal ion as well as the charging mechanism was previously studied.[112,113] One of the examples[113] is the case of ZnO with different surface charge. ZnO with negatively charge (-43.0 mV) can be obtained by dissolution in the citric acid or sodium citrate from the ZnO with neutral charge. Meanwhile, changing citrate into L-serine

or HEPES (4-(2-hydroxyethyl)-1-piperazineethanesulfonic acid), ZnO with positively charge (+26.3 mV) is achieved. They suggested that the attached organic molecules onto the ZnO surfaces is through either electrostatic interactions or partial coordination bonding. Also, the organic functionalization induced surface charge can also be found in the negatively charge Si as shown in **Fig. 1.16**. Silica particles was partially covered by 3-aminopropyl groups and 3-(trihydroxysilyl)-propylmethylphosphonate as the result of synthesis process using 3-aminopropyl-triethoxysilane. The surface charge was controlled by the organic molecules, instead of silica particles.
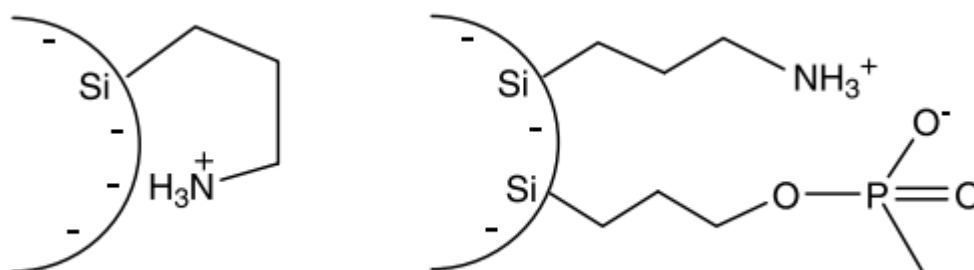
Fig. 1.16. Stabilization of nanoparticles by interaction between amine and phosphonate

1.5 Research Objectives

As introduced above, the semiconducting metal oxides (SMOX) are very promising materials for sensor applications to detect various kinds of dangerous gases including VOCs and non-VOCs which are the major environmental air pollutants. The sensor development based on SMOX materials has been started over centuries and is still progressing since the environmental air pollutions remains a grand challenge. Practically, the SMOX should be precisely designed to meet the sensors' performance demand, such as outstanding responsivity, excellent selectivity, low detection limit, high durability and cost-effective. Moreover, a fabrication method largely influences the phase structures, physicochemical and electronic properties of the metal oxides. Solvothermal treatment, in some extent, is a non-aqueous approach to excellently control these properties because their controllability upon the chemical reaction. The knowledge development on this synthetic method is at an early stage, especially on how the various combination of the solvents is affecting the surface effective charge, surface facet, particle size and porous structure of metal oxides and on how the tunable surface charge

can be beneficial for their hybridization with another metal oxides and/or non-oxides. In fact, although the combination of two or more sensing materials always lead to the enhancement of their gas sensing properties, the retention of their benefit from their original properties can be very difficult because the combination process involves chemical or physical reaction in a severe environment. Therefore, there are many opportunities that this thesis can contribute.

In short, the thesis focuses on 3 main research objectives:

1. Investigate the influence of mixed organic solvents on morphology, surface charge, and exposed facets of the metal oxides synthesized solvothermally and their gas sensing properties

2. Investigate the effect of the surface charge on the hybridization of metal oxides composites and their gas sensing performance

3. Develop a robust method for improving VOCs gas sensing performance of metal oxides and their hybrid with other oxides nanostructures or 2D materials.

1.6 References

1   K. Wetchakun, T. Samerjai, N. Tamaekong, C. Liewhiran, C. Siriwong, V. Kruefu, A. Wisitsoraat, A. Tuantranont and S. Phanichphant, Semiconducting metal oxides as sensors for environmentally hazardous gases, *Sensors Actuators, B Chem.*, 2011, **160**, 580–591.

2   J. Cherniwchan, Economic growth, industrialization, and the environment, *Resour. Energy Econ.*, 2012, **34**, 442–467.

3   A. Esplugues, F. Ballester, M. Estarlich, S. Llop, V. Fuentes-Leonarte, E. Mantilla and C. Iñiguez, Indoor and outdoor air concentrations of BTEX and determinants in a cohort of one-year old children in Valencia, Spain, *Sci. Total Environ.*, 2010, **409**, 63–69.

4   E. Cetin, M. Odabasi and R. Seyfioglu, Ambient volatile organic compound (VOC) concentrations around a petrochemical complex and a petroleum refinery, *Sci. Total Environ.*, 2003, **312**, 103–112.

5   T. Ohura, T. Amagai, X. Shen, S. Li, P. Zhang and L. Zhu, Comparative study on indoor air quality in Japan and China: Characteristics of residential indoor and outdoor VOCs, *Atmos. Environ.*, 2009, **43**, 6352–6359.

6   J. E. Colman Lerner, E. Y. Sanchez, J. E. Sambeth and A. A. Porta, Characterization and health risk assessment of VOCs in occupational environments in Buenos Aires, Argentina, *Atmos. Environ.*, 2012, **55**, 440–447.

7   T. Yang, P. Zhang, B. Xu and J. Xiong, Predicting VOC emissions from materials in vehicle cabins: Determination of the key parameters and the influence of environmental factors, *Int. J. Heat Mass Transf.*, 2017, **110**, 671–679.

8   W. P. L. Carter, Development of ozone reactivity scales for volatile organic compounds, *J. Air Waste Manag. Assoc.*, 1994, **44**, 881–899.

9   J. N. Cape, Effects of airborne volatile organic compounds on plants, *Environ. Pollut.*, 2003, **122**, 145–157.

10   D. R. Brower, The effects of cocaine on the central nervous system, *J. Am. Med. Assoc.*, 1886, **VI**, 59–62.

11   I. Kheirbek, S. Johnson, Z. Ross, G. Pezeshki, K. Ito, H. Eisl and T. Matte, Spatial variability in levels of benzene, formaldehyde, and total benzene, toluene, ethylbenzene and xylenes in New York City: A land-use regression study, *Environ. Heal. A Glob. Access Sci. Source*, 2012, **11**, 1.

12   N. Miura, T. Koga, M. Nakatou, P. Elumalai and M. Hasei, Electrochemical NOx sensors based on stabilized zirconia: Comparison of sensing performances of mixed-potential-type and impedancemetric NOx sensors, *J. Electroceramics*, 2006, **17**, 979–986.

13   A. Afzal, N. Cioffi, L. Sabbatini and L. Torsi, NO x sensors based on semiconducting metal oxide nanostructures: Progress and perspectives, *Sensors Actuators, B Chem.*, 2012, **171**–**172**, 25–42.

14   J. Liao, Z. Li, G. Wang, C. Chen, S. Lv and M. Li, ZnO nanorod/porous silicon nanowire hybrid structures as highly-sensitive NO2 gas sensors at room temperature, *Phys. Chem. Chem. Phys.*, 2016, **18**, 4835–4841.

15   B. Son, W. Yang, P. Breysse, T. Chung and Y. Lee, Estimation of occupational and nonoccupational nitrogen dioxide exposure for Korean taxi drivers using a microenvironmental model, *Environ. Res.*, 2004, **94**, 291–296.

16   E. G. C. Neiva, M. M. Oliveira, M. F. Bergamini, L. H. Marcolino and A. J. G. Zarbin,

One material, multiple functions: Graphene/Ni(OH)2 thin films applied in batteries, electrochromism and sensors, *Sci. Rep.*, 2016, **6**, 1–14.

17   H. Ji, W. Zeng and Y. Li, Gas sensing mechanisms of metal oxide semiconductors: A focus review, *Nanoscale*, 2019, **11**, 22664–22684.

18   P. H. Suman, A. A. Felix, H. L. Tuller, J. A. Varela and M. O. Orlandi, Comparative gas sensor response of SnO2, SnO and Sn3O4 nanobelts to NO2 and potential interferents, *Sensors Actuators, B Chem.*, 2015, **208**, 122–127.

19   A. Hermawan, Y. Asakura, M. Inada and S. Yin, One-step synthesis of micro-/mesoporous SnO2 spheres by solvothermal method for toluene gas sensor, *Ceram. Int.*, 2019, **45**, 15435–15444.

20   W. Li, S. Ma, Y. Li, G. Yang, Y. Mao, J. Luo, D. Gengzang, X. Xu and S. Yan, Enhanced ethanol sensing performance of hollow ZnO-SnO2 core-shell nanofibers, *Sensors Actuators, B Chem.*, 2015, **211**, 392–402.

21   A. Salehi, A highly sensitive self heated SnO2 carbon monoxide sensor, *Sensors Actuators, B Chem.*, 2003, **96**, 88–93.

22   Y. J. Choi, I. S. Hwang, J. G. Park, K. J. Choi, J. H. Park and J. H. Lee, Novel fabrication of an SnO2 nanowire gas sensor with high sensitivity, *Nanotechnology*, 2008, **19**, 095508.

23   N. Li, Y. Fan, Y. Shi, Q. Xiang, X. Wang and J. Xu, A low temperature formaldehyde gas sensor based on hierarchical SnO/SnO2 nano-flowers assembled from ultrathin nanosheets: Synthesis, sensing performance and mechanism, *Sensors Actuators, B Chem.*, 2019, **294**, 106–115.

24   J. Tamaki, T. Maekawa, N. Miura and N. Yamazoe, CuO-SnO2 element for highly sensitive and selective detection of H2S, *Sensors Actuators B. Chem.*, 1992, **9**, 197–203.

25   J. Liu, X. Huang, G. Ye, W. Liu, Z. Jiao, W. Chao, Z. Zhou and Z. Yu, H$_2$S detection sensing characteristic of CuO/SnO2 sensor, *Sensors*, 2003, **3**, 110–118.

26   X. Li, Y. Wang, Y. Lei and Z. Gu, Highly sensitive H 2S sensor based on template-synthesized CuO nanowires, *RSC Adv.*, 2012, **2**, 2302–2307.

27   B. Sakthivel and G. Nammalvar, Selective ammonia sensor based on copper

oxide/reduced graphene oxide nanocomposite, *J. Alloys Compd.*, 2019, **788**, 422–428.

28   O. Lupan, V. Postica, V. Cretu, N. Wolff, V. Duppel, L. Kienle and R. Adelung, Single and networked CuO nanowires for highly sensitive p-type semiconductor gas sensor applications, *Phys. Status Solidi - Rapid Res. Lett.*, 2016, **10**, 260–266.

29   F. Zhang, A. Zhu, Y. Luo, Y. Tian, J. Yang and Y. Qin, CuO nanosheets for sensitive and selective determination of H2S with high recovery ability, *J. Phys. Chem. C*, 2010, **114**, 19214–19219.

30   X. Liu, J. Zhang, Y. Kang, S. Wu and S. Wang, Brochantite tabular microspindles and their conversion to wormlike CuO structures for gas sensing, *CrystEngComm*, 2012, **14**, 620–625.

31   C. Yang, X. Su, J. Wang, X. Cao, S. Wang and L. Zhang, Facile microwave-assisted hydrothermal synthesis of varied-shaped CuO nanoparticles and their gas sensing properties, *Sensors Actuators, B Chem.*, 2013, **185**, 159–165.

32   H. J. Park, N. J. Choi, H. Kang, M. Y. Jung, J. W. Park, K. H. Park and D. S. Lee, A ppb-level formaldehyde gas sensor based on CuO nanocubes prepared using a polyol process, *Sensors Actuators, B Chem.*, 2014, **203**, 282–288.

33   L. Liao, Z. Zhang, B. Yan, Z. Zheng, Q. L. Bao, T. Wu, C. M. Li, Z. X. Shen, J. X. Zhang, H. Gong, J. C. Li and T. Yu, Multifunctional CuO nanowire devices: P-type field effect transistors and CO gas sensors, *Nanotechnology*, 2009, **20**, 085203.

34   H. J. Kim and J. H. Lee, Highly sensitive and selective gas sensors using p-type oxide semiconductors: Overview, *Sensors Actuators, B Chem.*, 2014, **192**, 607–627.

35   M. M. Gomaa, G. RezaYazdi, M. Rodner, G. Greczynski, M. Boshta, M. B. S. Osman, V. Khranovskyy, J. Eriksson and R. Yakimova, Exploring NiO nanosize structures for ammonia sensing, *J. Mater. Sci. Mater. Electron.*, 2018, **29**, 11870–11877.

36   J. Fu, C. Zhao, J. Zhang, Y. Peng and E. Xie, Enhanced gas sensing performance of electrospun Pt-functionalized NiO nanotubes with chemical and electronic sensitization, *ACS Appl. Mater. Interfaces*, 2013, **5**, 7410–7416.

37   H. Wang, J. Gao, Z. Li, Y. Ge, K. Kan and K. Shi, One-step synthesis of hierarchical α-Ni(OH)$_2$ flowerlike architectures and their gas sensing properties for NOx at room temperature, *CrystEngComm*, 2012, **14**, 6843–6852.

38 W. Huang, S. Ding, Y. Chen, W. Hao, X. Lai, J. Peng, J. Tu, Y. Cao and X. Li, 3D NiO hollow sphere/reduced graphene oxide composite for high-performance glucose biosensor, *Sci. Rep.*, 2017, **7**, 1–11.

39 W. Shang, D. Wang, B. Zhang, C. Jiang, F. Qu and M. Yang, Aliovalent Fe(iii)-doped NiO microspheres for enhanced butanol gas sensing properties, *Dalt. Trans.*, 2018, **47**, 15181–15188.

40 Y. Lv, K. Huang, W. Zhang, S. Ran, F. Chi, B. Yang and X. Liu, High-performance gas-sensing properties of octahedral NiO crystals prepared via one-step controllable synthesis route, *Cryst. Res. Technol.*, 2014, **49**, 109–115.

41 L. Liu, Y. Zhang, G. Wang, S. Li, L. Wang, Y. Han, X. Jiang and A. Wei, High toluene sensing properties of NiO-SnO$_2$ composite nanofiber sensors operating at 330 °c, *Sensors Actuators, B Chem.*, 2011, **160**, 448–454.

42 T. T. Le Dang, M. Tonezzer and V. H. Nguyen, Hydrothermal Growth and Hydrogen Selective Sensing of Nickel Oxide Nanowires, *J. Nanomater.*, 2015, **2015**, 1–8.

43 H. Gao, L. Zhao, L. Wang, P. Sun, H. Lu, F. Liu, X. Chuai and G. Lu, Ultrasensitive and low detection limit of toluene gas sensor based on SnO$_2$-decorated NiO nanostructure, *Sensors Actuators, B Chem.*, 2018, **255**, 3505–3515.

44 H. I. Chen, C. Y. Hsiao, W. C. Chen, C. H. Chang, T. C. Chou, I. P. Liu, K. W. Lin and W. C. Liu, Characteristics of a Pt/NiO thin film-based ammonia gas sensor, *Sensors Actuators, B Chem.*, 2018, **256**, 962–967.

45 T. Li, W. Zeng, H. Long and Z. Wang, Nanosheet-assembled hierarchical SnO$_2$ nanostructures for efficient gas-sensing applications, *Sensors Actuators, B Chem.*, 2016, **231**, 120–128.

46 L. Zhu, W. Zeng, Y. Li and J. Yang, Enhanced ethanol gas-sensing property based on hollow MoO3 microcages, *Phys. E Low-Dimensional Syst. Nanostructures*, 2019, **106**, 170–175.

47 X. Xiao, L. Liu, J. Ma, Y. Ren, X. Cheng, Y. Zhu, D. Zhao, A. A. Elzatahry, A. Alghamdi and Y. Deng, Ordered Mesoporous Tin Oxide Semiconductors with Large Pores and Crystallized Walls for High-Performance Gas Sensing, *ACS Appl. Mater. Interfaces*, 2018, **10**, 1871–1880.

48 N. S. Ramgir, S. K. Ganapathi, M. Kaur, N. Datta, K. P. Muthe, D. K. Aswal, S. K. Gupta and J. V. Yakhmi, Sub-ppm H_2S sensing at room temperature using CuO thin films, *Sensors Actuators, B Chem.*, 2010, **151**, 90–96.

49 C. Wang, L. Yin, L. Zhang, D. Xiang and R. Gao, Metal oxide gas sensors: Sensitivity and influencing factors, *Sensors*, 2010, **10**, 2088–2106.

50 C. Xu, J. Tamaki, N. Miura and N. Yamazoe, Grain size effects on gas sensitivity of porous SnO2-based elements, *Sensors Actuators B. Chem.*, 1991, **3**, 147–155.

51 A. Gurlo, M. Ivanovskaya, N. Bârsan, M. Schweizer-Berberich, U. Weimar, W. Göpel and A. Diéguez, Grain size control in nanocrystalline In_2O_3 semiconductor gas sensors, *Sensors Actuators, B Chem.*, 1997, **44**, 327–333.

52 T. Kida, T. Doi and K. Shimanoe, Synthesis of monodispersed SnO_2 nanocrystals and their remarkably high sensitivity to volatile organic compounds, *Chem. Mater.*, 2010, **22**, 2662–2667.

53 J. H. Lee, Gas sensors using hierarchical and hollow oxide nanostructures: Overview, *Sensors Actuators, B Chem.*, 2009, 140, 319–336.

54 C. J. Martinez, B. Hockey, C. B. Montgomery and S. Semancik, Porous tin oxide nanostructured microspheres for sensor applications, *Langmuir*, 2005, **21**, 7937–7944.

55 K. Il Choi, H. R. Kim and J. H. Lee, Enhanced CO sensing characteristics of hierarchical and hollow In_2O_3 microspheres, *Sensors Actuators, B Chem.*, 2009, **138**, 497–503.

56 H. R. Kim, K. Il Choi, J. H. Lee and S. A. Akbar, Highly sensitive and ultra-fast responding gas sensors using self-assembled hierarchical SnO2 spheres, *Sensors Actuators, B Chem.*, 2009, **136**, 138–143.

57 A. Rothschild and Y. Komem, The effect of grain size on the sensitivity of nanocrystalline metal-oxide gas sensors, *J. Appl. Phys.*, 2004, **95**, 6374–6380.

58 F. Gyger, M. Hübner, C. Feldmann, N. Barsan and U. Weimar, Nanoscale SnO_2 hollow spheres and their application as a gas-sensing material, *Chem. Mater.*, 2010, **22**, 4821–4827.

59 J. Zhang, X. Liu, S. Wu, M. Xu, X. Guo and S. Wang, Au nanoparticle-decorated porous SnO_2 hollow spheres: A new model for a chemical sensor, *J. Mater. Chem.*, 2010, **20**,

6453–6459.

60   X. M. Yin, C. C. Li, M. Zhang, Q. Y. Hao, S. Liu, Q. H. Li, L. B. Chen and T. H. Wang, SnO_2 monolayer porous hollow spheres as a gas sensor, *Nanotechnology*, , DOI:10.1088/0957-4484/20/45/455503.

61   A. Rothschild and Y. Komem, On the relationship between the grain size and gas-sensitivity of chemo-resistive metal-oxide gas sensors with nanosized grains, in *Journal of Electroceramics*, 2004, vol. 13, pp. 697–701.

62   Y. X. Li, Z. Guo, Y. Su, X. B. Jin, X. H. Tang, J. R. Huang, X. J. Huang, M. Q. Li and J. H. Liu, Hierarchical Morphology-Dependent Gas-Sensing Performances of Three-Dimensional SnO2 Nanostructures, *ACS Sensors*, 2017, **2**, 102–110.

63   A. A. Firooz, A. R. Mahjoub and A. A. Khodadadi, Effects of flower-like, sheet-like and granular SnO2 nanostructures prepared by solid-state reactions on CO sensing, *Mater. Chem. Phys.*, 2009, **115**, 196–199.

64   P. Rai, W. K. Kwak and Y. T. Yu, Solvothermal synthesis of ZnO nanostructures and their morphology-dependent gas-sensing properties, *ACS Appl. Mater. Interfaces*, 2013, **5**, 3026–3032.

65   S. Bai, L. Chen, S. Chen, R. Luo, D. Li, A. Chen and C. C. Liu, Reverse microemulsion in situ crystallizing growth of ZnO nanorods and application for NO2 sensor, *Sensors Actuators, B Chem.*, 2014, **190**, 760–767.

66   D. P. Volanti, A. A. Felix, M. O. Orlandi, G. Whitfield, D. J. Yang, E. Longo, H. L. Tuller and J. A. Varela, The role of hierarchical morphologies in the superior gas sensing performance of CuO-based chemiresistors, *Adv. Funct. Mater.*, 2013, **23**, 1759–1766.

67   Y. Qin, F. Zhang, Y. Chen, Y. Zhou, J. Li, A. Zhu, Y. Luo, Y. Tian and J. Yang, Hierarchically porous CuO hollow spheres fabricated via a one-pot template-free method for high-performance gas sensors, *J. Phys. Chem. C*, 2012, **116**, 11994–12000.

68   X. Song, L. Gao and S. Mathur, Synthesis, characterization, and gas sensing properties of porous nickel oxide nanotubes, *J. Phys. Chem. C*, 2011, **115**, 21730–21735.

69   G. Zhu, C. Xi, H. Xu, D. Zheng, Y. Liu, X. Xu and X. Shen, Hierarchical NiO hollow microspheres assembled from nanosheet-stacked nanoparticles and their application in a gas sensor, *RSC Adv.*, 2012, **2**, 4236–4241.

70   J. Xu, Z. Xue, N. Qin, Z. Cheng and Q. Xiang, The crystal facet-dependent gas sensing properties of ZnO nanosheets: Experimental and computational study, *Sensors Actuators, B Chem.*, 2017, **242**, 148–157.

71   C. Liu, Q. Kuang, Z. Xie and L. Zheng, The effect of noble metal (Au, Pd and Pt) nanoparticles on the gas sensing performance of SnO2-based sensors: a case study on the {221} high-index faceted SnO2 octahedra, *CrystEngComm*, 2015, **17**, 6308–6313.

72   D. Xue, P. Wang, Z. Zhang and Y. Wang, Enhanced methane sensing property of flower-like SnO2 doped by Pt nanoparticles: A combined experimental and first-principle study, *Sensors Actuators, B Chem.*, 2019, **296**, 126710–126719.

73   X. Lian, Y. Li, X. Tong, Y. Zou, X. Liu, D. An and Q. Wang, Synthesis of Ce-doped SnO 2 nanoparticles and their acetone gas sensing properties, *Appl. Surf. Sci.*, 2017, **407**, 447–455.

74   S. H. Yan, S. Y. Ma, X. L. Xu, W. Q. Li, J. Luo, W. X. Jin, T. T. Wang, X. H. Jiang, Y. Lu and H. S. Song, Preparation of SnO2-ZnO hetero-nanofibers and their application in acetone sensing performance, *Mater. Lett.*, 2015, **159**, 447–450.

75   M. Hjiri, L. El Mir, S. G. Leonardi, A. Pistone, L. Mavilia and G. Neri, Al-doped ZnO for highly sensitive CO gas sensors, *Sensors Actuators, B Chem.*, 2014, **196**, 413–420.

76   A. Yu, J. Qian, H. Pan, Y. Cui, M. Xu, L. Tu, Q. Chai and X. Zhou, Micro-lotus constructed by Fe-doped ZnO hierarchically porous nanosheets: Preparation, characterization and gas sensing property, *Sensors Actuators, B Chem.*, 2011, **158**, 9–16.

77   S. R. Gawali, V. L. Patil, V. G. Deonikar, S. S. Patil, D. R. Patil, P. S. Patil and J. Pant, Ce doped NiO nanoparticles as selective NO2 gas sensor, *J. Phys. Chem. Solids*, 2018, **114**, 28–35.

78   R. N. Mariammal, K. Ramachandran, G. Kalaiselvan, S. Arumugam, B. Renganathan and D. Sastikumar, Effect of magnetism on the ethanol sensitivity of undoped and Mn-doped CuO nanoflakes, *Appl. Surf. Sci.*, 2013, **270**, 545–552.

79   J. M. Walker, S. A. Akbar and P. A. Morris, Synergistic effects in gas sensing semiconducting oxide nano-heterostructures: A review, *Sensors Actuators, B Chem.*, 2019, **286**, 624–640.

80   Z. Li, H. Li, Z. Wu, M. Wang, J. Luo, H. Torun, P. Hu, C. Yang, M. Grundmann, X. Liu and Y. Fu, Advances in designs and mechanisms of semiconducting metal oxide nanostructures for high-precision gas sensors operated at room temperature, *Mater. Horizons*, 2019, **6**, 470–506.

81   C. W. Na, S. Y. Park, J. H. Chung and J. H. Lee, Transformation of ZnO nanobelts into single-crystalline Mn 3O4 nanowires, *ACS Appl. Mater. Interfaces*, , DOI:10.1021/am301670x.

82   T. Guo, M. S. Yao, Y. H. Lin and C. W. Nan, A comprehensive review on synthesis methods for transition-metal oxide nanostructures, *CrystEngComm*, , DOI:10.1039/c5ce00034c.

83   A. V. Nikam, B. L. V. Prasad and A. A. Kulkarni, Wet chemical synthesis of metal oxide nanoparticles: A review, *CrystEngComm*, , DOI:10.1039/C8CE00487K.

84   B. L. Cushing, V. L. Kolesnichenko and C. J. O'Connor, Recent Advances in the Liquid-Phase Syntheses of Inorganic Nanoparticles, *ChemInform*, , DOI:10.1002/chin.200447224.

85   W. T. Yao and S. H. Yu, Recent advances in hydrothermal syntheses of low dimensional nanoarchitectures, *Int. J. Nanotechnol.*, 2007.

86   T. D. Nguyen, From formation mechanisms to synthetic methods toward shape-controlled oxide nanoparticles, *Nanoscale*, 2013.

87   S. K. Ghosh and A. Böker, Self-Assembly of Nanoparticles in 2D and 3D: Recent Advances and Future Trends, *Macromol. Chem. Phys.*, 2019.

88   N. Pinna and M. Niederberger, Surfactant-free nonaqueous synthesis of metal oxide nanostructures, *Angew. Chemie - Int. Ed.*, 2008, **47**, 5292–5304.

89   M. Jansen and E. Guenther, Oxide Gels and Ceramics Prepared by a Nonhydrolytic Sol-Gel Process, *Chem. Mater.*, , DOI:10.1021/cm00059a019.

90   W. J. Dawson, Hydrothermal synthesis of advanced ceramic powders, *Am. Ceram. Soc. Bull.*, , DOI:10.4028/www.scientific.net/ast.45.184.

91   D. Chen, X. Jiao and G. Cheng, Hydrothermal synthesis of zinc oxide powders with different morphologies, *Solid State Commun.*, , DOI:10.1016/s0038-1098(99)00472-x.

92   T. Adschiri, Y. Hakuta, K. Sue and K. Arai, Hydrothermal Synthesis of Metal Oxide Nanoparticles at Supercritical Conditions, *J. Nanoparticle Res.*, , DOI:10.1023/A:1017541705569.

93   M. M. Titirici, M. Antonietti and A. Thomas, A generalized synthesis of metal oxide hollow spheres using a hydrothermal approach, *Chem. Mater.*, , DOI:10.1021/cm052768u.

94   H. Y. Xu, H. Wang, Y. C. Zhang, W. L. He, M. K. Zhu, B. Wang and H. Yan, Hydrothermal synthesis of zinc oxide powders with controllable morphology, *Ceram. Int.*, , DOI:10.1016/S0272-8842(03)00069-5.

95   A. Styskalik, D. Skoda, C. E. Barnes and J. Pinkas, The power of non-hydrolytic sol-gel chemistry: A review, *Catalysts*, 2017, **7**, 168.

96   G. Garnweitner and M. Niederberger, Organic chemistry in inorganic nanomaterials synthesis, *J. Mater. Chem.*, 2008, **18**, 1171–1182.

97   M. V. Kovalenko, M. I. Bodnarchuk, R. T. Lechner, G. Hesser, F. Schäffler and W. Heiss, Fatty acid salts as stabilizers in size- and shape-controlled nanocrystal synthesis: The case of inverse spinel iron oxide, *J. Am. Chem. Soc.*, , DOI:10.1021/ja0692478.

98   H. Kominami, M. Kohno, Y. Takada, M. Inoue, T. Inui and Y. Kera, Hydrolysis of titanium alkoxide in organic solvent at high temperatures: A new synthetic method for nanosized, thermally stable titanium(IV) oxide, *Ind. Eng. Chem. Res.*, , DOI:10.1021/ie9901170.

99   C. S. Kim, B. K. Moon, J. H. Park, B. C. Choi and H. J. Seo, Solvothermal synthesis of nanocrystalline TiO2 in toluene with surfactant, *J. Cryst. Growth*, , DOI:10.1016/S0022-0248(03)01468-4.

100   C. H. Lee, M. Kim, T. Kim, A. Kim, J. Paek, J. W. Lee, S. Y. Choi, K. Kim, J. B. Park and K. Lee, Ambient pressure syntheses of size-controlled corundum-type In 2O3 nanocubes, *J. Am. Chem. Soc.*, , DOI:10.1021/ja063227o.

101   Y. Li, M. Afzaal and P. O'Brien, The synthesis of amine-capped magnetic (Fe, Mn, Co, Ni) oxide nanocrystals and their surface modification for aqueous dispersibility, *J. Mater. Chem.*, pagfes , DOI:10.1039/b517351e.

102   L. Č. Xiaomeng, X. Jimin, S. Yuanzhi and L. Jiamin, Surfactant-assisted hydrothermal

preparation of submicrometer-sized two-dimensional BiFeO$_3$ plates and their photocatalytic activity, *J. Mater. Sci.*, , DOI:10.1007/s10853-006-1401-0.

103   M. Niederberger, G. Garnweitner, J. Ba, J. Polleux and N. Pinna, Nonaqueous synthesis, assembly and formation mechanisms of metal oxide nanocrystals, *Int. J. Nanotechnol.*, , DOI:10.1504/IJNT.2007.013473.

104   N. Pinna, G. Garnweitner, M. Antonietti and M. Niederberger, Non-aqueous synthesis of high-purity metal oxide nanopowders using an ether elimination process, *Adv. Mater.*, , DOI:10.1002/adma.200400460.

105   I. Bilecka, I. Djerdj and M. Niederberger, One-minute synthesis of crystalline binary and ternary metal oxide nanoparticles, *Chem. Commun.*, , DOI:10.1039/b717334b.

106   M. Niederberger, G. Garnweitner, N. Pinna and M. Antonietti, Nonaqueous and halide-free route to crystalline BaTiO3, SrTiO3, and (Ba,Sr)TiO$_3$ nanoparticles via a mechanism involving C-C bond formation, *J. Am. Chem. Soc.*, pages , DOI:10.1021/ja0494959.

107   N. Pinna, M. Antonietti and M. Niederberger, A novel nonaqueous route to V$_2$O$_3$ and Nb $_2$O$_5$ nanocrystals, in *Colloids and Surfaces A: Physicochemical and Engineering Aspects*, 2004. page information

108   Y. Yin and A. P. Alivisatos, Colloidal nanocrystal synthesis and the organic-inorganic interface, *Nature*, 2005.

109   N. Niederberger, M., & Pinna, Surfactant-Assisted Synthesis. Metal Oxide Nanoparticles in Organic Solvents, 2009*Surfactant-Assisted Synthesis. Metal Oxide Nanoparticles in Organic Solvents*. page information

110   K. D. Dobson, P. A. Connor and A. J. McQuillan, Monitoring Hydrous Metal Oxide Surface Charge and Adsorption by STIRS, *Langmuir*, page numbers, , DOI:10.1021/la961053q.

111   A. Mikolajczyk, A. Gajewicz, B. Rasulev, N. Schaeublin, E. Maurer-Gardner, S. M. Hussain, J. Leszczynski and T. Puzyn, Zeta Potential (ζ) for Metal Oxide Nanoparticles: A Predictive Model Developed by Nano-QSPR Approach, *Chem. Mater.*, page numbers , DOI:10.1021/cm504406a.

112   Y. Takayama, H. Negishi, S. Nakamura, N. Koura, Y. Idemoto and F. Yamaguchi, Zeta

potential of various oxide particles and the charging mechanism, *J. Ceram. Soc. Japan*, , page numbers, DOI:10.2109/jcersj.107.119.

113 K. M. Kim, M. H. Choi, J. K. Lee, J. Jeong, Y. R. Kim, M. K. Kim, S. M. Paek and J. M. Oh, Physicochemical properties of surface charge-modified ZnO nanoparticles with different particle sizes, *Int. J. Nanomedicine*, page numbers, DOI:10.2147/IJN.S57923.

Chapter 2

Materials and Methodology

2.1 Introduction

In this chapter, we introduced the experimental setup, chemical reagents, and material characterization in brief. The gas sensing apparatus is illustrated, and the gas sensing evaluation parameters are described in detail. The detailed synthesis process of each sample presented in this thesis will be systematically explained in the respective chapters.

2.2 Chemical and Reagents

All the reagents in the experiment were analytical grade and used without further treatment. Tin chloride ($SnCl_2$, anhydrous, 99.8%), anhydrous copper acetate ($Cu(OAc)_2$, 97.0%), Nickel (II) chloride ($NiCl_2$, 99.9%), ethanol (dehydrated, purity min. 99.5%), 1-propanol (dehydrated, purity min. 99.5%), n-butanol (dehydrated, purity min. 99.5%), benzyl alcohols (dehydrated, purity min. 99.5%) and acetic acid (anhydrous, purity min. 99.7 %) were purchased from FUJIFILM Wako Pure Chemicals Corporation.

2.3 Material Characterizations

X-ray diffraction (XRD, Bruker AXS D2 PHASER) using CuKα radiation (λ= 1.5418 Å) was employed to characterize the phase compositions and crystallographic features of the obtained samples. The morphology, particle size, and lattice parameters were examined by transmission electron microscopy (TEM, JEOL JEM–2010 and JEM-ARM200F) and field-emission scanning electron microscopy (FE-SEM, Hitachi S4800). Specific surface area and pore-size distribution were measured and calculated from the results of N_2 adsorption/desorption (Quantachrome, NOVA 4200e). X-ray photoelectron spectroscopy (XPS, ULVAC PHI5600) was performed to analyze the bonding and chemical state of the obtained samples. The carbon content was measured by CHN analysis (MICRO CORDER JM10). The UV–vis diffuse reflectance spectra (DRS) of obtained samples were collected by UV–vis spectrophotometer (JASCO V-670 Spectrophotometer). The effective electric surface charge of particles was determined by Zeta potential measurement (Malvern, Zetasizer Nano ZS). The chemical mixture of the supernatant was examined by nuclear magnetic resonance (^{1}H NMR, Varian Unity Inova, 500 MHz) to propose the chemical reaction during the solvothermal synthesis and formation mechanism of the metal oxide nanostructures.

2.4 Density Functional Theory (DFT) Calculation

The DFT calculation was solely conducted for gas adsorption onto NiO surface. Other than this material, even though they were synthesized and evaluated, the DFT calculation was not performed. DFT calculations are performed with plane-wave basis sets and periodic boundary conditions, using the slab model to simulate surface conditions. Generalized Gradient Approximation (GGA) exchange correlation functionals parametrized by Perdew, Burke, and Ernzerhof (PBE) [21] (so-called GGA-PBE) are chosen along with appropriate Hubbard U correction for NiO [22] to produce a more accurate electronic structure for Mott insulators. The effective Hubbard U parameter for NiO has been thoroughly explored and tested in previous works. Parameter values of $U_{eff} = U - J = 5.3$ eV, with $U = 6.3$ eV and $J = 1$ eV, are chosen according to a previous investigation of water adsorption on NiO (100) surface [23] and other, earlier investigations into NiO. [22, 24, 25] Core electrons are treated with projector-augmented wave (PAW) method. [26] All calculations are performed with the Vienna Ab Initio Simulation Package (VASP) software package. [27-30] NiO surface is modeled using slab models with a minimum of 4 atomic layers to approximate bulk effects to surfaces. Vacuum slabs between the 4 layers of NiO are used to prevent interaction with periodic images in the z-axis. In a similar way, 2×2 surface unit cells (corresponding to 0.25 ML coverage) are used to prevent interaction between the adsorbate molecules and its periodic images in the x- and y-axes. Geometry optimization calculations are used to model adsorptions, with adsorbates situated initially at 2 Å from the surface adsorption site. In order to ensure reliable calculations, the values of several calculation parameters are converged with respect to the total energy of the simulation cell. These parameters include the cutoff energy (in plane-wave DFT representing the size of the basis set used), the k-point grid for integrations (using Monkhorst-Pack grid [31]), and the aforementioned thickness of the vacuum slab. The calculations performed for this work uses a cutoff energy of 400 eV, a k-point grid of $5 \times 5 \times 1$, and a vacuum slab of thickness 10 Å, converging the total energy of calculated systems to a reliability of 0.001 eV/atom.

2.5 Gas Sensing Measurement System

The fabrication of the sensor device in the present research followed the step of our reported work.[1] A comb-type electrode was assembled on a silica glass by a drop-coated silver paste. Annealing in a furnace was carried out at 400 ^{o}C for 30 min to remove organic compounds from the fabricated-sensor device. The ramping rate was 10 ^{o}C/min. Then, after the system dropped to room temperature, the slurry containing designated amount of samples and ethanol was coated on the prepared electrode, carefully, until the sensing material fully covered the electrode.

Gas-sensing properties measurement was recorded by a home-built data acquisition system (see **Fig. 2.1**, Nanovolt-microohm Agilent 34420A with a measurement range of 100 Ω–100 MΩ and switch unit Agilent 34970A) based on Taguchi Gas Sensor (TGS) with the static system which measures the resistance variation upon the exposure to ambient air and target gas. The sensing measurement was conducted at the varied temperature ranging from 200 ^{o}C to 450 ^{o}C to determine the optimum working temperature where the sensor material exhibited the highest responsivity to toluene gas, as it is essential for the practical use. Initially, the sensor devices were exposed to ambient air at desired temperatures and kept about 45-60 min until the sensor resistance reaches a stable value. At this point, the measured resistance was named as *resistance in the air* (R_a). The condition was maintained for 10 min and then the target gas was injected, eventually led to the change in the sensor resistance. At this condition, the recorded resistance was denoted as *resistance in gas* (R_g). The sensor response in a reducing gas mixture was calculated as R_a/R_g for n-type semiconductor or R_g/R_a for p-type semiconductor. At the optimum working temperature, each sensor was introduced to 50 ppm of four different target gases, including H_2, toluene, methanol, and ethanol (nitrogen as base gas), to probe the sensor selectivity. Then, the sensors were exposed to a constant flowed testing gas at a concentration of 10, 20, 30, 40, and 50 ppm to examine the repeatability followed by structural and morphological characterizations to determine sensor stability and durability.
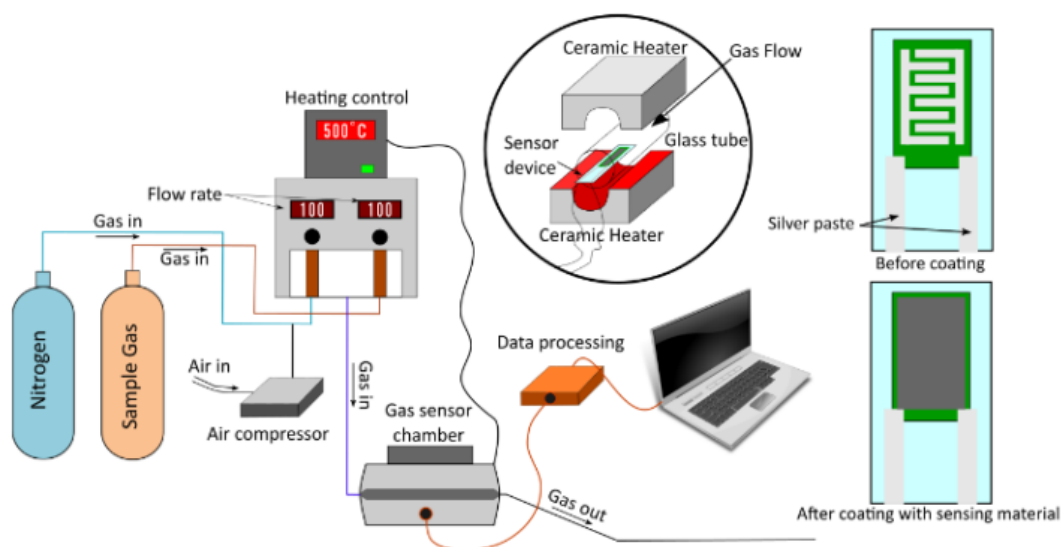
Figure 2.1 Schematic figure of gas sensing measurement system and the fabricated sensor device

2.6 References

1   A. Hermawan, Y. Asakura, M. Kobayashi, M. Kakihana and S. Yin, *Sensors Actuators, B Chem.*, 2018, **276**, 388–396.

Chapter 3

Synthesis process of n- and p-type metal oxide semiconductor with a controllable morphology, surface charge, and exposed facet for harmful gas detection

3.1 Synthesis of SnO₂ microspheres via water-controlled release solvothermal process (WCSRP) with micro/mesoporosity for high temperatures toluene gas detection

3.1.1 Introduction

Extensive exploration on metal oxide semiconductors (MOX) has been significantly increasing since this class of material holds a variety of valuable applications to support human society and life such as clean energy production,[1] poisonous organic pollutant degradation,[2] air pollution remediation and monitoring,[3–6] energy storage,[7] biomedical purpose,[8] smart building[9] and many more. One of the useful applications of MOX is gas sensing for the monitoring of gaseous pollutants including volatile organic compounds (VOCs; benzene, toluene, xylene, acetone, methanol, ethanol, formaldehyde, *etc.*) and the combustion process which results in toxic gases (CO_2, CH_4, NO_x, CO, SO_2, *etc.*) both inside the room and the extreme temperature.[10] The basic principle of gas sensing is based on the active surface interaction between sensor materials and the target gases, where this involves the alteration of electronic properties. Especially, the amount of the VOCs, which easily evaporate into our environment in a gaseous species due to low vapor pressure, have increased due to an increase of the consumption of paints, adhesives, rubber, and gasoline. Toluene (C_7H_8), one of the VOCs, can harm human bodies through inhalation causing a temporary health effect in the nervous system including dizziness, headache, and unconsciousness to induce permanent speech, hearing, and vision loss for the repeated exposure. Although toluene should be immediately detected for the protection of human health, the stability of toluene suppresses its detection by MOX sensors. Therefore, fast and ultra-sensitive gas sensing for toluene is needed.

Tin Oxide (SnO_2) is an important n-type transition MOX and well-known as one of the most sensitive materials for gas detection. It possesses a rutile-type crystal structure, exceptional physicochemical and electrical properties, which are of utmost importance for monitoring

environmental gas pollutant with high responsivity, considerable selectivity and good detectability.[11,12] However, the responsivity and selectivity for toluene in SnO_2 gas sensors have not been high. The three methods for the improvement of SnO_2 gas sensing property are as follows. (i) heterostructure fabrication with other metal oxides such as NiO, ZnO, or α-Fe_2O_3 to modify charge carrier concentration (N_d).[13,14] (ii) noble metals (Pt, Pd) loading to promote spill-over effect.[15–18] (iii) particle size (D) control of sensing material to be comparable or fewer than 2L (L is the depth of the surface space-charge layer) or designing the morphology in a special hierarchical structure, such as micro-/mesoporous, to remarkably increase the sensing property due to the abundance of accessible active sites, and the easier gas diffusion relates to its large surface area.[12,19–21] Compared to (i) and (ii) that involve secondary composition materials which often require multi-step preparation, (iii) is particularly convenient in terms of synthesis. Moreover, the responsivity can be competitive with those of (i) and (ii) with the right control of particle size and pore diameter. Nevertheless, a facile synthesis for a highly specific surface area material still requires significant effort, and therefore this study focuses on the development of a novel synthetic method for a unique hierarchical porous morphology of SnO_2.

In previous researches, micro-/mesoporous SnO_2 has been prepared through various methods. A hard templating by amorphous silica (SiO_2) is the most common route to yield ordered mesoporous SnO_2 structure. Zhu and co-workers successfully synthesized mesoporous SnO_2 single crystal via the silica-templated hydrothermal method.[22] Other structures of SnO_2 such as hollow spheres with mesoporosity could also be fabricated by *in situ* templating with SiO_2 according to a recent report.[23] Nevertheless, the hard-template method requires a further etching process using sodium hydroxide (NaOH) to remove the SiO_2 template. Soft-templating using surfactants or free-templating were also reported to be an alternative method for fabricating the mesoporous and double-shelled hollow structure of SnO_2.[24–28] Because this method was conducted at room temperature, it was difficult to directly produce high crystallinity of porous SnO_2, and post-synthesis for improvement of crystallinity often led to particle growth which damaged the porous structure.[29] In this regard, further development of a facile and single-step preparation of crystalline SnO_2 with micro-/mesopores can be advantageous for rapid acquirement and energy-saving production, and it is still a great challenge.

In the present work, we have succeeded in synthesizing a hierarchical nanostructure of SnO_2 spheres with micro-/mesoporosity through a novel one-step and template-free solvothermal method in a mixture containing dehydrated ethanol and acetic acid, the so-called 'water-controlled release solvothermal process' (WCSRP). The creative concept of this method was using the esterification reaction between alcohols and carboxylic acids to release a gradual amount of water molecules to hydrolysis metal precursors (such as alkoxide, chloride, carboxylate, etc.).[30–32] The method offers a controllable process that led to a homogeneous and well-defined nanostructure due to the slow reaction rate. Therefore, the precise control of the ratio of ethanol and acetic acid may be expected to affect the esterification process and the released water molecules may result in a controllable particle size. Moreover, an organic solution may involve the creation of a hierarchical structure. The XRD, SEM, TEM and N_2 adsorption-desorption observation revealed that the particle size, pore size distribution, pore volume, and specific surface area were dependent on the volume percentage (vol. %) of acetic acid to ethanol. The gas sensing properties of the micro-/mesoporous SnO_2 spheres were also investigated to understand the factors influencing the gas sensor responsivity.

3.1.2 Experimental Section

To prepare micro-/mesoporous SnO_2 spheres, 1 mmol of $SnCl_2$ was dissolved in a certain volume of ethanol. The solution was magnetic stirred at 400 rpm for 30 min. Subsequently, acetic acid was slowly added, and the solution was maintained under the same stirring conditions for another 30 min. The total volume of the mixture was 50 mL. Then, the mixture was transferred into a 100 mL Teflon-lined autoclave and heated for 20 h at 200 °C. After the vessel was cooled to room temperature, the obtained powder was washed with ethanol, followed by vacuum drying at 70 °C for 12 h. The samples were named SnO_2_0, SnO_2_10, and SnO_2_20 according to the adjusted volume percentage (vol. %) of acetic acid of 0 vol. %, 10 vol. % and 20 vol. %, respectively.

3.1.3 Results and discussion

Figure 3.1 shows the XRD patterns of the obtained micro-/mesoporous SnO_2 spheres synthesized by WCSRP in the mixture of ethanol/acetic acid with a different volume percentage

of acetic acid, together with the reference card (JCPDS No. 41–1445). All the diffraction peaks could be indexed to the (110), (101), (111), (211), (220), (002), (311), (301), (202), and (321) planes of tetragonal rutile-type SnO_2 without any other peaks. This indicated that the obtained samples possessed a single phase of SnO_2. From the XRD patterns, it is noted that each sample possessed distinct broadened peaks, indicating different crystallinity or particle size of the SnO_2. Accordingly, the following Debye-Scherrer equation[33] was used to estimate the average crystallite size (D) of SnO_2:

$$D = K\lambda / \beta \cos \theta \tag{1}$$

where K, λ, β and θ are the crystallite shape factor (K=0.9), the wavelength of the X-Rays radiation (λ=1.5418 Å), full width at half-maximum (FWHM) in radians, and Bragg angle in degree, respectively. Using the given equation and all diffraction peaks, the average crystallite sizes of SnO_2_0, SnO_2_10 and SnO_2_20 were estimated to be 2.70 nm, 4.63 nm, and 5.19 nm, respectively. This reflected that the volume percentage of acetic acid in the mixed solvent was essential to control the size of the nanoparticles.
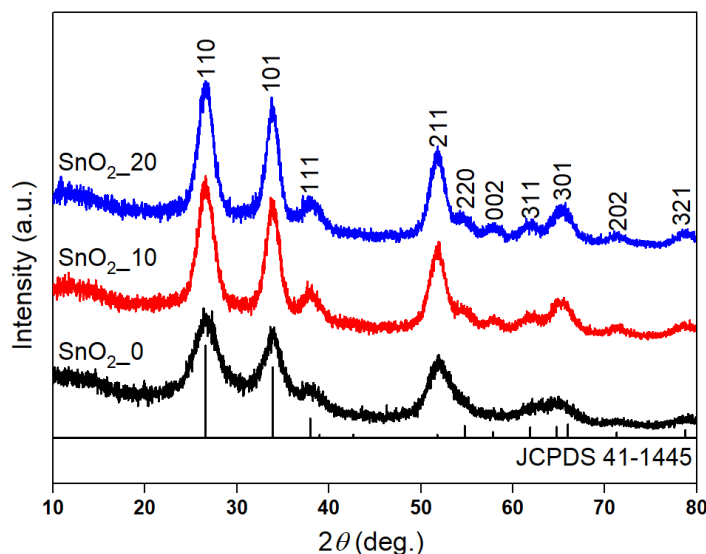
Figure 3.1 XRD patterns of micro-/mesoporous SnO_2 spheres synthesized in different volume percentage of acetic acid.

The morphology, nanostructure, and size distribution of the synthesized samples were characterized by SEM. **Figure 3.2** shows the SEM images of the micro-/mesoporous SnO_2 spheres and their particle size distribution. The morphology of SnO_2 was a microscale spherical shape with a distinct average diameter depending on the vol. % of acetic acid. For SnO_2 synthesized in only

dehydrated ethanol (SnO$_2$_0 sample), the average particle size was 0.65 μm. With the addition of 10 vol. % of acetic acid (SnO$_2$_10 sample) the size of the spheres increased to 0.90 μm, and the further added amount of acetic acid to 20 vol. % (SnO$_2$_20 sample) resulted in an additional increment of 1.5μm. Therefore, the size of the SnO$_2$ particle was tunable by changing the vol. % of the acetic acid.

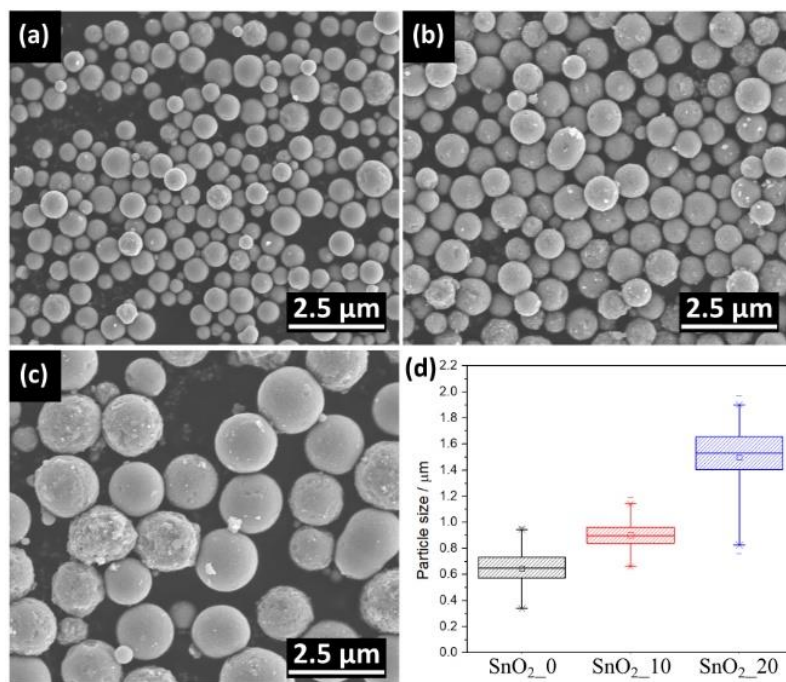**Figure 3.2** SEM images of micro-/mesoporous SnO$_2$ spheres (a) SnO$_2$_0, (b) SnO$_2$_10, (c) SnO$_2$_20 and (d) their particle distribution.
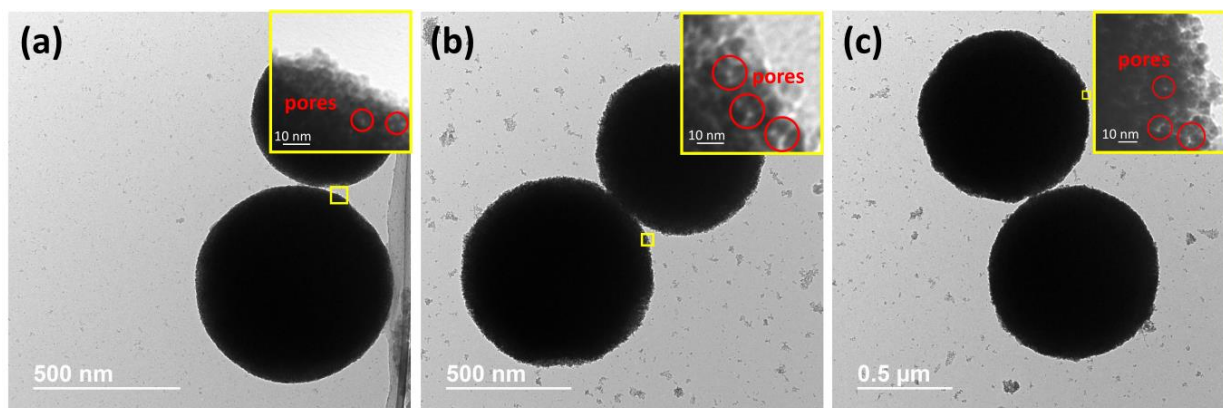

Figure 3.3 TEM images of (a) SnO$_2$_0, (b) SnO$_2$_10 and (c) SnO$_2$_20 (insets are high magnification and SAED).

TEM was conducted to get further insight about morphological feature of micro-/mesoporous SnO_2 spheres (**Fig. 3.3**). The insets were the magnification for a closer look of surface observation of the samples, and it turned out that interconnection of a large amount of nanocrystal as primary particles built a hierarchical SnO_2 sphere with mesopores on the surface, which was the void induced by the interconnection of the particles (**Fig. 3.3** insets). The diameter of these nanoparticles was also dependent on the vol. % of the acetic acid. Specifically, the size of SnO_2_0, SnO_2_10, and SnO_2_20 nanoparticles were in the range of 2–3 nm, 4–6 nm, and 6–9 nm, respectively, which matched the calculated crystallite size from the XRD results as mentioned earlier. Moreover, the corresponding SAED pattern indicated the polycrystalline feature of the SnO_2_10 sample. The diffraction rings could be assigned to 110, 101, 200, 211, and 002 lattice planes of tetragonal rutile-type SnO_2.
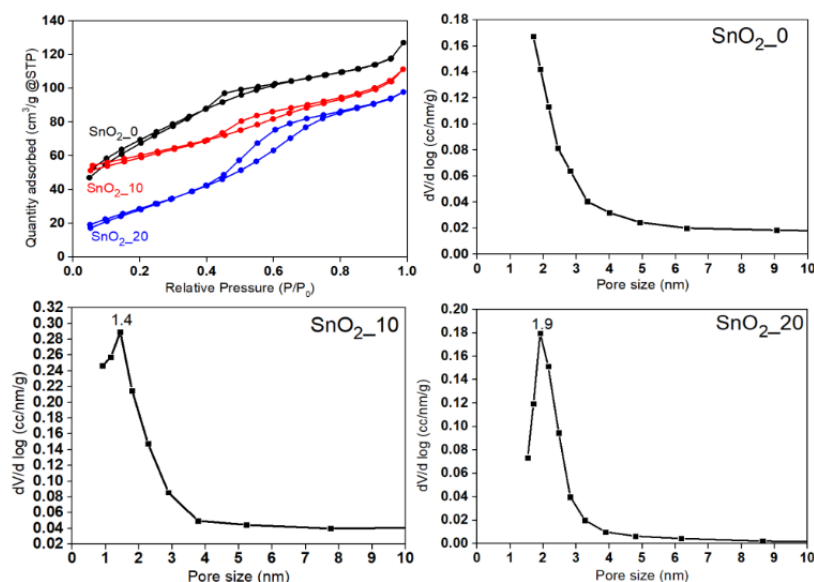
Figure 3.4. N_2 adsorption-desorption isotherm and BJH pore size distribution of the mesoporous SnO_2 spheres.

The nitrogen adsorption-desorption isotherms of the SnO_2 spheres are displayed in **Fig. 3.4** to elucidate the porosity nature. The results indicated that the obtained curves could be categorized as type IV isotherms with a hysteresis loop at a relative pressure (P/P₀) of 0.4–0.8, which is capillary condensation seen in typical micro-/mesoporous materials. The crystallite size obtained from the XRD results, particle size, BJH pore size distribution, pore volume, and specific surface area are summarized in **Table 3.1**. The various synthesized SnO_2 exhibited different pore size diameters, pore volumes, and specific surface areas. When the SnO_2 was synthesized in pure

ethanol, although the peak of pore size distribution was not observed, the sample possessed a microporous property and the pore size should be below 1.9 nm, which may be the smallest among the samples. It also possessed a low pore volume of about 1.334×10^{-1} cm^3/g. As the vol. % of acetic acid increased in the reaction, the pore size and pore volume of SnO$_2$ also enlarged, where SnO$_2$_20 possessed the highest pore size distribution of 1.9 nm and pore volume of 2.245×10^{-1} cm^3/g. From **Fig. 3.4**, it could be observed the existence of a pore larger than 2 nm in size, indicating that the samples exhibited micro-/mesoporosity. Normally, the specific surface area is also associated with the particle size. As the particle size decreases, the specific surface area increases due to the expansion of the surface-area-to-volume ratio.[34] However, in our case, the smallest particle size did not exhibit the largest specific surface area, indicating that the micro- and mesopores significantly contributed to not only the outer surface area, but also to the overall specific surface area of the sample (SnO$_2$_10 sample).
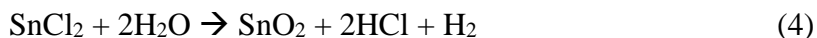
Table 3.1 Summaries of average size of the nanocrystal, particle size of the spheres, pore size distribution, pore volume and specific surface area of the samples.

Sample	Mean crystallite size[a] (nm)	Average particle size[b] (μm)	Pore size[c] (nm)	Pore volume (cm^3/g)	SSA[d] (m^2/g)
SnO$_2$_0	2.70	0.65	< 1.9	0.1334	136
SnO$_2$_10	4.63	0.90	1.4	0.1869	145
SnO$_2$_20	5.19	1.50	1.9	0.2245	113

[a]XRD calculation; [b]SEM and TEM observation; [c]BJH method; [d]BET method

A possible chemical pathway and formation mechanism of a SnO$_2$ nanosphere were proposed based on the above experimental results. Additionally, ^{1}H NMR technique was utilized to analyze the solutions after the solvothermal reaction. Prior to the NMR measurement, the supernatant was diluted with deuterated CD$_3$OD. **Fig. 3.5, Fig. 3.6 and Fig. 3.7** showed the ^{1}H NMR spectra of the supernatant solutions after the reactions for the synthesis of SnO$_2$_0 in only ethanol, SnO$_2$_10 in ethanol/acetic acid = 45 mL/5 mL, and SnO$_2$_20 in ethanol/acetic acid = 40 mL/10 mL, respectively, accompanied with their assignment following the literature.[35] In the case of SnO$_2$_0 synthesized in pure ethanol, the obtained solution possessed an ethanol signal ((**CH$_3$CH$_2$OH**: 1.19 ppm, CH$_3$**CH$_2$OH**: 3.6 ppm), a small amount of diethyl ether (**CH$_3$CH$_2$OCH$_2$CH$_3$**: 1.18 pm, CH$_3$**CH$_2$OCH$_2$CH$_3$**: 3.5 ppm) and hydrogen chloride (**H**Cl: 4.8 ppm). Some peaks were overlapped and peaks at 4.55 ppm and 5.22 ppm related to unknown

compounds appeared, although we cannot assign them at the present moment. In the case for SnO_2_10 and SnO_2_20 synthesized in the mixture of ethanol and acetic acid, ethyl acetate ($CH_3COOCH_2CH_3$: 1.25 ppm, $CH_3COOCH_2CH_3$: 2.01 ppm, $CH_3COOCH_2CH_3$: 4.1 ppm) was included in addition to ethanol, diethyl ether, and hydrogen chloride. It was also observed that no peaks in the ^1H NMR spectrum were assigned to acetic acid, meaning that it had been wholly reacted with ethanol under the solvothermal condition. The relatively higher peak intensities of ethyl acetate in the supernatant of the SnO_2_20 sample as compared to SnO_2_10 could ascribe to the larger volume percentage of acetic acid in the reaction medium. The existence of those compounds in the final solution was meaningful evidence that some chemical reactions took place during the solvothermal process. From these findings, it might be proposed that the sphere formation mechanisms including three consecutive stages, as visualized in **Fig. 3.8**. In the first step, upon heating at 200 ^oC, the water molecule was slowly released from the esterification reaction between ethanol and acetic acid, as shown in equation (2). The slow release reaction means a very small amount of water molecules are present at the beginning of the reaction. The amount of generated water molecules should be proportional to the amount of ethyl acetate, though the water signal did not appear in the spectrum. In the equation (3), the water molecules could still be produced from ethanol condensation without esterification. In the second step, the *in situ* generated water molecule then hydrolyzed and oxidized the tin (II) chloride and initiated the SnO_2 nucleation (equation (4)).[36] The entirety of the water molecules may be reacted completely thus the chemical shift of H_2O was not detected in the NMR spectrum. The Sn species might be hydrolyzed around the surface of the water drops and a simultaneous induction of water at every place in the solution occurred and led to the formation of the nanoparticle. Finally, in the last step, the SnO_2 nanoparticle aggregated into a hierarchical spheres structure, where the diameter of the spheres was strongly related to the amount of water. A large amount of water resulted to higher dielectric constant, leading to larger solubility, high supersaturation and finally resulted in the formation of a large particle.

$$CH_3CH_2OH + CH_3COOH \rightarrow CH_3COOCH_2CH_3 + H_2O \quad (2)$$

$$2CH_3CH_2OH \rightarrow CH_3CH_2OCH_2CH_3 + H_2O \quad (3)$$

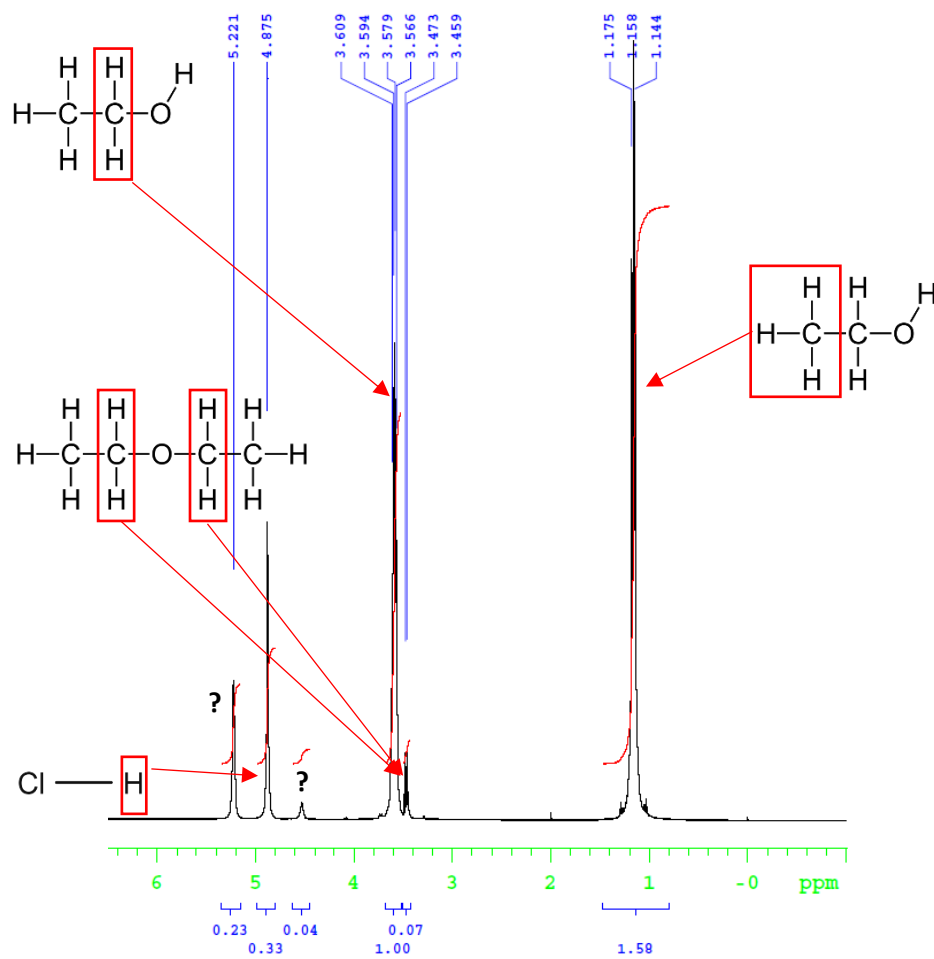$$SnCl_2 + 2H_2O \rightarrow SnO_2 + 2HCl + H_2 \quad (4)$$

Fig. 3.5. NMR spectra of the supernatant of SnO_2_0.

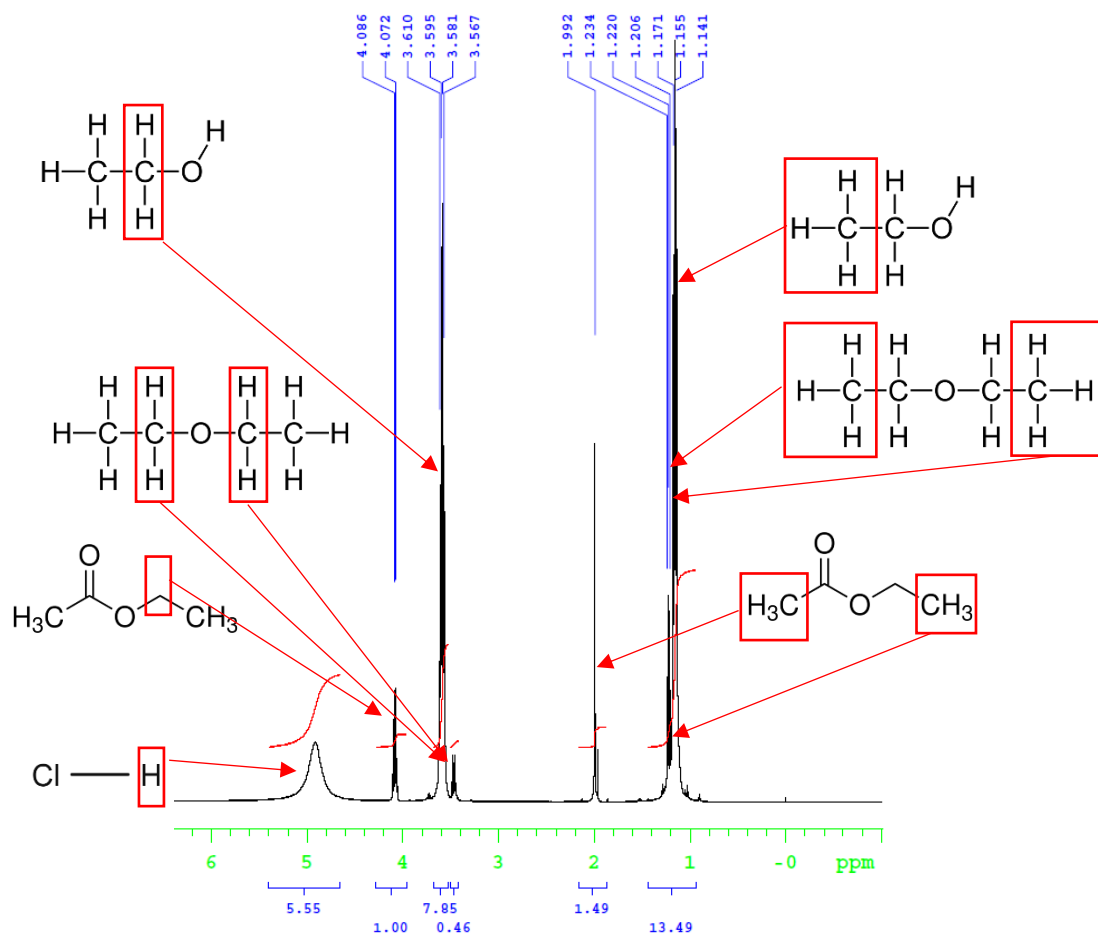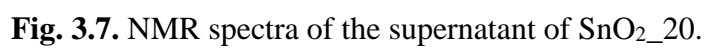**Fig. 3.6.** NMR spectra of the supernatant of SnO_2_10.

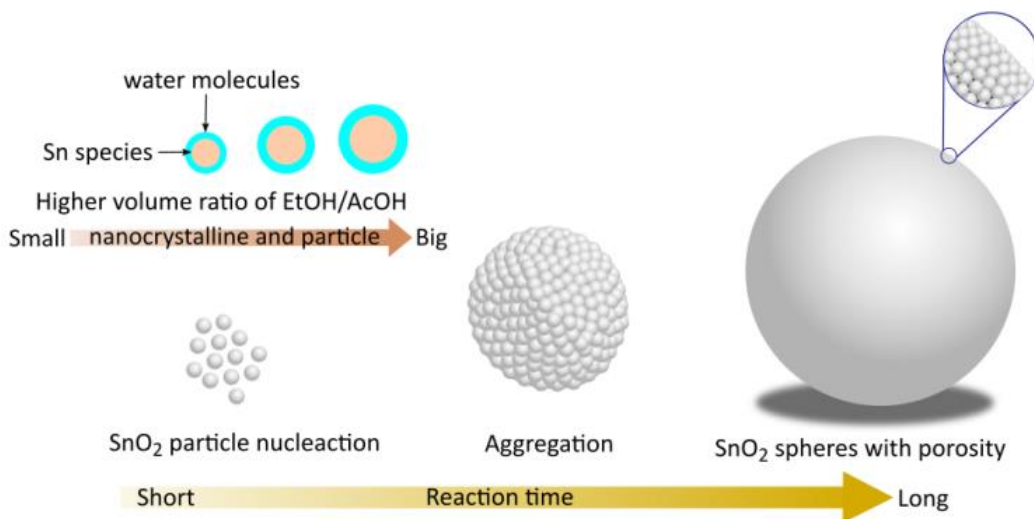**Fig. 3.7.** NMR spectra of the supernatant of SnO_2_20.

Figure 3.8. (b) The formation mechanism of SnO_2 spheres with mesoporous structure.

To support the above-proposed mechanism, the tin (II) chloride concentration was changed to 0.25, 0.5, 0.75 mmol and 1 mmol, while keeping the solvothermal reaction condition as same as the SnO_2_20 sample preparation. The SEM images displayed in **Fig. 3.9** clearly revealed that the average particle size of the SnO_2 sphere progressively increased from 350 nm to 1.50 μm with an increase of the amount of the precursor, suggesting that the spherical size of SnO_2 was also determined by how much Sn species hydrolyzed in the reaction. The greater number of Sn species, the greater amount of SnO_2 nanoparticles were formed, which led to the larger spherical structure.

An experiment for investigation of the effect of time-dependence was also conducted to roughly understand the growth process of the mesoporous structure of SnO_2 spheres. **Fig. 3.10** shows the TEM images of SnO_2 prepared in 20 vol.% acetic acid at 200 ^{o}C for different reaction times. As shown in the TEM images, nearly spherical nanoparticles with an average size of 5 nm were formed at incipient stages that were very close to the calculated crystallite size of SnO_2_20. With a prolonged reaction time, the nanoparticles were aggregated into a solid spherical structure with micro-/mesoporosity for the overall surface energy system minimization. The inner particle should be more densely packed than the surface. The aggregation process might be directly carried out by the organic mixture involved in the solvothermal reaction,[37] as when the mixture solvent was changed to pure deionized (DI) water, only the nanoparticles could be observed, as shown in **Fig. 3.11**. Moreover, its pore size distribution was larger and surface area was smaller than the

SnO$_2$ synthesized in the organic solvent. These are once again strengthening the proposed formation mechanism, indicating this method is essential to produce a hierarchical nanostructure with high specific surface area.
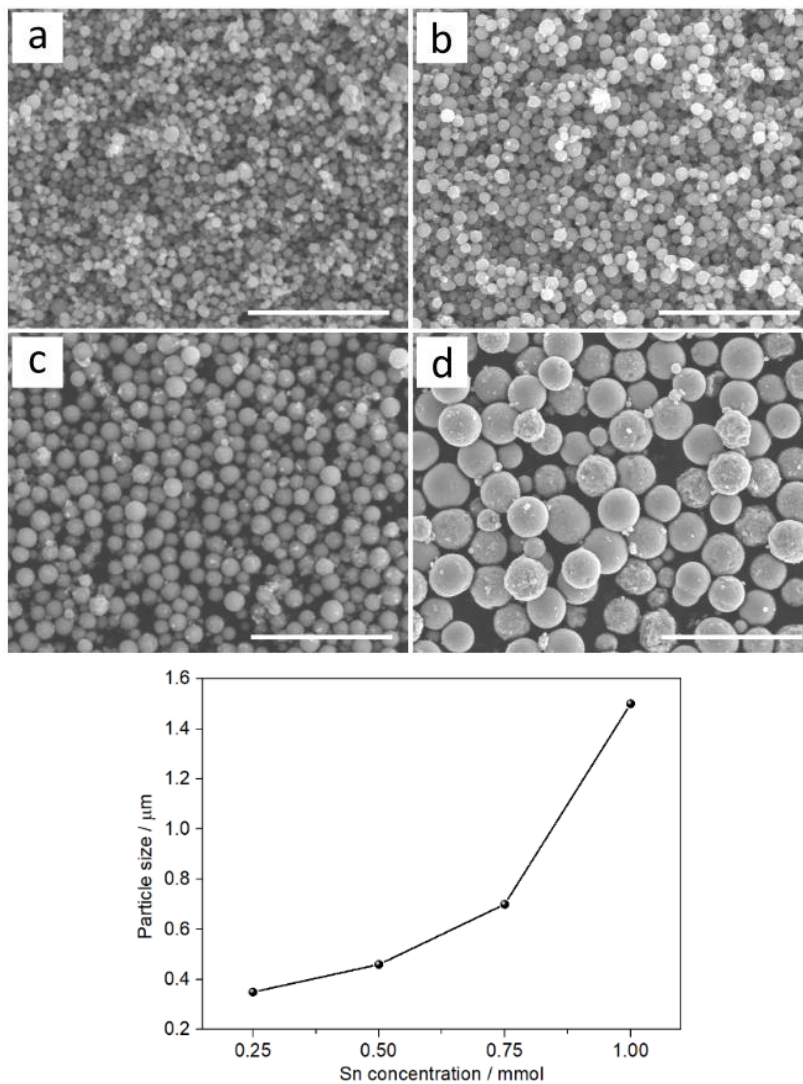
Fig. 3.9. SEM images of SnO$_2$ synthesized from (a) 0.25 mmol (b) 0.5 mmol (c) 0.75 mmol and (d) 1 mmol of SnCl$_2$ precursor; the scale bar is 5 μm.
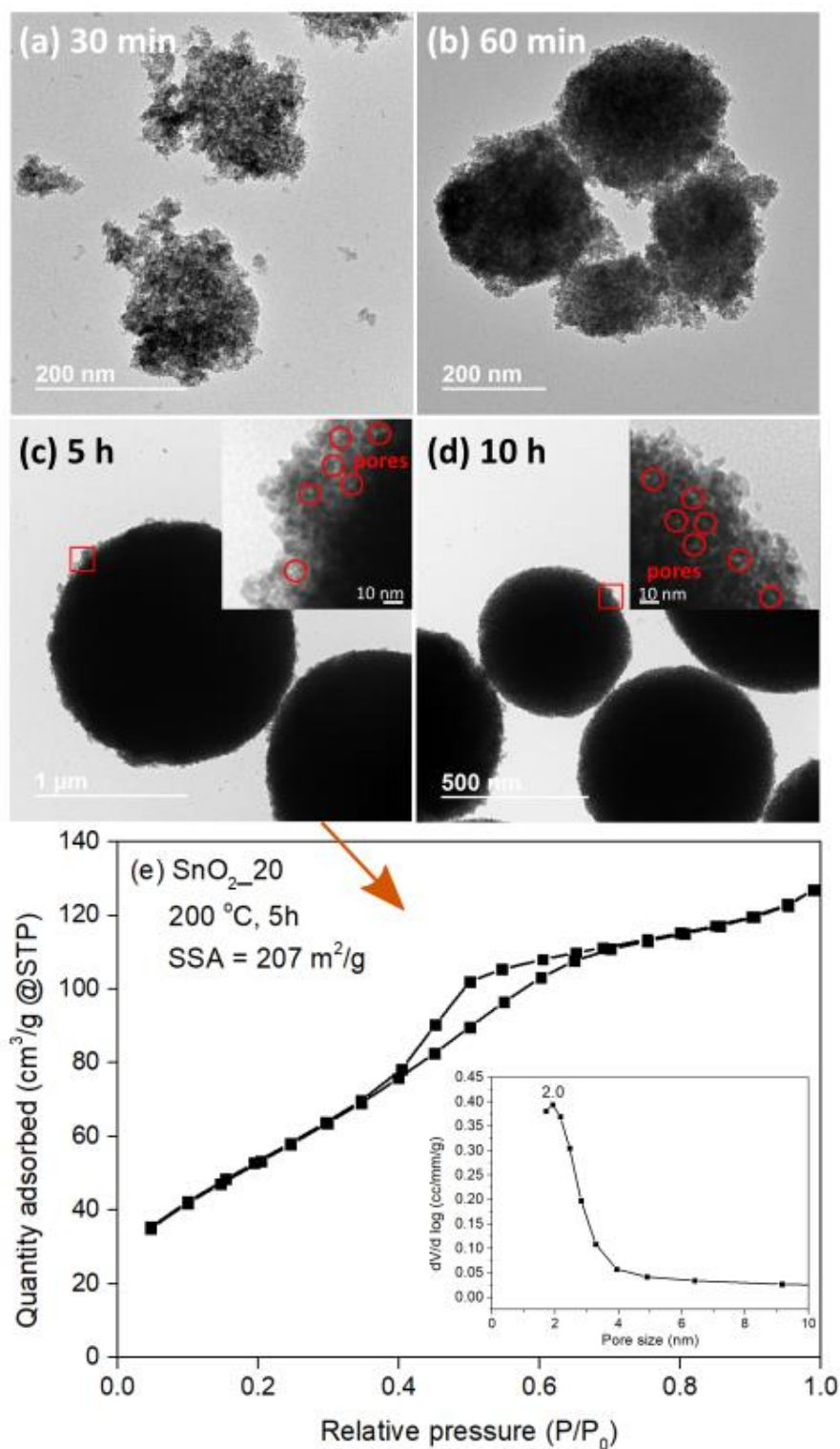
Fig. 3.10. (a-d) TEM images of SnO_2_20 synthesized at 200 °C with different reaction time. The inset is higher magnification of the red square area to observe the micro-/mesopores. (e) N_2 isotherm and BJH pore size distribution of SnO_2_20 synthesized at 200 °C for 5 h.
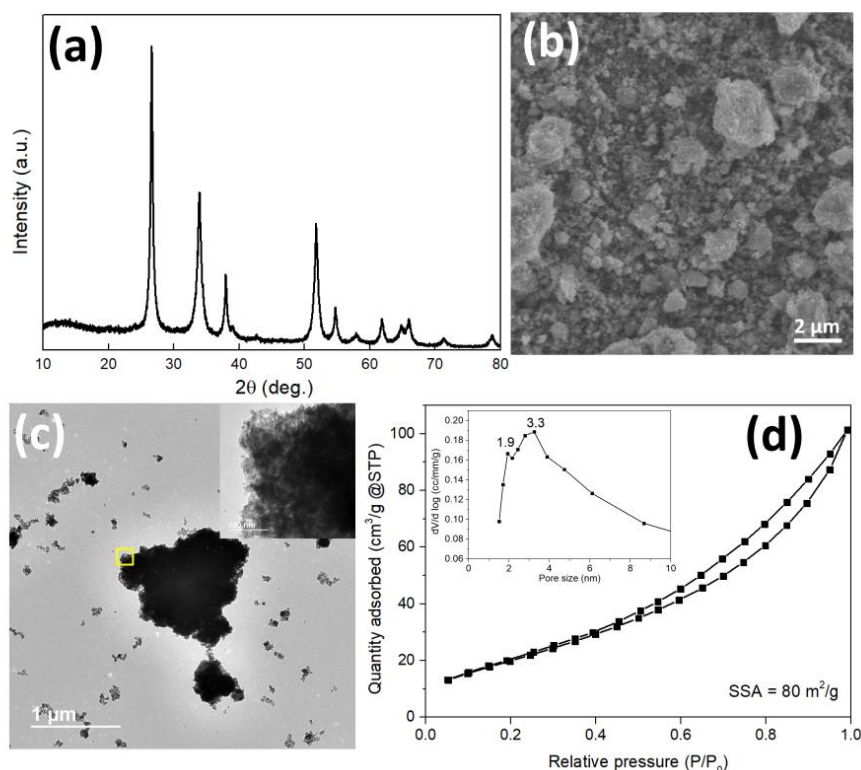
Fig. 3.11. (a) XRD pattern, (b) SEM image (c) TEM image and (d) N_2 isotherm (BJH pore distribution is inset) (e) toluene sensing property of SnO_2 synthesized in pure deionized water.

The influence of solvents variety on the metal oxides effective surface charge is demonstrated. Besides the use of ethanol and acetic acid, 1-propanol, benzyl alcohol, and water were utilized as solvents to synthesize SnO_2 nanostructures. The result of zeta potential is summarized in **Table 3.2**. One can see that there is a tendency in the effective surface charge of SnO_2 under different mixed solvents environment, that is whenever acetic acid is added into the reaction, the surface charge switched to negative value. It might be an evidence of the presence of different organic functional groups attached on the SnO_2 microsphere particles. Herein, we investigate these attached functional groups by the mean of FTIR. **Fig. 3.12** shows FTIR spectra of SnO_0, SnO_2_10 and SnO_2_20. There are 3 distinct peaks corresponded to O-H (3600 nm^{-1}), C-H stretch (2600-2800 nm^{-1}, alkyl group) and C-O stretch (1100-1000 nm^{-1}, ester group). The result indicates the presence of esters and alkyl group in the SnO_2 synthesized under mixed ethanol and acetic acid, probably contributed by the attachment of ethyl acetate. It is known as aprotic solvent (non-hydrogen donor), therefore it may likely contribute to charge negativity. In contrast,

when ethanol is the only used solvent, the presence of C-H stretch and C-O stretch was very less, indicating no attachment of ester group. Ethanol is a protic solvent (hydrogen donor), and therefore contribute to the positive charge of SnO_2_0.

Table 3.2 Solvents variation on their influence on zeta potential of SnO2 nanostructures

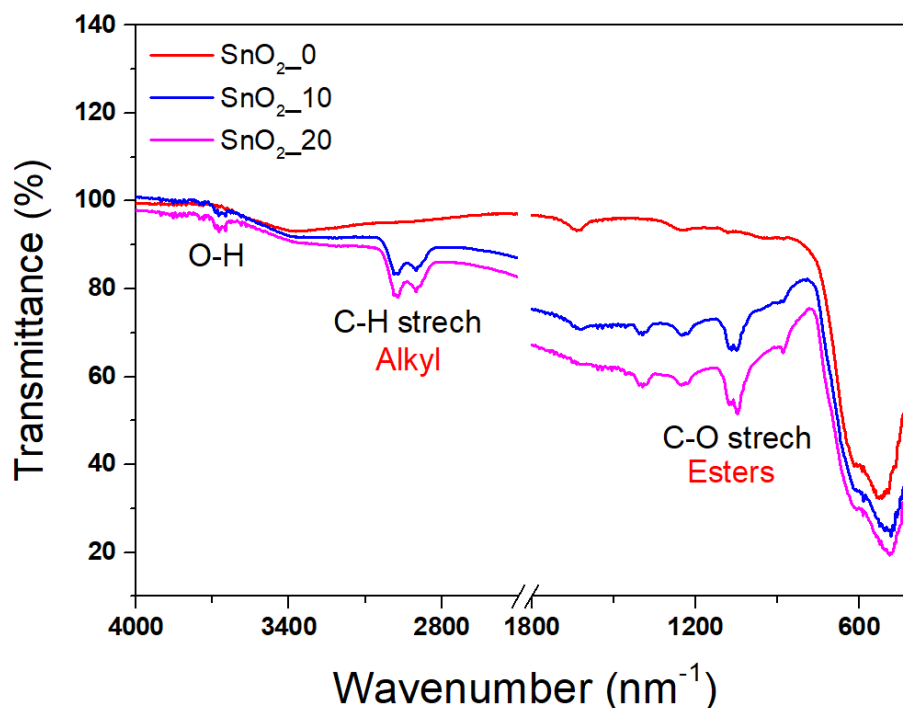| Samples	Solvents	Zeta potential (mV)
SnO_2_0	Ethanol 50 mL	19.3
SnO_2_10	Ethanol 45 mL Acetic Acid 5 mL	-7.76
SnO_2_20	Ethanol 40 mL Acetic Acid 10 mL	-15.7
SnO_2_PrOH	1-Propanol 50 mL	10.3
$SnO_2\_PrOH-AcOH$	1-Propanol 40 mL Acetic Acid 10 mL	-12.6
SnO_2_BzOH	Benzyl Alcohol 50 mL	3.7
$SnO_2\_BzOH-AcOH$	Benzyl Alcohol 40 mL Acetic Acid 10 mL	-2.5
SnO_2_Water	Distilled water 50 mL	-1.8

Fig. 3.12. FTIR spectra of SnO_0, SnO₂_10 and SnO₂_20.

The XPS measurement was applied to investigate the surface valence state and chemical configuration of the synthesized samples. **Figure 3.13** (a) shows the full-scan XPS spectra of the synthesized SnO_2. The result exhibited the existence of Sn, O and Cl element in all synthesized samples (elemental composition is summarized in **Table 3.3**). All remaining C peaks originated from the C-included compounds that existed in the atmosphere. The high–resolution spectra of Sn 3d peaks from SnO₂_0, SnO₂_10, and SnO₂_20 samples were compared in **Fig. 3.13** (b). The core–level of Sn 3d consisted of symmetrical doublet peaks at around 495 eV and 486 eV. The high binding energy at 495 eV was assigned to Sn $3d_{3/2}$ core–level and the low binding energy at 486 eV corresponded to Sn $3d_{5/2}$ levels, corresponding to the characteristic of the Sn^{4+} state of Sn in tetragonal rutile-type SnO_2. The existence of Cl element was found, indicated by two consolidated peaks at 199 eV ($2p_{3/2}$) and 200.6 eV ($2p_{1/2}$). These doublet values were closed to Sn-Cl bonding in the recent study.[38] One might suspect that it could have originated from the Cl incorporation in the SnO_2 lattice, revealing that the hydrolysis process in the proposed formation mechanism is critical for producing fewer impurities SnO_2. The comparison shows a relatively high amount of Cl atoms in the sample of SnO₂_0 might indicate a lower hydrolysis reaction. Furthermore, the

core–level of O 1s (**Fig. 3.13** (d–f)) was fitted using a Gaussian method, resulting in components with the smaller binding energy of 530–531 eV, which is attributed to the Sn–O bond via sp^3d^2 hybridization mode of Sn^{4+} and sp^2 hybridization mode of O^{2-}.[39–42] The larger binding energy centered at 532 eV belonged to C–O bonds which were probably caused by the interaction of X-ray with C-included compounds. It was noteworthy that the binding energy of Sn 3d in the SnO_2_0 sample was slightly shifted compared with the other samples. The presence of Sn with an oxidation state of +2 from the Sn-Cl bond might induce a chemical shift, as the Sn^{2+} lies at the lower binding energy.[43] Since the Cl amount in SnO_2_0 was higher than the others, the amount of Sn-Cl in SnO_2_0 should also be higher. Besides, the CHN analysis showed the existence of carbon with the content of 1.20 %, 1.43 %, and 1.77 % for SnO_2_0, SnO_2_10 and SnO_2_20, respectively. The carbon content was originated from the organic solution and directly proportional with the vol. % of acetic acid.
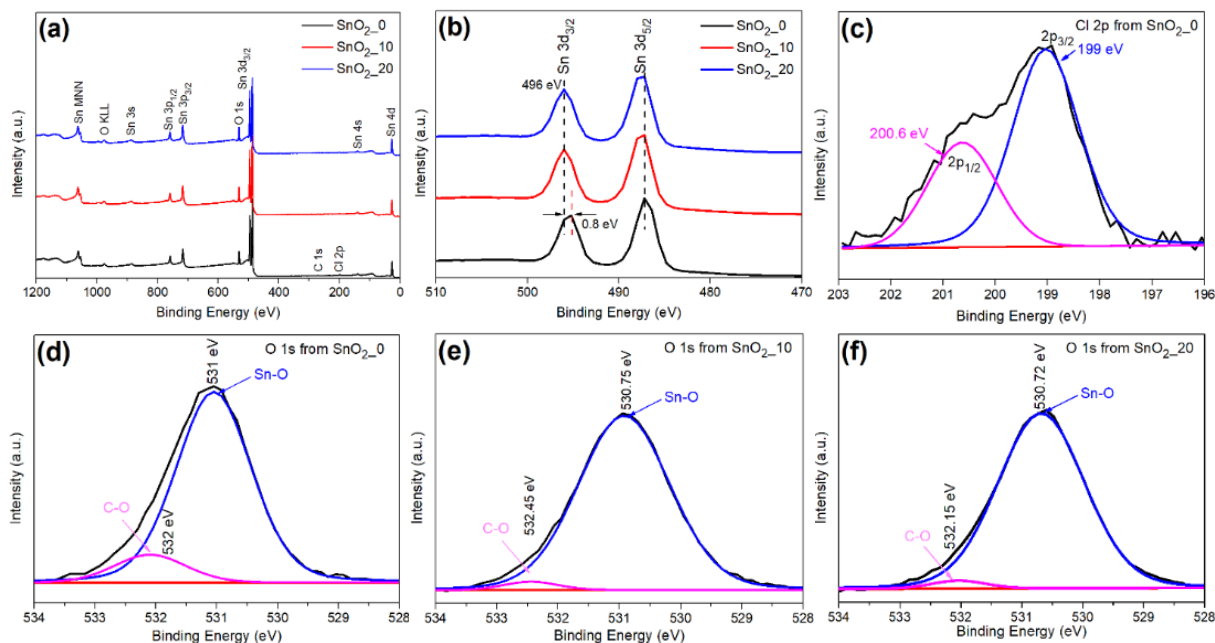

Fig. 3.13 (a) full scan XPS (b) Sn 3d (c) Cl 2p and (d–f) O 1s core–level spectra of mesoporous SnO_2 spheres

Table 3.3. Elemental composition of the synthesized SnO_2 obtained from XPS and CHN analysis

Sample	Elemental composition (at. %)			
	Sn	O	Cl	C
SnO_2_0	30.44	65.80	3.76	1.20
SnO_2_10	32.88	66.10	1.02	1.43
SnO_2_20	32.95	66.12	0.93	1.77

The existence of impurities could also interfere with the energy band structure of materials. Therefore, the absorption spectra of mesoporous SnO_2 spheres samples were collected using UV–Vis DRS in the region of 300–1000 nm. The three absorption spectrums **(Fig. 3.14)** revealed that SnO_2_0 possessed a longer absorption edge (435 nm) than that of SnO_2_10 or SnO_2_20 (421 nm). The slight red shift indicated the narrower band gap, which might be contributed by the more Cl impurities in SnO_0 in line with the previous report.[44] The shallower potential of the Cl 2p state than that of O 2p might be possible for the Cl-induced band gap narrowing. Furthermore, the optical band gap was calculated using the following equation: $(F(R)h\nu)^{1/n} = A(h\nu - E_g)$. By assuming direct allowed transition, the band gap of the SnO_2 was obtained by plotting $(F(R)h\nu)^2$ on the vertical axis against the $h\nu$ on the horizontal axis. The intersection of the straight line from the extrapolation with the vertical axis gives the estimated value of E_g as shown in the inset of **Fig 3.14**. The band gap energies of SnO_2_0, SnO_2_10 and SnO_2_20 were estimated to be 3.06, 3.1, and 3.1 eV respectively. These values were far from the ideal band gap of the bulk SnO_2 (3.6 eV) which may be due to Cl contamination and/or carbon doping.[45,46]
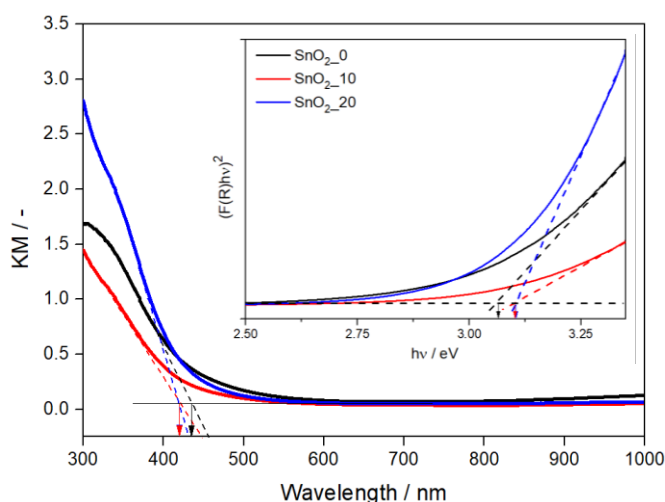
Fig. 3.14. Absorption spectra and band gap estimation (inset) of the mesoporous SnO_2 spheres.

3.1.4 Gas sensing properties

The micro-/mesoporous SnO_2 sphere sensors were initially exposed to the 50 ppm of toluene at different temperatures in the range of 200–425 ^{o}C. The optimum working temperature is the key parameter for the practicability of the proposed sensor material. It was confirmed by that previous study, that toluene decomposes at temperatures above 1125 ^{o}C, indicating its stablility under the mentioned experimental conditions.[47] As described in **Fig. 3.15**, the responses of micro-/mesoporous SnO_2 sphere showed a typical mountain–hill shape, where the response increased as the temperature rose from 200 ^{o}C to 375 ^{o}C, reached a maximum value at 400 ^{o}C, and finally declined to a lower value at 425 ^{o}C. The surface kinetic reaction between chemisorbed oxygen ions (O_2^-, O^- or O^{2-}) and analytes on surfaces of sensing materials as well as gas diffusion must be responsible for this phenomenon.[48] The gas adsorption should be more dominant as compared to the desorption in the low-temperature domain because the heat is not high enough to induce the reaction of toluene molecules with adsorbed oxygen species. At the optimum working temperature, heat energy for the acceleration of toluene and chemisorbed oxygen ions should make the toluene adsorption and desorption balanced, enabling the highest toluene response as well. At higher working temperatures, the gas adsorption on the suppressed, and the gas desorption should be dominant, resulting in the decrease of the sensing response.[49,50] At the optimum working temperature of 400 ^{o}C, the SnO_2_10 exhibited a higher sensing response of 20.2 in comparison to SnO_2_0 (2.7) and SnO_2_20 (3.2). This behavior was related to their high specific surface areas. The larger surface area could increase the number of active sites. However, the specific surface area is not the only factor affecting the properties of the SnO_2 gas sensor, because the response of SnO_2_20 with the lowest specific surface area showed exceeded response of the SnO_2_0. This is our provisional analysis, and a more detailed explanation of this enhancement will be discussed in the forthcoming gas sensing mechanism.
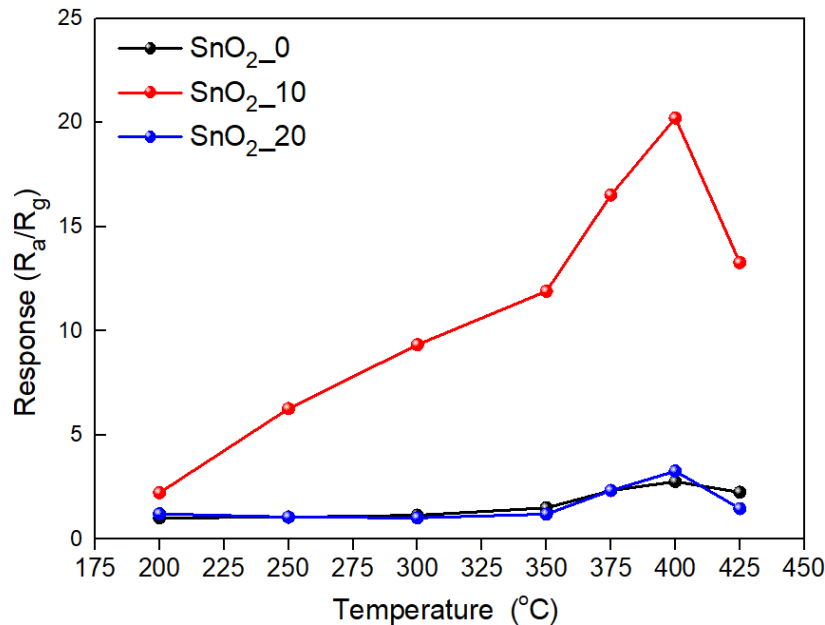
Fig. 3.15. The gas sensing performance of micro-/mesoporous SnO_2 spheres in the toluene exposure of 50 ppm at different working temperatures

The gas sensing performance of the micro-/mesoporous SnO_2 spheres was further tested towards different concentrations of toluene (10–50 ppm) at their optimum operating temperature (400 °C). **Fig. 3.16** (a) represents the dynamic gas sensing response of micro-/mesoporous SnO_2 spheres, which confirmed their n-type property. All SnO_2 samples responded to the toluene gas, and possessed the response-recovery performance as well as repeatability. In addition, at the same temperature, the initial resistance for each sample of SnO_2 was clearly varied. The value of the sensor resistance was related to the electron transports which largely depended on the particle size.[51,52] In our samples with porous hierarchical spheres, the electron migrated between nanoparticles in one spherical structure and between the spherical structure itself. But, because of the density of the inner sphere, all samples showed a similar characteristic, the spherical size was more critical to influence the sensor resistance. For instance, SnO_2_0 which possessed the smallest sphere size (0.65 µm), the average resistance was 225 kΩ. As for SnO_2_10 and SnO_2_20 where both samples had a slightly larger sphere size, the average resistance was 222 kΩ and 198 kΩ, respectively.
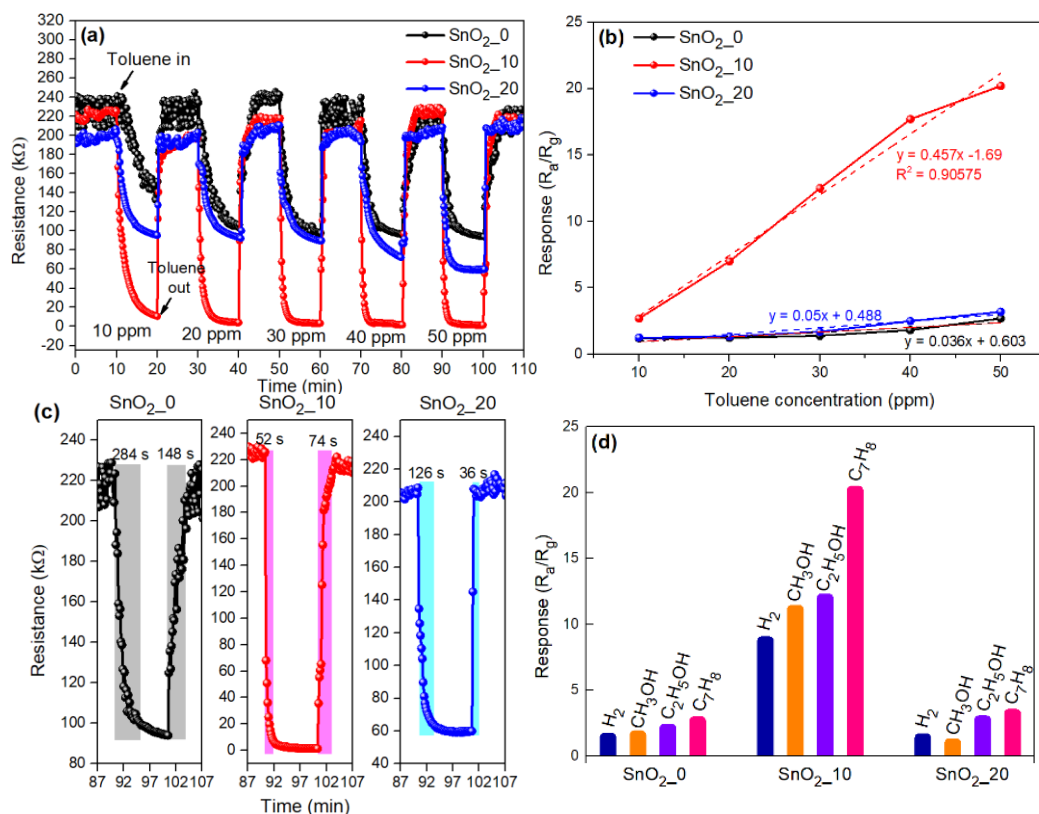
Fig. 3.16. (a) A typical gas sensing response. (b) linear fitting *vs* toluene concentration; the y axis shows sensing response; the x axis shows toluene concentration and R is fitting relationship quality. (c) response *vs* recovery time at 50 ppm of toluene and (d) selectivity of mesoporous SnO_2 spheres at 400 °C.

As seen in **Fig. 3.16** (b), the sensing response of SnO_2_10 increased from 2.7 to 20.2 as the toluene concentration increased from 10 to 50 ppm. To estimate the detection limit (DL) of the SnO_2_10 sample, the plot of toluene sensing response versus toluene concentration was linearly fitted. The theoretical estimation of DL in this study adopted the approach and definition proposed previously by Li *et al.*,[53] and the estimated DL of SnO_2_0, SnO_2_10 and SnO_2_20 was 4.3, 0.6, and 4.4 ppm, respectively. These values are far below the permissible exposure of toluene. Therefore, the mesoporous SnO_2 spheres are expected as a viable candidate for the sensitive toluene gas sensor.

Fig. 3.16 (c) displays the response/recovery times of the mesoporous SnO_2 spheres. The response time was defined as the required time from the gas injection to the point when the resistance reached 90% of the difference between initial and equilibrium resistance. The time needed to retrieve 90 % of the initial resistance after the stop of testing gas flow was regarded as

76

recovery time. The response time for SnO_2_0, SnO_2_10 and SnO_2_20 were 284, 52 and 126 s, respectively, indicating that the SnO_2_10 had the fastest response time to toluene than those of SnO_2_0 and SnO_2_20. However, the recovery speed of SnO_2_10 was slower than that of SnO_2_20 and faster than that of SnO_2_0. The affecting factor of response/recovery times in the gas sensing material will also be explained in detail on the gas sensing mechanism.

The selectivity is another foremost factor for designing the sensor device. Gas sensing selectivity of the mesoporous SnO_2 spheres was investigated by testing the sensor under the circumstance of various targeting gases include hydrogen (H_2), methanol (CH_3OH), ethanol (CH_3CH_2OH) and toluene (C_7H_8) with the same level of gas exposure (50 ppm) at 400 ℃. As shown in **Fig. 3.16** (d), all the samples exhibited a higher detection property to toluene than for other gases, indicated by their higher responsivity. However, only SnO_2_10 exhibited a 1.8–2.2 times higher response to toluene than those to other gases, revealing its potential selectivity to toluene. Furthermore, we also characterized the SnO_2_10 sample after the gas sensing test by XRD and SEM measurements (**Fig. 3.17**). The result suggested that the sample had an improved crystallinity indicated by a narrower peak. Although the crystallinity was slightly altered after the gas sensing test, the effect was not so large for the gas sensing properties, and after testing the device at 400 ℃ again, the responsivity was not largely changed. Moreover, the SEM observation disclosed the withstood overall morphology after the gas sensing test at such high temperatures, demonstrating a promise stable material for toluene gas sensor application.
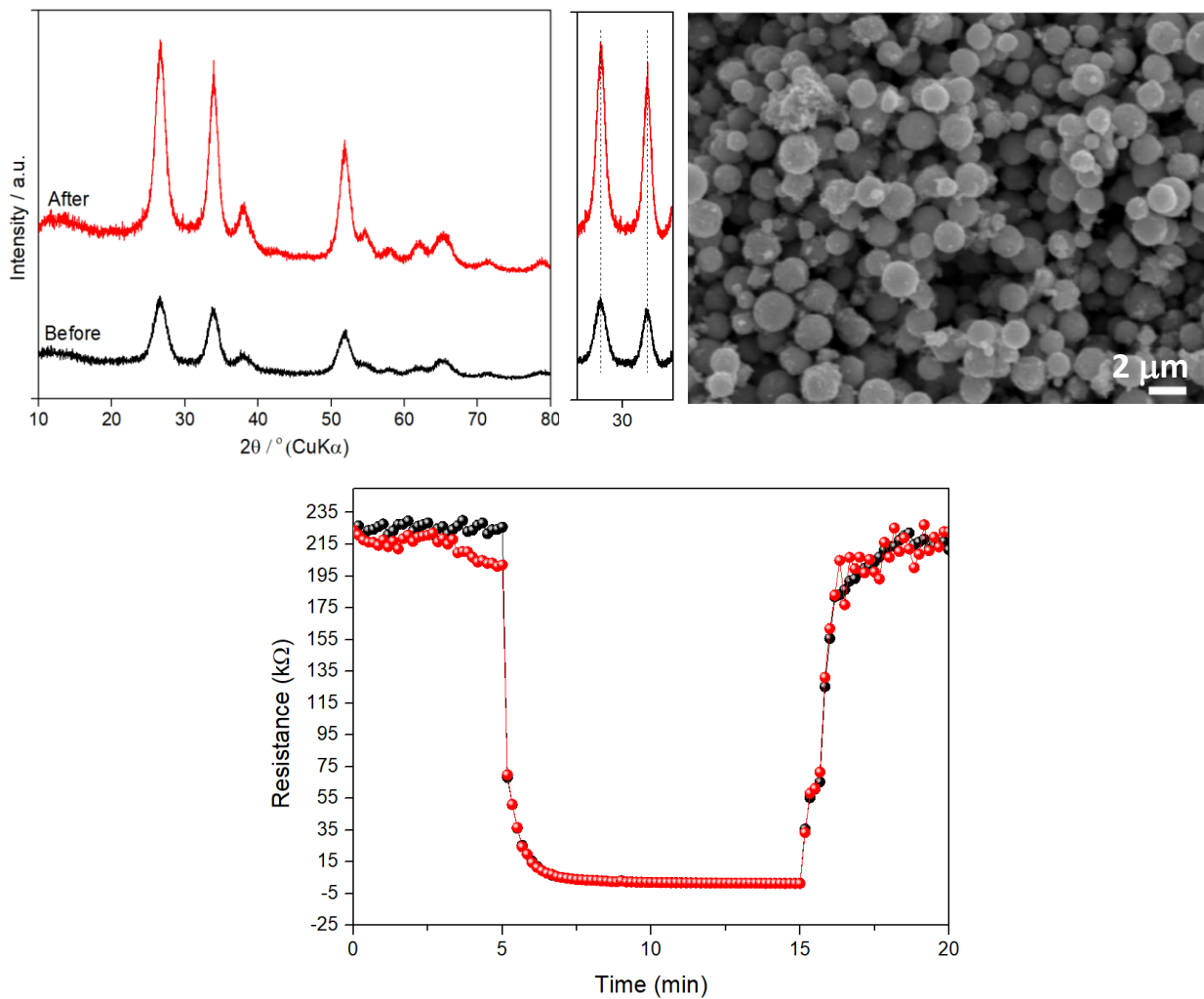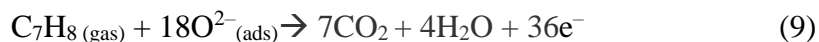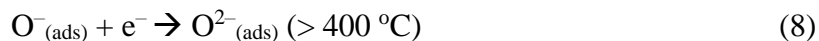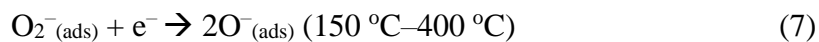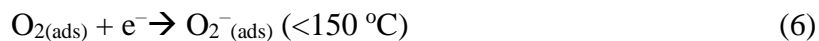
Fig. 3.17. XRD and SEM of SnO$_2$_10 after the gas sensing measurement and the gas sensing response at 400 °C.

3.1.5 Gas sensing mechanism

In an n-type semiconductor where electrons play a role as the main charge carrier, trapped electrons on the surfaces create space charge layers so-called electron depletion layers (EDLs) which increase the potential barrier to enlarge its resistance. Because the trapped electrons react with sensing molecules, the resistance is reduced by oxidation of sensing molecules by the oxygen species on the surfaces and subsequent release of electrons to the valence band.

In our case, with the obtained SnO_2 devices with an n-type semiconductor property, a similar mechanism should work in the sensing. The sensor device was first exposed to the atmospheric conditions at 200-400°C. The oxygen molecules in the air was adsorbed onto the surface of micro-/mesoporous SnO_2 spheres by trapping the electrons from the valence band resided near the surface, which led to the oxygen dissociation to form the chemisorbed ionized-oxygen species (O^{2-}, O^- or O^{2-}). The type of the chemisorbed ionized-oxygen species was largely affected by the working temperature as seen in equations (5), (6), (7) and (8).[54] When the sensor in our study was operated at 400 °C, the O^{2-} ions could be more abundant. In the case of toluene gas as a sensing gas, reaction proceeded as described in the equation (9).[55] This removal of O^{2-} ions by the reaction of toluene from the surfaces caused the thinner size of EDLs to decrease the potential barrier, resulting in the decrement of resistance, as observed in **Fig. 3.16** (a). As previously discussed, the particle size influenced the charge-carrier mobility in metal oxides due to the different conductive model. The effect of particle size of SnO_2-based sensors on its gas sensing response was theoretically and experimentally reported.[56] The improvement of sensitivity was usually attributed to the reduction of particle size to nearly the thickness of the charge depletion region.[57] However, our samples showed a contrast result in which the smallest particle size did not always maintain a linear connection with the enhanced sensitivity. Decreasing the particle size from 1.50 to 0.90 µm undoubtedly raised the response from 3.2 to 20.2, but further decrement to 0.65 µm dramatically depreciated the response to only 2.7. Therefore, the particle size was not the only focal factor, but apart from it, the pore size effect should also be taken into consideration as an influencing parameters.

$$O_{2(gas)} \rightarrow O_{2(ads)} \quad\quad (5)$$

$$O_{2(ads)} + e^- \rightarrow O_2^-{}_{(ads)} \; (<150\ ^oC) \quad\quad (6)$$

$$O_2^-{}_{(ads)} + e^- \rightarrow 2O^-{}_{(ads)} \; (150\ ^oC\text{–}400\ ^oC) \quad\quad (7)$$

$$O^-{}_{(ads)} + e^- \rightarrow O^{2-}{}_{(ads)} \; (>400\ ^oC) \quad\quad (8)$$

$$C_7H_{8\,(gas)} + 18O^{2-}{}_{(ads)} \rightarrow 7CO_2 + 4H_2O + 36e^- \quad\quad (9)$$

Gas sensing properties towards various target gases can be improved by controlling the porous architecture of the metal oxides which are directly associated to the pore size. During the sensing process, gas diffusion in the porous materials is mainly prevailed by Knudsen diffusion as expressed:[58]

$$D_K = \frac{2r}{3}\sqrt{\frac{8RT}{\pi M}} \quad\quad (10)$$

where D_K is the diffusion coefficient (cm^2/s), T is temperature (K), M is molecular weight (g/mol), R is gas constant (J/mol·K) and r is pore radius (cm). From the given formula, the Knudsen diffusion largely depends on three main factors. Firstly, the diffusion coefficient is proportional to the pore size, where the larger pore size leads to a higher diffusion rate for both oxygen and testing gas, which can allow the gas molecules to diffuse to the deeper region and reach the more inner surface of the sensing material. In our work, at 400 ^oC, the gas sensing response of SnO_2 was in the following order: $SnO_2\_10 > SnO_2\_20 > SnO_2\_0$, which was not exactly having a linear proportion to their pore size distribution. For example, with the smallest pore size detected in SnO_2_0 sample, it exhibited the lowest sensing response (2.7 to 50 ppm of toluene), whereas for SnO_2_10 sample with the medium pore size of 1.4 nm, the gas sensing response showed a very high sensing response of 20.2 under 50 ppm of toluene, which was approximately 6 times higher than those of SnO_2_0. The molecular size of toluene was estimated to be 0.59 nm,[59] which was sufficiently small to enter the sub-surface region of the meso-/microporous SnO_2 spheres through their porosity as illustrated in **Fig. 3.18**. Therefore, the enhanced toluene sensing response was attributed to the larger pore size, allowing the oxygen and the tested gas molecules to diffuse through the diffusible path to penetrate to the interior of the micro-/mesoporous SnO_2 spheres. Therefore, the frequency of collision between the surface of materials and the gas molecules

probably increased. However, the SnO_2_20 with further larger pores (1.9 nm) exhibited a lower toluene sensing response (3.2 to 50 ppm). Although the diffusion rate probably increased to a certain value with the larger pore size, the reduced specific surface area dominated the gas sensing performance, rather than the pore size. The response of SnO_2 sample synthesized in the pure water also showed the same trend. The reduced surface area led to a reduction in the number of active sites. This suggested that pore size and specific surface area synergistically enhanced the sensitivity. Secondly, following to equation (10), diffusion rate increased as temperature rose; at higher temperatures, the faster gas molecules motion should be in the porous material, which became another reason for the much high working temperature besides to the toluene molecular stability. Lastly, the Knudsen diffusion also relied on the molecular weight of the analytes, where the lighter analyte could have faster diffusivity and surface reaction. For the case of toluene gas, SnO_2_0 with the smallest pore size exhibited the slowest response/recovery time of 284/148 s. By modulating pore size to 1.4 and 1.9 nm, the response/recovery time markedly escalated to 52/74 s and 126/36 s, respectively. This enhancement should be attributed to the better permeability in the micro-/mesoporous material with larger porosity which led to a shorter diffusion time.[60] It was interesting that the response time of SnO_2_10 was faster than that of SnO_2_20, but the recovery time was double that of SnO_2_20. Our result agreed with the work of Tang *et al.*[61] in which they concluded that material with strong adsorbed property could likely exhibit a fast response and longer recovery time. For the detection of hydrogen gas which lighter than toluene (**Fig. 3.19**), the response/recovery time of SnO_2_10 was 24/32 s was consistent with the Knudsen equation.
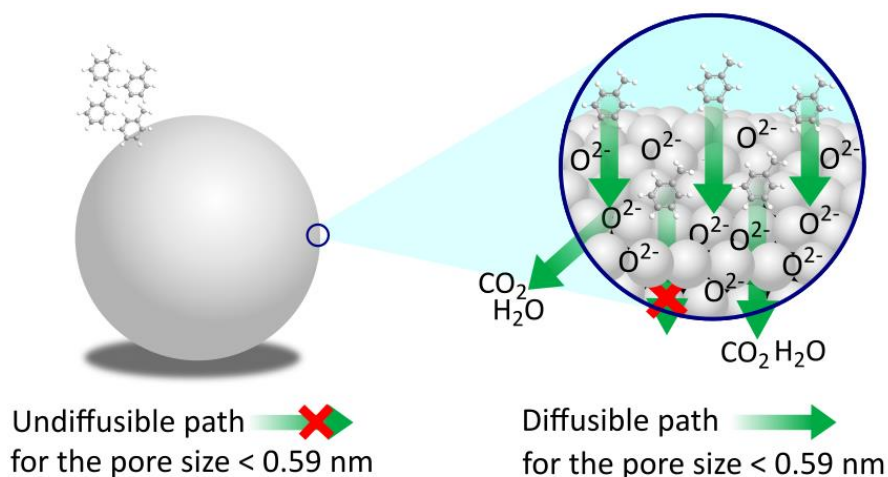
Fig. 3.18. Diffusion mechanism on the surface and sub-surface of the micro-/mesoporous SnO_2 spheres during the exposure to toluene gas.

Since the samples included a considerable amount of Cl, where Cl could modify the carrier concentration (N_d) of SnO_2, the effect of Cl was also considered. The Cl was expected to replace the O site, raising the N_d to some extent. In excess or in a saturated value, the Cl incorporation might be in the interstitial site, changing its role from donor to acceptor, which led to the fall of N_d.[62] This was being reasonable considering the sample with the highest Cl content exhibited the largest resistivity and poor responsivity. These explanations suggested that the sophisticated control of SnO_2 micro-/meso structures including particle size, pore size, specific surface area as well as impurity amount by simple synthetic method enabled the highly sensitive and selective toluene gas sensor.

Fig. 3.19. H_2 sensing response of SnO_2_10

3.2 Facet controlled synthesis of NiO nanostructures for NO_x detection: Experiment and DFT calculation

3.2.1 Introduction

The industrialization era has brought unignorable environmental downgrade aside to economic growth and human prosperity.[63,64] Air quality worsening, one of the serious environmental issues caused by automotive engine and industrial exhaust gases has become an utmost concern for s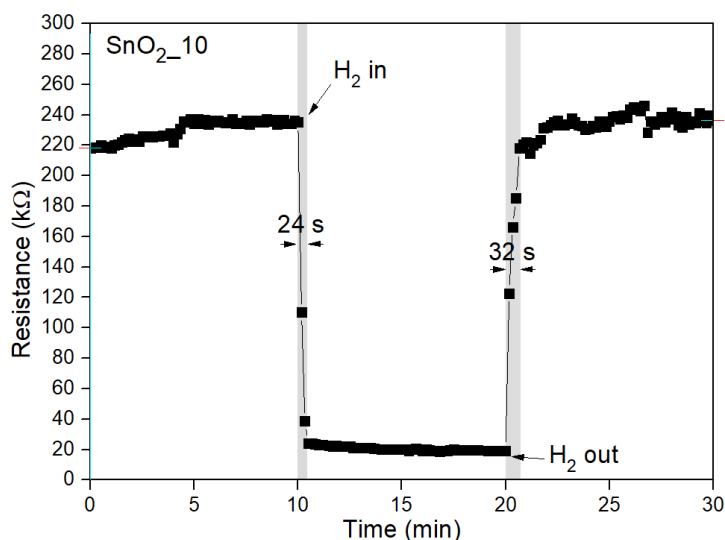cientists, engineers, and environmentalists due to their effect on human health and surrounding eco-system.[65] For instance, Nitrogen oxides, NO_x, are deadly atmospheric contaminants produced from hydrocarbons combustion processes such as vehicle engines or power plants which usually occur at high temperature.[65–67] Not to mention electrical generation from non-renewable fuels, the massive use of vehicles, especially in the metropolitan city, has made the condition is getting worse by the time.[68] Hence, there is an urgent need for the development of highly responsive materials towards NO_x detection for environmental pollution control. In addition, a single material that can be applied in multiple applications is desirable for technological simplicity.[69]

Many different kinds of NOx sensor materials have been extensively studied, especially semiconductor metal oxides (SMOX) owing to their tailorable physical and chemical properties.[30,65,70–74] Due to these, SMOX exhibits a very promising and outstanding performance alongside with reversibility and long term stability. Nickel Oxide (NiO), is a rock-salt type metal oxides and well-known p-type semiconductor metal oxides for multifunctionality of environmentally benefit applications such as photocatalyst and sensor for the hazardous gas.[72,75,76] However, NiO wide-bandgap value ranging from 3.6 to 4.0 eV has set drawbacks which may limit its NO_x sensor responsivity.[77] Various approaches have been attempted to design a high-performance semiconductor photocatalyst and sensor, involving morphological control, atomic doping incorporation, and surface defect engineering.[78–80] Precise control of exposed facets has been proven to be advantageous for the improved performance of sensor and photocatalyst nanocrystals and even more versatile than specific surface area, porosity, and other influencing factors.[81,82] Desired exposed facet can provide a highly energetic and active site through high-density of low-coordinated atoms for selective molecular adsorption.[82] The facet selective property hinders the material to adsorb undesired molecules target from the surrounding environment, leading to an exceptional activity for sensors application.

As a typical rock-salt structure, NiO has three thermodynamically favorable crystal facets, e.g. (100), (110), and (111). (100) facet, specifically, has the lowest formation energy and is the most stable form thermodynamically.[83] Thus, molecular adsorption onto NiO (100) facet has been done in the majority of the previous investigation.[84] However, with the development of the materials synthesis method, it is potentially possible to design a rock-salt type material with dominantly (110) and (111) facets.[84] Mesopores NiO with (110) facet has been successfully obtained by a post-treatment of β-Ni(OH)$_2$.[85] CoO with (111) facet can be directly prepared by calcination of CoCl$_2$ precursor.[86] Other studies also show the preparation of MgO (111) facets via the inexpensive wet chemical method.[87] These investigations showed the formation of exposed facet of rock-salt crystals, including NiO, is largely dependent on synthesis conditions such as initial precursors, or ligands. While NiO can be prepared through the calcination of β-Ni(OH)$_2$ at elevated temperatures at around 400 °C to preserve the morphology of the parent β-Ni(OH)$_2$,[72,88] there is still limited knowledge on the phase and morphological transformation to NiO from other starting material.

In this work, we present a newly developed route to synthesize NiOHCl, a layered structure hydroxychloride, as a potential precursor to produce NiO with highly polar exposed (111) facet. In all investigations to date, NiOHCl has not been transformed to NiO,[89–92] although its layer structure holds a promise to be translated into rock salt structure and Cl$^-$ in its structure may stabilize the polar (111) facet through electrostatic stabilization during the transformation.[93] NO$_x$ gas sensing property and photocatalytic ability of NiO (111) facet were superior to NiO (110) facet obtained by annealing of β-Ni(OH)$_2$ for which the DFT ab initio calculation revealed that Bridge site in (111) facet is the most favourable place for NO$_x$ adsorption. The Crystal Orbital Hamilton Population (COHP) was utilized to deeply understand the physical origin of how the adsorption and charge transfer mechanism from NiO to the molecular orbital of NO$_x$ occurred which led to NO$_x$ decomposition.

3.2.2 Experimental

Preparation of NiOHCl hexagonal plate and NiO (111) octahedral morphology

The hexagonal morphology of nickel hydroxychloride (NiOHCl) was synthesized by a water-controlled release solvothermal process (WCRSP).[94] 77.8 mg of anhydrous Nickel (II)

Chloride ($NiCl_2$) was dissolved into 50 mL of 1-propanol (1-PrOH) anhydrous with vigorous stirring with a constant speed of 500 rpm for 25 min at RT. Then, 10 mL of anhydrous acetic acid (AcOH) followed by the same stirring condition. The resulting solution was transferred to 100 mL Teflon lined-autoclaved and solvothermally treated at 200 °C for 10 h. After cooled to room temperature, the light green powder was recovered by a vacuum-filtration, dried at 60 °C, and ground by mortar. Finally, to obtain NiO with octahedral morphology, the obtained NiOHCl was calcined at 400 °C for 3 h. The sample was named as NiO Octa-(111).

Synthesis of NiO (110) with hexagonal morphology

Hexagonal morphology of NiO with (110) exposed facet was produced by following the previous report.[85] 0.02 mol of anhydrous $NiCl_2$ was dissolved in 10 mL of DI water followed by the addition of 6 M NaOH under the stirring condition. Then, 0.6 mmol of sodium sulfate (Na_2SO_4) was added into the solution. After transferring to Teflon-lined autoclave with 100 mL capacity, the solution was treated at 170 °C for 24 h. The green $Ni(OH)_2$ product was collected by vacuum filtration and dried at 60 °C. Then, it was finally calcined at 400 °C for 3 h to obtain the NiO-Hexa (110) sample.

DFT Calculation

Density Functional Theory (DFT) calculations are performed with plane-wave basis sets and periodic boundary conditions, using the slab model to simulate surface conditions. Generalized Gradient Approximation (GGA) exchange-correlation functionals parametrized by Perdew, Burke, and Ernzerhof (PBE)[95] are chosen along with appropriate Hubbard U correction for NiO to produce a more accurate electronic structure for Mott insulators.[96] The effective Hubbard U parameter for NiO has been thoroughly explored and tested in earlier works. Parameter values of Ueff = U-J = 5.3 eV, with U = 6.3 eV and J = 1 eV is chosen according to a previous investigation of water adsorption on NiO (100) surface[97] and other, earlier investigations into NiO.[96,98,99] Core electrons are treated with the projector-augmented wave (PAW) method.[100] Calculations are performed with the Vienna Ab Initio Simulation Package (VASP) software package.[101–104]

Visualization of crystal structures, both for input and output of first-principles calculations, is performed with the Visualization for Electronic and Structural Analysis (VESTA) program.[105]

NiO surface is modeled using slab models with a minimum of 4 atomic layers to approximate bulk effects to surfaces. Vacuum slabs between the 4 layers of NiO are used to prevent interaction with periodic images in the z-axis. Similarly, 2×2 surface unit cells (corresponding to 0.25 ML coverage) are used to prevent interaction between the NO adsorbate molecule and its periodic images in the x- and y-axes. Geometry optimization calculations are used to model adsorptions, with adsorbates situated initially at 2Å, from the surface adsorption site.

In order to ensure reliable calculations, the values of several calculation parameters are converged with respect to the total energy of the simulation cell. These parameters include the cut-off energy (in plane-wave DFT representing the size of the basis set used), the k-point grid for integrations (using Monkhorst-Pack grid),[106] and the aforementioned thickness of the vacuum slab. The calculations performed for this work uses a cut-off energy of 400 eV, a k-point grid of $5 \times 5 \times 1$, and a vacuum slab of thickness 10 Å, converging the total energy of calculated systems to a reliability of 0.001 eV/atom. The antiferromagnetic ground state of NiO is also taken into account as initial magnetic moments for every calculation are set as antiferromagnetic in the [111] direction. Meanwhile, the adsorbate molecule NO is relatively much easier to model. Starting from the experimental work of Kukolich, the initial N-O bond length in vacuum was set as 1.154 Å.[107] Geometry optimization with the GGA-PBE exchange correlation functional slightly stretches the N-O bond length to 1.1692 Å, which is in good agreement with 1.16 Å from a previous ab initio work by Beheshtian et al.[108]

Distinguishing the contribution of hybridized orbitals to interatomic bonding is key to analyzing binding or adsorption between two systems. In this way, Crystal Orbital Hamilton Population (COHP) analysis is an effective tool in distinguishing bonding and antibonding orbitals resulting from hybridization between two atoms. In the theoretical portion of this work, we employ the Local Orbital Basis Suite Towards Electronic Structure Reconstruction (LOBSTER) code which applies the projected COHP (pCOHP) method to extract similar atom resolved chemical information from wavefunctions with plane-wave basis sets.[109–112] The pCOHP method projects the plane-wave basis set representation of the wavefunction onto atomic orbital-like contributions to the molecular orbitals, from which a more chemical picture may be shown.

Gas sensing evaluation

To fabricate the sensor device, 0.010 g of the obtained NiO samples were mixed with ethanol to obtain a slurry which then was brush-coated onto an Au interdigitated electrode (IDE). The gas sensing evaluation for the obtained material was conducted using a home-built electrical measurement system (Agilent Keysight 34970A) with 2 probe method at various temperatures from room temperature to 300 °C to mimic the challenging condition of automobile engine exhaust system. The variation of temperatures is critical to determine the optimum working temperature of the sensor device for the real application. It is noteworthy to mention that to minimize the photocatalytic effect of NiO, our sensing equipment used a metal chamber with an insignificant possibility of light to irradiate the samples. The sensing response (R) was calculated by following formula $R(\%) = ((R_g-R_a)/R_a) \times 100\ \%$ where Rg is resistance in targeting gas and Ra is the resistance in ambient air. The response and recovery times were also assessed by calculating the time needed to reach a 90 % variation of saturated resistance during the injection and rejection of testing gas, respectively.

3.2.3 Result and discussion

3.2.3.1 Crystal structure and morphology characterization

Fig. 3.20 (a) shows XRD patterns of NiOHCl and β-Ni(OH)$_2$ precursors. For NiOHCl, the (003) plane located at 15.6° was very intense compared to (012), (015), (009), (107), and (110) planes centered at 33.3°, 41.3°, 48.0°, 49.4°, and 56.5°, respectively. To determine the quality of the crystal structure of the NiOHCl sample, Rietveld analysis was employed using RIETAN-FP software.[113] As shown in Fig. **3.21** (a), the Rietveld refinement assuming the rhombohedral structures (space group $\overline{R3}m$) has converged resulting in a lattice parameters of a = 3.2674 Å, c = 17.068 Å Rwp (%) = 3.977, Rp (%) = 2.428, Re (%) = 0.646 and S = 6.1596. The goodness-of-fit, S, was very large due to XRD profile of NiOHCl has a high base line. The refined results for structural parameters was summarized in **Table 3.4**. Additionally, the Ni-O and Ni-Cl bonding distances are 2.036(6) Å and 2.453(5) Å, respectively. Due to the disorder behaviour of anion site, average bond distance of Ni[(OH),Cl]$_6$ is 2.036(6) ~ 2.453(5) Å.

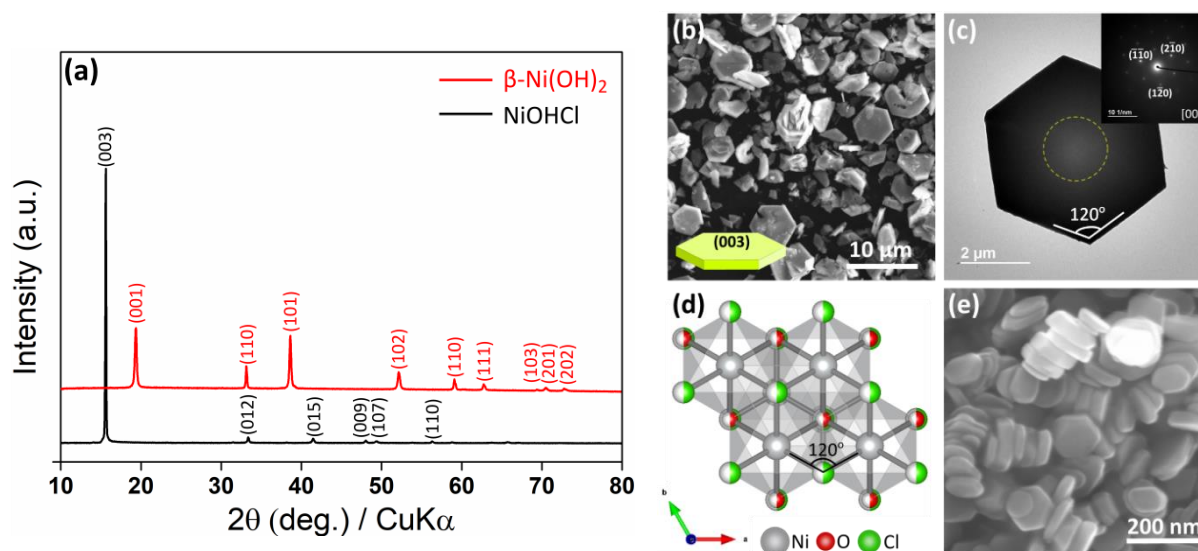**Fig. 3.20** (a) XRD pattern of NiOHCl and β-Ni(OH)₂, (b) SEM image (c) TEM image (inset is SAED pattern taken from area indicated by a dashed-line circle) (d) crystal structure of NiOHCl along the (003) facet showing oxygen and chlorine atoms possess other atom occupancies and (e) SEM image of β-Ni(OH)₂.
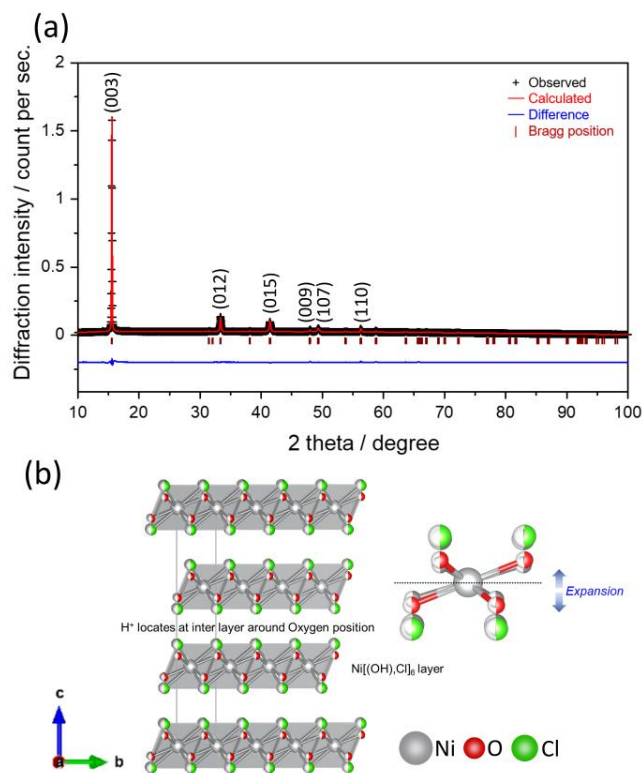

Fig. 3.21 (a) Rietveld refinement of powder X-Ray Diffraction (PXRD) and (b) crystal structures of NiOHCl after refinement

Table 3.4 Refined structural parameters of NiOHCl (space group = $R\bar{3}m$)

Atom	Wyckoff	Occ.	x	y	z	$U_{iso.}$ (nm^2)
Ni1	3a	1	0	0	0	0.043(1)
O1	6c	0.5	1/3	2/3	0.0448(8)	0.012(5)
Cl1	6c	0.5	1/3	2/3	0.0919(4)	0.023(2)

Comparing to earlier study (summarized in **Table 3.5**),[90] NiOHCl sample in this work has a slightly higher structural parameter value, suggesting a structural expansion (**Fig. 3.21** (b)) which might be attributed to a small organic molecules incorporation, revealed by CHN analysis (C= 2.6 wt.%, H = 3.95 wt.% and O=17.34 wt.%) Meanwhile, the emerged peaks of β-Ni(OH)$_2$ were in a good agreement with the standard (PDF card 14-0117).

Table 3.5. Comparison of refined structural parameters of NiOHCl with earlier work

	This work	Reported[114]
Crystal system	Rhombohedral	
Space group		$R\bar{3}m$
a (Å)	3.2674(1) [+0.2%]	3.26061(8)
c (Å)	17.068(1) [+0.3%]	17.00619(89)
V (Å^3)	157.80(1) [+0.8%]	156.57
Ni1	0	0
O1	0.0448(8)	0.03500(22)
Cl1	0.0919(4)	0.08790(8)
Ni-O (Å)	2.036(6)	1.9744(12)
Ni-Cl (Å)	2.453(5)	2.4038(9)

Morphology and particle size of NiOHCl and β-Ni(OH)$_2$ phases were observed by SEM and TEM. As revealed by the SEM and TEM images in **Fig. 3.20** (b) and (c), NiOHCl has a nearly perfect hexagonal morphology with the size of approx. 5 µm, angle of 120° at each corner, and

acceptable homogeneity although some split particle was observed. From the corresponding selected area electron diffraction (SAED) pattern taken from the yellow circle area, the hexagonal NiOHCl exhibited a single crystalline property (inset of **Fig. 3.20** (c)) with ($\bar{1}\,\bar{1}0$), ($2\bar{1}0$), and ($1\bar{2}0$) planes from [003] zone axis. This may indicate the electron beam is perpendicular with (003) facet of hexagonal morphology as well NiOHCl crystal structure. It is reasonable considering the (003) facet of the NiOHCl crystal structure refined by the Rietveld analysis (**Fig. 3.20** (d)) clearly shows that the hexagonal morphology with an angle of 120º. Furthermore, TG/DTA and elemental analysis were utilized to provide further insight into the stoichiometric and phase transformation of NiOHCl. From the TG-DTA measurement (**Fig. 3.22**), the weight loss of NiOHCl was 36.4 wt. % due to the evaporation of HCl, leading to the transformation into the NiO phase based on the following reaction: NiOHCl → NiO + HCl. The weight loss is very close to the theoretical molecular weight of HCl (36.4 wt. %). Additionally, the elemental analysis confirmed the Cl amount in NiOHCl was 36.57 wt. % that agreed with an atomic mass of Cl (35.4 wt. %). Thus, the formation of NiOHCl is fully convincing based on the result above. The obtained β-Ni(OH)$_2$ phase also shows a similar hexagonal structure with a smaller particle size (ca. 150 nm). Based on the previous investigation, the hexagonal morphology of β-Ni(OH)$_2$ possessed (001) exposed facet with a high ratio to the total surface.[85]

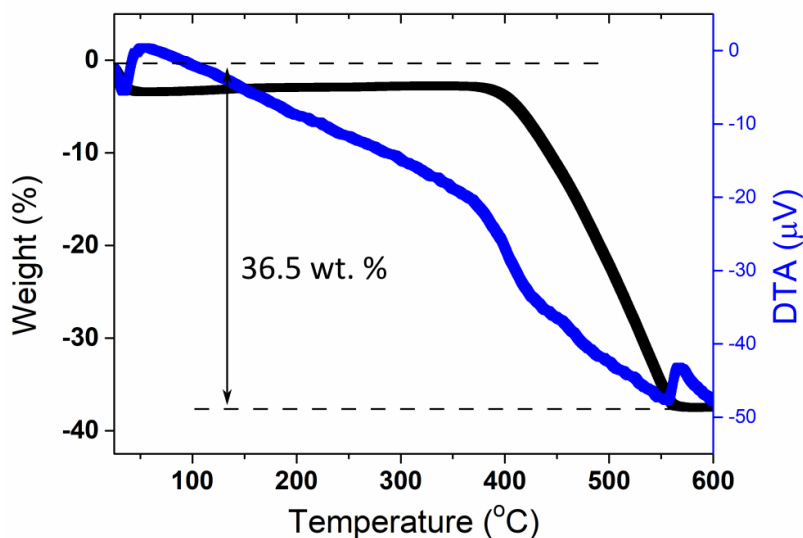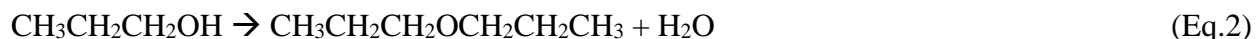**Fig. 3.22** TG/DTA curve of NiOHCl

It is widely known that the formation pathway of β-Ni(OH)$_2$ involved the hydrolysis of nickel salt precursors. However, the formation of NiOHCl in organic solvents is not well-

investigated. Thus, it is of foremost importance to understand the chemical reactions involved in the formation of the NiOHCl phase. Herein, we performed ^{1}H NMR analysis to elucidate the chemical composition of solvents after the solvothermal process and propose the reaction pathway accordingly. In preparation for ^{1}H NMR measurement, the supernatant was diluted with deuterate CD$_3$OD. ^{1}H NMR spectrum (**Fig. 3.23**) indicates a signal of starting 1-propanol solution (C*H*$_3$CH$_2$CH$_2$OH: 0.909 ppm, CH$_3$C*H*$_2$CH$_2$OH: 1.513 ppm, CH$_3$CH$_2$C*H*$_2$OH: and 3.482 ppm). In addition to these signals, we have detected the formation of propyl acetate (C*H*$_3$CH$_2$CH$_2$OOCCH$_3$: 0.922 ppm, CH$_3$CH$_2$C*H*$_2$OOCCH$_3$: 3.973 ppm, and CH$_3$CH$_2$CH$_2$OOCC*H*$_3$: 1.995 ppm), dipropyl ether (CH$_3$CH$_2$C*H*$_2$OC*H*$_2$CH$_2$CH$_3$: 3.482 ppm, CH$_3$C*H*$_2$CH$_2$OCH$_2$C*H*$_2$CH$_3$: 1.586 ppm and C*H*$_3$CH$_2$CH$_2$OCH$_2$CH$_2$C*H*$_3$: 0.922 ppm) and hydrogen chloride (*H*Cl: 4.84 ppm).[35] However, acetic acid signal was not detected, indicating it was fully reacted during the treatment. The presence of mixed chemicals provided direct evidence of the occurrence of esterification, dehydration, and hydrolysis. Thus, we propose a possible chemical pathway during the water-controlled release solvothermal process (WCRSP) based on the NMR analysis as shown in the reaction (Eq.1)-(Eq.3). At the first step, esterification reaction between 1-propanol and acetic acid, yielding certain amount of water molecules equal to the amount of acetic acid. The dehydration of 1-propanol also produced a small fraction of water molecules. Finally, these water molecules hydrolysed the NiCl$_2$ into NiOHCl. It might be suspected that propyl acetate plays a major role as structure-assisting surfactant by attaching to polar (003) planes inhibiting its growth along (003) planes, although the detailed mechanism is still uncertain at present moment, yet should be investigated in the future study. It seems that NiOHCl also undergoes a hydrolysis reaction, but it is limited by the amount of generated water molecules from the esterification reaction. However, we could not obtain either NiOHCl or β-Ni(OH)$_2$ phase when the solution was changed from mixed 1-PrOH/AcOH to distilled (DI) water. It may imply that NiOHCl was preferably formed in the acidic condition rather than in the neutral condition. This also supports earlier studies.[89–91]

CH$_3$CH$_2$CH$_2$OH + CH$_3$COOH → CH$_3$CH$_2$CH$_2$OOCH$_3$ + H$_2$O   (Eq. 1)

CH$_3$CH$_2$CH$_2$OH → CH$_3$CH$_2$CH$_2$OCH$_2$CH$_2$CH$_3$ + H$_2$O   (Eq.2)

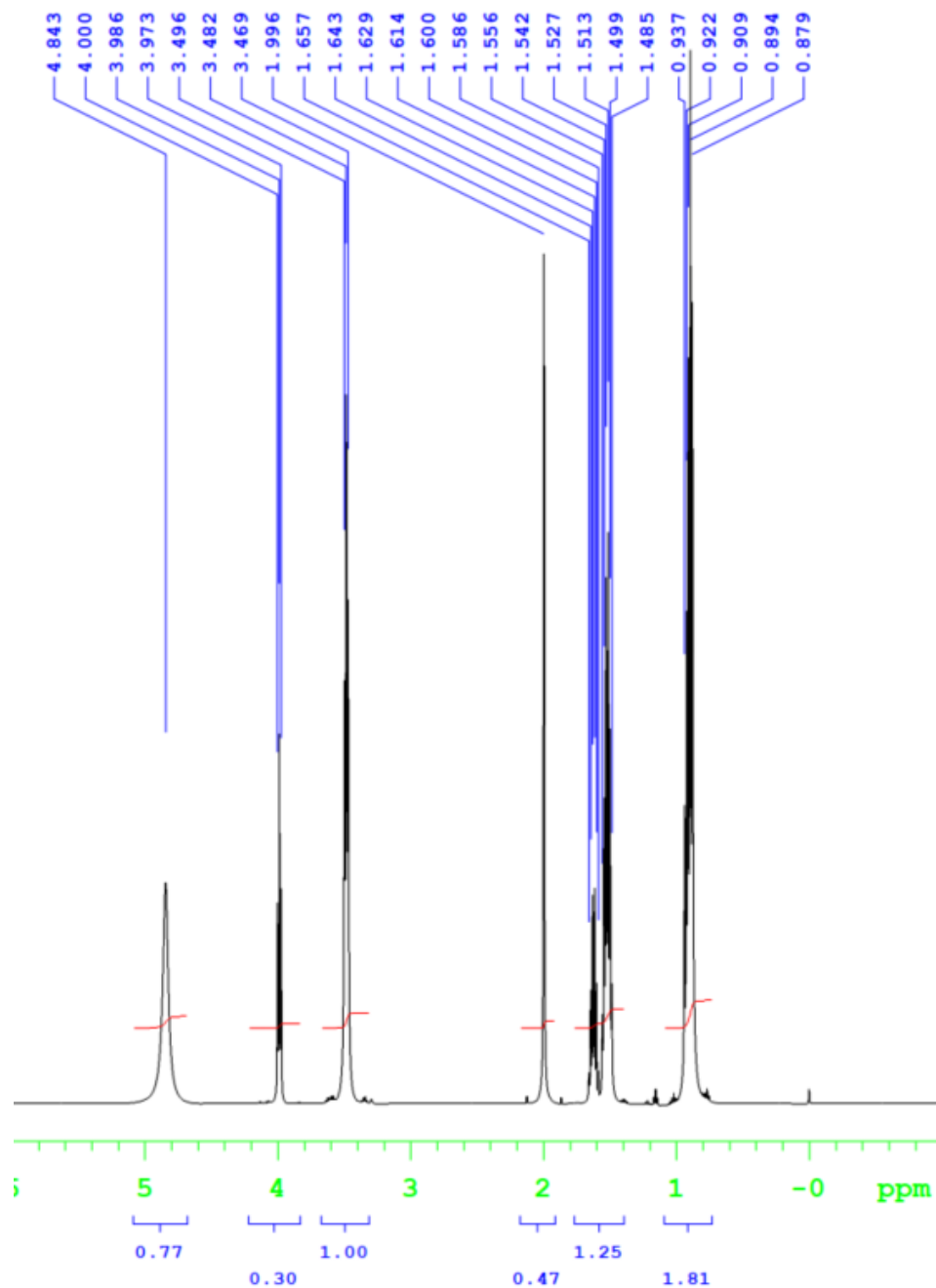NiCl$_2$ + 2H$_2$O → NiOHCl + HCl   (Eq.3)

Fig. 3.23 NMR analysis from NiOHCl final solution synthesis

The XRD patterns of NiO obtained from the calcination of NiOHCl and β-Ni(OH)$_2$ were shown in Fig. 2 (a). Regardless the precursors' phase, the well-defined peaks appeared at 37.2, 43.2, 62.8, 75.3, 79.3o correspond to the (111), (200), (220), (311) and (222) of cubic structures NiO with a monoclinic phase which agreed to standard (PDF Card 47-1049). The obtained NiO was also a pure phase proven by no observed impurities peak. Textural coefficient (TC) can determine the preferred orientation of a material. TC is calculated as:[86]

$$TC(hkl) = \frac{I(hkl)/I_o(hkl)}{\frac{1}{N}\sum I(hkl)/I_o(hkl)}$$

where I(hkl) is the intensity of the (hkl) obtained from XRD measurement, I$_o$(hkl) is the diffraction intensity of the NiO according to the PDF card 47-1049 , and N is the number of diffraction peaks used in the calculation. Any material with a random crystal orientation, the TC should be 1. We obtained that the TC(111) for NiO-Octa (111) and NiO-Hexa (110) are 1.110 and 0.985, a strong indication of more (111) preferred orientation in NiO-Octa (111) than that in NiO-Hexa (110).

As can be seen in SEM and TEM images (**Fig. 3.24** (b)-(c)), after the calcination at 400 °C, the hexagonal morphology of NiOHCl was drastically transformed into octahedral morphology with dominantly exposed (111) facet on the geometrical system. Inclusive of nanosized particles (100-500 nm), the octahedral morphology of NiO (111) exhibited a smooth surface. **Fig. 3.24** (d) displayed high-resolution TEM (HRTEM) shows the lattice distance of 0.149 nm, 0.150 nm, and 0.153 nm attributed to d-spacing of 202, 022, and 220, respectively, very close to reports from Kim and co-workers.[88] Moreover, the corresponding Fast-Fourier-Transform (FFT) pattern (**Fig. 3.24** (d), inset), and selected area diffraction pattern (SAED) depicted in **Fig. 3.24** (e) suggests that NiO with octahedral morphology is single-crystalline. All FFT and SAED spots can be indexed along [111] zone axis of octahedral NiO. These results demonstrated that (111) plane (**Fig. 3.24** (e), inset) is parallel with the surface of NiO octahedral morphology, revealing the dominant facet is (111). All characterization results agreed to the previous reports of NiO 111 facet. On the contrary, the NiO morphology and particle size obtained from β-Ni(OH)$_2$ precursor were identical with the parent hexagonal morphology (SEM, **Fig. 3.24** (f)). Nonetheless, due to the evaporation of H$_2$O, the NiO hexagonal morphology showed a mesoporosity architecture (TEM, **Fig. 3.24** (g)).

Although it possesses the porous structure that may induce the formation of another facet, only one d-lattice spacing was observed (0.24 nm) which is attributed to (111) crystal plane. However, the amount of another possible facet such as (002), (11$\bar{1}$), and (1$\bar{1}$1), however, the (110) facet is still dominant as its amount is more than 66% revealed by the previous study.[85] The SAED pattern shown in **Fig. 3.24** (h) implies the single-crystalline nature of NiO hexagonal morphology from which the indexed planes indicate the [110] zone axis is concurrent with the TEM incident beam and parallel with the top surface of NiO hexagonal morphology. The above results confirmed NiO hexagonal morphology has dominantly (110) exposed facet and were consistent with the reproduced report.[22] From now on, the NiO samples in this study were labeled as NiO-Octa (111) and NiO-Hexa (110).

An interesting phenomenon on how dramatical change on the morphology after the calcination occurs should be investigated. Thus, it is also noteworthy to reveal the transformation mechanism from NiOHCl hexagonal to NiO octahedral morphology with (111) facet by varying calcination temperatures while taking XRD and SEM measurement at each temperature. As can be seen in **Fig. 3.25** (a), almost no alteration in the XRD patterns after the calcination up to 350 ^{o}C, demonstrating NiOHCl phase stability under 400 ^{o}C, being consistent with TG/DTA. Only at 400 ^{o}C, full phase transformation has occurred. This also indicates that no intermediate chemical was formed. In **Fig. 3.25** (b), SEM images showed the morphological transformation of NiOHCl. The hexagonal morphology can still be observed even at 350 ^{o}C. However, it was broken up into a very fine crystal due to the start of HCl evaporation. TEM image (**Fig. 3.25** (c)) reveals that octahedral nanostructures have already formed within the porous hexagonal morphology at this temperature. Therefore, it might conclude that the evaporation-recrystallization-facet arrangement process has simultaneously occurred. The simplified illustration of the structural transformation is displayed in **Fig. 3.24** (j).
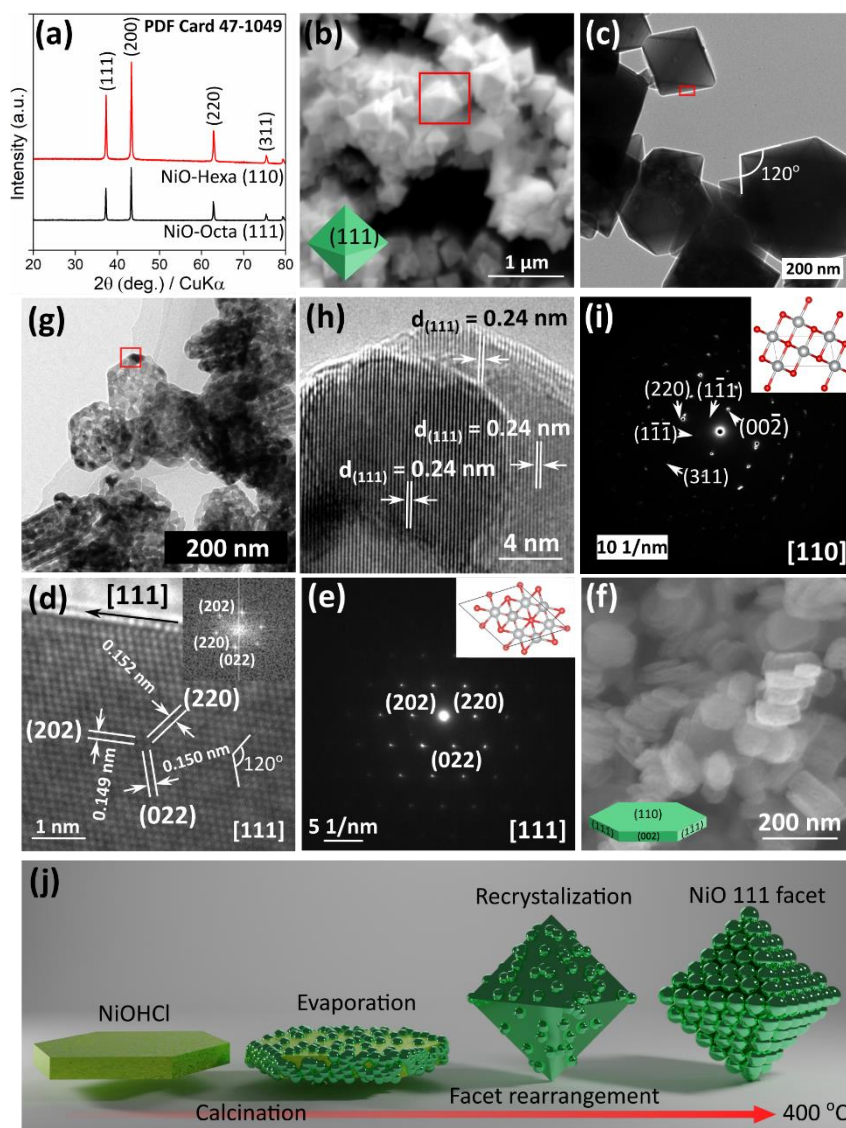
Fig. 3.24 (a) XRD patterns of the NiO Octa (111) and NiO Hexa (110), (b) SEM, (c) TEM, (d) HRTEM (inset is FFT), (e) SAED pattern taken from red area (inset is corresponding crystal structure with cut-off in [111] zone axis) of NiO-Octa (111) sample. (f) SEM, (g) TEM, (h) HRTEM, (i) SAED pattern taken from red area (inset is corresponding crystal structure with cut-off in [110] zone axis) of NiO-Hexa (110) sample. (j) a simplified illustration of morphological transformation of NiOHCl hexagonal into NiO octahedral.

Fig. 3.25. (a) XRD patterns and (b) SEM image of NiOHCl calcined at elevated temperatures, and (c) HRTEM image of NiOHCl calcined at 350 °C.

The subsequent investigation is how NiO (111) facet could form in the case of NiOHCl, but could not in β-Ni(OH)$_2$ case. Both precursors possess similar layer structures. The only difference is that the existence of Cl$^-$ and OH$^-$ in NiOHCl and β-Ni(OH)$_2$, respectively. There is a possibility that Cl$^-$ served as a capping agent to the Ni^{2+} during the calcination proces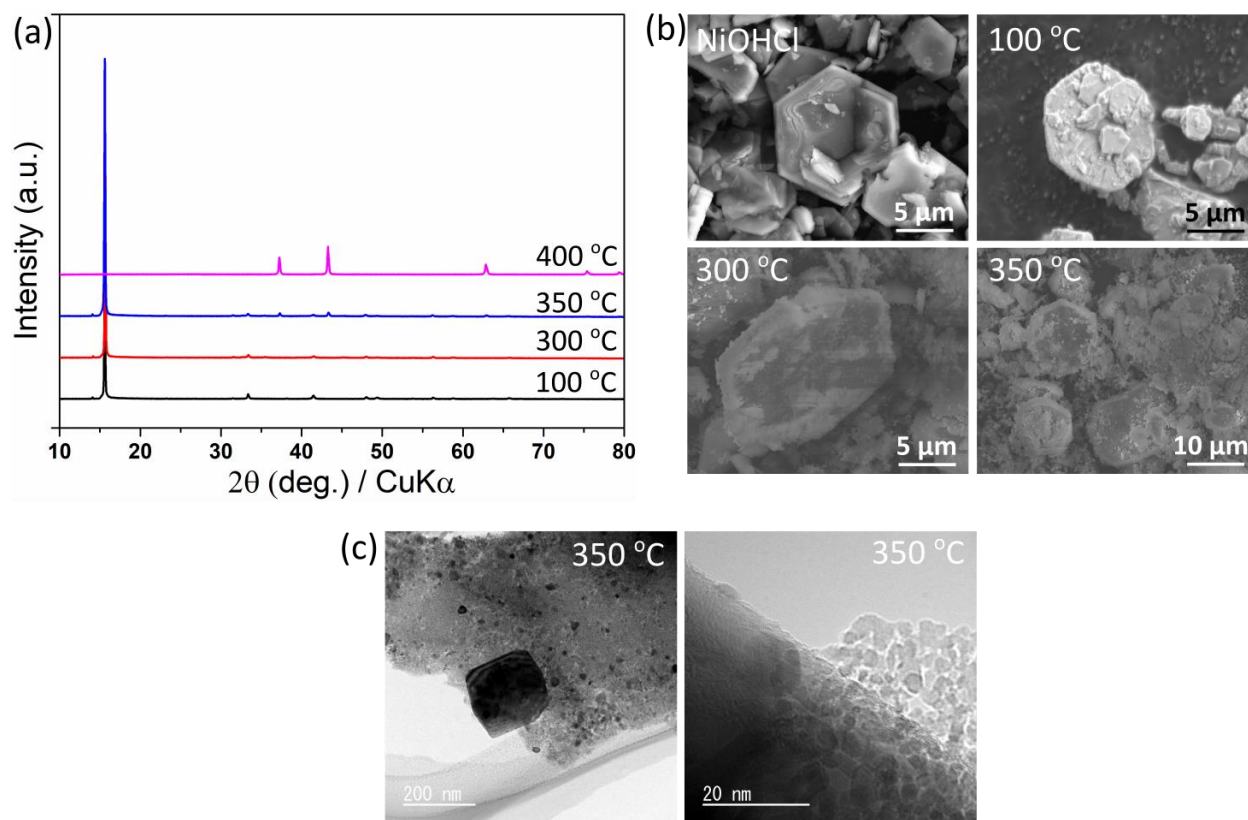s as Ni atom is abundant in the clean (111) surface layer. Moreover, Ni atom in (111)-terminated surfaces exhibited a positive charge (+1.37) based on the previous investigation.[115] It is likely that Cl$^-$ attached to and coordinated with Ni by electronic interaction and it may inhibit the growth of NiO in the (111) direction. The Cl ligand-capped (111) facet can also be found in the CoO case which has the same rock-salt structure.[86] The NiO octahedral morphology was also obtained by heating the irregular particle of NiCl$_2$ precursor at 400 °C at ambient pressure for 3 h inside a covered crucible similar to that of NiOHCl calcination. **(Fig. 3.26)** Nevertheless, the pure NiO phase was not obtained in such conditions, revealing that (i) Cl$^-$ can assist the (111) facet formation, (ii) pre-existed oxygen in NiOHCl phase may be helpful to acquire the pure phase and (iii) facet

rearrangement may occur at the nanoscale interface. Recent work also reveals NiO with several exposed facets ({311}, {611}, {100} and {111}) can be achieved, from nickel salt precursors, only by the aid of anion and alkali cation of molten salts.[116] This may support our hypothesis.
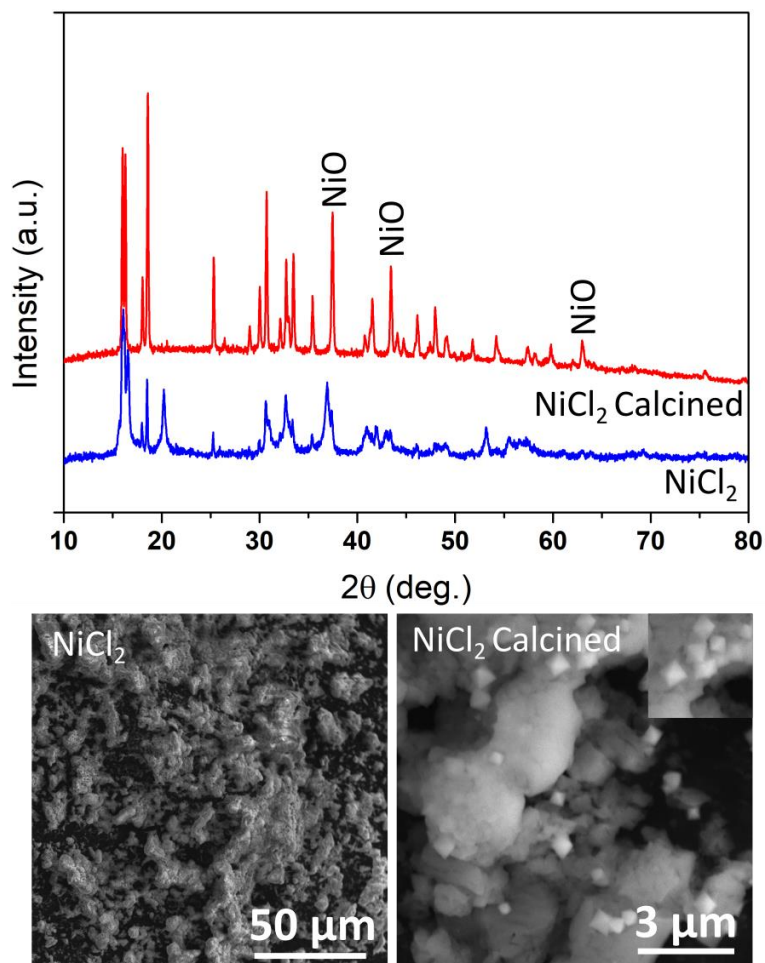

Fig. 3.26. XRD patterns and SEM image of $NiCl_2$ before and after calcination at 400 °C for 3h.

3.2.3.2 Electronic and optical properties

X-ray photoelectron spectroscopy analysis was employed to explore the chemical composition and oxidation state of Octahedral NiO (111) facet. The full survey spectrum indicates a distinct chemical element of Ni and O and a tiny peak of Cl (**Fig. 3.27** (a)). EDX-equipped SEM elemental scanning (**Fig. 3.27** (b)) taken from **Fig. 3.24** (b) also suggested the presence of Ni and O. **Fig. 3.28** (a) displays Ni 2p core-level spectra. Using the Gaussian fitting function within Shirley background, it was deconvoluted into two spin doublets positioned at 856.3 eV (Ni $2p_{3/2}$) and 874.1 eV (Ni $2p_{1/2}$) and two shake-up satellites (862.4 eV and 879.6 eV). The fitting peaks at binding energies of 856.7 eV and 874.0 eV were attributed to Ni^{2+} state, while other fitting peaks located at 854.0 eV and 871 eV are ascribed to Ni^{3+} state.[117–119] The existence of doublets of Ni 2p together with their satellite confirmed the magnetic chemical state in Ni^{2+} and Ni^{3+}.[120] The formation of Ni^{3+} might be attributed to O-rich nickel oxides.[121] However, other phrases related to Ni^{3+} were negligible as only pure NiO is detected in XRD patterns. The Cl content was confirmed to be 0.74 wt.% by elemental analysis. **Fig. 3.28** (b) displayed O1s core spectra that were deconvoluted using gaussian fitting. The peak at 530.7 is a typical metal bond with oxides, and fitting peak emerged at 533.1 eV may be attributed to physically adsorbed water molecules at surface, since it was found that NiO with 111-exposed facet is water molecule sensitive.[122,123]

The optical properties of the obtained NiO were further scrutinized. The UV-Vis absorption of octahedral NiO in the Kubelka-Munk unit is depicted in **Fig. 3.29** (a). As can be seen, the two samples have similar emerged peaks. The sharp peak at the UV region (342 nm) can be assigned to bandgap absorption of NiO, while other three broad absorption edges at 378 nm, 429 nm, and 720 nm are a typical d-d transition existed within the bandgap of NiO with Ni^{2+} state that is surrounded six O^{2-} at the octahedral site. This octahedral configuration splits d-electron of ground state $^3A_{2g}$ to $1E_g$, $^3T_{2g}(G)$, and $^3T_{1g}(F)$, respectively.[124–126] Then, employing the Tauc-method to the KM absorption spectra, the estimated bandgap for NiO Octa (111) and NiO Hexa (110) were 3.26 and 3.25 eV (**Fig. 3.29** (b)). This result suggests that Cl impurity in NiO Octa (111) does not infer the electronic band structures.
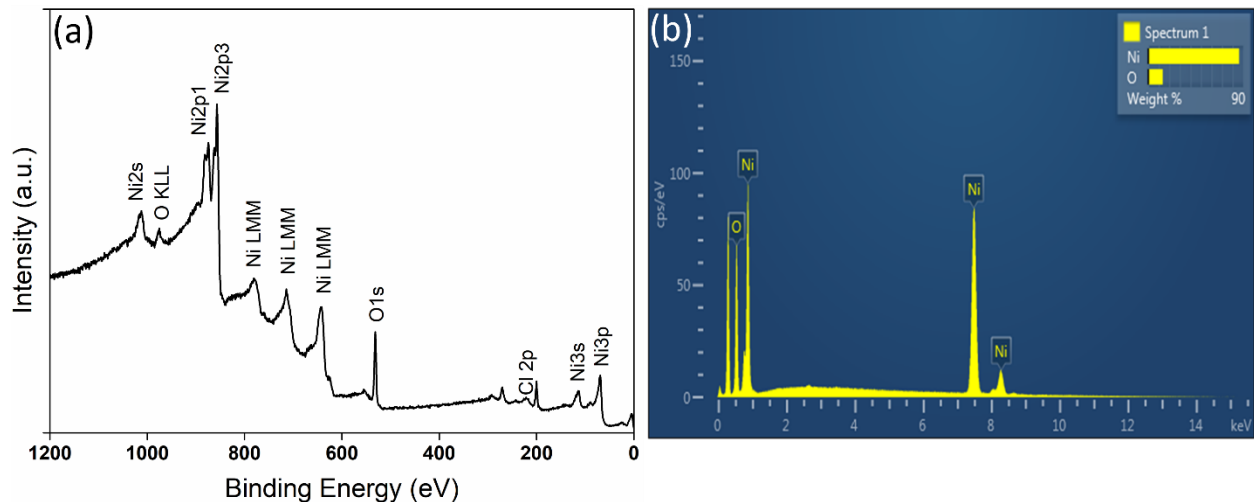
Fig. 3.27 (a) Full scan XPS spectra and (b) EDS spectra of NiO Octa (111)
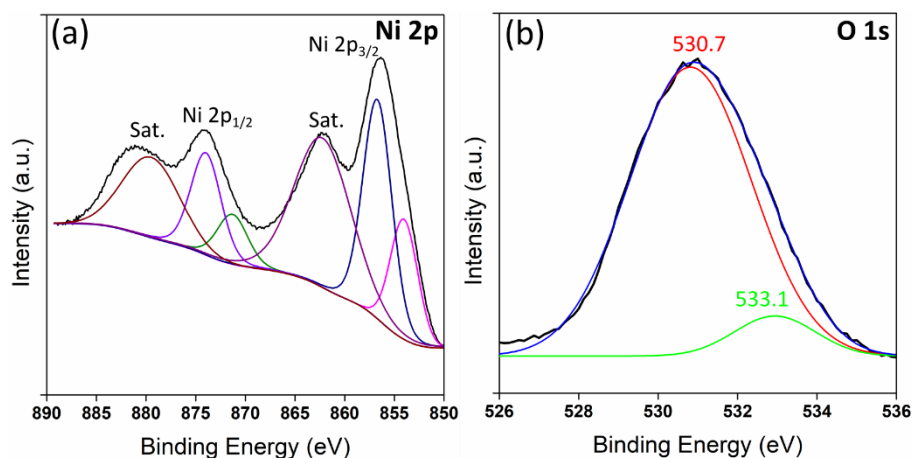
Fig. 3.28 XPS core level spectra of (a) Ni 2p and (b) O 1s of NiO-Octa (111).
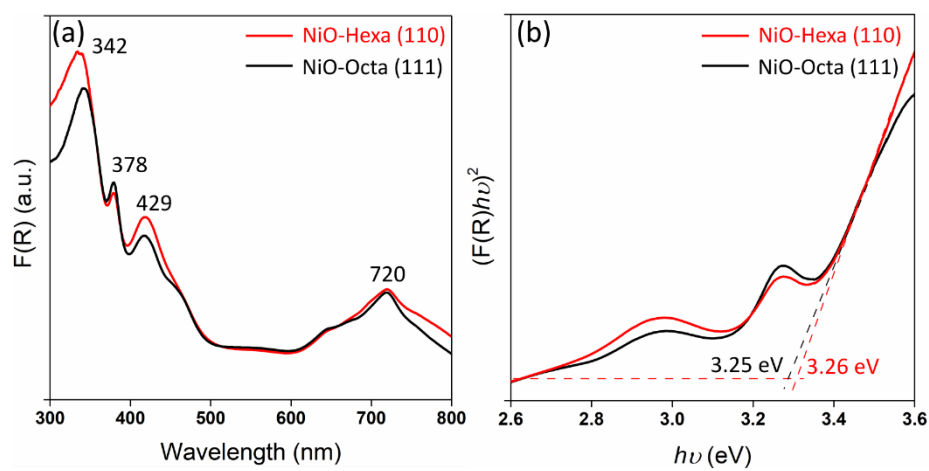
Fig. 3.29 (a) Kubelka-Munk Absorption spectra and (b) corresponding Tauc plot of NiO Hexa (110) and NiO Octa (111)

3.2.3.3 NO$_x$ gas sensing properties

The NiO with a polycrystalline property without specific exposed facet was also synthesized for comparison. The synthesis process was the same as that of NiO-Octa (111), except the nonexistence of acetic acid during WCRSP. As illustrated in **Fig. 3.30** (a-d), the XRD pattern, TEM, HRTEM, and SAED confirmed the formation of NiO phase that has irregular morphology, the lattice fringe of 0.21 nm (d$_{(200)}$) and 0.245 nm (d$_{(111)}$) and a diffuse ring of polycrystalline material. Thus, this sample is denoted as NiO-irregular. Also, UV-Vis DRS (**Fig. 3.30** (e), shows similar characteristic with other two samples. Moreover, the Cl content was 0.70 wt.%, very close to that of NiO-Octa (111).
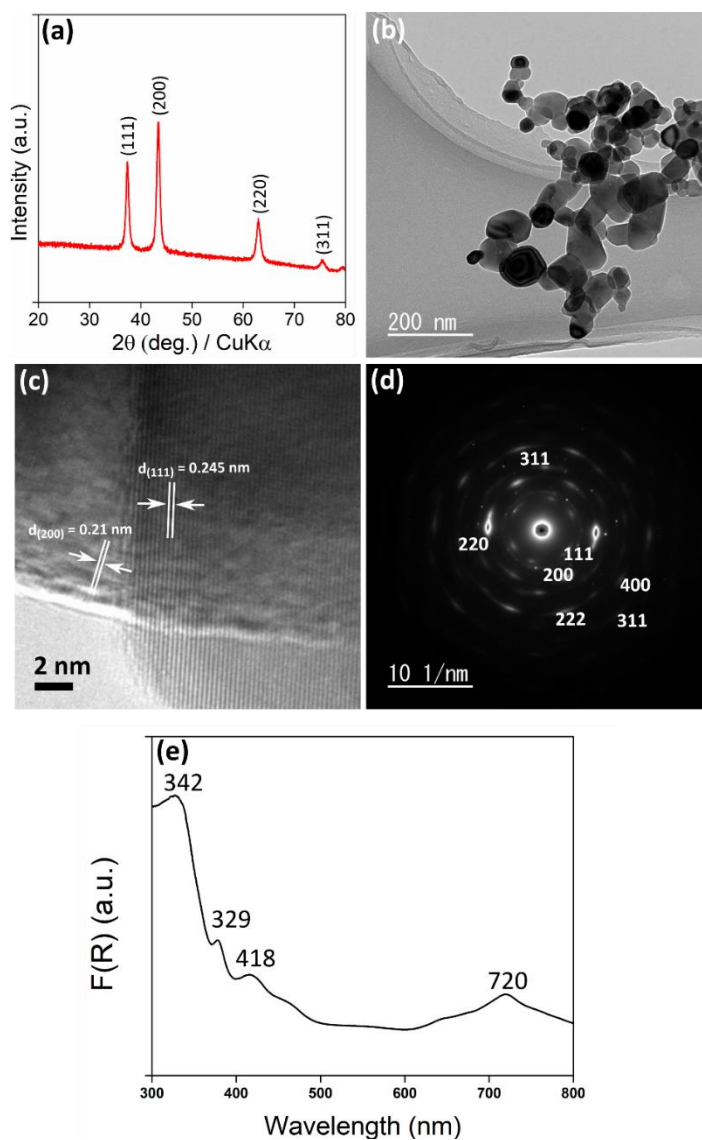
Fig. 3.30. (a) XRD pattern (b) TEM (c) HRTEM image (d) corresponding SAED pattern and (e) UV-Vis Absorption spectra of NiO irregular.

The sensor devices containing NiO samples with distinctive morphology and exposed face, namely NiO-Octa (111), NiO-Hexa (110), and NiO irregular were tested at different temperatures from room temperatures to 300 °C toward NO_x gas detection. The concentration of NO_x was determined to 3 ppm. As depicted in **Fig. 3.31** (a), the sensing response of NiO samples increased with the rise of operating temperature. All NiO samples exhibited a mountain hill feature from which the optimum operating condition can be determined.This characteristic is influenced mainly by the adsorption-desorption process. As practically proposed, NiO-Octa (111) sample may be more suitable as an integrated gas sensing material in the vehicle combustion system for real-time pollution monitoring. The NO_x response of NiO-Octa (111) at 250 °C was 24.85 %, which is about 3 times higher than that of NiO-Hexa (110) (9.34 %) and 13 times higher than NiO-Irregular (1.9 %). **Fig. 3.31** (b) shows the transient response/recovery feature of NiO-Octa (111), NiO-Hexa (110), and NiO-Irregular underexposure of NO_x with a concentration range of 1.8 ppm to 3.0 ppm. All samples manifest similar response/recovery times where the resistance increased upon the exposure of NO_x. However, the NiO-Irregular demonstrated a strong noise in contrary to NiO-Octa (111) and NiO-Hexa (110). The noise may be due to a low or unstable adsorption/desorption process. Also, the different base resistance, *e.g.* the resistance in air atmosphere, observed on all samples indicated the dependency of electrical resistance on particle size or impurities .[127] It is clear that the gas responses of NiO-Octa (111), NiO-Hexa (110) and NiO-Irregular linearly increase with the NO_x concentration as displayed in **Fig. 3.31** (c). Specifically for the case of NiO-Octa (111), it still has good response value (16.5%) even to 300 ppb of NO_x exposure, which is a substantial indication of NiO-Octa (111) potentiality for low-limit detection of NO_x gas. Moreover, under 3 ppm of NOx at 250 °C the response/recovery features of NiO-Octa (111) are repeatable for at least 5 times with no obvious changes in the electrical resistance during the NO_x injection and ejection. These repeatability features are a very crucial parameter of gas sensing materials for long-term use. **Fig. 3.31** (e) depicted gas sensing response of NiO samples under 3 ppm of various gases e.g. Nitrogen Oxides (NO_x), Methanol (MeOH), Ethanol (EtOH) and Acetone. NiO-Octa (111) sample possessed a highly selective properties to NO_x gas indicated by the degree of selectivity ($R_{NOx}/R_{othergas}$) is above 2. The NO_x sensing response of NiO-Octa (111) under different relative humidity (RH) was futher studied because most of oxides are also sensitive to moisture. As shown in **Fig. 3.31** (f), the response of NiO-Octa (111) to NO_x increased as the RH increased. It is may likely NiO-Octa (111) also strongly adsorbed the water molecules that increase the

resistance, in line with reported literature.[122] NiO-Octa (111) NO$_x$ dynamic response was repeatable for several consecutive days (**Fig. 3.32**), reflecting its good stability against such dynamic condition.

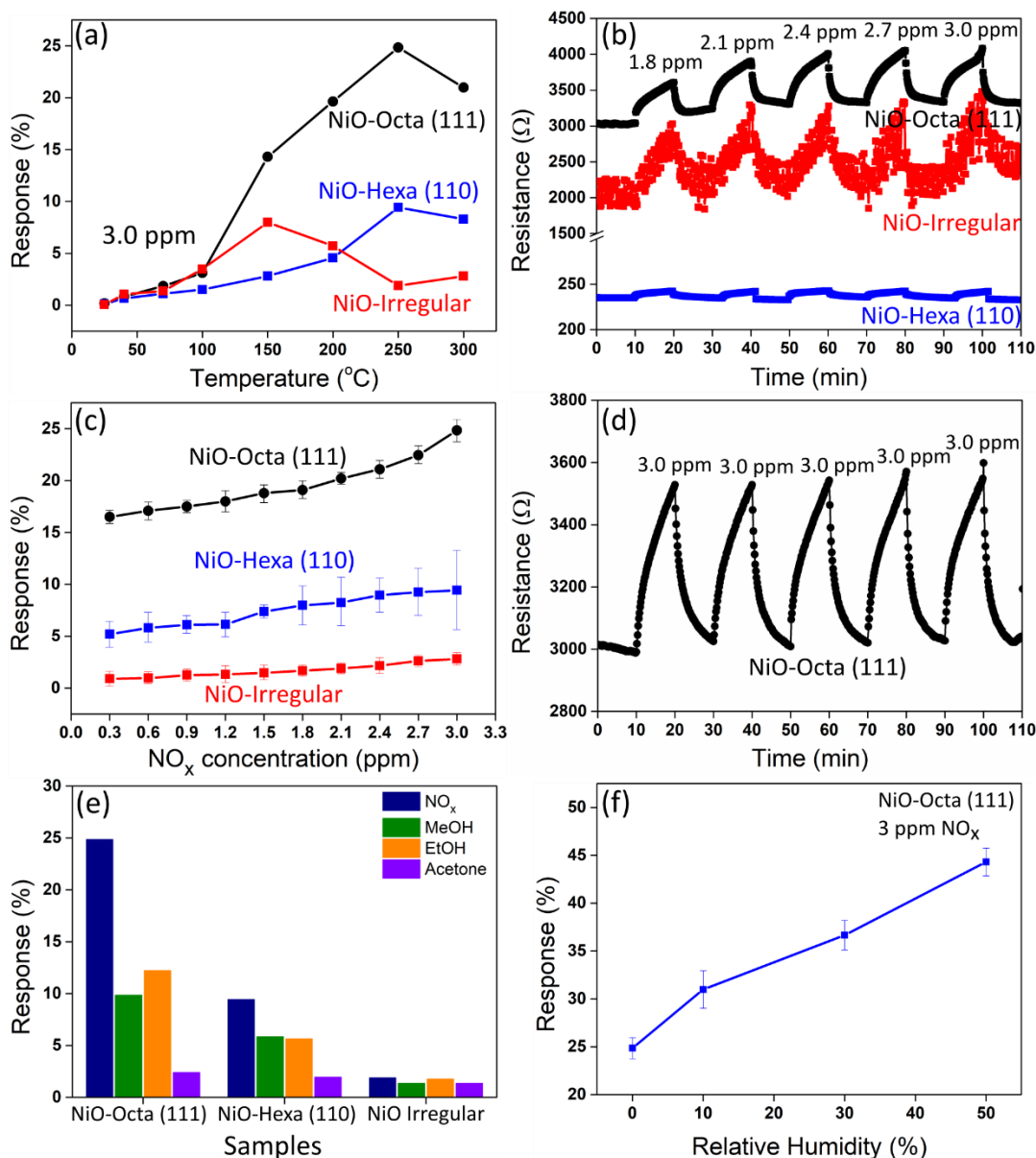**Fig. 3.31** (a) Temperature dependent NO$_x$ gas sensing properties, (b) NO$_x$ concentration-dependent responses at 250 ^{o}C, (c) response *vs* NO$_x$ concentration of the synthesized NiO samples; (d) repeatability response under 3 ppm of NO$_x$ gas of NiO-Octa (111) sample; selectivity of NiO samples under 3 of different gases and (e) NO$_x$ response of NiO-Octa (111) under different relative humidity.
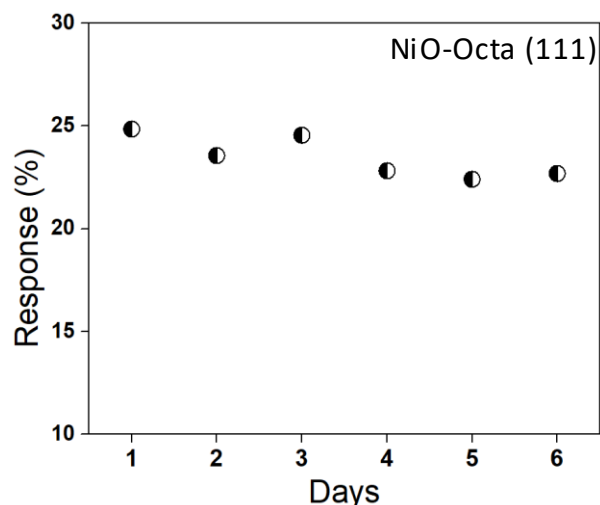
Fig. 3.32. Stability feature of NiO-Octa (111). NO_x gas sensing measurement was conducted for last 2 h each days. NO_x concentration was 3 ppm.

3.2.3.4 DFT calculation and gas sensing mechanism

To investigate the adsorption mechanism of NO on the NiO surface, *ab initio* calculations are performed. We have successfully prepared two facets, (110) and (111). Therefore, these facets together with a naturally formed (100) facet. Furthermore, it is useful to consider the electronic structure of the NO molecule as the adsorbate in question. **Fig. 3.33** (a) shows a rough molecular orbital diagram for NO, specifically for the resultant hybrid orbitals from the N and O 2p orbitals. It can be seen that one electron occupies the $\pi*$ antibonding orbital, with the rest of the $\pi*$ antibonding orbitals empty just above the Fermi level. It then follows by analyzing the projected COHP (pCOHP) of the N-O bond after adsorption and comparing it with the rough diagram for the NO molecule, it is possible to see the effects of NO adsorption on the N-O molecular antibonding orbitals. This comparison can also shed light on the mechanism of NO adsorption during gas sensing and photocatalytic process.

The combination of possible adsorption sites and adsorbate conformation generates a series of conformations as shown in **Fig. 3.33** (b). The horizontal orientation of the adsorbate (NO bond parallel to the surface) is likely to occur at the bridge site with two bonds to the surface, while vertical or tilted orientation is possible on either top, hollow, or bridge sites. Some conformations are more energetically favorable than others, lowering the adsorption energy associated.

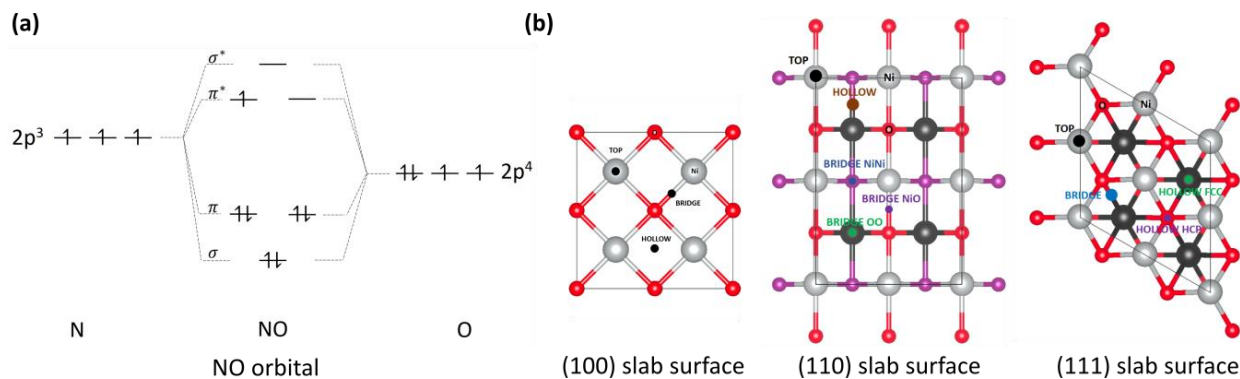**Fig. 3.33** (a) Diagram of NO molecular orbital as a result of hybridization between N and O 2p orbitals, (b) model of NiO (100), (110) and (111) slab surfaces. Gray and red are Ni and O atoms on the surface layer, while black and purple are Ni and O atoms are on the subsurface layer (subsubsurface layer for Ni atoms in (111) facet).

The adsorption energy is defined as the energy required for adsorption to occur and is mathematically defined as:

$$E_{ads} = E_{tot} - E_{surface} - E_{mol} \qquad \text{(Eq. 4)}$$

where E_{ads} denotes the adsorption energy, E_{tot} denotes the total energy of the adsorbed system, $E_{surface}$ the total energy of the slab model, and E_{mol} the total energy of the adsorbate (molecule) in a vacuum. This mathematical definition is akin to binding or cohesive energy, and it represents the strength of adsorption.

From the selected calculation results as summarized in **Table 3.6** it can be observed that bridge site adsorption is particularly favorable for NO in NiO (100) surface, especially with the nitrogen adatom. Two of the striking results are from conformations 31_BridN and 33_BridPar, both of which include a (relatively) stronger Ni-N bond and the oxygen in NO adsorbate elevated at some distance from the surface. NO adsorption on NiO (100) surface of the adsorbate results in a tilted end position of NO molecule, suggesting that NO is adsorbed in a tilted conformation for all sites on NiO (100). These results agree well with previous theoretical works on NiO (100) surfaces[97,128] which predict that adsorptions of oxygen gas and water vapor on NiO (100) often rely instead on defects (oxygen vacancies) present in the surface. The calculation results indicate that it is likely that the pure NiO (100) surface is not favorable for the adsorption of NO as well.

The weak adsorption energies on (100) facet suggest that it is not a good surface for use in gas sensing and photocatalyst application, which confirms one part of the facet-selective property of NiO surfaces.

As with the (100) facet, the (110) surface facet is nonpolar, containing both Ni and O atoms. Its surface energy is roughly in between the (100) and (111) facets, and it has 3 different bridge sites: between the Ni atoms, between the O atoms, and between one Ni and one O atom. Calculations are done for 3 adsorbate conformation ("vertical", horizontal, and parallel) for the three bridge sites. The adsorption energies again show that NO adsorbs with N adatom instead of O, that the Ni-N bond is most significant, and that the bridge and hollow sites are most favourable, producing the strongest adsorption. It also shows that NO adsorption is generally more favourable towards this (110) surface compared to the (100) surface.

The (111) surface facet of NiO is comprised of alternating layers of Ni and O atoms in the close-packed structure. By far the (111) surface shows the most favorable sites for NO adsorption, again for the hollow and bridge sites with a tilted NO conformation, continuing the trend from (110) surface. Again, the Ni-N bond seems to be of significant importance, as seen in the prominence of adsorption on Ni top, bridge, and hollow sites compared with the rest, with the strongest adsorption at the hollow HCP site (**Fig. 3.33** (b) and **Fig. 3.34**). This pattern closely resembles that of the (110) surface, with even stronger adsorption energies. The calculated results confirm the facet selectivity property of the NiO surface, from the (111) surface is being most favorable toward NO adsorption, to (110), and lastly to the (100) surface producing the weakest adsorption.

The increased favourability in adsorption is easily attributable to the abundance of Ni atoms in the clean (111) surface layer (Ni-terminated). O-terminated (111) surface is not investigated in this work, but from the previous results, it can be safely extrapolated that such a surface would not be favored toward NO adsorption. For nearly all cases, N-O or O-O adsorption is far weaker in comparison with the Ni-N adsorption, which effectively rules out the O-terminated (111) surface as favorable towards NO adsorption compared to Ni terminated (111) surface.

Table 3.6 NO adsorption on NiO (100), (110) and (111) surfaces

| Surface	Conformation	E_{ads} (eV)
(100)	11_TopNiN	-0.150
	12_TopNiO	-0.134
	13_TopON	-0.182
	14_TopOO	-0.118
	21_HolN	-0.181
	22_HolO	-0.050
	31_BridN	-0.458
	32_BridO	-0.122
	33_BridPar	-0.423
(110)	11_TopNiN	-0.858
	12_TopNiO	-0.253
	13_TopON	-0.269
	14_TopOO	-0.086
	21_HolN	-1.231
	22_HolO	-0.110
	31_BridNiNiN	-1.248
	32_BridNiNiO	-0.087
	33_BridNiNiPar	-0.956
	34_BridOON	-0.145
	35_BridOOO	-0.109
	36_BridOOPar	-0.314
	37_BridNiON	-0.862
	38_BridNiOO	-0.235
	39_BridNiOPar	-0.870
(111)	11_TopN	-2.345
	12_TopO	-1.125
	21_HolFCCN	-1.915
	22_HolFCCO	-0.527
	23_HolHCPN	-2.429
	24_HolHCPO	-0.922
	31_BridN	-2.395
	32_BridO	-0.973
	33_BridPar	-2.094
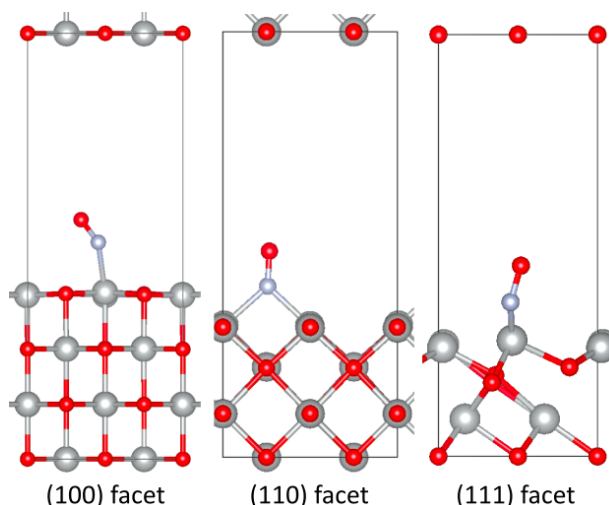
Fig. 3.34 xz-plane views of optimized geometries for 31_BridN site in (100) facet, 31_BridNiNiN site in (110) facet, and 31_BridN site in (111) facet, showing significant Ni-N bond and tilted conformation of adsorbate (NO molecule).

To reveal the mechanism of NO adsorption in NiO Octa (111), the 31_BridN site is taken as an example, with a significant adsorption energy and a clear adsorption between adatom N and single surface Ni atom. The plane-wave basis set wavefunction is projected onto atomic orbital like contributions to the molecular orbitals by the projected COHP method. At the same time, the density of states (DOS) and projected DOS (PDOS) information are also extracted from a single-point calculation of the adsorbed system. **Fig. 3.35** shows the PDOS of the 2p orbitals of both N and O atoms from the adsorbate as well as the pCOHP analysis of the N-O bond. The $\pi*$ orbital just below the Fermi surface (seen in **Fig. 3.33** (a)) has been delocalized, stretching to up to 3 eV below the Fermi level. This shows the increased occupation of the antibonding orbital because of a small charge transfer from the NiO surface, which is likely considering the difference in electronegativity between Ni and N atoms. Therefore, NO adsorption onto the NiO surface likely occurs by a small charge transfer from the surface to the N atom. The above mechanism produces an expectation of a weakening N-O bond, due to the occupation of the $\pi*$ antibonding orbital. This is easy to achieve considering that the orbital in question is both the HOMO and LUMO levels of the NO molecule at the same time. Geometry optimization precisely shows this effect, with post-adsorption N-O bond length stretched to 1.2231 Å from the initial bond length 1.1692 Å (in a vacuum). The stretching of the bond length suggests a weakening in the N-O bond and provides

evidence of adsorption by charge transfer from the NiO surface. It agreed with the increased resistance of NiO, regardless of the exposed facet, during the exposure of NO gas. This mechanism also explains the importance of Ni surface atoms as adsorption sites considering the electronegativity of Ni as opposed to O atoms. It explains the significance of Ni-N bonding as well as the trend of adsorption strength dependence on the surface facet of NiO, from (111) > (110) > (100). The DFT calculation was also conducted to reveal the good selectivity of NiO with (111) facet. The methanol, ethanol, and acetone molecules were place on Hollow HCP site (HolHCP) of (111) plane. The calculated adsorption energies were -1.083, -1.182, -1.002 eV, -0.505 eV, -1.811 eV for methanol, ethanol, acetone, hydrogen and ammonia, respectively. This prediction by theoretical calculation tracks well with the experimental results.
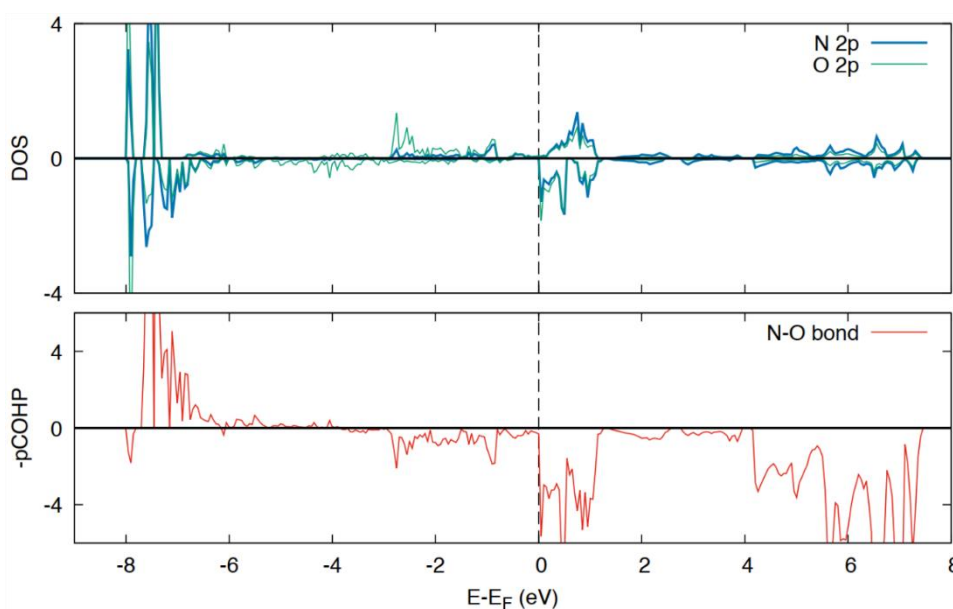

Fig. 3.35 PDOS and pCOHP plots of the adsorbate (NO) for 31_BridN site in (111) facet case. pCOHP plot is inversed to follow the chemistry convention of presenting bonding orbitals on positive axis of plot.

3.3 Summary and Conclusion

Micro-/mesoporous hierarchical structured SnO_2 spheres with controllable particle and pore size distribution were successfully synthesized by simply adjusting the reaction parameters such as vol. % of acetic acid to ethanol, Sn species concentration involved in the system and the solvothermal treatment time in the water controlled-release solvothermal process (WCRSP). The fabricated SnO_2 sensor showed an optimum working temperature at 400 $^{\circ}$C, regardless of the particle diameter. The highest sensing response (20.2) to 50 ppm of toluene with comparable to the response/recovery time of 52/74 s and good selectivity was obtained, if the synthesized SnO_2 had a pore size of 1.4 nm, the particle size of 0.90 μm together with the largest surface area of 145 m^2/g. In addition, the sensors responsivity was superior to the SnO_2 sample synthesized in the pure water, indicating the promising strategy of the SnO_2 preparation for toluene gas sensor.

NiO with dominantly exposed facets, (110) and (111), were successfully obtained by the calcination of different precursors. The Cl^- ion from NiOHCl precursor may hypothetically assist the crystal growth and lower the formation energy of (111) surface facet. This sample, NiO Octa (111), exhibited the best NO_x gas sensing response (24.85 %) at 250 $^{\circ}$C exceeding all examined samples. The *ab initio* calculation revealed that the NO gas is likely to be adsorbed on Ni terminated surface with N adatom rather than O. The NO adsorption energy was -0.458, -1.248, and -2.429 eV on NiO with (100), (110), and (111) facet, respectively, well-agreed with the experimental results. The charge transfer occurred from NiO to NO, promoting the increased internal resistance in NiO and weakening the N-O bonding. The above combination of experimental and calculation results demonstrates that the surface-engineering approach offers the potential to design high-performance gas sensing materials.

3.4 References

1   B. D. Alexander, P. J. Kulesza, I. Rutkowska, R. Solarska and J. Augustynski, *J. Mater. Chem.*, 2008, **18**, 2298–2303.

2   U. I. Gaya and A. H. Abdullah, *J. Photochem. Photobiol. C Photochem. Rev.*, 2008, **9**, 1–12.

3   C. Wang, L. Yin, L. Zhang, D. Xiang and R. Gao, *Sensors*, 2010, **10**, 2088–2106.

4   Y. M. Lin, Y. H. Tseng, J. H. Huang, C. C. Chao, C. C. Chen and I. Wang, *Environ. Sci. Technol.*, 2006, **40**, 1616–1621.

5   K. Suematsu, Y. Shin, Z. Hua, K. Yoshida, M. Yuasa, T. Kida and K. Shimanoe, *ACS Appl. Mater. Interfaces*, 2014, **6**, 5319–5326.

6   J. Liu, M. Dai, T. Wang, P. Sun, X. Liang, G. Lu, K. Shimanoe and N. Yamazoe, *ACS Appl. Mater. Interfaces*, 2016, **8**, 6669–6677.

7   J. Jiang, Y. Li, J. Liu, X. Huang, C. Yuan and X. W. Lou, *Adv. Mater.*, 2012, **24**, 5166–5180.

8   H. Rui, R. Xing, Z. Xu, Y. Hou, S. Goo and S. Sun, *Adv. Mater.*, 2010, **22**, 2729–2742.

9   R. Baetens, B. P. Jelle and A. Gustavsen, *Sol. Energy Mater. Sol. Cells*, 2010, 94, 87–105.

10   S. Das and V. Jayaraman, *Prog. Mater. Sci.*, 2014, **66**, 112–255.

11   Y. Wang, C. Ma, X. Sun and H. Li, *Microporous Mesoporous Mater.*, 2001, **49**, 171–178.

12   A. Aoki and H. Sasakura, *Japanese J. Appl. Physics, Part 1 Regul. Pap. Short Notes Rev. Pap.*, 1970, **9**, 582.

13   L. Liu, Y. Zhang, G. Wang, S. Li, L. Wang, Y. Han, X. Jiang and A. Wei, *Sensors Actuators, B Chem.*, 2011, **160**, 448–454.

14   J. Tian, J. Wang, Y. Hao, H. Du and X. Li, *Sensors Actuators, B Chem.*, 2014, **202**, 795–802.

15   J. H. Kim and S. S. Kim, *ACS Appl. Mater. Interfaces*, 2015, **7**, 17199–17208.

16   R. Malik, V. K. Tomer, V. Chaudhary, M. S. Dahiya, S. P. Nehra, S. Duhan and K. Kailasam, *Sensors Actuators, B Chem.*, 2018, **255**, 3564–3575.

17   J. Tian, J. Wang, Y. Hao, H. Du and X. Li, *Sensors Actuators, B Chem.*, 2014, **202**, 795–802.

18   L. Qiao, Y. Bing, Y. Wang, S. Yu, Z. Liang and Y. Zeng, *Sensors Actuators, B Chem.*, 2017, **241**, 1121–1129.

19   N. Yamazoe, *Sensors Actuators, B Chem.*, 1991, **5**, 7–19.

20   T. Wagner, S. Haffer, C. Weinberger, D. Klaus and M. Tiemann, *Chem. Soc. Rev.*, 2013, **42**, 4036–4053.

21   J. Huang, X. Xu, C. Gu, W. Wang, B. Geng, Y. Sun and J. Liu, *Sensors Actuators B. Chem.*, 2012, **173**, 599–606.

22   Z. Zhu, X. Zheng, Y. Bai, T. Zhang, Z. Wang, S. Xiao and S. Yang, *Phys. Chem. Chem. Phys.*, 2015, **17**, 18265–18268.

23   P. M. Bulemo, H. J. Cho, D. H. Kim and I. D. Kim, *ACS Appl. Mater. Interfaces*, 2018, **10**, 18183–18191.

24   T. Hyodo, N. Nishida and Y. Shimizu, 2002, **83**, 209–215.

25   Y. De Wang, C. L. Ma, X. H. Wu, X. D. Sun and H. De Li, *Sensors Actuators, B Chem.*, 2002, **85**, 270–276.

26   D. Chandra, N. Mukherjee, A. Mondal and A. Bhaumik, *J. Phys. Chem. C*, 2008, **112**, 8668–8674.

27   J. Liu and D. Xue, *Nanoscale Res. Lett.*, 2010, **5**, 1525–1534.

28   J. Liu, H. Xia, D. Xue and L. Lu, *J. Am. Chem. Soc.*, 2009, **131**, 12086–12087.

29   Q. Fu, M. Ai, Y. Duan, L. Lu, X. Tian, D. Sun, Y. Xu and Y. Sun, *RSC Adv.*, 2017, **7**, 52312–52320.

30   C. Guo, X. Wu, M. Yan, Q. Dong, S. Yin, T. Sato and S. Liu, *Nanoscale*, 2013, **5**, 8184–8191.

31   C. Wang, Z. X. Deng, Y. Li, S. Compounds, M. Hu, J. Xu, J. Gao, S. Yang, J. S. P. Wong, R. K. Y. Li, M. Ivanda, S. Musić, S. Popović and M. Gotić, *Inorg. Chem.*, 1999, **481**, 5210–5214.

32   A. Styskalik, D. Skoda, C. E. Barnes and J. Pinkas, *Catalysts*, 2017, **7**, 168.

33   P. Scherrer and P. Debye, *Nachr. Ges. Wiss. Göttingen, Math.-physik. Klasse*, 1918, **2**, 101–120.

34   E. R. Leite, I. T. Weber, E. Longo and J. A. Varela, *Adv. Mater.*, 2000, **12**, 965–968.

35   H. E. Gottlieb, V. Kotlyar and A. Nudelman, *J. Org. Chem.*, 1997, **62**, 7512–7515.

36   E. J. H. Lee, C. Ribeiro, T. R. Giraldi, E. Longo, E. R. Leite and J. A. Varela, *Appl. Phys. Lett.*, 2004, **84**, 1745–1747.

37   X. Qiao, H. Yang, C. Chen, X. Lou, J. Sun, L. Chen, X. Fan, L. Zhang and Q. Shen, *Procedia Eng.*, 2014, **94**, 58–63.

38   R. Félix, N. Llobera-Vila, C. Hartmann, C. Klimm, M. Hartig, R. G. Wilks and M. Bär, *RSC Adv.*, 2018, **8**, 67–73.

39   C. Sun, K. Li and D. Xue, *J. Rare Earths*, 2019, 37, 1–10.

40   D. Xue, C. Sun and X. Chen, *Chinese J. Chem.*, 2017, **35**, 1452–145.

41   D. XUE, C. SUN and X. CHEN, *J. Rare Earths*, 2017, **35**, 837–843.

42   D. F. Xue and C. T. Sun, *Sci. China Technol. Sci.*, 2017, **60**, 1767–1768.

43   A. Kolmakov, S. Potluri, A. Barinov, T. O. Menteş, L. Gregoratti, M. A. Niño, A. Locatelli and M. Kiskinova, *ACS Nano*, 2008, **2**, 1993–2000.

44   Y. Y. Lin, H. Y. Lee, C. S. Ku, L. W. Chou and A. T. Wu, *Appl. Phys. Lett.*, 2013, **102**, 111912.

45   F. J. Arlinghaus, *J. Phys. Chem. Solids*, 1974, **35**, 931–935.

46   W. Z. Xiao, L. L. Wang and Z. Tan, *Comput. Mater. Sci.*, 2014, **83**, 5–11.

47   M. A. Oehlschlaeger, D. F. Davidson and R. K. Hanson, *Proc. Combust. Inst.*, 2007, **31 I**, 211–219.

48   G. Sakai, N. Matsunaga, K. Shimanoe and N. Yamazoe, *Sensors Actuators, B Chem.*, 2001, **80**, 125–131.

49   Y. F. Sun, S. B. Liu, F. L. Meng, J. Y. Liu, Z. Jin, L. T. Kong and J. H. Liu, *Sensors*, 2012, 12, 2610–2631.

50   W. Shang, D. Wang, B. Zhang, C. Jiang, F. Qu and M. Yang, *Dalt. Trans.*, 2018, **47**, 15181–15188.

51   N. Yamazoe and K. Shimanoe, *Sensors Actuators, B Chem.*, 2011, **160**, 1352–1362.

52   Y. Tsujimoto, Y. Matsushita, S. Yu, K. Yamaura and T. Uchikoshi, *J. Asian Ceram. Soc.*, 2015, **3**, 325–333.

53   J. Li, Y. Lu, Q. Ye, M. Cinke, J. Han and M. Meyyappan, *Nano Lett.*, 2003, **3**, 929–933.

54   N. Barsan and U. Weimar, *J. Electroceramics*, 2001, **7**, 143–167.

55   A. Mirzaei, J.-H. Kim, H. W. Kim and S. S. Kim, *J. Mater. Chem. C*, 2018, **6**, 4342–4370.

56   Y. F. Sun, S. B. Liu, F. L. Meng, J. Y. Liu, Z. Jin, L. T. Kong and J. H. Liu, *Sensors*, 2012, **12**, 2610–2631.

57   G. Zhang and M. Liu, *Sensors Actuators, B Chem.*, 2000, **69**, 144–152.

58   J. W. Veldsink, R. M. J. van Damme, G. F. Versteeg and W. P. M. van Swaaij, *Chem. Eng. J. Biochem. Eng. J.*, 1995, **57**, 115–125.

59   Y. Weng, S. Qiu, L. Ma, Q. Liu, M. Ding, Q. Zhang, Q. Zhang and T. Wang, *Catalysts*, 2015, **5**, 2147–2160.

60   O. K. Varghese, D. Gong, M. Paulose, K. G. Ong, C. A. Grimes and E. C. Dickey, *J. Mater. Res.*, 2002, **17**, 1162–1171.

61   Z. Tang, Y. Zhang, X. Deng, Y. Dai, W. Zhang, F. Fan, B. Qing, C. Zhu, J. Fan and Y. Shi, *Dalt. Trans.*, 2018, **47**, 15331–15337.

62   C. Agashe and S. S. Major, *J. Mater. Sci. Lett.*, 1996, **15**, 497–499.

63   K. Wetchakun, T. Samerjai, N. Tamaekong, C. Liewhiran, C. Siriwong, V. Kruefu, A. Wisitsoraat, A. Tuantranont and S. Phanichphant, *Sensors Actuators, B Chem.*, 2011, **160**, 580–591.

64   J. Cherniwchan, *Resour. Energy Econ.*, 2012, **34**, 442–467.

65   N. Miura, T. Koga, M. Nakatou, P. Elumalai and M. Hasei, *J. Electroceramics*, 2006, **17**, 979–986.

66   A. Afzal, N. Cioffi, L. Sabbatini and L. Torsi, *Sensors Actuators, B Chem.*, 2012, **171–172**, 25–42.

67   J. Liao, Z. Li, G. Wang, C. Chen, S. Lv and M. Li, *Phys. Chem. Chem. Phys.*, 2016, **18**, 4835–4841.

68   B. Son, W. Yang, P. Breysse, T. Chung and Y. Lee, *Environ. Res.*, 2004, **94**, 291–296.

69   E. G. C. Neiva, M. M. Oliveira, M. F. Bergamini, L. H. Marcolino and A. J. G. Zarbin, *Sci. Rep.*, 2016, **6**, 1–14.

70   T. yang Wang, Y. yuan Li, T. tian Li, H. Yu, Y. Yang, H. Yang and X. ting Dong, *Solid State Ionics*, 2018, **326**, 173–182.

71   J. Ma, H. Wu, Y. Liu and H. He, *J. Phys. Chem. C*, 2014, **118**, 7434–7441.

72   Q. Dong, S. Yin, C. Guo, X. Wu, N. Kumada, T. Takei, A. Miura, Y. Yonesaki and T. Sato, *Appl. Catal. B Environ.*, 2014, **147**, 741–747.

73   S. Yin, 2015, 823–834.

74   S. Yin and Y. Asakura, *Tungsten*, 2019, **1**, 5–18.

75   H. J. Kim and J. H. Lee, *Sensors Actuators, B Chem.*, 2014, **192**, 607–627.

76   N. D. Hoa and S. A. El-Safty, *Chem. - A Eur. J.*, 2011, **17**, 12896–12901.

77   B. Sasi, K. G. Gopchandran, P. K. Manoj, P. Koshy, P. Prabhakara Rao and V. K. Vaidyan, *Vacuum*, 2002, **68**, 149–154.

78   H. Tong, S. Ouyang, Y. Bi, N. Umezawa, M. Oshikiri and J. Ye, *Adv. Mater.*, 2012, **24**, 229–251.

79   A. Mikolajczyk, A. Malankowska, G. Nowaczyk, A. Gajewicz, S. Hirano, S. Jurga, A. Zaleska-Medynska and T. Puzyn, *Environ. Sci. Nano*, 2016, **3**, 1425–1435.

80   T. Li, Z. Shen, Y. Shu, X. Li, C. Jiang and W. Chen, *Environ. Sci. Nano*, 2019, **6**, 1740–1753.

81   M. H. Huang and P. H. Lin, *Adv. Funct. Mater.*, 2012, **22**, 14–24.

82   J. Pal and T. Pal, *Nanoscale*, 2015, **7**, 14159–14190.

83   A. Wander, I. J. Bush and N. M. Harrison, *Phys. Rev. B - Condens. Matter Mater. Phys.*, 2003, **68**, 1–4.

84   C. A. Cadigan, A. R. Corpuz, F. Lin, C. M. Caskey, K. B. H. Finch, X. Wang and R. M. Richards, *Catal. Sci. Technol.*, 2013, **3**, 900–911.

85   D. Su, M. Ford and G. Wang, *Sci. Rep.*, 2012, **2**, 1–7.

86   B. Liu, L. Ma, L. C. Ning, C. J. Zhang, G. P. Han, C. J. Pei, H. Zhao, S. Z. Liu and H. Q. Yang, *ACS Appl. Mater. Interfaces*, 2015, **7**, 6109–6117.

87   Z. Li, C. V. Ciobanu, J. Hu, J. P. Palomares-Báez, J. L. Rodríguez-López and R. Richards, *Phys. Chem. Chem. Phys.*, 2011, **13**, 2582–2589.

88   C. W. Kim, Y. S. Son, A. U. Pawar, M. J. Kang, J. Y. Zheng, V. Sharma, P. Mohanty and Y. S. Kang, *J. Mater. Chem. A*, 2014, **2**, 19867–19872.

89   K. He, G. Zhao and G. Han, *CrystEngComm*, 2014, **16**, 11050–11057.

90   S. Hu and X. Wang, *J. Am. Chem. Soc.*, 2010, **132**, 9573–9575.

91 S. Fu, L. Li, Y. Zhang, S. Chen, S. Fang, Y. Jing and G. Li, *ACS Appl. Energy Mater.*, 2018, **1**, 1522–1533.

92 S. H. Lim, G. D. Park, D. S. Jung, J. H. Lee and Y. C. Kang, *J. Mater. Chem. A*, 2020, **8**, 1939–1946.

93 H. Zhang, B. M. May, J. Serrano-Sevillano, M. Casas-Cabanas, J. Cabana, C. Wang and G. Zhou, *Chem. Mater.*, 2018, **30**, 692–699.

94 A. Hermawan, Y. Asakura, M. Inada and S. Yin, *Ceram. Int.*, 2019, **45**, 15435–15444.

95 J. P. Perdew, K. Burke and M. Ernzerhof, *Phys. Rev. Lett.*, 1996, **77**, 3865–3868.

96 S. Dudarev and G. Botton, *Phys. Rev. B - Condens. Matter Mater. Phys.*, 1998, **57**, 1505–1509.

97 N. Yu, W. B. Zhang, N. Wang, Y. F. Wang and B. Y. Tang, *J. Phys. Chem. C*, 2008, **112**, 452–457.

98 G. Rohrbach, J. Hafner and G. Kresse, *Phys. Rev. B - Condens. Matter Mater. Phys.*, 2004, **69**, 1–13.

99 W. B. Zhang, Y. L. Hu, K. L. Han and B. Y. Tang, *Phys. Rev. B - Condens. Matter Mater. Phys.*, 2006, **74**, 3–7.

100 P. E. Blöchl, *Phys. Rev. B*, 1994, **50**, 17953–17979.

101 G. Kresse and J. Hafner, *Phys. Rev. B*, 1993, **47**, 558–561.

102 G. Kresse and J. Hafner, *Phys. Rev. B*, 1994, **49**, 14251–14269.

103 G. Kresse and J. Furthmüller, *Comput. Mater. Sci.*, 1996, **6**, 15–50.

104 G. Kresse and J. Furthmüller, *Phys. Rev. B - Condens. Matter Mater. Phys.*, 1996, **54**, 11169–11186.

105 K. Momma and F. Izumi, *J. Appl. Crystallogr.*, 2011, **44**, 1272–1276.

106 H. J. Monkhorst and J. D. Pack, *Phys. Rev. B*, 1976, **13**, 5188–5192.

107 S. G. Kukolich, *J. Am. Chem. Soc.*, 1982, **104**, 4715–4716.

108 J. Beheshtian, M. Kamfiroozi, Z. Bagheri and A. Ahmadi, *Phys. E Low-Dimensional Syst. Nanostructures*, 2011, **44**, 546–549.

109 V. L. Deringer, A. L. Tchougréeff and R. Dronskowski, *J. Phys. Chem. A*, 2011, **115**, 5461–5466.

110 R. Dronskowski and P. E. Blöchl, *J. Phys. Chem.*, 1993, **97**, 8617–8624.

111 S. Maintz, V. L. Deringer, A. L. Tchougréeff and R. Dronskowski, *J. Comput. Chem.*, 2013, **34**, 2557–2567.

112 S. Maintz, V. L. Deringer, A. L. Tchougréeff and R. Dronskowski, *J. Comput. Chem.*, 2016, **37**, 1030–1035.

113   F. Izumi and K. Momma, *Solid State Phenom.*, 2007, **130**, 15–20.

114   S. Bette, R. E. Dinnebier and D. Freyer, *J. Appl. Crystallogr.*, 2015, **48**, 1706–1718.

115   N. Erdman, O. Warschkow, D. E. Ellis and L. D. Marks, *Surf. Sci.*, 2000, **470**, 1–14.

116   M. D. Susman, H. N. Pham, X. Zhao, D. H. West, S. Chinta, P. Bollini, A. K. Datye and J. D. Rimer, *Angew. Chemie Int. Ed.*, 2020, **59**, 1–6.

117   C. Yuan, J. Li, L. Hou, X. Zhang, L. Shen and X. W. Lou, *Adv. Funct. Mater.*, 2012, **22**, 4592–4597.

118   C. Long, M. Zheng, Y. Xiao, B. Lei, H. Dong, H. Zhang, H. Hu and Y. Liu, *ACS Appl. Mater. Interfaces*, 2015, **7**, 24419–24429.

119   S. Chen, G. Yang, Y. Jia and H. Zheng, *J. Mater. Chem. A*, 2017, **5**, 1028–1034.

120   P. Dubey, N. Kaurav, R. S. Devan, G. S. Okram and Y. K. Kuo, *RSC Adv.*, 2018, **8**, 5882–5890.

121   M. S. Jo, S. Ghosh, S. M. Jeong, Y. C. Kang and J. S. Cho, *Nano-Micro Lett.*, 2019, **11**, 1–18.

122   W. Zhao, M. Bajdich, S. Carey, A. Vojvodic, J. K. Nørskov and C. T. Campbell, *ACS Catal.*, 2016, **6**, 7377–7384.

123   M. A. Peck and M. A. Langell, *Chem. Mater.*, 2012, **24**, 4483–4490.

124   M. Lenglet, F. Hochu, J. Dürr and M. H. Tuilier, *Solid State Commun.*, 1997, **104**, 793–798.

125   Y. Qi, H. Qi, J. Li and C. Lu, *J. Cryst. Growth*, 2008, **310**, 4221–4225.

126   Y. Cui, C. Wang, S. Wu, G. Liu, F. Zhang and T. Wang, *CrystEngComm*, 2011, **13**, 4930–4934.

127   A. Mirzaei, J. H. Kim, H. W. Kim and S. S. Kim, *Sensors Actuators, B Chem.*, 2018, **258**, 270–294.

128   J. M. McKay and V. E. Henrich, *Phys. Rev. B*, 1985, **32**, 6764–6772.

Chapter 4

Enhancement of toluene sensing property of n-type SnO₂ porous microsphere by decorating with p-type CuO nanoparticles

4.1 Introduction

Toluene (C_7H_8) is an important industrial compound and intensively employed for synthesizing other chemical intermediates such as adhesives, cosmetics, solvents, pharmaceuticals, dyes, medicines, agricultural chemicals, explosive and a constituent of fuels. It is produced traditionally from coal or crude oil by fractional distillation.[1–4] Recently, toluene industrial production has been realized by alkylation of the methanol-benzene system with the aid of a catalyst and generally operating at about 400 °C to obtain a high yield of toluene.[5,6] On the other hand, toluene can also leak during production, which becomes hazardous emission to both human health and environment owing to its high volatility, especially for the most vulnerable object such as toluene-related industrial production workers, air, and groundwater quality in the nearby area. It can cause several acute diseases for longtime exposure to humans, such as headaches, nausea, skin irritation, *etc.*[7–9] In this regard, to monitor leak probability and minimize the harmful effect of toluene emission for both humans and the environment, it should be detected immediately before reaching to open air. However, advanced researches regarding the toluene sensor are generally aiming for outdoor and indoor toluene gas monitoring from household uses such as paint, thinner, cigarette, adhesive, gasoline, and so on, which could be operated at room temperature.[10–12] To the extent of our knowledge, a toluene gas sensor for a high-temperature application that can be employed during toluene production is rather less attempted.

Toluene gas sensing materials based on metal oxide semiconductors (MOS) have been extensively studied due to their facile synthesis, and nanostructurization of MOS (1 – 100 nm) can lead to an increase of gas sensing performance due to nanosized effects.[13,14] For example, nanomaterials possess a high specific surface area, which provides an abundant site for gas adsorption.[14] Additionally, nanoparticles serve better surface contact for electrons and/or holes transport in their interparticle.[15] Tin (IV) oxide (SnO_2), one of the transition metal oxides, is the most well-known gas sensing material, and recent studies about nanostructures of SnO_2 have shown its responsivity to toluene at high temperature (above 350 °C).[16,17] For further improvement

of SnO$_2$ gas sensing properties, decoration with other materials has been reported. There are two types of composite formation; (i) noble metals and (ii) p-type semiconductors. (i) Loading with noble metal nanoparticles such as Au, Ag, Pt or Pd can effectively enhance its toluene gas sensing property. For example, SnO$_2$ decorated with Pd nanoparticle, improved their responsivity as well as selectivity because of the "spill-over" effect that bring much active sites for oxygen species and strengthen adsorption energies (E$_{ads}$) between target gas and sensing material.[18–22] Actually, (ii) addition of p-type to n-type will create p-n junction at particle interface that will consequently increase charge carrier concentration, modify band-gap structure, and inhibit charge recombination. Thus, decoration of n-type SnO$_2$ with p-type counterparts should contribute largely to the enhancement of gas sensing performance as compared to a single n- or p- component.[23–25] While utilization of noble metals hinders sensor devices from cost-effective fabrication, copper (II) oxide (CuO) can lead to the preparation of cost-effective sensors due to its abundance. Therefore, a p-n junction CuO/SnO$_2$-based gas sensing material is expected to be developed for practical applications. Conventionally, p-type CuO/n-type SnO$_2$ combination has been and is still being explored for its utility to detect H$_2$S gas.[26–29] However, investigation of CuO/SnO$_2$ for high temperature toluene gas sensing property is still less pronounced but profoundly needed.

In the present research, we report on a successful uniform decoration of a spherical SnO$_2$ with CuO nanoparticles at room temperature, enabling the time-effective and energy-saving process and scaling-up to the industrial level. We found that electrostatic force interaction occurred at the surface between positively charged CuO and negatively charged SnO$_2$ has led to this uniform self-decoration. With the utilization of different mixed organic solvents in solvothermal synthesis, the surface charge of metal oxides can be controlled. The prepared CuO-decorated SnO$_2$ demonstrated an excellent toluene gas sensing performance in the term of response and selectivity even at high temperatures which is mainly attributed to p-n heterojunction, ohmic junction and spill-over effect due to the partially reduced CuO to Cu metal nanoparticles during the introduction of reducing gas that has a similar phenomenon with addition of Pd or Pt metal nanoparticles. We also systematically proposed the gas sensing mechanism of electrostatic self-decoration.

4.2 Experimental Section

4.2.1 Preparation of CuO nanoparticles and spherical SnO$_2$

CuO nanoparticle was prepared using a solvothermal method by modifying a reported study.[30] In the mentioned report, 50 mL of copper acetate alcoholic solution was utilized. In our synthesis process, 0.3 mmol of anhydrous copper acetate (Cu(OAc)$_2$, 97.0%) was dissolved in 30 mL dehydrated ethanol (EtOH, 99.5%). A transparent light green solution was obtained after stirring 500 rpm for 30 min at 50 $^{\circ}$C. Then, the solution was transferred to 100 mL Teflon-lined autoclave and treated at 150 $^{\circ}$C for 20 h. The black precipitate was collected by vacuum filtration and washed with ethanol several times and placed inside a depressurized drying oven at 70 $^{\circ}$C for 12 h.

To synthesize spherical SnO$_2$, a newly developed-technique, namely water controlled-release solvothermal process (WCRSP), has been utilized.[31] The synthesis method started by dissolving 1 mmol of anhydrous tin chloride (SnCl$_2$, 99.8%) in 40 mL of dehydrated ethanol. The solution was stirred at 400 rpm for 30 min. Subsequently, 10 mL of acetic acid (HOAc, 99.7 %) was added dropwise and the solution was maintained under the same stirring condition for another 30 min. Then, the solution was moved into a 100 mL Teflon-lined autoclave and heated for 20 h at 200 $^{\circ}$C. After the system cooled to room temperature, the obtained powder was washed with ethanol followed by vacuum drying at 70 $^{\circ}$C for 12 h.

4.2.2 Preparation of CuO nanoparticles decoration on spherical SnO$_2$

A simple preparation method of a uniform CuO nanoparticles decoration on spherical SnO$_2$ (SnO$_2$@CuO) was designed. 0.1 mmol of the prepared CuO nanoparticles were dispersed in 10 mL ethanol and placed in ultrasonic bath for 30 min to obtain a homogenous solution. Then, 0.5 mmol of the obtained spherical SnO$_2$ was added to the solution containing CuO nanoparticles, and the mixture was stirred for another 30 min and recovered by filtration. After drying at 70 $^{\circ}$C, the SnO$_2$@CuO was crushed by agate mortar. To reveal the effect of amount of CuO nanoparticles decoration on gas sensing properties, SnO$_2$@CuO samples with variation amount of CuO nanoparticles (0.05, 0.2 and 0.3 mmol) were also prepared.

4.3 Results and Discussion

4.3.1 Structure and morphology of CuO nanoparticles, spherical SnO₂ and SnO₂@CuO

The XRD patterns of the CuO nanoparticles, spherical SnO$_2$ and SnO$_2$@CuO are compared in **Fig. 4.1**. In the XRD pattern of the CuO nanoparticles (**Fig. 4.1** (a)), all the appeared peaks were originated to 110, 002, 111, -202, 020, -113, 022, 220, 311, and 004 diffractions of CuO with monoclinic phase, being in good agreement to the standard pattern (JCPDS 48-1548). While for the spherical SnO$_2$ (**Fig. 4.1** (b)), the peaks could be assigned to tetragonal rutile-type SnO$_2$ (JCPDS 77-447). Furthermore, no characteristic peaks related to other phases in both XRD patterns indicated the obtained samples had no impurity. As shown in **Fig. 4.1** (c), after the SnO$_2$ decoration treatment, the emerged peaks only belong to SnO$_2$, or in other words, the monoclinic phase of CuO was not detected in SnO$_2$@CuO sample due to the low amount of CuO. However, in the case of the higher amount of CuO nanoparticles (0.3 mmol), the 002 and 111 peaks started to be appeared (see XRD patterns in **Fig. 4.2**), demonstrating necessary amount to detect CuO phase in SnO$_2$@CuO system should at least 0.3 mmol. All the prepared samples had broadened peaks, suggesting their nanocrystalline property. According to the Debye-Scherrer formula, $D = K\lambda/\beta cos\theta$,[33] where K is crystallite-shape factor with value of 0.9, λ is the used X-Ray radiation, β is full width at half-maximum (FWHM, radians) and θ is Bragg angle (degree), the crystallite sizes (D) of SnO$_2$ (110) and CuO (111) were estimated to 4.1 nm and 6.9 nm, respectively.
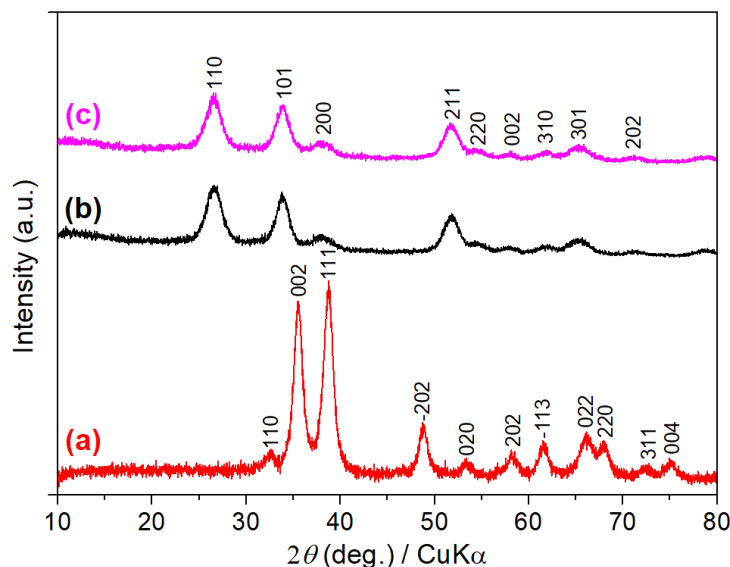

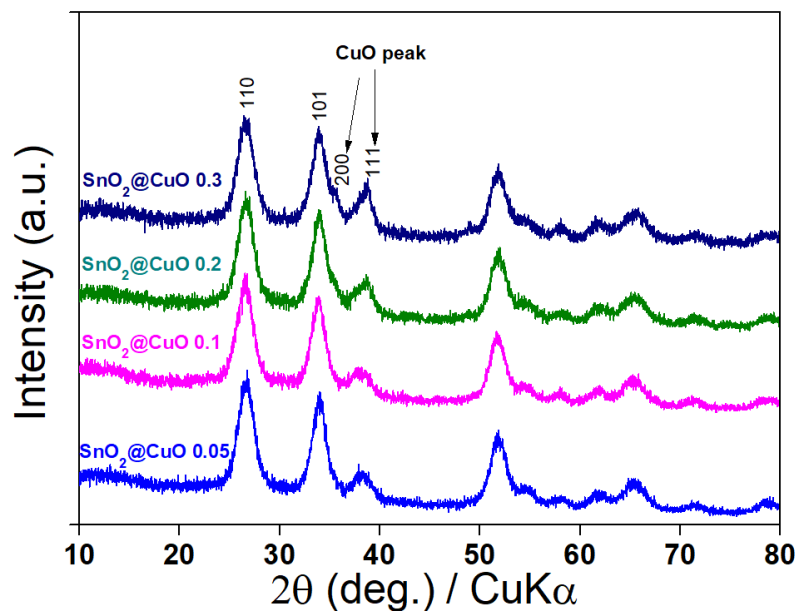**Fig. 4.1** XRD patterns of (a) CuO nanoparticles, (b) Spherical SnO₂ and (c) SnO₂@CuO

Fig. 4.2 XRD pattern of SnO_2@CuO with different amount of CuO
nanoparticles (0.05, 0.1, 0.2 and 0.3 mmol)

The morphological feature, crystal structure and elemental distribution were investigated
by TEM, corresponding selected area electron diffraction (SAED) patterns, high-resolution TEM
(HRTEM) and electron diffraction spectroscopy (EDS) mapping. **Fig. 4.3** (a) represents the TEM
observation of the pure CuO, and the inset is the corresponding SAED patterns The TEM image
clearly shows that the CuO consists of spherical nanoparticles with an average size of about 7 nm,
being consistent with the estimated number obtained from the XRD results. Furthermore, as shown
by the SAED patterns (inset), the diffuse diffraction rings are corresponded to the 110, 002, 111,
-202, 202 and -113 diffractions of CuO, confirming the polycrystalline property of the obtained
CuO nanoparticles. Additionally, the HRTEM image in **Fig. 4.3** (b) demonstrates a lattice space
of 0.27 nm which corresponds to the (111) plane of monoclinic phase CuO, which is in agreement
with its XRD pattern. Considering that no other d lattice spacing, the CuO nanoparticles may
possess single-crystalline property. **Fig. 4.3** (c) shows the TEM image of SnO_2. It shows the
spherical morphology of the obtained SnO_2. The average size of spherical SnO_2 was about 1.2 μm,
and the corresponding SAED pattern depicted in the inset suggests that the spherical SnO_2 also
possessed a polycrystalline feature. The diffraction rings could be assigned to 110, 101, 200, 211
and 002 diffractions of tetragonal rutile-type SnO_2. Based on our previous results,[31] the spherical
morphology was actually constructed by many interconnected nanoparticles which their presence

can be confirmed by HRTEM image shown in **Fig. 4.3** (d). It is clear that interplanar lattice distance of 0.33 nm was corresponding to the 110 diffraction of tetragonal rutile-type SnO_2, confirming that SnO_2 nanoparticles may be a single crystal, although the spherical structure is polycrystalline. **Fig. 4.3** (e) displays the TEM observation of SnO_2 after CuO decoration. As seen in the TEM images, its morphology was similar to that of the parent morphology of the SnO_2. As expected, the spherical morphology observed in the TEM images of the SnO_2@CuO sample was verified to be SnO_2 as SAED pattern shown in the inset indicates the diffraction rings of tetragonal rutile-type SnO_2 with 110, 101, 200, 211 and 002 diffractions. The SAED patterns are also in good agreement with SAED pattern of the bare SnO_2, inferring that the decorative nanoparticles have no effect on the tetragonal crystal structure of SnO_2. From **Fig. 4.3** (e), it can also be observed that the spherical SnO_2 was surrounded by a massive number of nanoparticles after CuO decoration. The HRTEM presented in **Fig. 4.3** (f) identifies the lattice fringes of the surface of the SnO_2@CuO sample. Two different lattice spaces with d values of 0.33 nm and 0.27 nm were observed, which are attributed to the 110 diffraction of tetragonal SnO_2 and 110 diffraction of monoclinic CuO, respectively. Moreover, the nanoparticles of CuO had intimate contact with SnO_2 particles, forming p-n heterojunction which is presumed to be beneficial for the gas sensing response.
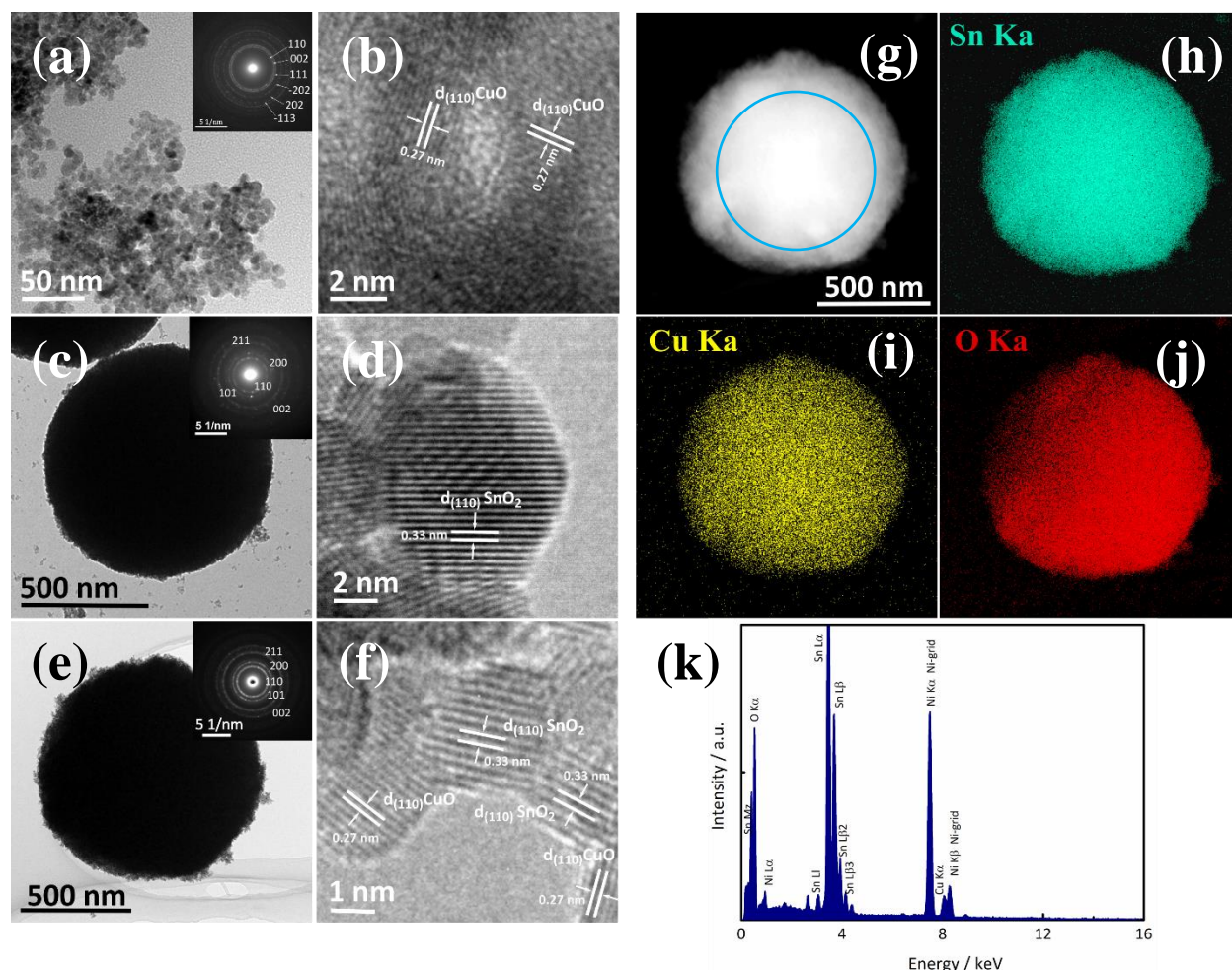
Fig. 4.3 TEM images (inset is ED pattern) and the corresponding HRTEM image of (a-b) CuO nanoparticle (c-d) spherical SnO_2 (e-f) $SnO_2@CuO$. (g) Dark-field image and elemental mapping of (h) Sn (i) Cu (j) O and (k) EDX profile of $SnO_2@CuO$.

To examine the nanoparticles distribution of the CuO on the surface of spherical SnO_2, STEM and EDS mapping were conducted. DF-STEM images of the $SnO_2@CuO$ shown in **Fig. 4.3** (g) revealed gradient in contrast where middle region of the spherical SnO_2 is denser than the outer surface. **Fig. 4.3** (h-j) show the elemental mapping of each individual element, demonstrating Cu, Sn, and O elements were homogeneously distributed throughout the whole observe region. The results strongly supported that CuO nanoparticles were well-decorated on the surface of spherical SnO_2, creating p-n junction which might play as a carrier regulator for the improvement of toluene gas detection. The EDS profile (**Fig. 4.3** (k)) from selected area (blue circle) of $SnO_2@CuO$ confirms the existence of Cu, Sn and O elements. Additionally, the detected Ni signals

are associated to Ni grid. The measured atomic percentage of Cu, Sn, and O are 4.3, 36.5, 59.2 %, respectively.

^{1}H NMR analysis for the filtrates after the solvothermal reaction and the following collection of the precipitate by vacuum filtration was conducted to propose a possible formation mechanism of CuO nanoparticles and spherical SnO_2. **Fig. 4.4** displayed the ^{1}H NMR spectrum of the final solution from the CuO synthesis using copper acetate as a precursor and dehydrated ethanol as a solvent. The ^{1}H NMR spectrum shows triplet peaks at 1.146 ppm to 1.177 ppm (C*H*$_3$CH$_2$OH) and quartet peaks at 3.569 to 3.612 ppm (CH$_3$C*H*$_2$OH), indicating the existence of residual ethanol after the reaction. Additionally, the last singlet peak located at 4.890 ppm corresponded to water molecule (*H*$_2$O).[34] From the ^{1}H NMR result, the presence of water molecule directly pointed to reaction mechanism during the treatment. Similar fashion has been studied by Joo et al. [35] utilizing zinc acetate and octyl alcohol to synthesize zinc oxide nanocrystal. They proposed a mechanism so-called ester elimination reaction and proved the presence of ethyl acetate detected by GC-FID. Similar to their work, CuO formation in this study is predicted by following steps: (4.1) Lewis acid enabled-nucleophilic oxygen attack to acetate ligand due to the lack of electron density and (4.2) CuO and in situ water are generated through polycondensation of $Cu(OH)_2$. It is noted that even though ethyl acetate should be formed during chemical process as shown in step (4.1), it was not presence in NMR, which might be caused by very low amount of ethyl acetate in final solution considering the amount of precursor was only 0.3 mmol. Additionally, NMR might less sensitive than GC-FID.

$$\text{(4.1)}$$

$$-Cu-OH \ + \ HO-Cu- \ \xrightarrow{\text{H}_2\text{O}} \ -Cu-O-Cu- \quad \text{(4.2)}$$
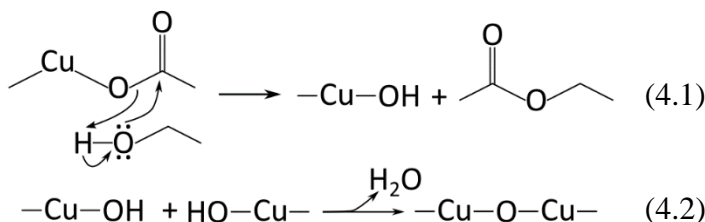
In the case of spherical SnO_2, the formation mechanism has been reported in our earlier study.[31] In brief, the ^{1}H NMR study clarified the existence of ethyl acetate (CH$_3$COOCH$_2$CH$_3$) in addition to the ethanol solution. The ethyl acetate was an esterification product between ethanol and acetic acid during solvothermal condition and at the same time, the water molecule was slowly generated. These water molecules hydrolyzed the $SnCl_2$ precursor to induce nucleation and crystal growth to form SnO_2 nanoparticle subsequently. The nanoparticle finally aggregated to build a

spherical structure with spherical morphology as it has been confirmed by the TEM observation (**Fig. 4.3**). It was found that the size of sphere largely depended on the volume ratio of ethanol/acetic acid, solvothermal reaction time, temperature process and precursor concentration. There were also other compounds detected in ^{1}H NMR, such as diethyl ether ($CH_3CH_2OCH_2CH_3$) and hydrochloric acid (HCl), indicating the dehydration yields of ethanol and by-product from $SnCl_2$ hydrolysis.
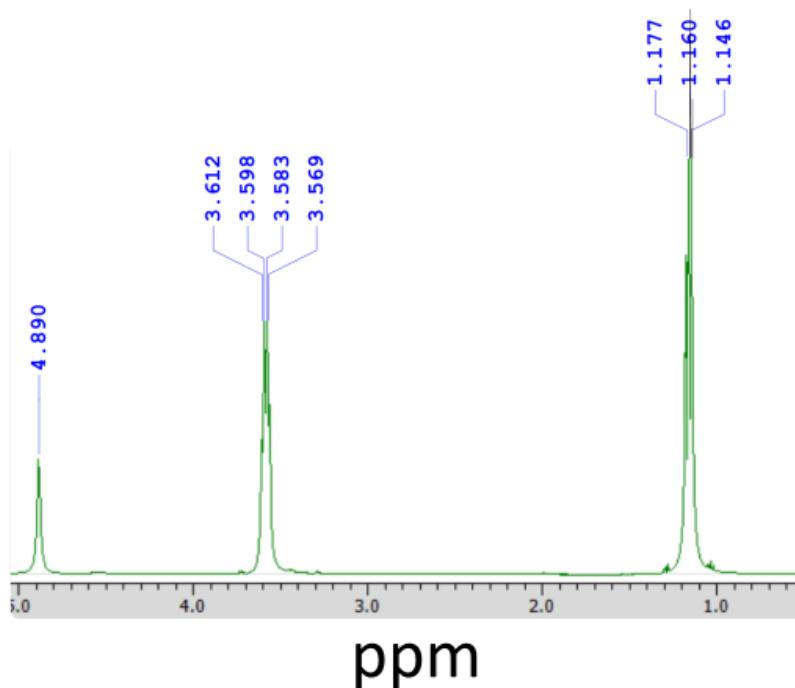

Fig. 4.4 NMR Spectra of supernatant from CuO synthesis

We performed zeta potential analysis to determine charged particles and clarify the reason for the excellent contact between p-type CuO nanoparticles decoration and n-type spherical SnO_2. As depicted in **Fig. 4.5 (a-b)**, CuO nanoparticles surface possessed positively charged (22.9 ± 4 mV), while spherical SnO_2 surface has negatively charged (−3.39 ± 1.3 mV). The positive charge of CuO nanoparticle might originate from adsorbed ethanol during the solvothermal treatment, as it is well-accepted that ethanol is a protic solvent that has positive charge from a labile (H^+). This is different from that of synthesis of spherical SnO_2, which is the utilization of $SnCl_2$ as precursor and esterification-induced ethyl acetate production besides ethanol solvent. Small fraction of Cl^- might remain at SnO_2 surface, giving a negative charge at surface. Moreover, ethyl acetate is aprotic solvent where the two oxygen atoms on carbonyl and ethyl groups have a highly

electronegative charge. It is inferred, from these results, the electrostatic force interaction induced a uniform CuO nanoparticle decoration on SnO$_2$ spherical surface.
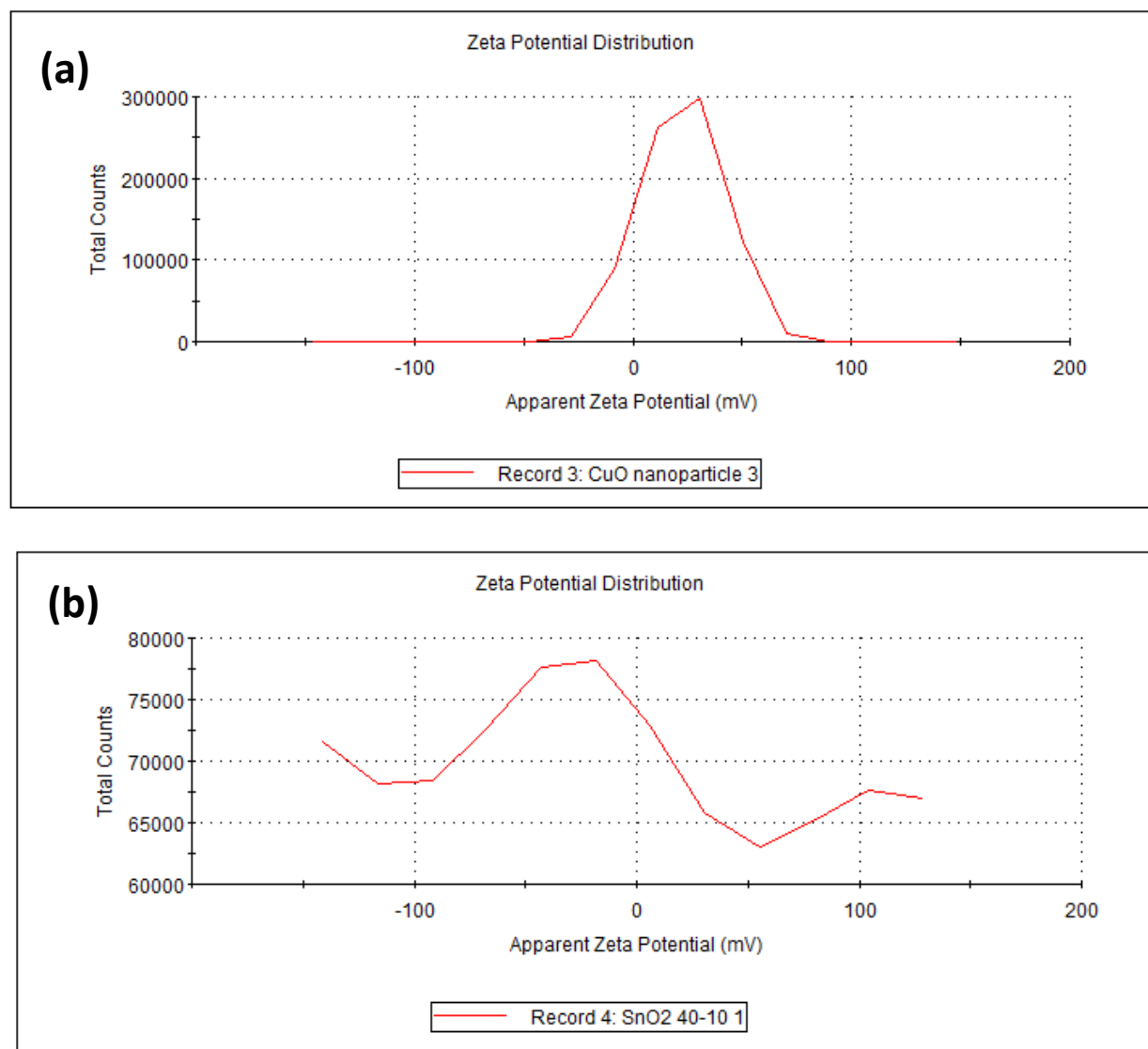
(a)

Zeta Potential Distribution

Record 3: CuO nanoparticle 3

(b)

Zeta Potential Distribution

Record 4: SnO2 40-10 1

Fig. 4.5 Zeta Potential of (a) CuO nanoparticles and (b) spherical SnO$_2$
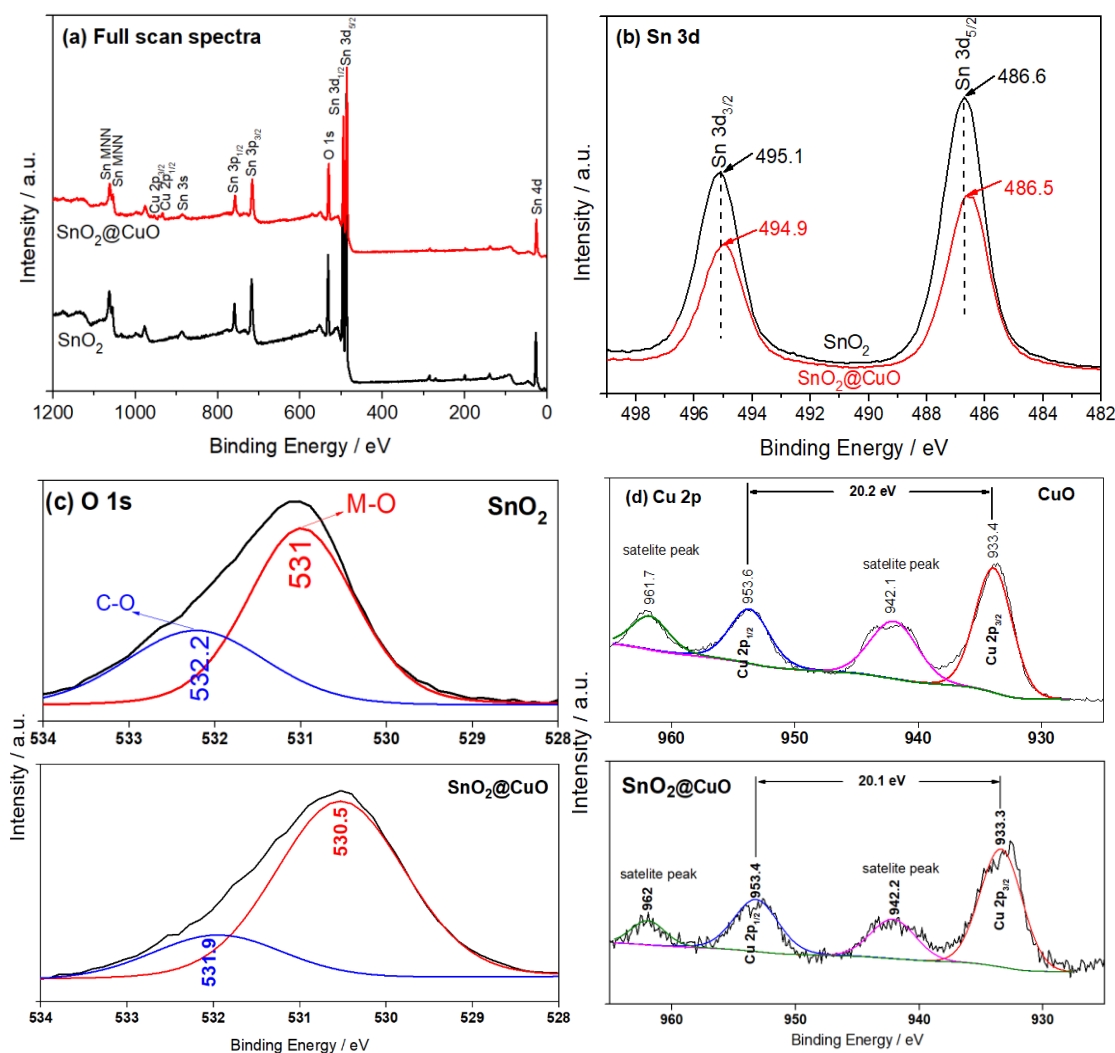
Fig. 4.6 (a) XPS spectra of $SnO_2@CuO$ sample. (b-d) High-resolution spectra of Sn 3d, O 1s and Cu 2p, respectively.

To analyze the core level surface electronic state of the synthesized samples, the XPS analysis was performed. A full scan XPS spectra of pure SnO_2 and $SnO_2@CuO$ are shown in **Fig. 4.6** (a). The result confirms the strong spectra of Sn and O element in the pure SnO_2 and the addition of Cu element in $SnO_2@CuO$. In **Fig. 4.6** (b), the Sn3d peaks of both pure SnO_2 and $SnO_2@CuO$ are compared. The symmetrical doublet peaks located at 495.1 and 486.6 eV are assigned to Sn $3d_{3/2}$ and Sn $3d_{5/2}$ levels, respectively. These peaks are corresponded to Sn^{4+} state of Sn in tetragonal rutile-type SnO_2.[36] After the CuO nanoparticle decoration, the peaks have been slightly shifted to lower binding energies of 494.9 eV for Sn $3d_{3/2}$ and 486.5 eV for Sn $3d_{5/2}$. **Fig.**

126

4.6 (c) displays the O1s XPS scan of pure SnO_2 and SnO_2@CuO. The O1s spectra in both samples consisted of overlapping components, and they were fitted with Gaussian function to obtain resolved peaks. The binding energy peaks from 531 to 530.5 eV were related to oxygen binding to Sn^{4+} in metal oxide lattice, while for the peaks around 532.2 to 531.9 eV were referred to an atmospheric carbon-oxygen related compound adsorbed on the SnO_2 surface. The high-resolution Cu 2p scan depicted in **Fig. 4.6** (d) shows four peaks centered at 933.4, 942.2, 953.3, and 962 eV. The peaks at 933.3 and 953.3 eV can be ascribed to Cu $2p_{3/2}$ and Cu $2p_{1/2}$, respectively. These peaks are the feature of Cu with the oxidation state of 2+, further confirming the presence of CuO phase in the SnO_2@CuO system. The remaining peak observed at 942.2 eV is the satellite peaks of Cu $2p_{3/2}$ and 962 eV is for Cu $2p_{1/2}$ satellite peak. These satellite peaks appeared due to a partially filled $3d^9$ orbital in Cu^{2+} state.[37] It is noteworthy to mention the peak shift in Sn 3d, O1s and Cu 2p core-level spectra after decorating with CuO nanoparticles, which may be contributed by a weak bonding between components in SnO_2@CuO, such as Cu-Sn-O bond similar to that in $CuSnO_3$ material where Sn 3d, O 1s and Cu 2p exhibited a slight shift toward lower binding energy.[38] The EDS and XPS results convinced the attachment of CuO phase on the spherical SnO_2 surface. We also found a small fraction of Cl (0.93 at. %) originating from $SnCl_2$ precursor used in SnO_2 synthesis, though this Cl effect on gas sensing properties were negligible.[31]

The nitrogen adsorption-desorption analysis has been performed to give further insight into the textural properties of CuO nanoparticles, spherical SnO_2 and SnO_2@CuO. The N_2 isotherm and corresponding Barret-Joyner-Halenda (BJH) pore size distribution plot (inset) derived from desorption data are demonstrated in **Fig. 4.7**. According to the IUPAC classification, all the isotherms are classified into type IV with a hysteresis curve at 0.4-0.9 of relative pressure (P/P$_o$), suggesting the existence of porosity. As calculated by BJH method, all the samples exhibit an average pore size of 1.9 nm and small mesopores of 3.2 nm for the CuO nanoparticles sample. The micro-/mesopores have also been observed in TEM images (**Fig. 4.3**), which probably due to unfilled space between the attached nanoparticles. Additionally, the SnO_2 sample presents the highest specific surface area of 113 m^2/g. After the decoration with CuO nanoparticles, the specific surface area slightly decreased to 107 m^2/g because the CuO had a lower specific surface area (90 m^2/g) than that of the SnO_2.
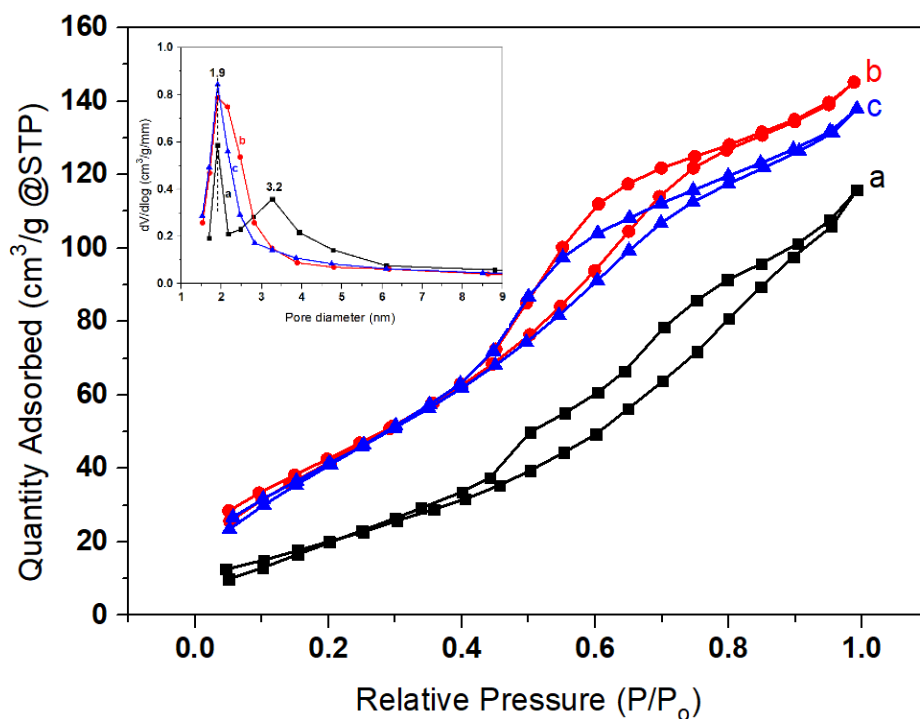
Fig. 4.7 N$_2$ isotherm graph and inset is pore diameter of (a) CuO nanoparticles, (b) spherical SnO$_2$ and (c) SnO$_2$@CuO.

Optical properties of the p-type CuO and n-type SnO$_2$ obtained from non-hydrolytic technique were characterized by UV-Vis diffuse reflectance spectra to predict band gap structures that will be utilized in proposing the gas sensing mechanism of p-n junction based sensor material. As shown in **Fig. 4.8**, it was observed that the absorption edge of CuO (925 nm) is much longer than that of SnO$_2$ (421 nm), reflecting CuO has a narrower band gap energy. Using a well-known Tauc's formula : $(F(R)h\nu)^{1/n} = A(h\nu - E_g)$, where $F(R)$ is Kubelka-Munk equation, h is Planck's constant, ν is the frequency of vibration, α is absorption coefficient, A is proportional constant and E$_g$ is band gap. The estimation of band gap can be obtained from the intersection of $(F(R)h\nu)^{1/n}$ plot with the vertical axis. By assuming direct allowed transition (n=1/2), the estimated band gap of CuO nanoparticle and spherical SnO$_2$ in this study were 1.5 eV and 3.1 eV, respectively, in which these values were far from an ideal band gap of bulk CuO (1.2 eV) or SnO$_2$ (3.6 eV) that may be caused by carbon or chlorine doping originated from organic solutions and precursors during solvothermal treatment.
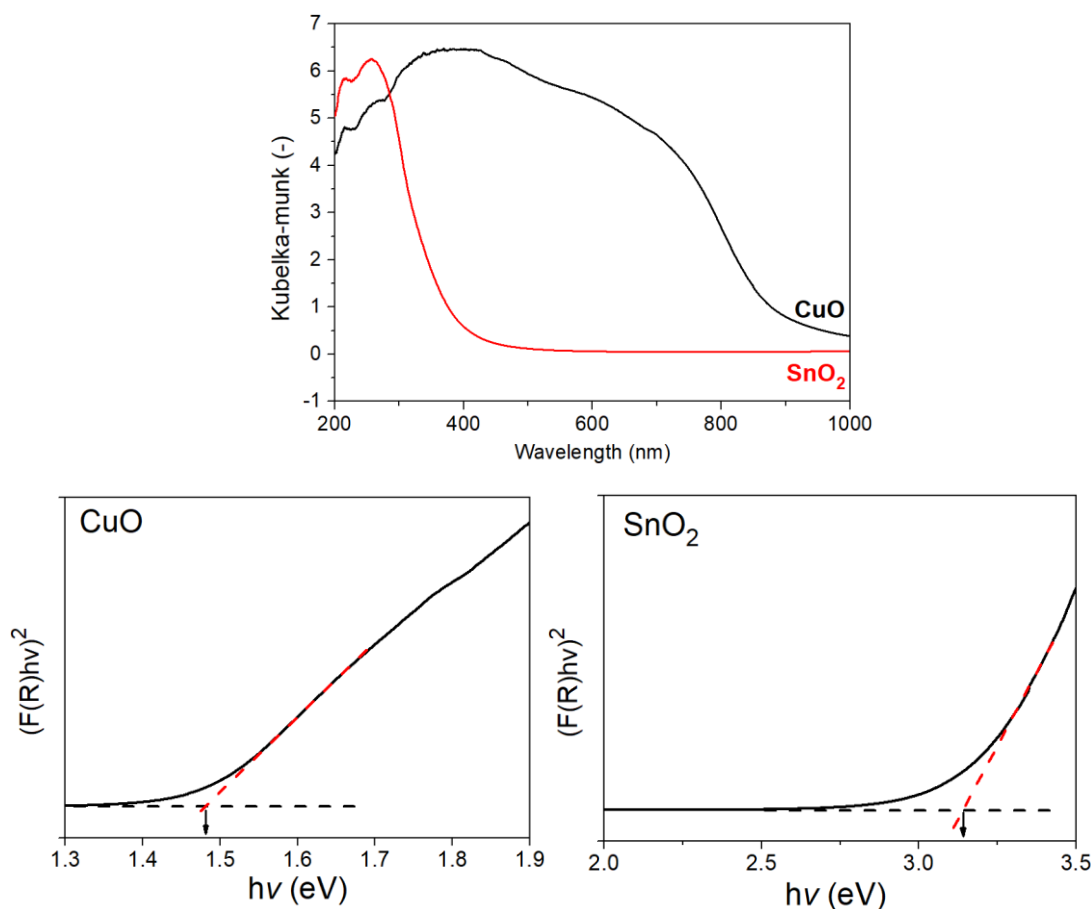
Fig. 4.8 UV Vis DRS spectra and band-gap prediction of the obtained CuO and SnO$_2$

4.3.2 Gas sensing properties of CuO nanoparticle, spherical SnO$_2$ and SnO$_2$@CuO

Effect of CuO nanoparticles decoration on gas sensing performance of SnO$_2$@CuO

Gas sensing response towards 75 ppm toluene gas as a function of working temperature is thoroughly investigated. As shown in **Fig. 4.9** (a), the toluene sensing performance of spherical SnO$_2$ was significantly enhanced by the decoration of CuO nanoparticles compared with the decoration material itself, meaning that the improved sensing response is affected by synergistic performance of p- CuO and n- SnO$_2$ creating p-n heterojunction. Especially, the toluene sensing response of SnO$_2$@CuO starts to increase at above 300 $^{\circ}$C and reach the highest sensing response (S=R$_a$/R$_g$) value of 540 at its optimum working temperature of 400 $^{\circ}$C which is about 100 times greater than the pure SnO$_2$ or CuO. At higher temperature above 400 $^{\circ}$C, sensing response decreased gradually. It is well-documented that surface reaction based on kinetic adsorption-

desorption of oxygen species with sample gas on sensing material should be the reason for this phenomenon.[39–41] At relatively low working temperature, the oxygen adsorption is more dominant than desorption, leading to a lower reaction between tested gas and oxygen ion species and insufficient response. The balance of oxygen adsorption-desorption process is attained at their best operating temperature at which the material exhibits the highest sensing response. Oxygen desorption becomes more dominant at further high temperature, therefore the adsorb oxygen species was not enough to complete reaction with detecting gas. Generally, there are two types of semiconductor gas sensing, *i.e.,* n-type and p-type. In reducing gases environment, sensor resistance of n-type semiconductor reduces during gas exposure and increases during gas release, while p-type shows a contrary characteristic.[42] In **Fig. 4.9** (b-d), pure CuO and SnO_2 showed typical p-type and n-type property, respectively and even after decoration of CuO, SnO_2@CuO exhibits similar characteristics with the parent n-type SnO_2. This is due to a relatively low amount of decorative material. However, we observed a remarkable change in the base sensor resistance of SnO_2@CuO sample. For example, the decorative material CuO has the lowest resistance (~250 Ω) and parent material SnO_2 possesses an intermediate value of resistance (~200 kΩ). When decorating material is added to spherical SnO_2, the resistance greatly increased to ~15 MΩ, which about 75 times higher than SnO_2 before decoration. It was also observed that the response time of SnO_2@CuO (100 s) was shorter than those of pure SnO_2 (126 s) and CuO (9 min), which may indicate a slightly faster surface reaction after decoration with CuO nanoparticles. Although the recovery time was not improved, the SnO_2@CuO still exhibits a rather fast recovery rate which is an extremely important parameter for gas sensor material.
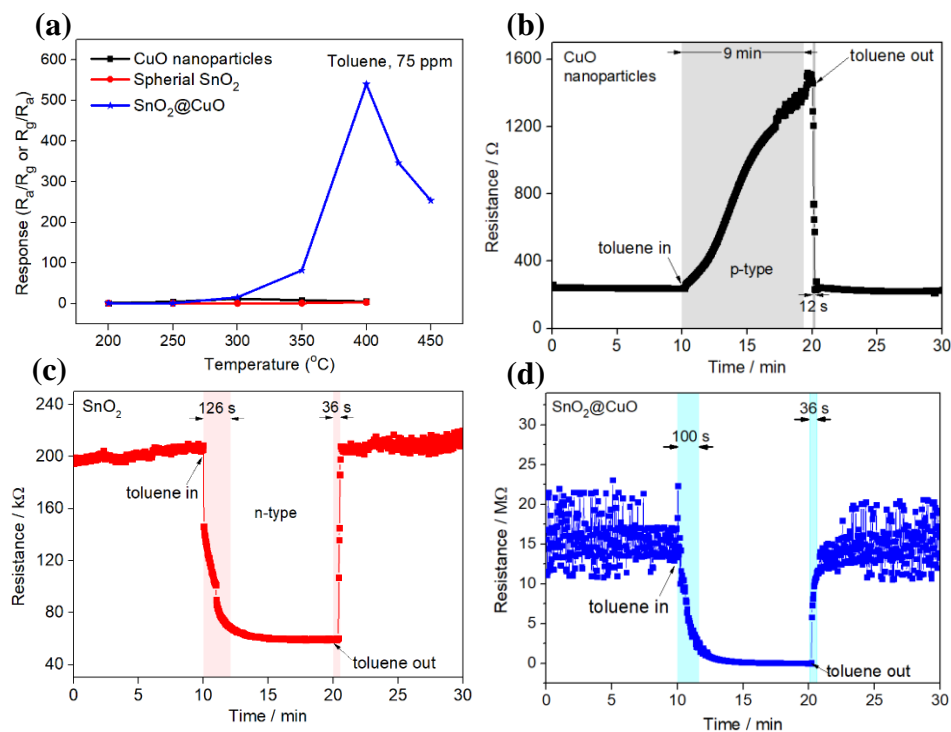
Fig. 4.9 (a) The gas sensing response of all samples at different working temperature and response/recovery time of (b) CuO, (c) SnO$_2$ and (d) SnO$_2$@CuO at 400 °C

To examine the repeatability performance, the CuO decorated-SnO$_2$ based sensor was exposed to different toluene concentrations. **Fig. 4.10** (a) displays a transient toluene sensing response of SnO$_2$@CuO to 10 –75 ppm toluene gas at its best working temperature (400 °C). It clearly shows that the SnO$_2$@CuO sensor had good remarkable response-recovery property as indicated by recovering of sensor resistance after the ejection of toluene gas even though noise of base resistance is observed. Moreover, the sensor response increases with the increment of toluene gas concentration, as shown in **Fig. 4.10** (b). In many cases, the response value will have a linear relationship with testing gas concentration using double-logarithmic plot (Y=mX+C, with Y and X are sensing response and concentration, respectively). However, in our study, the sensor response of the SnO$_2$@CuO shows a linear relation with toluene concentration only up to 30 ppm and an exponential improvement of sensing response occurred above 30 ppm which the relationship between response and toluene concentration can be approximately predicted by a exponential function y = exp (–117.25/(x – 10)) where y is sensor response and x is toluene concentration. We pre-suspected that above 30 ppm of toluene gas exposure, change of physicochemical property of SnO$_2$@CuO sample may probably occur which might be caused by

131

phase or surface state alteration. From the standpoint of real implementation, selectivity of sensing material also should be another critical aspect. Thus, gas sensing performance of $SnO_2@CuO$ towards exposure of different reducing gas such as methanol, ethanol and hydrogen was examined. Sensor selectivity is defined as a ratio between response of toluene compared to other gas response ($S_{toluene}/S_{othergas}$). **Fig. 4.10** (c) obviously shows the response of $SnO_2@CuO$ to 75 ppm of toluene gas is about 5 times higher than during the introduction to ethanol ($S_{toluene}/S_{ethanol}$) as compared to n-type SnO_2 (1.1) and p-type CuO (2.6), which demonstrates a promise for an excellent and selective toluene gas sensor. The results of the current study are compared to the previous work as listed in Table 1 and it can be seen from the data in **Table 4.1**, $SnO_2@CuO$ exhibited a comparably high toluene sensing performance, especially for its response and selectivity.

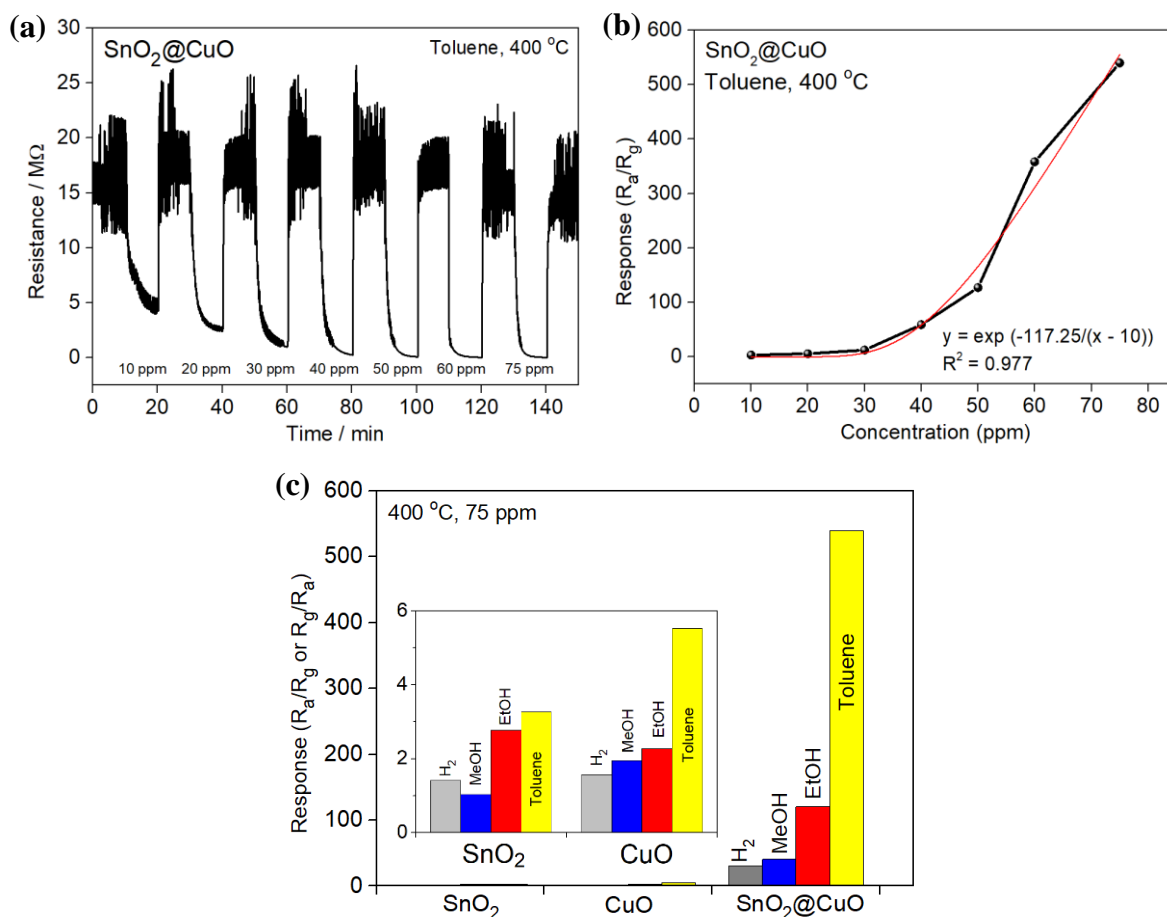**Fig. 4.10** (a) A transient sensing response of $SnO_2@CuO$ to different concentrations of toluene gas (b) exponential fitting *vs.* toluene concentration; y and x-axis represents sensing response and toluene concentration, respectively and R shows quality of fitting, (c) selectivity of $SnO_2@CuO$.

Table 4.1. Comparison of SnO_2-based toluene gas sensing performance

Material	T (ºC)	Conc. (ppm)	Response (R_a/R_g or R_g/R_a)	Selectivity $R_{toluene}/R_{othergas}$	Response/ recovery times (s)	Ref.
SnO_2-decorated NiO nanostructure	250	100	60	2	N/A	[10]
NiO –SnO_2 composite nanofiber	330	50	11	3.8	11.2 /4 s	[43]
SnO_2– Fe_2O_3 Interconnected Nanotubes	260	50	25.3	7	6/10	[44]
Pd-loaded flower-like SnO_2 microspheres	250	10	17.4	1.7	N/A	[20]
Pd- loaded SnO_2 cubic nanocages	230	20	41.4	4.1	0.4/16.5	[18]
SnO_2−ZnO core-shell nanowires	300	1	73	2.8	N/A	[45]
CuO-decorated spherical SnO_2	400	75	540	5	100/36	This work

After the gas sensing measurement, the samples were recovered from the sensor device and characterized by SEM and XPS to investigate their stability. The SEM images (**Fig. 4.11 (a-c)**) clearly showed that without CuO loading, morphology of the spherical SnO_2 was damaged. However, after decorating material was loaded, the most of spherical morphology were retained which a significant proof that the decoration with CuO nanoparticles not only enhanced toluene gas sensing property but also increased thermal stability of the spherical SnO_2 base material as it may act as a protective barrier to prevent thermal oxidation. Furthermore, XPS study as displayed in **Fig. 4.12** suggested that surface chemical states (Sn 3d, O 1s and Cu 2p) of SnO_2@CuO sample were generally similar with that of fresh sample except for a peak at 932.4 eV attributed to other valence state of Cu which probably Cu (0), indicating good stability of the sensing material even at higher temperature and reducing gas environment.
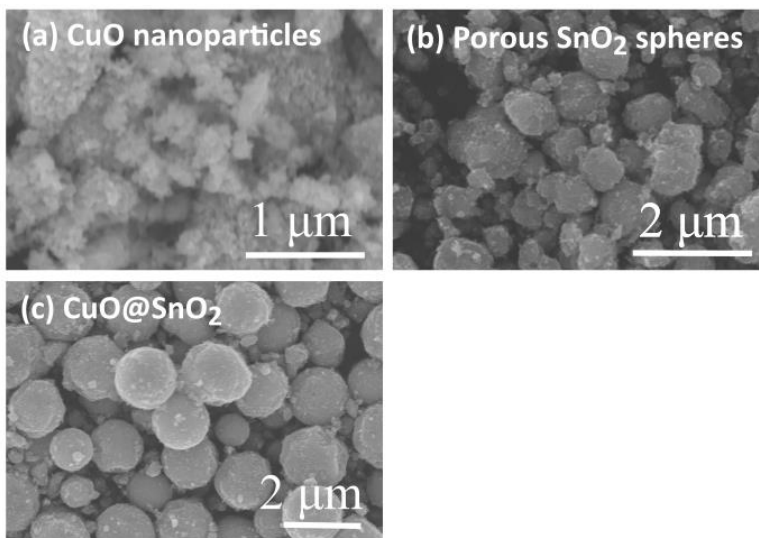
Fig. 4.11 SEM images of (a) CuO nanoparticles (b) porous SnO$_2$ spheres and (c) CuO@SnO$_2$ after the gas sensing measurement.
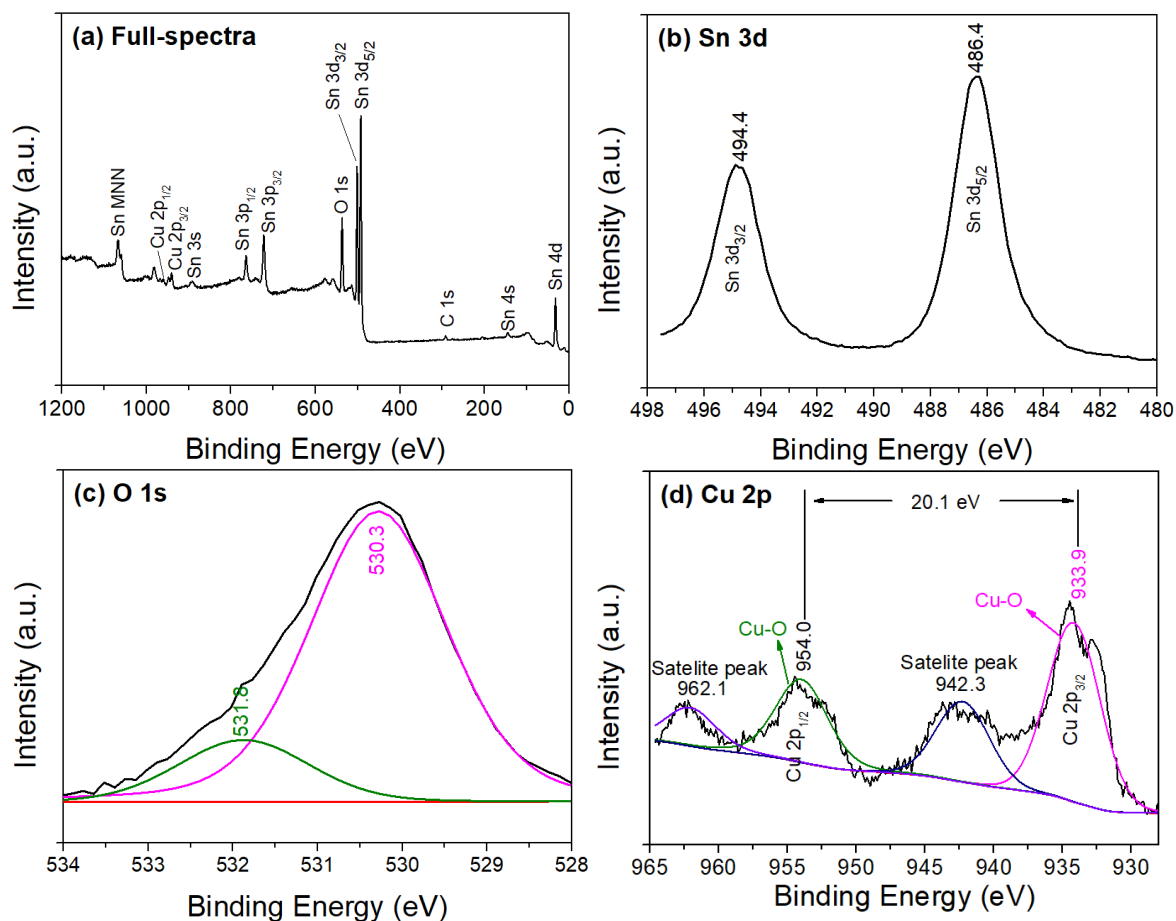

Fig. 4.12 (a) Full-scan XPS spectra and core spectra of (b) Sn 3d (c) O 1s and (d) Cu 2p CuO@SnO$_2$ sample after gas sensing measurement

Effect of amount and particle size of the decorative nanoparticles

We also investigated the effect of the amount of decorative material on toluene sensing response of $SnO_2@CuO$ -based sensor. The amount of CuO nanoparticles loaded onto spherical SnO_2 was varied from 0.05 to 0.3 mmol. **Fig. 4.13** (a) shows the gas sensing response of 0.05, 0.1, 0.2 and 0.3 mmol of CuO loading to 10-50 ppm toluene gas. It is noticed that regardless of the amount of decorating materials, gas sensing response increases as toluene concentration increases. It is also found that the optimum loading amount which exhibits the highest response is 0.1 mmol of CuO. An increase of non p-n junction contact due to an excess amount of p-type CuO has led to the decrement of gas sensing response. In the case of lower amount of CuO, some spherical SnO_2 may not be fully decorated by CuO which also reduces sensor response. The relation between addition of CuO on $SnO_2@CuO$ sensor base resistance and their sensor response is further investigated. As presented in **Fig. 4.13** (b), without addition of CuO, spherical SnO_2 possessed conductive property, as indicated by low resistance during their exposure to ambient air. Addition of 0.05 mmol CuO as decorating particle on spherical SnO_2 increased the resistance greatly due to the development of p-n heterojunction and eventually led to increment of sensor response due to the presumably suppressing charge carrier process. Also, we found a good correlation between the sensor resistance and its sensing response i.e., when our sensing material possesses the largest base resistance, it also shows the highest gas sensing response and *vice versa*. This larger base resistance means more oxygen species adsorbed on the surface of material during the exposure to air and consequently increases more reactions with the target gas leading to higher response.[21,22] Additionally, larger resistance contributed to low concentration of toluene gas. This finding, we believe, is meaningful for the future development of gas sensing materials.
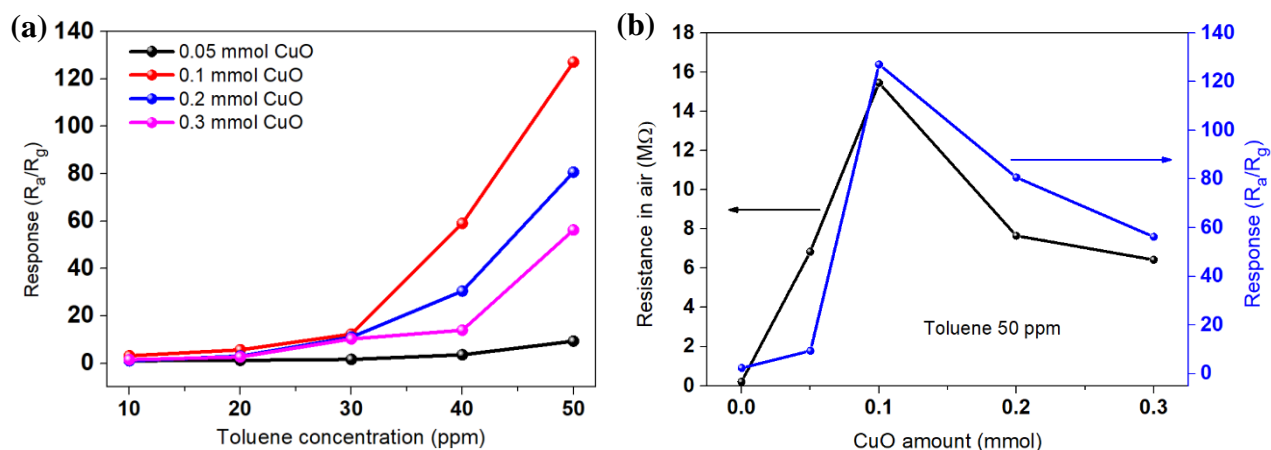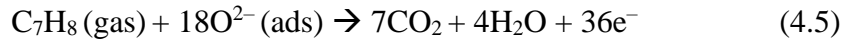
Fig. 4.13 (a) Gas sensing response as a function of toluene concentration and (b) relationship between sensor base resistance and toluene sensing response of SnO_2@CuO based-sensor with different amount of decorating material.

4.3.3 Gas sensing mechanism of SnO_2@CuO

The toluene gas sensing mechanisms of SnO_2@CuO based-sensor should differ from n-type SnO_2 based-sensor due to the creation of p-n heterojunction by the decoration with CuO nanoparticles, although SnO_2@CuO has shown similar sensing response/recovery charateristics to that n- SnO_2. The evidence of p-n heterojunction development at the particle interface has been demonstrated by the HRTEM images as discussed in the earlier section. Moreover, the larger resistance of SnO_2@CuO in air (~15 MΩ) compared to that of pure SnO_2 (~200 kΩ) is another evidence of formation p-n heterojunction.[27,29,46] Therefore, the role of heterojunction structure should be considered for the analysis of sensing mechanism.

The great improvement of gas sensing performance of SnO_2@CuO based-sensor may be attributed to the following enhancement factors. (i) Heterostructures of SnO_2@CuO with micro-/mesoporosity and large specific surface area can provide better gas diffusion to inner surface of hierarchical structures and more abundant active sites for gas adsorption/desorption reaction during sensing process, respectively. Therefore, they can contribute to faster response/recovery time. (ii) p-n junction formation at the interface between both oxides inhibited charge carrier recombination. In thermal equilibrium, once CuO nanoparticles have attached to the surface of spherical SnO_2, electrons in n-type SnO_2 will diffuse in reverse direction because of the difference of charge carrier concentration in each oxide, creating an internal electric field at the interface until

the balance of carrier concentration is achieved. Consequently, at the depletion layer, energy band bends to develop equal fermi energy level (E_F). When the $SnO_2@CuO$-based sensor was exposed to open atmosphere, oxygen molecules were firstly adsorbed on both surface of CuO and SnO_2 particles (Eq. 4.3). To note, although CuO in TEM images has fully covered SnO_2 microsphere, the gas molecules can still be adsorbed on SnO_2 surface through the porosity. Then, the adsorbed oxygen was dissociated into ionized-oxygen species (Eq. 4.4) by taking charge carrier near the surface of p-type CuO and n-type SnO_2 leading to the formation of depletion layer at interface as shown in step (1) of **Fig. 4.14** which increased potential barrier and thus the charge carrier diffusion was blocked. Therefore, compared to pure n-type SnO_2 which has only n-n homojunction, the sensor resistance of $SnO_2@CuO$ in air was larger due to the thicker depleted-layer and p-n junction potential barrier. During the sensor exposure to toluene gas, the oxygen species was removed from the surface of $SnO_2@CuO$, giving the charge carrier back to respective oxide. This also led to the depleted-layer narrowing which results in the decrement of sensor resistance (step (2) of **Fig. 4.14**). The whole process will be repeated once the flow of toluene is stopped and air atmosphere is flown.
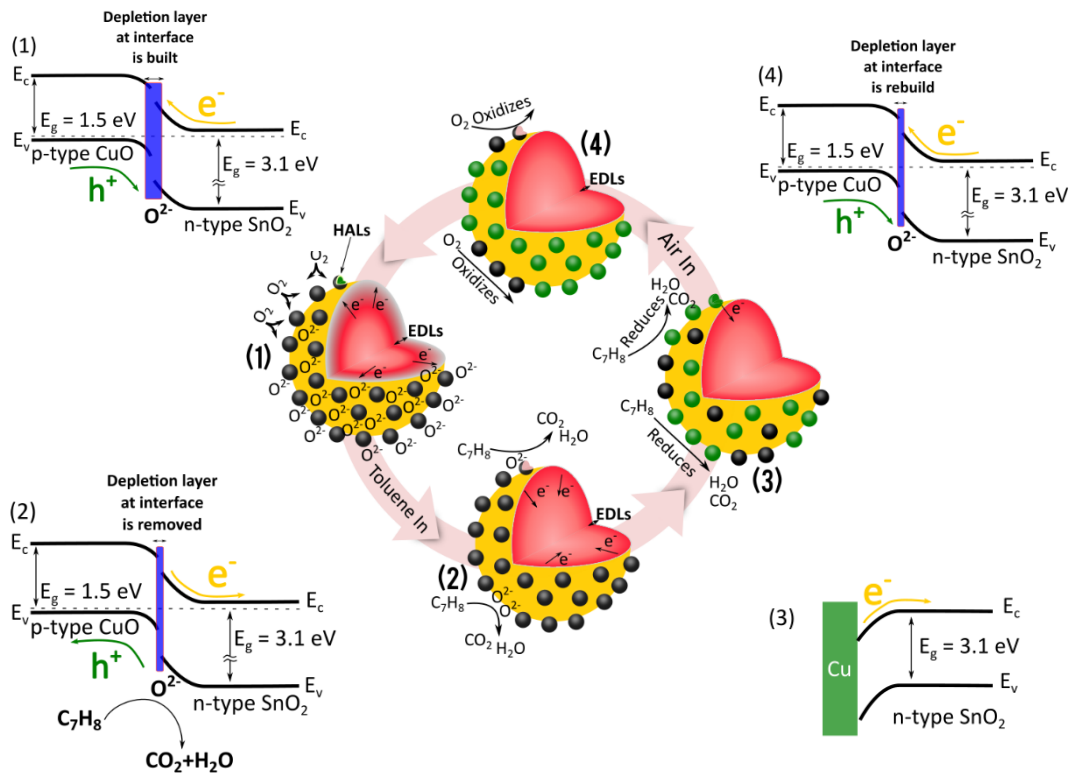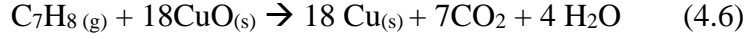
$$O_2 \text{ (gas)} \rightarrow O_2\text{(ads)} \tag{4.3}$$

$$O_2\text{(ads)} + 4e^- \rightarrow 2O^{2-} \text{ (ads)} (> 400 \text{ }^oC) \tag{4.4}$$

$$C_7H_8 \text{ (gas)} + 18O^{2-} \text{ (ads)} \rightarrow 7CO_2 + 4H_2O + 36e^- \tag{4.5}$$

Fig. 4.14. Gas sensing mechanism of CuO nanoparticles-decorated SnO_2 microsphere. EDLs = Electron Depletion Layers. HALs = Hole Accumulation Layers.

However, as we observed in **Fig. 4.10** (b) that the sensor response is not linear with toluene concentration, especially above 40 ppm. Thus, we proposed more detail sensing mechanism to explain this phenomenon. In the case of high toluene concentration (~40 ppm), i.e., when all oxygen ions species are removed in step 2, the process proceeds to the partial reduction of CuO nanoparticles to form Cu metal by excess toluene gas (Eq. 4.6), destroying the p-n heterocontact and charge depletion layer. This process will create another heterocontact between metallic Cu nanoparticles and n-type SnO_2 (step 3) so-called by ohmic-contact (non-rectifying contact) where this type of heterocontact possesses very low resistance junction. The same phenomenon was also found in H_2S exposing environment.[47,48] The SnO_2 band bent downward due to the work function of the metallic phase Cu is lower than that of SnO_2.[49,50] As a result, the sensor resistance will further decrease. In the final step, the flow of air at high temperatures caused oxidation of Cu metal to CuO nanoparticles and the depletion region at the interface is rebuilt at the latter process (step 4).

138

$$C_7H_{8\,(g)} + 18CuO_{(s)} \rightarrow 18\ Cu_{(s)} + 7CO_2 + 4\ H_2O \qquad (4.6)$$

$$2Cu_{(s)} + O_2 \rightarrow CuO_{(s)} \qquad\qquad\qquad\qquad (4.7)$$

The existence of Cu metal was confirmed by the XPS study. The sample for XPS characterization was taken after the gas sensing test. However, after exposing the sensor device to 75 ppm of toluene gas for 10 min, instead of ambient airflow, pure nitrogen was used to remove toluene gas until the measurement system cooled down to room temperature in order to prevent oxidation. As displayed in **Fig. 4.15** (a), the XPS confirmed the presence of Sn, O and Cu elements. Specifically, as seen in **Fig. 4.15** (b), Cu 2p core-level spectra (Cu $2p_{1/2}$ and Cu $2p_{3/2}$) was slightly shifted to lower binding energy than that of the fresh sample in **Fig. 4.6** (d) which may be contributed by Cu metal (Cu (0)) since the peak of Cu metal located at lower binding energy (932.4 and 952.2 eV) than Cu with the oxidation state of +2 in CuO (935.7 eV). Our XPS study result is very close to the past study [51]. They suggested that Cu (0) binding energy is located at 932.6 eV which has a similar value in case of our recent study. Additionally, disappearance of satellite peaks (~942 eV and ~962 eV) further confirm the presence of Cu metal, although the binding energy at 935.7 eV confirmed a small fraction of CuO phase. These facts strongly suggest the partial formation of Cu metal during the exposure of high concentration of toluene. The partial reduction of CuO may become a reason for why pure CuO still exhibiting p-type property, where the resistance increased under the high ppm of toluene gas.

The sensor device containing SnO_2@CuO sample was re-evaluated to investigate the thermal stability since we found a small fraction of Cu (0) phase may still present. The gas sensing reevaluation was performed at 400 ^{o}C under exposure of 75 ppm of toluene gas. As shown in **Fig. 4.16**, the sensor device still shows a transient response/recovery curve similar to the first investigation. However, a slight change in the base resistance of sensor device as well as its responsivity (S = 604) can be observed. The existence of Cu (0) in the SnO_2@CuO sample may induce the ohmic contact and thus altering the base sensor resistance and toluene sensing response. Last, we performed toluene gas sensing response of SnO_2@CuO under different relative humidity (RH) and as shown in **Fig. 4.17,** it can be found that the response of SnO_2@CuO samples decreased

as RH increased which was probably attributed to the competition between water vapor and toluene gas to react with the adsorbed oxygen ion [14,40,52].
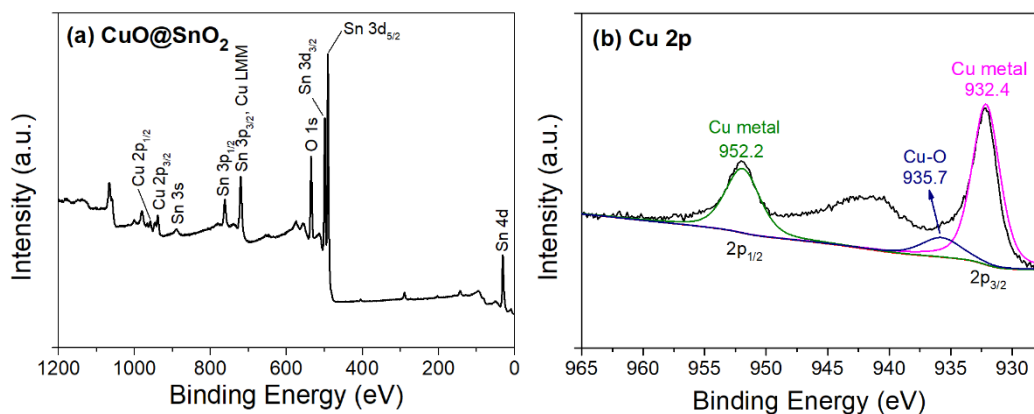

Fig. 4.15 (a) Full spectra and (b) Cu 2p core spectra of $SnO_2@CuO$ after exposure to 75 ppm of toluene gas and cooled down in nitrogen atmosphere.

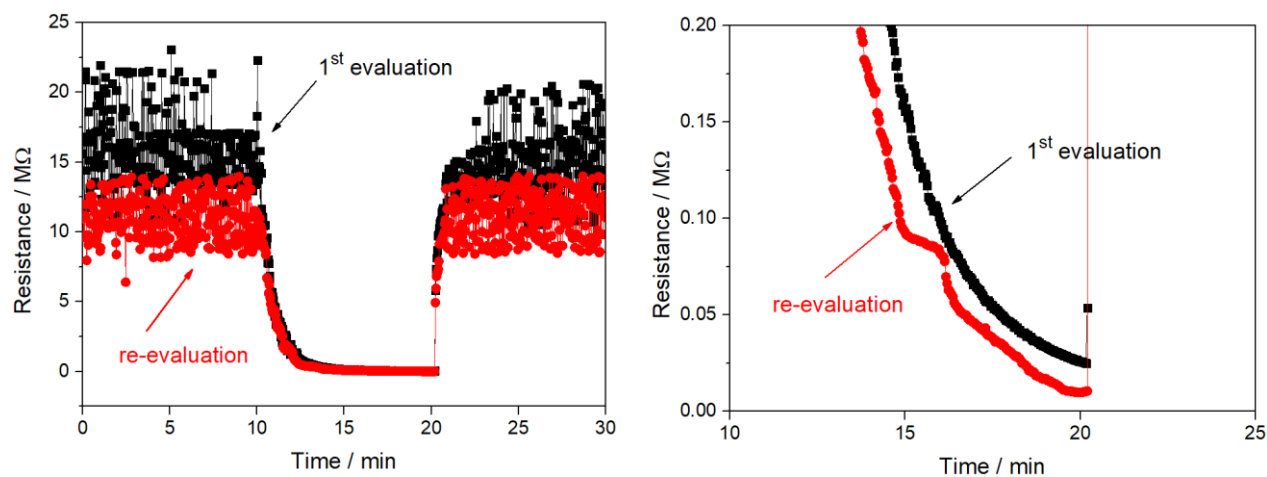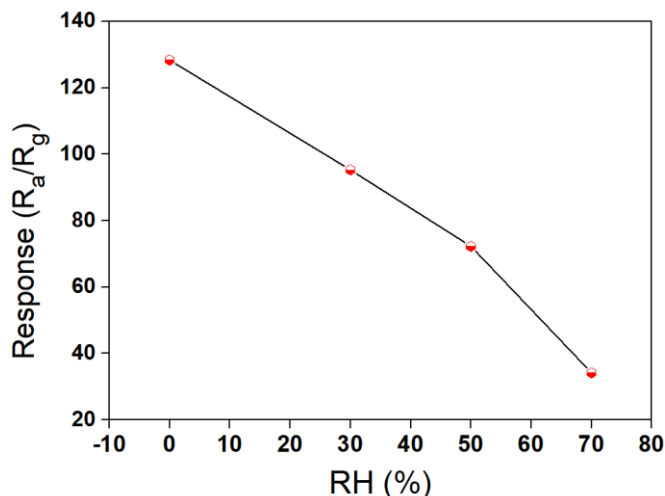**Fig. 4.16** (a) Transient sensing response/recovery feature of $SnO_2@CuO$ on first evaluation and reevaluation.

Fig. 4.17. Toluene gas sensing response (75 ppm) of SnO_2@CuO sample sunder different humidity

4.4 Conclusions

In conclusion, CuO nanoparticles and spherical SnO_2 with high specific surface area (over 90 m^2/g) was successfully synthesized by non-hydrolytic approach. Using a facile decoration process, we were able to decorate spherical SnO_2 with CuO nanoparticles with good uniformity which caused by electrostatic interaction. Owing to (i) p-n heterojunction structure in combination with a high specific surface area and porous property, CuO nanoparticles decorated-spherical SnO_2 showed a significant improvement to toluene gas sensing responsivity (R_a/R_g = 540, 75 ppm) as well as excellent gas selectivity. Moreover, (ii) the formation of Cu metal during the exposure of high concentration toluene which destroying p-n junction and create ohmic contact with n-type further improve the gas sensing properties. The SnO_2@CuO based sensor also demonstrated very high chemical and morphological stability at harsh environment that may meet the requirement for high temperature toluene gas sensor applications.

4.5 References

1   P. C. A. Bruijnincx and B. M. Weckhuysen, *Angew. Chemie - Int. Ed.*, 2013, **52**, 11980–11987.

2   R. Hilten, R. Speir, J. Kastner and K. C. Das, *Bioresour. Technol.*, 2011, **102**, 8288–8294.

3   W. Partenheimer, *Catal. Today*, 1995, **23**, 69–158.

4   G. W. Huber, S. Iborra and A. Corma, *Chem. Rev.*, 2006, **106**, 4044–4098.

5   P. Dong, Z. Li, X. Wang, H. Yun and G. Li, *Green Chem. Lett. Rev.*, 2018, **11**, 158–164.

6   P. Dong, Z. Li, D. Wang, X. Wang, Y. Guo, G. Li and D. Zhang, *Catal. Letters*, 2019, **149**, 248–258.

7   A. K. Low, J. R. Meeks and C. R. Mackerer, *Toxicol. Ind. Health*, 1988, **4**, 49–75.

8   L. FISHBEIN, *Sci. of Total Environ.*, 1981, **3**, 165–183.

9   V. Acetate, *Appl. Occup. Environ. Hyg.*, 1991, **6**, 966–977.

10   H. Gao, L. Zhao, L. Wang, P. Sun, H. Lu, F. Liu, X. Chuai and G. Lu, *Sensors Actuators, B Chem.*, 2018, **255**, 3505–3515.

11   Y. Seekaew, A. Wisitsoraat, D. Phokharatkul and C. Wongchoosuk, *Sensors Actuators, B Chem.*, 2019, **279**, 69–78.

12   L. K. Yeh, J. C. Luo, M. C. Chen, C. H. Wu, J. Z. Chen, I. C. Cheng, C. C. Hsu and W. C. Tian, *Sensors (Switzerland)*, 2016, **16**, 1–11.

13   A. Dey, *Mater. Sci. Eng. B Solid-State Mater. Adv. Technol.*, 2018, **229**, 206–217.

14   Y. F. Sun, S. B. Liu, F. L. Meng, J. Y. Liu, Z. Jin, L. T. Kong and J. H. Liu, *Sensors*, 2012, **12**, 2610–2631.

15   X. Chen and S. S. Mao, *Chem. Rev.*, 2007, **107**, 2891–2959.

16   Q. Qi, T. Zhang, L. Liu and X. Zheng, *Sensors Actuators, B Chem.*, 2009, **137**, 471–475.

17   A. Hermawan, Y. Asakura, M. Inada and S. Yin, *Ceram. Int.*, 2019, **45**, 15435–15444.

18   L. Qiao, Y. Bing, Y. Wang, S. Yu, Z. Liang and Y. Zeng, *Sensors Actuators, B Chem.*, 2017, **241**, 1121–1129.

19   K. Zhang, X. Yang, Y. Wang, Y. Bing, L. Qiao, Z. Liang, S. Yu, Y. Zeng and W. Zheng, *Sensors Actuators, B Chem.*, 2017, **243**, 465–474.

20   J. Tian, J. Wang, Y. Hao, H. Du and X. Li, *Sensors Actuators, B Chem.*, 2014, **202**, 795–802.

21   W. Liu, J. Sun, L. Xu, S. Zhu, X. Zhou, S. Yang, B. Dong, X. Bai, G. Lu and H. Song, *Nanoscale Horizons*, 2019, **4**, 1361–1371.

22   Z. Li, H. Li, Z. Wu, M. Wang, J. Luo, H. Torun, P. Hu, C. Yang, M. Grundmann, X. Liu and Y. Fu, *Mater. Horizons*, 2019, **6**, 470–506.

23   F. Wang, H. Li, Z. Yuan, Y. Sun, F. Chang, H. Deng, L. Xie and H. Li, *RSC Adv.*, 2016, **6**, 79343–79349.

24   S. W. Choi, A. Katoch, J. H. Kim and S. S. Kim, *ACS Appl. Mater. Interfaces*, 2015, **7**, 647–652.

25   O. Lupan, V. Postica, V. Cretu, N. Wolff, V. Duppel, L. Kienle and R. Adelung, *Phys. Status Solidi - Rapid Res. Lett.*, 2016, **10**, 260–266.

26   V. R. Katti, A. K. Debnath, K. P. Muthe, M. Kaur, A. K. Dua, S. C. Gadkari, S. K. Gupta and V. C. Sahni, *Sensors Actuators, B Chem.*, 2003, **96**, 245–252.

27   M. K. Verma and V. Gupta, *Sensors Actuators, B Chem.*, 2012, **166**–**167**, 378–385.

28   J. Liu, X. Huang, G. Ye, W. Liu, Z. Jiao, W. Chao, Z. Zhou and Z. Yu, *Sensors*, 2003, **3**, 110–118.

29   I. Giebelhaus, E. Varechkina, T. Fischer, M. Rumyantseva, V. Ivanov, A. Gaskov, J. R. Morante, J. Arbiol, W. Tyrra and S. Mathur, *J. Mater. Chem. A*, 2013, **1**, 11261–11268.

30   Z. shan Hong, Y. Cao and J. fa Deng, *Mater. Lett.*, 2002, **52**, 34–38.

31   A. Hermawan, Y. Asakura, M. Inada and S. Yin, *Ceram. Int.*, 2019, 0–1.

32   A. Hermawan, Y. Asakura, M. Kobayashi, M. Kakihana and S. Yin, *Sensors Actuators, B Chem.*, 2018, **276**, 388–396.

33   P. Scherrer and P. Debye, *Nachr. Ges. Wiss. Göttingen, Math.-physik. Klasse*, 1918, **2**, 101–120.

34   H. E. Gottlieb, V. Kotlyar and A. Nudelman, *J. Org. Chem.*, 1997, **62**, 7512–7515.

35   J. Joo, S. G. Kwon, J. H. Yu and T. Hyeon, *Adv. Mater.*, 2005, **17**, 1873–1877.

36   M. Kwoka, L. Ottaviano, M. Passacantando, S. Santucci, G. Czempik and J. Szuber, *Thin Solid Films*, 2005, **490**, 36–42.

37   S. Poulston, P. M. Parlett, P. Stone and M. Bowker, *Surf. Interface Anal.*, 1996, **24**, 811–820.

38   Y. Zhang, L. Zhou, F. Xiong, H. Tang, Q. An and L. Mai, *Inorg. Chem. Front.*, 2018, **5**, 2756–2762.

39   P. K. Clifford and D. T. Tuma, *Sensors and Actuators*, 1982, **3**, 255–281.

40   C. Wang, L. Yin, L. Zhang, D. Xiang and R. Gao, *Sensors*, 2010, **10**, 2088–2106.

41   N. Yamazoe, G. Sakai and K. Shimanoe, *Catal. Surv. from Asia*, 2003, **7**, 63–75.

42   H. J. Kim and J. H. Lee, *Sensors Actuators, B Chem.*, 2014, **192**, 607–627.

43   L. Liu, Y. Zhang, G. Wang, S. Li, L. Wang, Y. Han, X. Jiang and A. Wei, *Sensors Actuators, B Chem.*, 2011, **160**, 448–454.

44   H. Shan, C. Liu, L. Liu, J. Zhang, H. Li, Z. Liu, X. Zhang, X. Bo and X. Chi, *ACS Appl. Mater. Interfaces*, 2013, **5**, 6376–6380.

45   J. H. Kim and S. S. Kim, *ACS Appl. Mater. Interfaces*, 2015, **7**, 17199–17208.

46   L. Liu, C. Guo, S. Li, L. Wang, Q. Dong and W. Li, *Sensors Actuators, B Chem.*, 2010, **150**, 806–810.

47   N. Y. Jun Tamaki, Tomoki Maekawa, *Sensors Actuators, B Chem.*, 1992, **9**, 197–203.

48   T. Pagnier, M. Boulova, A. Galerie, A. Gaskov and G. Lucazeau, *Sensors Actuators, B Chem.*, 2000, **71**, 134–139.

49   P. A. Anderson, *Phys. Rev.*, 1949, **76**, 388–390.

50   T. Minami, T. Miyata and T. Yamamoto, *Surf. Coatings Technol.*, 1998, **108**–**109**, 583–587.

51   M. C. Biesinger, *Surf. Interface Anal.*, 2017, **49**, 1325–1334.

52   T. Yang, P. Zhang, B. Xu and J. Xiong, *Int. J. Heat Mass Transf.*, 2017, **110**, 671–679.

Chapter 5

CuO Nanoparticles/Ti$_3$C$_2$T$_x$ MXene Hybrid Nanocomposites for Detection of Toluene Gas

5.1 Introduction

Volatile organic compounds (VOCs) induced by recent situations including rapid industrialization, massive fuels combustion and utilization of chemical in many household products[1–3] should be immediately detected because VOCs can potentially harm the human body through inhalation.[2,4] Since VOCs are quickly evaporated at relatively low temperature, VOCs amount in the atmosphere can gradually increase over time making our environment and other living creatures endangered.[2,5–7] Among various harmful VOCs, gaseous toluene (C$_7$H$_8$) is poisonous for both humans and environment produced from paints, thinners, adhesives, cleaning agents, leather tanning processes.[8,9] Therefore, early detection of toluene gas is of great importance to reduce health risk from its exposure and monitoring its concentration at the indoor and outdoor environment.

Chemiresistive-type gas sensors based on semiconductor metal oxide (SMOX) materials are the most explored type of gas sensing systems because of its cost-effective materials, facile fabrication and responsivity to a wide number of gases including VOCs.[10–13] Copper monoxide (CuO) with p-type semiconductor property has many applications, especially used for gas sensors. CuO is sensitive to various VOCs such as C$_2$H$_5$OH, BTEX, H$_2$S, and NH$_3$,[14–19] and its selectivity in use for the sensor may be comparable with the n-type semiconductor counterparts.[20] However, the gas sensing sensitivity, and response/recovery times, are still inadequate to meet the demand due to low carrier mobility. In general, gas sensing properties of SMOX material has been improved by hybridization with conductive material.[21–23] In this strategy, several factors in SMOX materials for hybridization should be considered for high sensing performance; (i) morphology of SMOX material and (ii) assembled state and (iii) work function (Φ) modulation. (i) For the increase of contact points, SMOX material should possess a high specific surface area. (ii) Facile assembling methods should lead to hybrid materials with a lot of contact points between SMOX, and conductive materials are needed for practical fabrication of sensors. (iii) The position of work function influences the band alignment at SMOX and conductive materials interface, consequently governing the charge transfer process. From these viewpoints, nanoparticle morphology with high

specific surface area and easy fabricability should be suitable as that of SMOX material for such hybrid preparation. Therefore, our strategy to improve the gas sensor performance is by hybridizing CuO nanoparticles with a conductive material that possessed different work functions.

MXene is a new family of two-dimensional (2D) materials consisting of transition metal carbides, carbonitrides and nitrides. Generally, MXene has a formula of $M_{n+1}X_n$ where M and X represent transition metals (Ti, Sc, V, Zr, *etc.*) and carbon and/or N, respectively. They have been gaining a special interest because they offer exceptionally electronic, physical, chemical, and mechanical properties and high specific surface area that contrast from their 3D structure counterpart (MAX phase, A represent Al layers). These exceptional performances make MXene a suitable candidate for energy and environmental applications such as supercapacitors, solid-state batteries, thermoelectric device, fuel production, and photodegradation etc..[24] Moreover, considering their free-standing crystal, layered structures, and unique stacking of delaminated layers, 2D MXene materials provide an easy-to-assemble building block for nanoparticle insertion, forming nanoarchitectures.[24] $Ti_3C_2T_x$ (T=–F, –OH, –O) is the first synthesized 2D MXene and one of the most explored among the MXene family. And it has been utilized for various applications due to its large specific surface area, very narrow bandgap and fast electron transfer ability.[25–28] One recent application of $Ti_3C_2T_x$ is gas sensing material for various hazardous gas. The 2D structure of $Ti_3C_2T_x$ prepared by hydrofluoric acid (HF) etching of one of the MAX phases, $Ti_3CAl_2C_2$, by hydrofluoric acid (HF) shows the response to NOx detection at room temperature.

Compared to the other 2D materials such as graphene, black phosphorus (BP), and h-BN, $Ti_3C_2T_x$ exhibited much higher responsivity with a high signal-to-noise ratio (SNR).[29] The excellent NO_x sensing properties were attributed to (1) widespread of functional groups on the surfaces of MXene, which strongly bonds with NO_x and (2) metallic conductivity of $Ti_3C_2(OH)_2$ to realize fast electron transfer and mobility. Additionally, the metallic phase $Ti_3C_2T_x$ has a relatively work function Considering such interesting properties can lead to utilization of $Ti_3C_2T_x$ not only as a stand-alone gas sensing material but also as conducting, host and transfer layers for charges in the SMOX gas sensing material. An assemble of the layered structure of $Ti_3C_2T_x$ with nanoscale metal oxides forming a hybrid heterostructure and their application for VOCs gas sensor is very limited, although drastic improvement of the gas sensing properties is expected.

Though $Ti_3C_2T_x$ MXene shows responsivity to some VOCs and ammonia gases,[29,30] the sensing response to toluene gas is not observed at all due to non-polar structures of toluene.[31] However, $Ti_3C_2T_x$ MXene can play a role as a support layer for CuO, the best candidate sensing material. Here, for the first time, we reported the fabrication of CuO nanoparticles/$Ti_3C_2T_x$ hybrid heterostructures and demonstrated their novel functionality for relatively low-temperature toluene gas sensing applications. The CuO nanoparticles/$Ti_3C_2T_x$ hybrid heterostructures were prepared by a facile assembling process. The CuO nanoparticles were successfully covered on the top and bottom surfaces of MXene-$Ti_3C_2T_x$ as well as inserted into spaces of $Ti_3C_2T_x$ interlamination. This structure can be beneficial for the effective and fast charge carrier transport. The large coverage of CuO nanoparticles can be attributed to Van der Waals surface electrostatic force between positively charged CuO nanoparticles and negatively charged $Ti_3C_2T_x$. The prepared CuO nanoparticles/$Ti_3C_2T_x$ hybrid heterostructures offered better gas sensing response to 50 ppm of toluene compared to the individual CuO or $Ti_3C_2T_x$, even still superior to other hybrids of CuO with highly conductive 2D family such as CuO/MoS_2 and CuO/rGO heterostructures. This is mainly due to different work function of $Ti_3C_2T_x$, MoS_2 and rGO that lead to creation of Schottky or Ohmic junction. The hybridization of CuO with $Ti_3C_2T_x$ conducting layers also improved response/recovery time to as short as 270 s / 10 s. A gas sensing mechanism was also proposed for various 2D material.

5.2 Experimental

5.2.1 CuO nanoparticles synthesis

A facile solvothermal treatment was utilized to synthesize CuO nanoparticles, as previously reported.[32] Firstly, 0.6 mmol of copper acetate (FUJIFILM WAKO, Cu(OAc)$_2$, 97.0%) was dissolved in 60 mL anhydrous ethanol (FUJIFILM WAKO, EtOH, 99.5%) inside a 100 mL Teflon lined-autoclave. Then, the solution was magnetically stirred at 500 rpm for about 30 min until a transparent green solution was obtained. The solvothermal treatment was carried out at 150 °C for 12 h. After the system was cooled to room temperature, the black precipitate was collected by filtration and washed with ethanol and distilled water to remove organics solvents. Finally, the precipitate was dried at 70 °C for 12 h.

5.2.2 Preparation of Ti₃AlC₂ MAX phase

The precursor Ti_3AlC_2 powders were prepared by a vacuum pressure-less sintering method based on the previous report.[33,34] In a typical synthesis, Ti (99.5% purity, 50 μm), Al (99.5% purity, 75 μm), and TiC (99.5% purity, 75 μm) powders, in the molar ratio of 1:1.2:2, were mixed uniformly via the mechanical ball-milling. Subsequently, the obtained mixture was sintered at 1350 °C for 2 h in a vacuum environment. Then the resultant Ti_3AlC_2 sample was broke up to fine powders by high-energy ball-milling and collected for further use.

5.2.3 Preparation of Ti₃C₂Tₓ MXene

$Ti_3C_2T_x$ was prepared via the liquid etching method.[35] Typically, 5.0 g of the as-prepared Ti_3AlC_2 powder was added into HF (80 ml, 40% v/v) aqueous solution under vigorous stirring for a whole day at room temperature. After that, the resulting suspension was washed with distilled water and absolute ethanol for removing the residual HF and impurities until the pH is 6. The obtained precipitate was dried in an oven at 40 °C for 24 h, and then, the $Ti_3C_2T_x$ MXene powders were finally obtained.

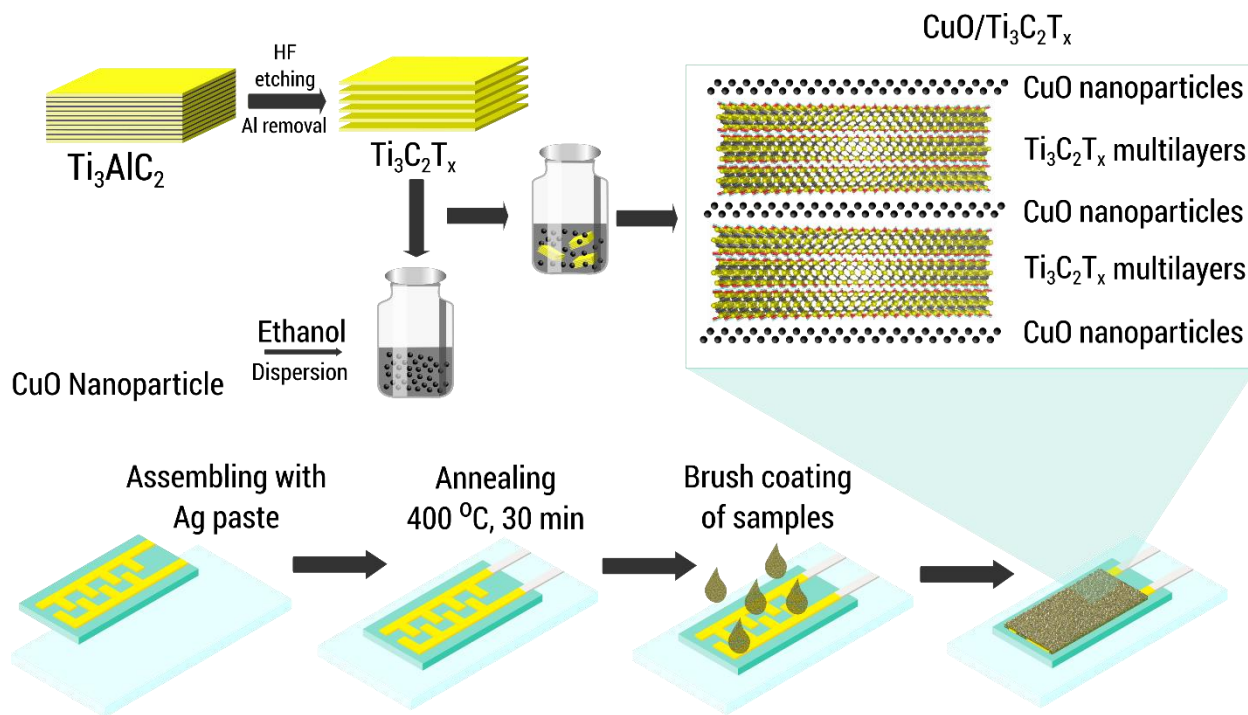### 5.2.4 CuO nanoparticles/Ti₃C₂Tₓ MXene

CuO nanoparticles were dispersed in ethanol solution (99.5% in purity) and placed in an ultrasonic bath to prepare CuO nanoparticles/$Ti_3C_2T_x$ hybrid heterostructures. The ultrasonication process was carried out at room temperature for 20 min to disperse nanoparticles. Then, the prepared $Ti_3C_2T_x$ MXene powder with a designated amount (10, 20, 30, 40 wt. %) was then mixed into solution followed by stirring 500 rpm for 10 min. The mixed powder was recollected by vacuum filtration, washed with ethanol, and dried at 70 °C for 12 h. The sample with the addition of 30 wt. % $Ti_3C_2T_x$-MXene was taken as representative for the detailed characterization.

5.2.5 Fabrication and analysis of a gas sensing device

The following steps described sensor device fabrication. An interdigitated electrode (IDE) consisted of two comb-type Au networks was assembled to silicate glass by silver paste at each end. The electrode was heated in a furnace at 400 °C for 30 min at ambient air to remove the organic solvent in the silver paste. Then, the synthesized CuO nanoparticles, $Ti_3C_2T_x$ MXene or CuO/ $Ti_3C_2T_x$ MXene was mixed with ethanol and brushed coated onto the fabricated electrode until the electrode was entirely covered with the samples. The simplified illustration of CuO/

Ti$_3$C$_2$T$_x$ MXene preparation and gas sensor device fabrication was illustrated in **Scheme 5.1**. The evaluation of gas sensing properties of the samples was collected using a data acquisition unit (Agilent 34970A) with two points probe method. A tailor-made gas sensing measurement was utilized to control some designated parameters in this study, such as operating temperature, analyzing chemicals, and gas concentration. The operating temperature was varied from 100 ^{o}C – 350 ^{o}C to find out optimum temperatures for the sensor device. The analytes, including toluene, methanol, ethanol, acetone, and hydrogen with a concentration of (10 – 50 ppm), were carried out to a sensor device to measure sensor responsivity and selectivity. Humidity in the testing chamber was controlled by temperature and humidity oven (Espec SH-222). The injection time of analytes was 10 min, with intervals of 10 min to re-introduce the air atmosphere. The gas sensing response was defined as a ratio of sensor resistance in the air (R_a) and sensor resistance in analyte gas (R_g). Since all analytes were classified as reducing gas, the sensor response for a p-type semiconductor can be calculated as R_g/R_a. The response time (t_{res}) of the sensor has been defined as the time needed to reach the steady response value after the flow of testing gas, which is calculated from 90 % change of the initial resistance. As for the recovery time (t_{rec}), it is the required needed for the sensor to recover 90 % of its initial resistance.

Scheme 5.1. Schematic representation of a facile preparation of CuO nanoparticles/Ti$_3$C$_2$T$_x$ hybrid heterostructures and gas sensor device fabrication

5.3 Results and Discussion

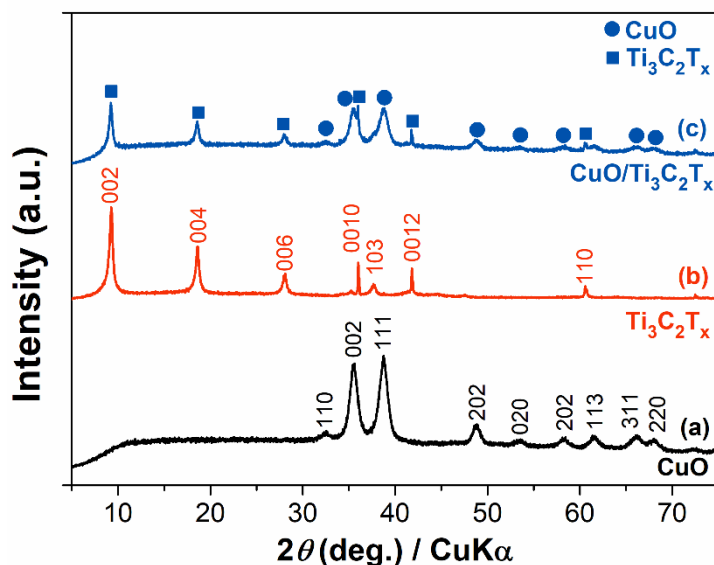### 5.3.1 Crystalline phase, morphology, and electronic structure

Fig. 5.1. XRD patterns of (a) CuO nanoparticles, (b) $Ti_3C_2T_x$ after etching by HF and (c) $CuO/Ti_3C_2T_x$

The phase and crystal structures were firstly examined by X-ray diffraction (XRD) analysis. The XRD pattern shown in **Fig. 5.1** (a) is associated with the product obtained solvothermally from $Cu(ac)_2$. The peaks at 32.5°, 35.5°, 38.7°, 48.8°, 53.5°, 58.3°, 61.5°, 66.1°, and 68.0° were attributed to (110), ($\bar{1}$11), (111), ($\bar{2}$02),(020), (202), (113), (311), and (220) crystal planes of monoclinic CuO (JCPDS Card No. 48-1548), and no other peaks related to secondary compounds were observed. This result means that pristine CuO was formed by a solvothermal reaction without byproduct. **Fig. 5.1** (b) shows the XRD pattern of a typical $Ti_3C_2T_x$ MXene after the etching process by the HF solution. The emerged peaks at 9.2°, 18.5° and 28.1° were different from those in the XRD patterns of MAX-phase Ti_3AlC_2 (**Fig. 5.2** (a)) and was ascribed to a typical (002), (004) and (006) planes of 2D $Ti_3C_2T_x$ MXene, respectively, indicating a complete elimination of Al layers in Ti_3AlC_2. Also, the residual peaks (0010), (103) (0012), and (110) were contributed to –OH terminated surface group, implying the formation of metallic phase-$Ti_3C_2(OH)_2$ in line with reported literature.[27,36,37] As reported in previous studies, metallic –OH terminated Ti_3C_2 exhibited the electrical conductivity as high as 6500 S·cm^{-1}.[38] Accordingly, after the combination with CuO nanoparticles, the diffraction pattern of $CuO/Ti_3C_2T_x$ (**Fig. 5.1** (c)) indicated the presence of each independent compound, demonstrating the successful preparation of $CuO/Ti_3C_2T_x$. Additionally,

the (002) peak of $Ti_3C_2T_x$ corresponding to interlayer distance was not shifted to either a lower or higher angle, indicating no expansion on the interlayer spacing of $Ti_3C_2T_x$. Instead, CuO nanoparticles inserted in between gaps of delaminated sheets which comprised of several layers.
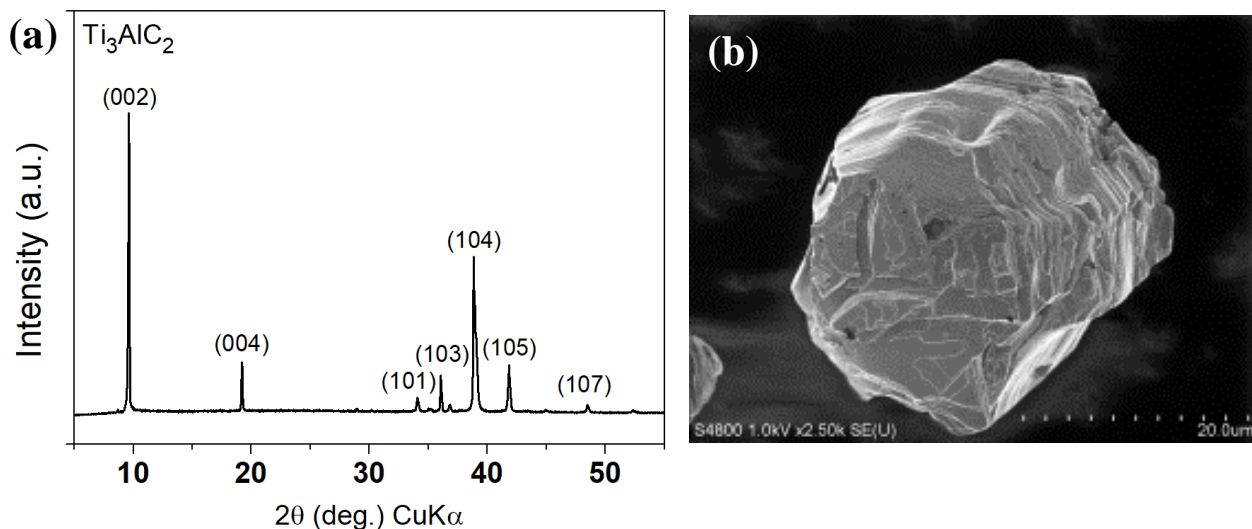

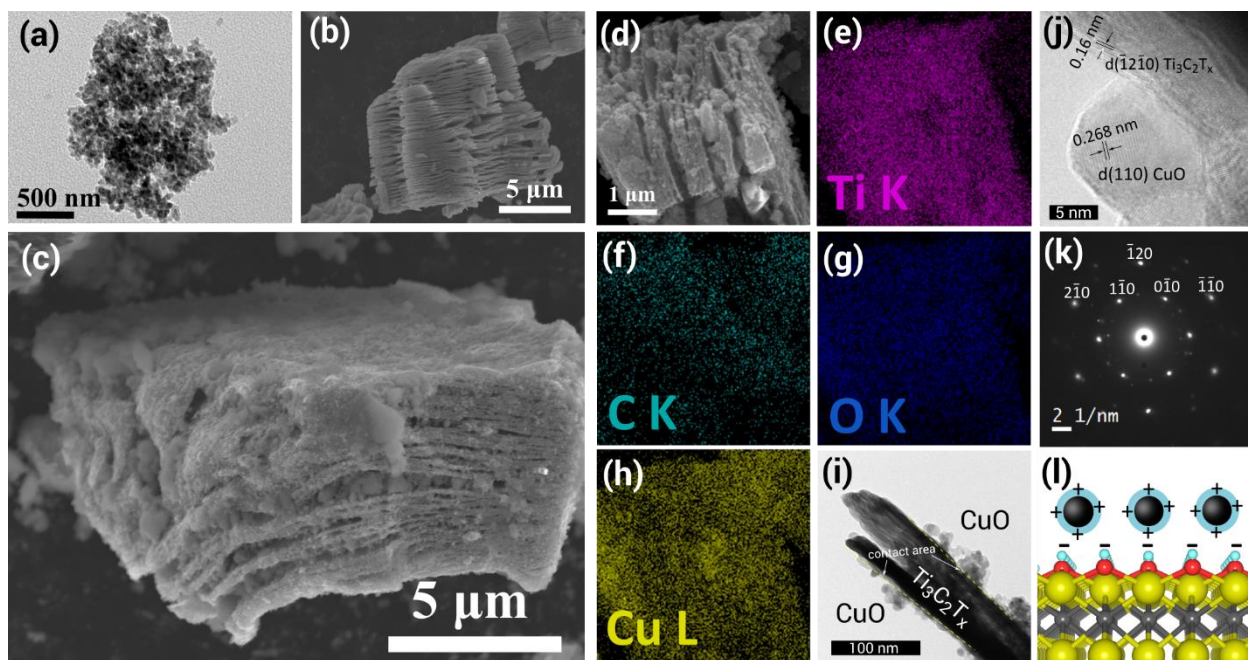Fig. 5.2 XRD pattern and SEM images of MAX phase-Ti_3AlC_2

Fig. 5.3. TEM images of (a) CuO nanoparticles; SEM images of (b) $Ti_3C_2T_x$ MXene and (c) CuO/$Ti_3C_2T_x$; (d) SEM images of CuO/$Ti_3C_2T_x$ and (e-h) its corresponding elemental mapping. (i) TEM image, (j) HRTEM image (k) ED patterns and (l) illustration of electrostatic interaction of CuO/$Ti_3C_2T_x$

Observations of morphological features of the obtained CuO nanoparticles, $Ti_3C_2T_x$, and $CuO/Ti_3C_2T_x$ hybrid heterostructures, were performed using FESEM and TEM. As shown in **Fig. 5.3** (a), CuO synthesized by the solvothermal approach using the pristine ethanol solvent possessed well-defined nanostructures with an average size of 7 nm. **Fig. 5.3** (b) depicted a typical exfoliated morphology of delaminated $Ti_3C_2T_x$, which indicated a successful removal Al layer from MAX phase-Ti_3AlC_2 (SEM is shown in **Fig. 5.2** (b)). The bulk size and interlamination spaces of $Ti_3C_2T_x$ were estimated to be 1–2 μm and 10–50 nm, enabling a possibility of CuO insertion into the deeper region of bulk $Ti_3C_2T_x$. The morphology of $CuO/Ti_3C_2T_x$ structures is shown in **Fig. 5.3** (c)-(d). FESEM images clearly showed that CuO nanoparticles had been uniformly distributed on both $Ti_3C_2T_x$ surfaces and interlayer spaces, demonstrating that the combination of sonication and stirring technique produced well-decorated $Ti_3C_2T_x$ delaminated structures. This approach can also be applicable for 2D materials hybridization with other metal oxides nanostructure.

Moreover, to further confirm chemical distribution in the $CuO/Ti_3C_2T_x$, EDS mapping equipped in FESEM was utilized. **Fig. 5.3** (d) shows FESEM image of $CuO/Ti_3C_2T_x$, and **Fig. 5.3** (e-h) show the corresponding EDS mapping of chemical elements in $CuO/Ti_3C_2T_x$, confirming the signal of Ti K, C K, O K, and Cu L. It might be seen that the distribution of Cu and O element in $CuO/Ti_3C_2T_x$ composite were homogeneous in the characterized area. In contrast, elemental mapping of pristine $Ti_3C_2T_x$ (**Fig. 5.4**) showed the absence of Cu and O. These results demonstrated that CuO nanoparticles were uniformly distributed over $Ti_3C_2T_x$ structures and might also exist in the inner region of the particle. Moreover, the HRTEM image shown in **Fig. 5.3** (i) presented good contact between CuO nanoparticles and $Ti_3C_2T_x$, which can be favorable for a rapid charge transfer. **Fig. 5.3** (j) shows the lattice fringes of $CuO/Ti_3C_2T_x$ taken in the contact area. It was observed that estimated lattice spacings of CuO nanoparticles and $Ti_3C_2T_x$ were 0.268 nm and 0.256 nm, which could be attributed to (110) plane of CuO and (110) plane of $Ti_3C_2T_x$, respectively. From the selected area diffraction pattern (SAED) around CuO and $Ti_3C_2T_x$ interface presented in **Fig. 5.3** (k), a typical hexagonal spot of $Ti_3C_2T_x$ with a diffuse diffraction ring originates from the polycrystalline feature of CuO nanoparticles could be confirmed.[39–41]

Here, we investigated the valid surface charge of CuO nanoparticles and $Ti_3C_2T_x$ by zeta potential measurement to reveal the cause of well-connection in CuO/ $Ti_3C_2T_x$. As depicted in **Fig. 5.4**, the zeta value of $Ti_3C_2T_x$ was -3.94 mV, showing a negative charge of the MXene surface caused by the –OH terminated group. In contrast, CuO surface has a positive charge with a zeta value of 20.8 mV. Ethanol solvent used in solvothermal treatment might still attach to the outer surface of CuO, contributing to its positive surface charge due to the proticity nature (hydrogen bond donor) of ethanol. The electrostatic force interaction was illustrated in **Fig. 5.3** (l). In short, the hybrid heterostructures containing CuO nanoparticles and 2D $Ti_3C_2T_x$ MXene were successfully prepared *via* electrostatic self-assembly at room temperature.
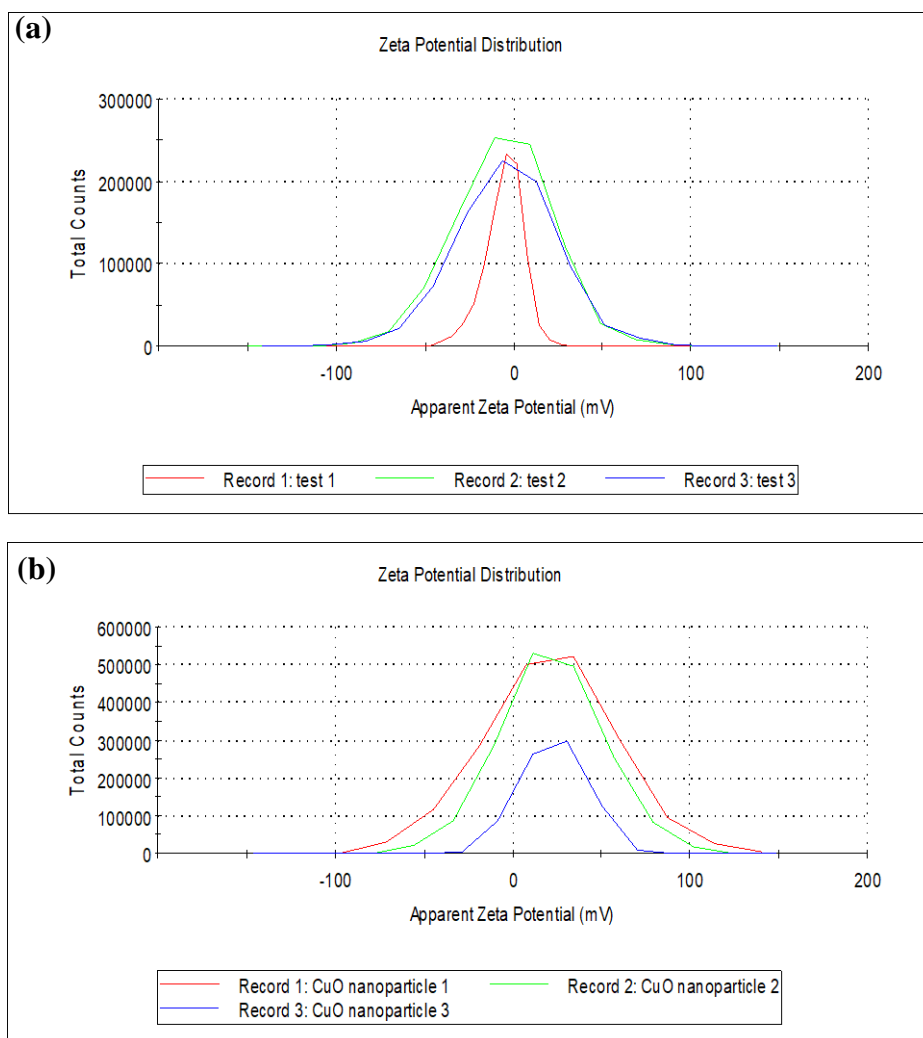

Fig. 5.4. Zeta potential of (a) $Ti_3C_2Ti_x$ MXene (-3.94 mV) and (b) CuO nanoparticles (20.8 mV)

The XPS measurement was performed to determine the chemical state and surface functionalization of CuO/Ti$_3$C$_2$T$_x$. The obtained spectrum of an individual element was analyzed by Gaussian fitting. The full scan spectra CuO/Ti$_3$C$_2$T$_x$ displayed in **Fig. 5.5** (a) confirmed the presence of the constituent element in CuO/Ti$_3$C$_2$T$_x$. **Fig. 5.5** (b) shows core level signals in the region of Ti 2p consisting doublet Ti 2p$_{1/2}$ (460.7 eV) and Ti 2p$_{3/2}$ (455.0 eV), which can be further fitted into 3 main components ; Ti–C (Ti$^+$) centered at 454.4 and 460.7 eV, Ti–X (Ti^{2+}) which generally substoichiometric titanium carbide or titanium oxycarbide located at 455.2 and 461.8 eV, and Ti$_x$O$_y$ (Ti^{3+}) culminated at 456.4 eV and 463.7 eV.[26–28,33–35,38] Another signal corresponded to TiO$_2$ (Ti^{4+}) located at 458.7 eV indicated that some samples might be slightly oxidized or might be caused direct bonding between Ti with O from CuO. The C 1s signals (**Fig. 5.5** (c)) were deconvoluted into four components located at 281.7, 284.5, 285.7 and 287.9 eV which could be assigned to Ti–C, C–C, C–O, and C=O bonding, respectively, demonstrating a typical carbon bonding in Ti$_3$C$_2$T$_x$.

For the Cu 2p core level signals, as shown in **Fig. 5.5** (d), the emerged doublet signals located at 933.2 and 953.5 eV were assigned to Cu 2p$_{3/2}$ and Cu 2p$_{3/2}$, respectively. The difference in the binding energy between the two signals was 20.2 eV. These results confirmed the presence of Cu with an oxidation state of 2+ in CuO/Ti$_3$C$_2$T$_x$ hybrid heterostructures. The satellite signals of Cu 2p$_{3/2}$ (942.1 eV) and Cu 2p$_{1/2}$ (953.5 eV) were observed because of 3d^9 filled partially 3d9 in Cu^{2+} state.[42] The core level of O 1s is shown in **Fig. 5.5** (e). Deconvolution result showed three signals at 529.4 eV assigned to metal–O bond, which most likely to be Cu–O, 531.0 eV attributed to C–O, and at 532.8 eV ascribed to –OH group. Thus, it might be a general indication that the surface terminated group (*T*) in Ti$_3$C$_2$T$_x$ was –OH, confirming the presence of the Ti$_3$C$_2$(OH)$_x$ phase. Another general –F surface terminated group was vanished (**Fig. 5.5** (f)), probably due to the dissolution process in ethanol solution (99.5%), which may contain some water molecules during the hybridization self-assembly process. It is in line with the previous study.[43] The overall results suggested that the hybrid heterostructure comprised of CuO and Ti$_3$C$_2$T$_x$ layer was formed, with a good distribution of CuO nanoparticles over the Ti$_3$C$_2$T$_x$ layer as confirmed by EDS mapping.
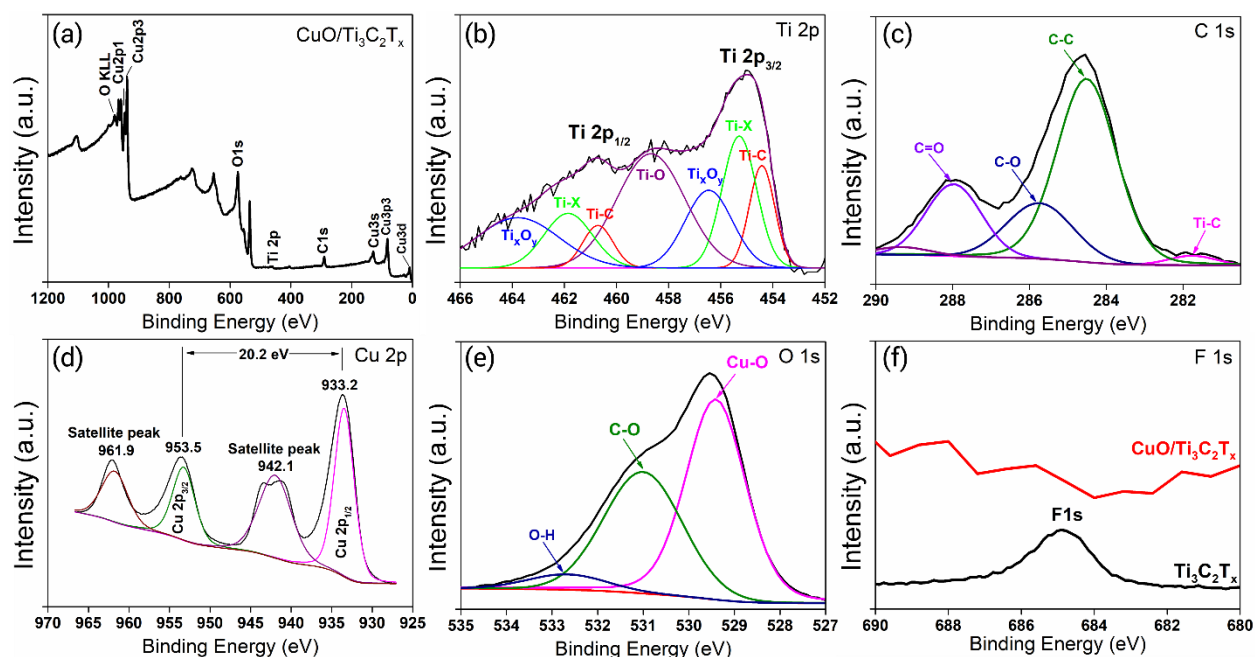
Fig. 5.5. XPS spectra of (a) Full survey, (b) Ti 2p core, (c) C 1s core, (d) Cu 2p core and (e) O 1s and (f) F 1s core of $CuO/Ti_3C_2T_x$. The comparison with pristine $Ti_3C_2T_x$ is only for F 1s.

To deeply understand the textural feature of the obtained samples, N_2 adsorption/desorption measurements were conducted. Additionally, their specific surface area was calculated based on the Brunauer-Emmett-Teller (BET) method. As shown in **Fig. 5.6** (a), pristine CuO nanoparticles exhibited a hysteresis curve at the relative pressure (P/P_o) of 0.4-0.9 which indicated porous property, while the pristine $T_3C_2T_x$ did not. The porosity of CuO nanoparticles should originate from interparticle voids. For $CuO/Tii_3C_2T_x$, the hysteresis feature was still observed, suggesting that the voids were present, and could be helpful for better gas diffusivity even after the attachment of CuO nanoparticle onto $T_3C_2T_x$. The specific surface area (BET) of CuO, $Ti_3C_2T_x$, and $CuO/Ti_3C_2T_x$ were 90, 25, and 43 m^2/g. In addition, the effect of the $Ti_3C_2T_x$ amount on the N_2 adsorption/desorption property, as well as on their specific surface area was further investigated. The variation amount of $Ti_3C_2T_x$ was predetermined to be 10, 20, 30, and 40 wt. %. As displayed in **Fig. 5.6** (b), the SSA was inversely proportional to the $Ti_3C_2T_x$ amount. For example, with addition 10 wt. % of $Ti_3C_2T_x$, the SSA slightly decreased from 90 m^2/g to 89 m^2/g.. As the $T_3C_2T_x$ increased to 40 wt. %, the SSA of the sample was severely decreased to only 29 wt. %, which was very close to the SSA of pristine $Ti_3C_2T_x$.
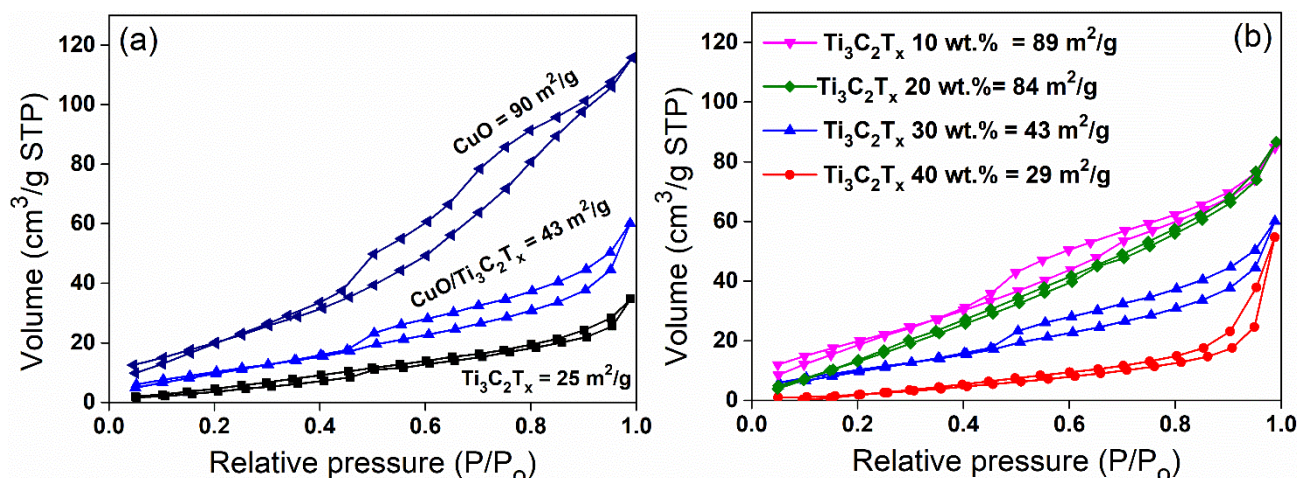
155

Fig. 5.6 N_2 adsorption/desorption of (a) CuO nanoparticles, $Ti_3C_2T_x$ and $CuO/Ti_3C_2T_x$, and (b) $CuO/Ti_3C_2T_x$ sample with different wt. % of $Ti_3C_2T_x$.

5.3.2 Gas sensing properties

Before gas sensing evaluation, the samples were characterized by TG/DTA to study their thermal stability, and the maximum working temperature for the sensing device was simultaneously determined. **Fig. 5.7** (a) and (b) shows the TG/DTA curves of pristine $Ti_3C_2T_x$ and $CuO/30$ wt.% $Ti_3C_2T_x$, respectively. From the TG/DTA curves, the pristine $Ti_3C_2T_x$ showed a slight loss (~3.2 wt.%) started at 125 °C and gained significant weight (~11 wt. %) at above 250 °C. The weight loss was caused by the evaporation of pre-adsorbed water molecules, especially on the interlaminated gap or surface terminated group of $Ti_3C_2T_x$ MXene itself. Then, at a temperature higher than 250 °C, TiO_2 formed due to high-temperature oxidation of $Ti_3C_2T_x$. Compared to $CuO/30$ wt.% $Ti_3C_2T_x$, significant thermal stability improvement could be observed above 250 °C. Namely, after combination with CuO nanoparticles, the $CuO/30$ wt.% $Ti_3C_2T_x$ sample exhibited relatively higher thermal oxidation stability indicated by insignificant weight gain. Therefore, attachment of CuO nanoparticles on the surface and interlayer space of $Ti_3C_2T_x$ MXene might prevent it from thermal oxidation, indicating its additional benefit for the practical use. From these results, we determined that the temperature range for gas sensing evaluation was 100 – 250 °C to prevent oxidation of the material.

The gas sensing evaluation was performed at a temperature range of 100 – 250 °C for pristine $Ti_3C_2T_x$ and $CuO/Ti_3C_2T_x$. For pristine CuO nanoparticle, the operating temperature was

156

set from 100 °C to 350 °C, based on our previous research. **Fig. 5.8** shows sensor response of CuO, $Ti_3C_2T_x$, and $CuO/Ti_3C_2T_x$ sample under the exposure of 50 ppm of toluene (C_7H_8) at different operating temperature. As mentioned earlier, sensor response (S) was defined as a ratio of resistance sensor in the air (R_a) and test gas (R_g). Notably, for p-type semiconductors, the sensor resistance would exhibit an increase upon the exposure of reducing gas,[35,] and S was calculated based on R_g/R_a formula.
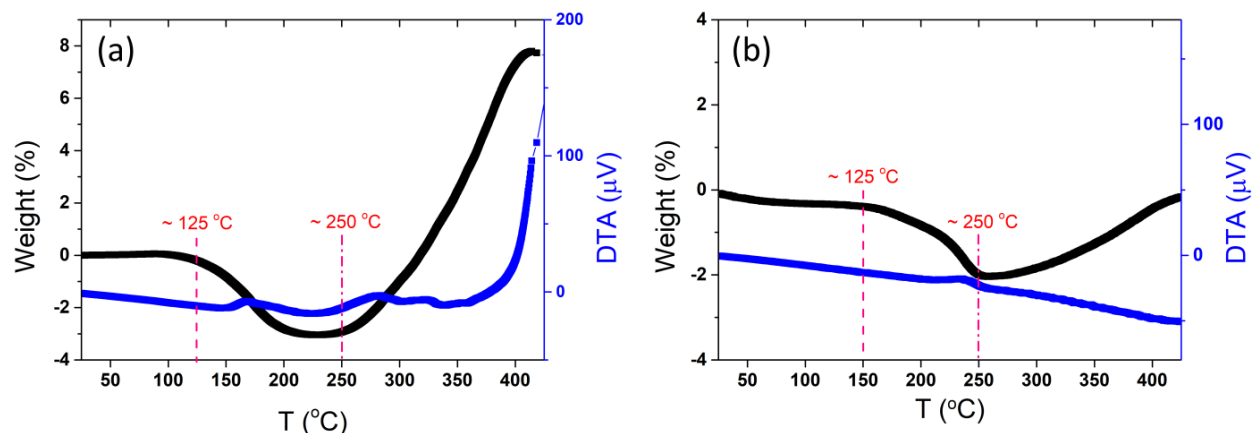

Fig. 5.7 TG/DTA of pristine (a) $Ti_3C_2T_x$ and (b) CuO/30 wt. %$Ti_3C_2T_x$.

As shown in **Fig. 5.8** (a), pristine $Ti_3C_2T_x$ had nearly no response to toluene gas at all tested temperatures agreed to reported literature.[31]. In contrast, toluene sensing response of CuO nanoparticles exhibited mountain-hill characteristic, in which its response increased from 1.12 to 4.8 with temperature elevating from 100 °C to 300 °C, respectively, and decreased gradually to 2.3 with a further increment of the temperature to 350 °C. The shown mountain-hill characteristic response of CuO nanoparticle could be explained by the gas adsorption-desorption phenomenon. At low working temperature, energy activation for the reaction of the tested gas molecules with adsorbed oxygen species barrier could not be achieved to exhibit low responsivity. As the working temperature went up, the reactivity between tested gas molecules and adsorbed oxygen species could be enhanced, resulting in a higher sensing response. However, when the working temperature was higher, the number of adsorption oxygen species were less dominant rather than the tested molecules to suppress the surface reaction, leading to decrease sensing response. On the other hand, the toluene sensing response of CuO nanoparticle was significantly increased by the combination with the $Ti_3C_2T_x$ phase. Even though the optimum working temperature was not

provided for CuO/Ti$_3$C$_2$T$_x$, its sensing response (11.4) at 250 °C exceeded response of CuO at 300 °C, indicating that the addition of Ti$_3$C$_2$T$_x$ led to not only a significant improvement of toluene sensing response but also a decrease in the working temperature.
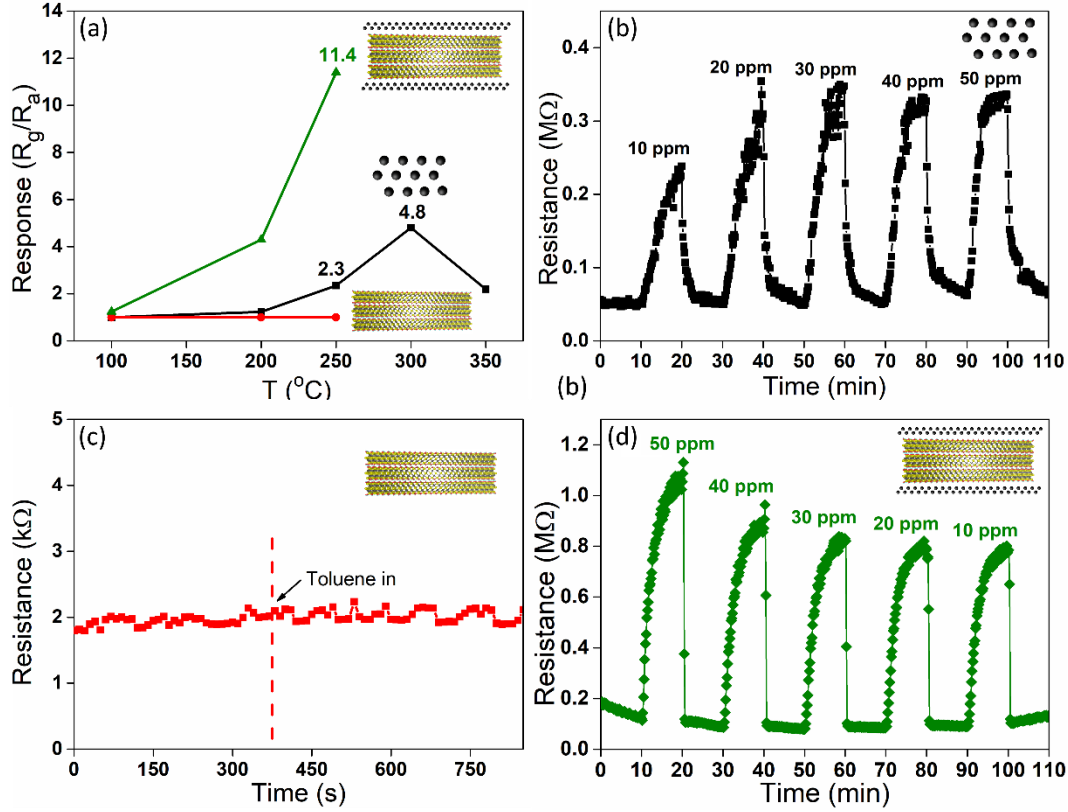

Fig. 5.8. Gas sensing response of CuO, T$_3$C$_2$T$_x$ MXene and CuO/T$_3$C$_2$T$_x$ MXene tested at (a) different working temperatures and (b-d) toluene concentrations.

Fig. 5.8 (b), (c) and (d) shows dynamic response-recovery curves of CuO nanoparticle, Ti$_3$C$_2$T$_x$, and CuO/Ti$_3$C$_2$T$_x$ samples at their optimum working temperature under exposure of different toluene concentration (10-50 ppm). For CuO nanoparticle and CuO/Ti$_3$C$_2$T$_x$, the resistance increased during the introduction of toluene gas, which was a typical behavior of p-type semiconductor sensing material, and the curves showed reproducible response during the evaluation with the exchange between air and toluene gas. Pristine Ti$_3$C$_2$T$_x$ showed negligible change on its resistance, suggesting that no adsorption-desorption reaction probably occurred on the surface of the Ti$_3$C$_2$T$_x$ phase. It could be observed that the base resistance of CuO nanoparticle and Ti$_3$C$_2$T$_x$ was approximately 50 kΩ and 2 kΩ, respectively. The combination of these materials

to form a hybrid heterostructure increased the resistance to nearly 138 kΩ. The increase of resistance in the air atmosphere might result from the change of electrical properties after combination.
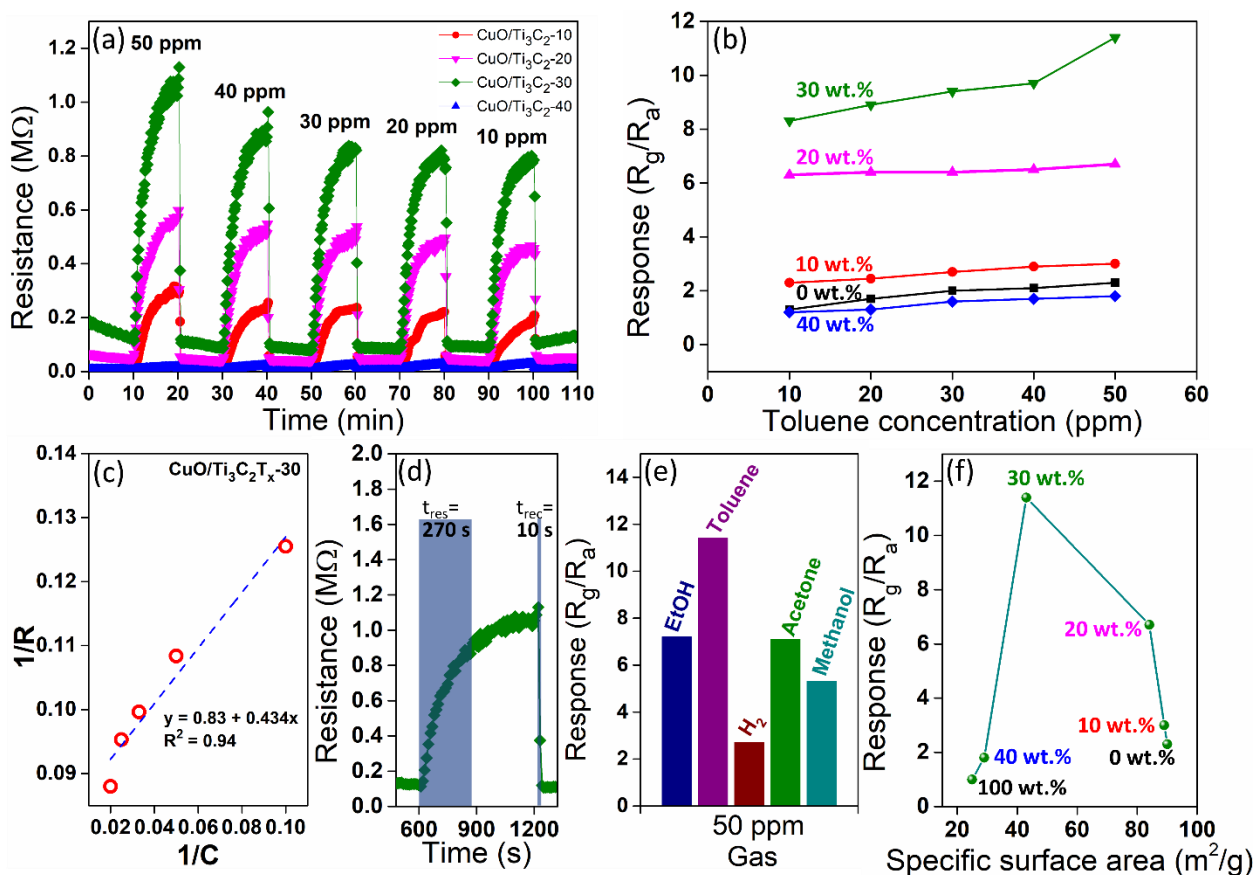
Fig. 5.8 (a) Transient response/recovery curves and (b) response values of CuO/Ti$_3$C$_2$T$_x$ with different Ti$_3$C$_2$T$_x$ amount; black, red, pink, green and blue colors represent 0, 10, 20, 30 and 40 wt. % of Ti$_3$C$_2$T$_x$, respectively; (c) linear fitting of R^{-1} *vs* C^{-1} based on the Langmuir isotherm model, (d) response/recovery times, and (e) selectivity of CuO/Ti$_3$C$_2$T$_x$-30 wt.% to 50 ppm of tested gas and (f) relationship of response value with specific surface area.

Furthermore, we tested the gas sensing performance of a series $CuO/Ti_3C_2T_x$ samples with a variation of $Ti_3C_2T_x$ MXene amount, i.e., 10, 20, 30, 40 wt. % denoted as $CuO/Ti_3C_2T_x$-10, $CuO/Ti_3C_2T_x$-20, $CuO/Ti_3C_2T_x$-30 and $CuO/Ti_3C_2T_x$-40, respectively. As shown in **Fig. 5.8** (a), regardless of the amount of $Ti_3C_2T_x$ loaded, the gas sensing response still exhibited p-type semiconductor behavior where the resistance increased upon the exposure of reducing gas, except that of $CuO/Ti_3C_2T_x$-40. Only $CuO/Ti_3C_2T_x$-40 exhibited no apparent response, and this should be mainly due to the excessive addition of $Ti_3C_2T_x$ has lowered the sensor resistance, which may not be advantageous for gas sensors. Comparing the responses in the various amount of $Ti_3C_2T_x$ (**Fig. 5.8** (b)), the higher amount of the added $Ti_3C_2T_x$ continuously increased the toluene sensing response. It reached to the maximum response value in the addition of 30 wt. % $Ti_3C_2T_x$. It is fundamentally important to estimate the detection limit of the sensor devices, which can be approached theoretically according to the earlier report.[44] Based on the given equation, the detection limit of the $CuO/Ti_3C_2T_x$-30 sample was estimated to be as low as 0.32 ppm.

The gas concentration-dependent response was approximated by the Langmuir isotherm equation, which primarily emphasizes the gas-solid adsorption.[45] **Fig. 5.8** (c) shows a linear fitting of R^{-1} versus C^{-1}, demonstrating the adsorption of toluene onto the $CuO/Ti_3C_2T_x$ surface follows the Langmuir isotherm model. From **Fig. 5.8** (d) and (e), it was clear that the $CuO/Ti_3C_2T_x$ had a good response time of 270 s and a rapid recovery time of 10 s to 50 ppm of toluene. It also showed adequate selectivity when it was exposed to different VOCs such as ethanol (C_2H_5OH), acetone (C_3H_6O), methanol (CH_3OH) and hydrogen gas with the same concentration as toluene. High responsivity and selectivity gas monitoring were indicated. **Fig. 5.8** (f) depicts the relationship of the specific surface area (SSA) of the samples with their sensing responses under 50 ppm of toluene. The addition of a higher amount of $Ti_3C_2T_x$ resulted in the lower SSA of $CuO/Ti_3C_2T_x$ samples. In many cases, higher SSA will lead to higher gas sensing performance due to more abundant of the active site for the gas adsorption/desorption process.[10–12,46,47] However, in our present work, the higher SSA did not enhance the toluene sensing responsivity. This result means that the effect of SSA, in this case, is insignificant for the enhanced sensing properties of $CuO/Ti_3C_2T_x$, and there are other factors responsible for the enhancement.

To scrutinize the excellent gas sensing properties of $Ti_3C_2T_x$ MXene hybridized with CuO nanoparticles, we compared the $CuO/Ti_3C_2T_x$ samples with other CuO/2D material combinations such as CuO/MoS_2 and CuO/rGO with a similar composition (30 wt.% of the 2D materials). The synthesis process, XRD patterns, SEM, TEM images, and Zeta potential of CuO/MoS_2 and CuO/rGO are shown in Supporting Information (**Fig. 5.9** and **Fig. 5.10**). The gas sensing temperature was determined based on TG-DTA measurement. From the transient response/recovery curves (**Fig. 5.11** (a-c)), CuO/MoS_2 transient response was similar to that of $CuO/Ti_3C_2T_x$. At the same time, CuO/rGO showed no response at all to 50 ppm of toluene in addition to the unstable base resistance. Also, the resistance in the air (R_a) of CuO/MoS_2 was slightly lower compared to that of $CuO/Ti_3C_2T_x$. The corresponding response value displayed in **Fig. 5.11** (d) revealed toluene sensing response of $CuO/Ti_3C_2T_x$ was higher than those of CuO/MoS_2 and CuO/rGO. **Fig. 5.11** (e) shows the response/recovery time and the response value of $CuO/Ti_3C_2T_x$ and CuO/MoS_2. The response time of $CuO/Ti_3C_2T_x$ was slightly faster than that of CuO/MoS_2, even though the recovery time was almost the same. The response value of $CuO/Ti_3C_2T_x$ was 1.3 times higher than that of CuO/MoS_2 and 9 times higher than that of CuO/rGO. The surface charge potential did not possess a meaningful influence for the better performance of $CuO/Ti_3C_2T_x$ over CuO/MoS_2 and CuO/rGO, because the zeta value of $Ti_3C_2T_x$ (-3.94 mV) was on between other 2D materials used for the hybrids (MoS_2: -32.7 mV, rGO: -1.24 mV). MoS_2 ideally has the strongest electrostatic interaction with CuO, and better sensing properties should be provided than in the case of $CuO/Ti_3C_2T_x$. However, the strongest interaction did not lead to better performance, meaning that another significant factor should be taken into consideration. Consequently, 2D $Ti_3C_2T_x$ MXene was suitable for hybridization with CuO nanoparticles compared with the other available 2D materials from the viewpoint of their gas sensing properties.
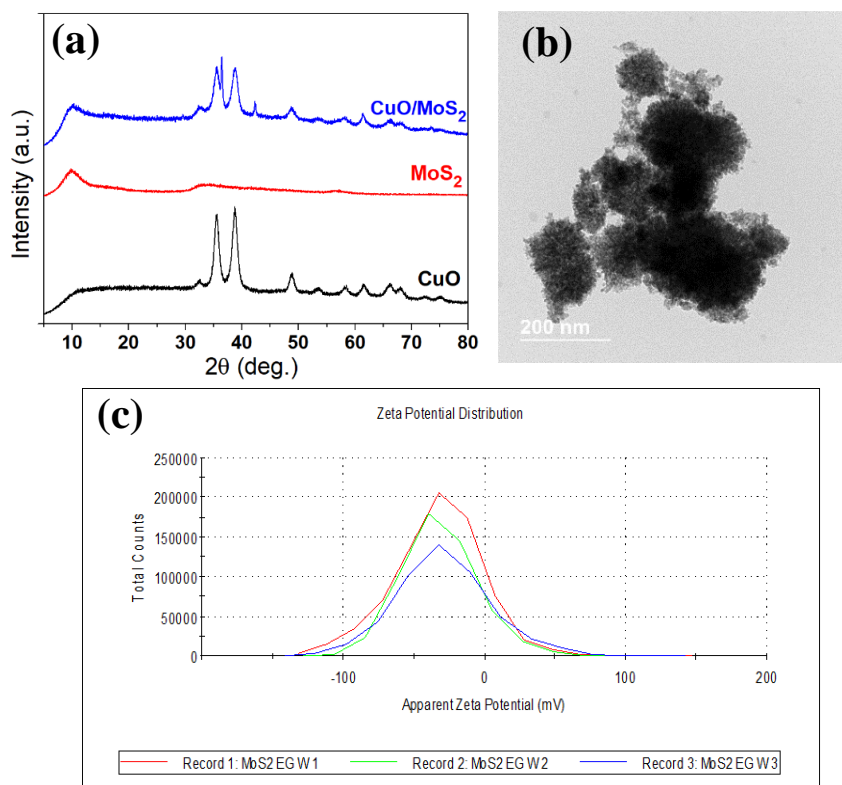
Fig. 5.9 (a) XRD patterns and (b) TEM images of CuO/MoS$_2$ and (c) Zeta potential of MoS$_2$ (-32.7 mV)
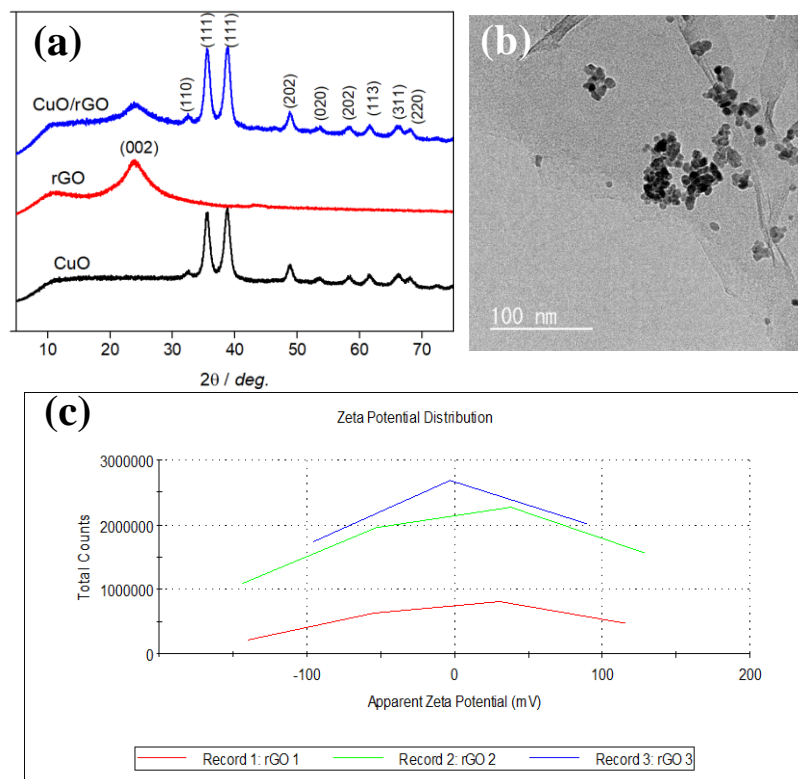

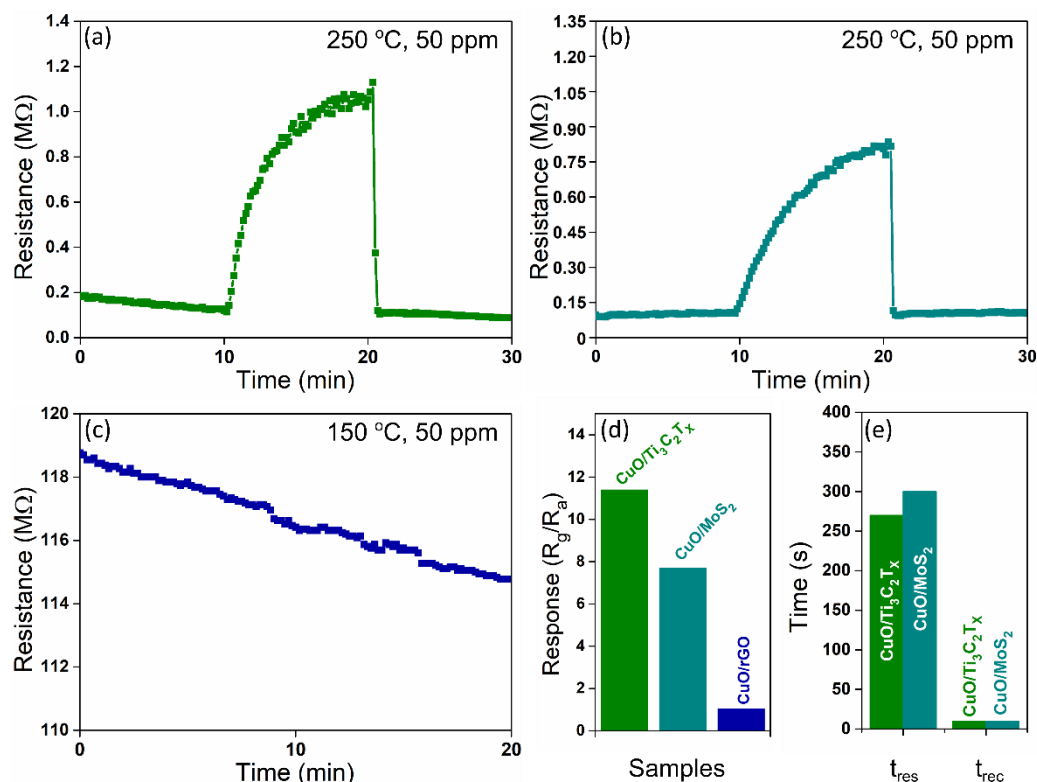**Fig. 5.10** (a) XRD patterns and (b) TEM images of CuO/rGO and (c) Zeta potential of rGO (-1.24 mV)

162

Fig. 5.11 Transient response/recovery curves of (a) CuO/Ti$_3$C$_2$T$_x$, (b) CuO/MoS$_2$, (c) CuO/rGO, (d) Corresponding response value and (e) response/recovery time of CuO/Ti$_3$C$_2$T$_x$ and CuO/MoS$_2$.

Gas sensor performance under high relative humidity was also examined to investigate the effect of humidity on gas sensing performance, which was an important point for practical application. **Fig. 5.12** indicates the response variation of the CuO/Ti$_3$C$_2$T$_x$-based sensor to 50 ppm of toluene at 250 $^{\circ}$C under different relative humidity (RH) ranges of 0-70 %. The response of CuO/Ti$_3$C$_2$T$_x$ to 50 ppm of toluene started to decrease with an increase of the relative humidity gradually. With 0 % RH, toluene response value was 11.4 (R$_g$/R$_a$). The increase of RH to 30 %, 50 %, and 70 % led to the response value to 7.8, 5.6, and 2.1, respectively, indicating that the relative humidity possessed a large influence on the CuO/Ti$_3$C$_2$T$_x$ sensor. These behaviors might be caused by competitive interaction between toluene gas and water molecules on the CuO and Ti$_3$C$_2$T$_x$ surfaces under high relative humidity to suppress the alteration of the resistance. Moreover, at high temperatures, this surface interaction might probably be higher than that at room temperature. We then remeasured the XRD of CuO/Ti$_3$C$_2$T$_x$-30 after the gas sensing evaluation, and as displayed in **Figure S8**, the appearing peaks are almost similar to that of the fresh sample.

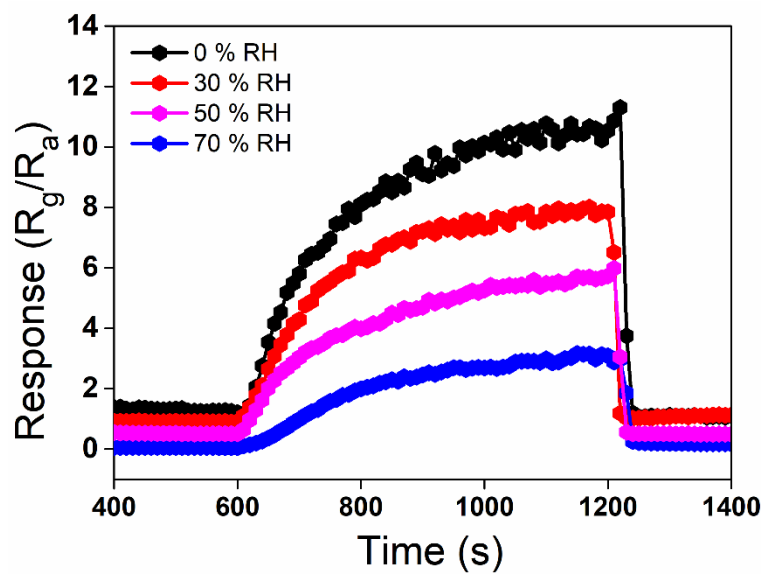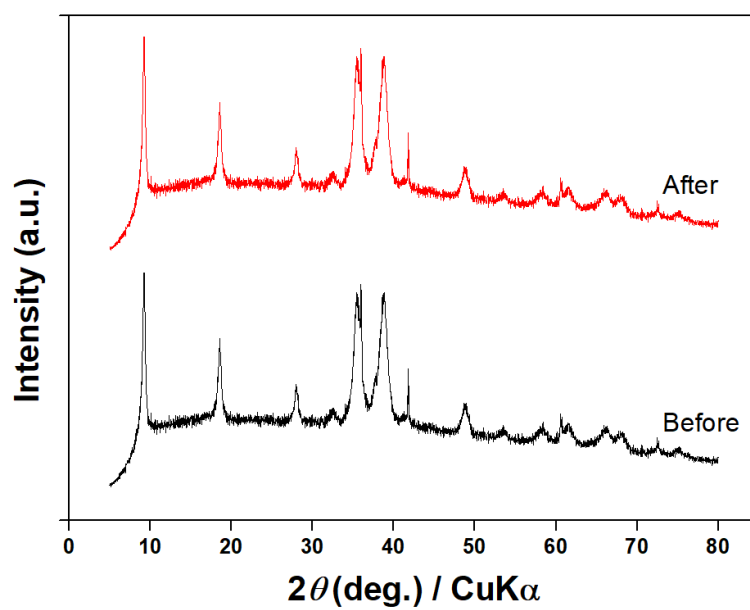**Fig. 5.12**. Influence of relative humidity on gas sensing properties of CuO/Ti$_3$C$_2$T$_x$

Fig. 5.13 XRD pattern of CuO/Ti$_3$C$_2$T$_x$-30 before and after gas sensing measurement.

The results of the present study are compared to similar works done previously. **Table 5.1** lists the metal oxide-based gas sensor for the detection of toluene. It is seen that $CuO/Ti_3C_2T_x$-based sensor exhibited a comparably high toluene sensing performance, especially for its selectivity, recovery times and low detection limit.

Table. 1 Toluene sensing comparison of metal-oxide based sensor

Material	T (°C)	Conc. (ppm)	Response (R_a/R_g or R_g/R_a)	Selectivity	Response/ recovery times (s)	Detection limit (ppm)	Ref.
Co_3O_4	180	200	8.5	N/A	10/30	N/A	[48]
$NiO-SnO_2$ composite	330	50	11	2.2 ($R_{toluene}/R_{ethanol}$)	11/4	N/A	[49]
In(III)-SnO_2 loaded g-C_3N_4	90	50	2.4	3.8 ($R_{toluene}/R_{butanol}$)	60/85	1	[50]
Hierarchical α-Fe_2O_3/NiO composites	300	100	18.68	1.86 ($R_{toluene}/R_{ethanol}$)	1/12	N/A	[51]
1D α-MoO_3/$Fe_2(MoO_4)_3$ composites	250	50	5.3	1.82 ($R_{toluene}/R_{xylene}$)	30/30	N/A	[52]
CoPP-Functionalized TiO_2 Nanoparticles	327	10	13.5	1.1 ($R_{toluene}/R_{p-xylene}$)	40/80	0.20	[53]
hexagonal WO_3 nanosheets	320	50	27.7	2.25 ($R_{toluene}/R_{benzene}$)	17/14	N/A	[54]
$CuO/Ti_3C_2T_x$ MXene	250	50	11.4	1.64 ($R_{toluene}/R_{ethanol}$)	270/10	0.32	This work
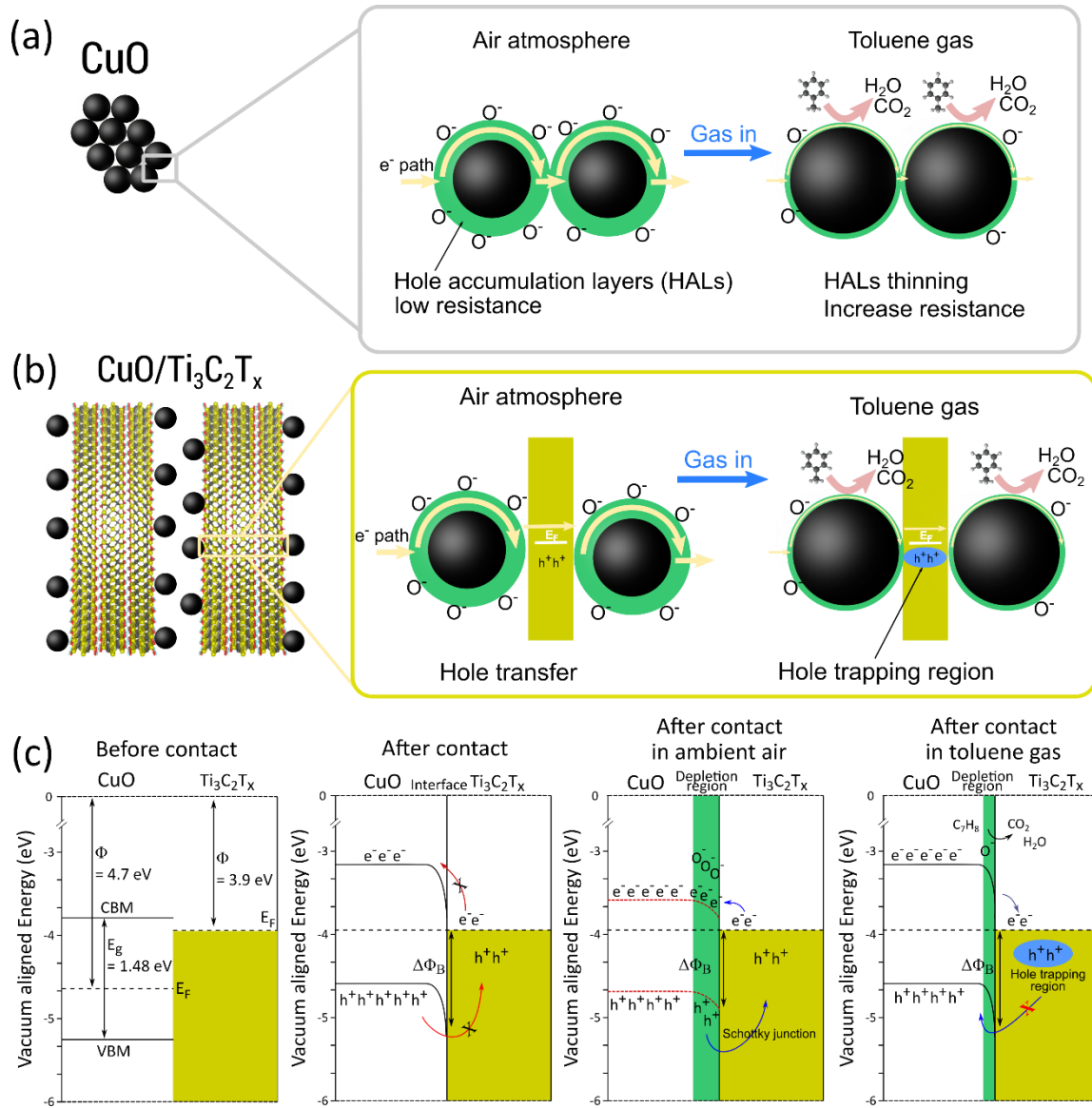
Fig. 5.14 Gas sensing mechanism of (a) pristine CuO nanoparticles and (b) CuO nanoparticles/$Ti_3C_2T_x$ MXene hybrid heterostructures. (c) Band structures alignment of CuO/$Ti_3C_2T_x$ before contact, after contact, in ambient air and in toluene gas.

5.3.3 Gas sensing mechanism

According to the above gas sensing results, we comprehensively propose a novel approach for the gas sensing mechanism of pristine CuO and CuO/ $Ti_3C_2T_x$ MXene composite. It is well accepted that CuO is p-type gas sensing semiconductor materials in which holes play as a significant charge carrier. At the temperature range of 100-500 ^{o}C in air atmosphere, oxygen

molecules in the air are adsorbed onto metal oxide semiconductors and ionized into O_2^-, O^-, and O^{2-} by catching the electrons near the surface.[55]

The O^- species is dominant in the temperature range of 150 to 400 °C.[56] Based on these facts, O^- species is likely adsorbed onto CuO nanoparticles and can lead to the formation of core-shell electronic configuration depletion layers composed of the Hole Accumulation Layers (HALs) near the surface and the insulating core region. They should possess low and high resistivity, respectively, as shown in **Fig. 5.14** (a). Because of its low resistivity, the electron can easily flow from one CuO nanoparticles to another through this conductive shell layers to exhibit a low resistance under ambient atmosphere. The established core-shell configuration in CuO nanoparticles should be destroyed upon the exposure of testing gas, because the adsorbed O^- species will actively react with the toluene gas, releasing electrons back to the insulating core with the production of CO_2 and water as a byproduct.[57] As a result, HALs conducting channel can be thinned to compress electron mobility. Consequently, the material resistivity should be increased. During the ejection of gas and injection of air, the core-shell configuration can be re-established. The gas sensing mechanism of the pristine CuO should differ after the hybridization with $Ti_3C_2T_x$ MXene. As represented in SEM and HRTEM images (**Fig. 5.4** (c), (i)−(j)), CuO nanoparticles are contacted intimately at interlamination surface of $Ti_3C_2T_x$ MXene, and as confirmed in XRD and XPS, $Ti_3C_2T_x$ exhibited more –OH terminated group which is considered as a metallic phase rather than a semiconductor because of its high carrier mobility.[25]

Fig. 5.14 (b)-(c) shows a simplified illustration of the gas sensing mechanism of $CuO/Ti_3C_2T_x$ hybrid heterostructures. From the standpoint of work function (Φ) reported by previous works, the –OH terminated $Ti_3C_2T_x$ MXene has shown a work function ca. 3.9 eV[58] which is lower than that of CuO (~4.7 eV)[59], establishing a Schottky barrier at their interfaces upon the contact to equalize the Fermi energy level. Our CuO sample has a bandgap estimation of 1.48 eV (**Fig. 5.15**), while the conduction band (CB) and valence band (VB) of CuO have been adopted from Diao and co-workers.[60]   The charge transfer should equally occur from metal to semiconductor through the interface and *vice versa*. Nevertheless, due to the barrier height, $\Delta\Phi_B$, the charge mobility is hindered, resulting in a very high resistivity of $CuO/Ti_3C_2T_x$ at room temperature.

Similar to that of pristine CuO nanoparticles, during the heating process at ambient air condition, the adsorption of O^- species create core-shell electronic configuration within CuO nanoparticles in CuO/Ti$_3$C$_2$T$_x$ MXene sample. The O^- ion sorption is lowering the band bending at the interface, allowing the better charge transfer between the two components. As a result, the sensor device becomes more conductive as operating temperature increases. Still, due to the Schottky barrier height, the charge mobility in CuO/Ti$_3$C$_2$T$_x$ heterostructure is more miserable than that in the homojunction of pristine CuO. This approach can explain why the CuO/Ti$_3$C$_2$T$_x$ possessed a slightly higher R$_a$ than CuO despite the superior electrical conductivity of Ti$_3$C$_2$T$_x$. Also, because of this charge carrier migration, much more O^- are adsorbed. When toluene gas is flown, it removes O^- species from the CuO surface, resulting in a thinner depletion region (HALs) and an increase of sensor resistance. The removal of O^- also induces the band bends upward, restores the Schottky barrier height ($\Delta\Phi_B$). Consequently, some of the holes are trapped in Ti$_3$C$_2$T$_x$, called hole trapping region (HTR). The concept of Schottky junction hole trapping phenomena has been previously reported for the Ti$_3$C$_2$T$_x$ MXene/metal oxide hybrid structures.[27,61–64]
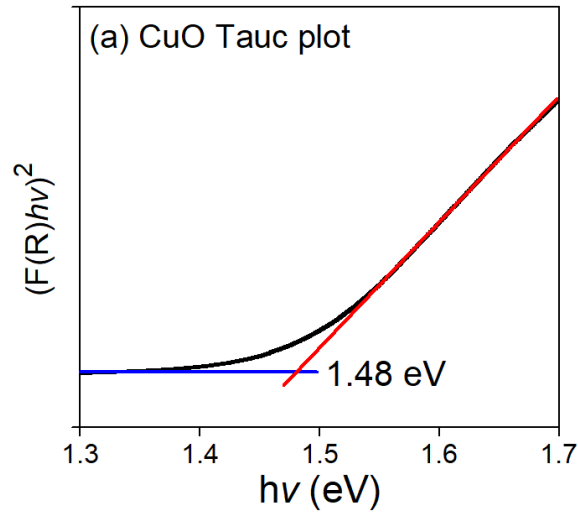
Fig. 5.15 Tauc plot of CuO/Ti$_3$C$_2$T$_x$ derived from UV-Vis DRS spectra

The hole trapping process may also exist in CuO/MoS$_2$ but not in CuO/rGO samples due to the work function of CuO is higher than that of MoS$_2$ (4.4 eV) but lower than that of rGO (4.8 eV).[65,66] Therefore, we can observe the response of CuO/MoS$_2$ is higher than that of CuO/rGO. Due to the rGO work function, contact between CuO and rGO may likely establish ohmic junction rather than Schottky junction results in a high conductivity, as observed in **Fig. 5.11** (c). We also believe that in the excess amount of Ti$_3$C$_2$T$_x$, the Schottky junction is destroyed, and the metallic

property of $Ti_3C_2T_x$ will play a significant role in the gas sensing performance. Additionally, the $Ti_3C_2T_x$ may play a supporting role as a conductive layer for the faster charge carrier mobility from CuO nanoparticles in one side to another side, which contributes a quick response and recovery speed agree to the experimental results. In summary, work function modulation is a crucial factor for designing high-performance gas sensing material based on metal oxides hybrid with metal oxides nanostructures.

5.4. Conclusions

The CuO nanoparticles/ $Ti_3C_2T_x$ MXene have been successfully prepared by a room temperature electrostatic self-assembly approach. The CuO nanoparticles with an average particle size of 7 nm were uniformly attached to $Ti_3C_2T_x$ and inserted into its interlaminations gap with a plausible interface contact. The positive surface charge of CuO and the negatively charged $Ti_3C_2T_x$ from –OH terminated group contributed to the interface contact through the electrostatic assembly. $Ti_3C_2T_x$ acted as conductive layers for charge carrier transport and hole trapping region (HTR) during the exposure to testing gas due to work function difference. The CuO nanoparticles/ $Ti_3C_2T_x$ MXene hybrid heterostructures exhibited good gas sensing value (R_g/R_a) of 11.4 and comparable response/recovery speed of 270 s/10 s under 50 ppm of toluene, exceeding the amount of pristine CuO nanoparticles and $Ti_3C_2T_x$. The gas performance of CuO nanoparticles/ $Ti_3C_2T_x$ MXene was superior compared to other CuO/2D materials such as CuO/MoS_2 and CuO/rGO. However, the response of CuO nanoparticles/ $Ti_3C_2T_x$ MXene was decreased by high relative humidity (up to 70%), which might be an improvement point for future research. These results indicate the potential application of CuO nanoparticles/ $Ti_3C_2T_x$ MXene for highly responsive VOC sensors, especially for toluene gas. Moreover, the electronic self-assembly and work function matching strategy, presented in this work, maybe also extended for other metal oxides/2D MXene hybrid heterostructures and related applications.

5.5 References

1   A. Esplugues, F. Ballester, M. Estarlich, S. Llop, V. Fuentes-Leonarte, E. Mantilla and C. Iñiguez, *Sci. Total Environ.*, 2010, **409**, 63–69.

2   E. Cetin, M. Odabasi and R. Seyfioglu, 2003, **312**, 103–112.

3   T. Ohura, T. Amagai, X. Shen, S. Li, P. Zhang and L. Zhu, *Atmos. Environ.*, 2009, **43**, 6352–6359.

4   J. E. Colman Lerner, E. Y. Sanchez, J. E. Sambeth and A. A. Porta, *Atmos. Environ.*, 2012, **55**, 440–447.

5   T. Yang, P. Zhang, B. Xu and J. Xiong, *Int. J. Heat Mass Transf.*, 2017, **110**, 671–679.

6   W. P. L. Carter, *J. Air Waste Manag. Assoc.*, 1994, **44**, 881–899.

7   J. N. Cape, *Environ. Pollut.*, 2003, **122**, 145–157.

8   D. R. Brower, *J. Am. Med. Assoc.*, 1886, **VI**, 59–62.

9   I. Kheirbek, S. Johnson, Z. Ross, G. Pezeshki, K. Ito, H. Eisl and T. Matte, *Environ. Heal. A Glob. Access Sci. Source*, 2012, **11**, 1.

10   A. Dey, *Mater. Sci. Eng. B Solid-State Mater. Adv. Technol.*, 2018, **229**, 206–217.

11   N. Barsan, D. Koziej and U. Weimar, *Sensors Actuators, B Chem.*, 2007, **121**, 18–35.

12   K. Wetchakun, T. Samerjai, N. Tamaekong, C. Liewhiran, C. Siriwong, V. Kruefu, A. Wisitsoraat, A. Tuantranont and S. Phanichphant, *Sensors Actuators, B Chem.*, 2011, **160**, 580–591.

13   C. Wang, L. Yin, L. Zhang, D. Xiang and R. Gao, *Sensors*, 2010, **10**, 2088–2106.

14   D. Gopalakrishna, K. Vijayalakshmi and C. Ravidhas, *J. Mater. Sci. Mater. Electron.*, 2013, **24**, 1004–1011.

15   X. Liu, J. Zhang, Y. Kang, S. Wu and S. Wang, *CrystEngComm*, 2012, **14**, 620–625.

16   F. Zhang, A. Zhu, Y. Luo, Y. Tian, J. Yang and Y. Qin, *J. Phys. Chem. C*, 2010, **114**, 19214–19219.

17   M. He, L. Xie, X. Zhao, X. Hu, S. Li and Z. G. Zhu, *J. Alloys Compd.*, 2019, **788**, 36–43.

18   M. Mashock, K. Yu, S. Cui, S. Mao, G. Lu and J. Chen, *ACS Appl. Mater. Interfaces*, 2012, **4**, 4192–4199.

19   F. Ren, L. Gao, Y. Yuan, Y. Zhang, A. Alqrni, O. M. Al-Dossary and J. Xu, *Sensors Actuators, B Chem.*, 2016, **223**, 914–920.

20   S. W. Choi, A. Katoch, J. H. Kim and S. S. Kim, *ACS Appl. Mater. Interfaces*, 2015, **7**, 647–652.

21   W. Guo, B. Zhao, Q. Zhou, Y. He, Z. Wang and N. Radacsi, *ACS Omega*, 2019, **4**, 10252–10262.

22   B. Sakthivel and G. Nammalvar, *J. Alloys Compd.*, 2019, **788**, 422–428.

23   V. Galstyan, E. Comini, I. Kholmanov, G. Faglia and G. Sberveglieri, *RSC Adv.*, 2016, **6**,

34225–34232.

24   J. Zhu, E. Ha, G. Zhao, Y. Zhou, D. Huang, G. Yue, L. Hu, N. Sun, Y. Wang, L. Y. S. Lee, C. Xu, K. Y. Wong, D. Astruc and P. Zhao, *Coord. Chem. Rev.*, 2017, **352**, 306–327.

25   M. Naguib, M. Kurtoglu, V. Presser, J. Lu, J. Niu, M. Heon, L. Hultman, Y. Gogotsi and M. W. Barsoum, *Adv. Mater.*, 2011, **23**, 4248–4253.

26   Q. Tang, Z. Zhou and P. Shen, *J. Am. Chem. Soc.*, 2012, **134**, 16909–16916.

27   C. Peng, X. Yang, Y. Li, H. Yu, H. Wang and F. Peng, *ACS Appl. Mater. Interfaces*, 2016, **8**, 6051–6060.

28   M. Han, X. Yin, H. Wu, Z. Hou, C. Song, X. Li, L. Zhang and L. Cheng, *ACS Appl. Mater. Interfaces*, 2016, **8**, 21011–21019.

29   S. J. Kim, H. J. Koh, C. E. Ren, O. Kwon, K. Maleski, S. Y. Cho, B. Anasori, C. K. Kim, Y. K. Choi, J. Kim, Y. Gogotsi and H. T. Jung, *ACS Nano*, 2018, **12**, 986–993.

30   W. Yuan, K. Yang, H. Peng, F. Li and F. Yin, *J. Mater. Chem. A*, 2018, **6**, 18116–18124.

31   P. K. Kalambate, S. W. Zote, Y. Shen, D. N. Navale, D. K. Kulal, J. Wu, P. B. Ranade, R. Pothu, R. Boddula and Y. Huang, in *MXenes: Fundamentals and Applications*, Materials Research Foundations, 2019, pp. 204–215.

32   Z. shan Hong, Y. Cao and J. fa Deng, *Mater. Lett.*, 2002, **52**, 34–38.

33   F. Wang, C. H. Yang, C. Y. Duan, D. Xiao, Y. Tang and J. F. Zhu, *J. Electrochem. Soc.*, 2015, **162**, B16–B21.

34   B. Zhang, J. Zhu, P. Shi, W. Wu and F. Wang, *Ceram. Int.*, 2019, **45**, 8395–8405.

35   X. Li, J. Zhu, Y. Fang, W. Lv, F. Wang, Y. Liu and H. Liu, *J. Electroanal. Chem.*, 2018, **817**, 1–8.

36   M. Ghidiu, M. R. Lukatskaya, M. Zhao, Y. Gogotsi and M. W. Barsoum, *Nature*, 2014, **516**, 78–81.

37   C. Peng, H. Wang, H. Yu and F. Peng, *Mater. Res. Bull.*, 2017, **89**, 16–25.

38   B. Anasori, M. R. Lukatskaya and Y. Gogotsi, *Nat. Rev. Mater.*, 2017.

39   O. Mashtalir, M. Naguib, V. N. Mochalin, Y. Dall'Agnese, M. Heon, M. W. Barsoum and Y. Gogotsi, *Nat. Commun.*, 2013, **4**, 1–7.

40   R. Li, L. Zhang, L. Shi and P. Wang, *ACS Nano*, 2017, **11**, 3752–3759.

41   B. Dai, B. Zhao, X. Xie, T. Su, B. Fan, R. Zhang and R. Yang, *J. Mater. Chem. C*, 2018, **6**, 5690–5697.

42   S. Poulston, P. M. Parlett, P. Stone and M. Bowker, *Surf. Interface Anal.*, 1996, **24**, 811–820.

43   X. Guo, X. Xie, S. Choi, Y. Zhao, H. Liu, C. Wang, S. Chang and G. Wang, *J. Mater. Chem. A*, 2017, **5**, 12445–12452.

44   J. Li, Y. Lu, Q. Ye, M. Cinke, J. Han and M. Meyyappan, *Nano Lett.*, 2003, **3**, 929–933.

45   Y. Xia, J. Wang, L. Xu, X. Li and S. Huang, *Sensors Actuators, B Chem.*, 2020, **304**, 127334.

46   T. Wagner, S. Haffer, C. Weinberger, D. Klaus and M. Tiemann, *Chem. Soc. Rev.*, 2013, **42**, 4036–4053.

47   S. Das and V. Jayaraman, *Prog. Mater. Sci.*, 2014, **66**, 112–255.

48   R. Zhang, S. Gao, T. Zhou, J. Tu and T. Zhang, *Appl. Surf. Sci.*, 2020, **503**, 144167.

49   L. Liu, Y. Zhang, G. Wang, S. Li, L. Wang, Y. Han, X. Jiang and A. Wei, *Sensors Actuators, B Chem.*, 2011, **160**, 448–454.

50   R. Malik, V. K. Tomer, V. Chaudhary, M. S. Dahiya, S. P. Nehra, S. Duhan and K. Kailasam, *Sensors Actuators, B Chem.*, 2018, **255**, 3564–3575.

51   C. Wang, X. Cheng, X. Zhou, P. Sun, X. Hu, K. Shimanoe, G. Lu and N. Yamazoe, *ACS Appl. Mater. Interfaces*, 2014, **6**, 12031–12037.

52   J. Li, L. Wang, H. Liu, J. Zhao, X. Li, H. Wei and Y. Han, *J. Alloys Compd.*, 2017, **694**, 939–945.

53   Y. Kang, K. Kim, B. Cho, Y. Kwak and J. Kim, *ACS Sensors*, 2020, **5**, 754–763.

54   D. Zhang, Y. Fan, G. Li, Z. Ma, X. Wang, Z. Cheng and J. Xu, *Sensors Actuators, B Chem.*, 2019, **293**, 23–30.

55   H. J. Kim and J. H. Lee, *Sensors Actuators, B Chem.*, 2014, **192**, 607–627.

56   N. Barsan and U. Weimar, *J. Electroceramics*, 2001, **7**, 143–167.

57   A. Mirzaei, J.-H. Kim, H. W. Kim and S. S. Kim, *J. Mater. Chem. C*, 2018, **6**, 4342–4370.

58   T. Schultz, N. C. Frey, K. Hantanasirisakul, S. Park, S. J. May, V. B. Shenoy, Y. Gogotsi and N. Koch, *Chem. Mater.*, 2019, **31**, 6590–6597.

59   J. Morasch, H. F. Wardenga, W. Jaegermann and A. Klein, *Phys. Status Solidi Appl. Mater. Sci.*, 2016, **213**, 1615–1624.

60   F. Diao, F. Tian, W. Liang, H. Feng and Y. Wang, *Phys. Chem. Chem. Phys.*, 2016, **18**, 27967–27975.

61   T. Chen, G. Tong, E. Xu, H. Li, P. Li, Z. Zhu, J. Tang, Y. Qi and Y. Jiang, *J. Mater. Chem. A*, 2019, **7**, 20597–20603.

62   C. Hou, H. Yu and C. Huang, *J. Mater. Chem. C*, 2019, **7**, 11549–11558.

63   Y. Sun, X. Meng, Y. Dall'Agnese, C. Dall'Agnese, S. Duan, Y. Gao, G. Chen and X. F. Wang, *Nano-Micro Lett.*, 2019, **11**, 1–22.

64   G. Huang, S. Li, L. Liu, L. Zhu and Q. Wang, *Appl. Surf. Sci.*, 2020, **503**, 1–8.

65   S. Y. Lee, U. J. Kim, J. Chung, H. Nam, H. Y. Jeong, G. H. Han, H. Kim, H. M. Oh, H. Lee, H. Kim, Y. G. Roh, J. Kim, S. W. Hwang, Y. Park and Y. H. Lee, *ACS Nano*, 2016, **10**, 6100–6107.

66   G. H. Jun, S. H. Jin, B. Lee, B. H. Kim, W. S. Chae, S. H. Hong and S. Jeon, *Energy Environ. Sci.*, 2013, **6**, 3000–3006.

Chapter 6

Summary and Outlook

This thesis focused on the synthesis of metal oxide nanostructures with morphological and surface charge controllability by solvothermal nonaqueous approach under variety of organic solvents. Their hybridization was attempted by a facile electrostatic self-assembly at room temperature, harnessing their opposite surface charge. The thesis is presented in six chapters with three experimental chapters.

Chapter 1 presented general environmental air pollution problems and the potentiality of metal oxides to detect them in an excellent manner. The challenge and opportunity of metal oxide as gas sensing materials are introduced together with some versatile strategies to improve their performances. The synthetic processes of metal oxide nanostructures, in general, are compared to emphasize the reason for the synthetic choice of metal oxide nanostructures in the presented thesis. The thesis objectives were also clearly stated in a chronological manner.

Chapter 2 introduced universal experimental procedures include chemical reagent, characterization equipment, gas sensing device fabrication and measurement system as well as density functional theory (DFT) *ab initio* calculation parameters.

Chapter 3 Demonstrated a facile solvothermal synthesis in an ethanol/acetic acid mixture for the fabrication of SnO_2 with a controllable hierarchical spherical size and micro-/mesoporosity. SEM, TEM and N_2 adsorption/desorption investigation unveiled that the obtained SnO_2 spheres exhibited a particle size in the range of $0.6 - 1.6$ μm and a pore size of about $1.4-1.9$ nm depending on the volume ratio of acetic acid to ethanol in the reaction mixture, and the spheres were constructed by nanoscale particles. The gas sensing property of SnO_2_10 without an additional noble metal co-catalyst exhibited a large toluene sensing response (R_a/R_g) of 20.2 at 400 °C, which was about 6 times higher and acceptable selectivity compared to those of other samples. The study found that the sensing performance in the SnO_2 hierarchical spheres was influenced by several factors *e.g.* particle morphology, pore size and specific surface area rather than only a single parameter. Therefore, a precise control of those influencing parameters may lead to the optimum sensing property. This chapter introduced the facet design in metal oxide semiconductors which is an efficient approach to boost their gas sensing performances due to desirable active sites. We

demonstrate the synthesis of NiO with a dominantly (111) facet from the transformation of NiOHCl with a layered structure. Among other crystal facets, NiO-Octa (111) exhibited the best NO_x gas sensing response (16.5 %) to 300 ppb level. The DFT calculation revealed that the abundance of Ni atoms in the clean (111) surface layer allows the favorable adsorption of N adatoms, forming the Ni-N bond. The charge transfer took place from NiO to NO orbital has proven to be a cause of bond weakening and stretching from 1.1692 Å to 1.2231 Å, leading to NO_x molecular decomposition, consistent with the experimental results.

Chapter 4 reported a facile preparation of a uniform decoration of spherical n-type SnO_2 by p-type CuO nanoparticles as well as their utilization for enhanced performance on toluene gas detection. CuO nanoparticles and spherical SnO_2 were synthesized by a facile non-hydrolytic solvothermal reaction, which can easily control their morphology. A uniform CuO nanoparticles decoration onto spherical SnO_2 was achieved by a simple sonication and vigorous stirring at room temperature. We revealed organic solvents used in the oxide synthesis have a considerable influence on its surface charge that is beneficial for a uniformly electrostatic self-decoration between positively charged p-type CuO nanoparticles and negatively charged n-type spherical SnO_2. Interestingly, CuO was partially reduced to Cu metal during high concentration of toluene exposure destroying p-n contact and developing new metal-semiconductor contact so-called ohmic junction, resulting in extraordinarily responsive and selective to toluene gas at 400 °C as compared to a single p- CuO and n- SnO_2. It was also found that the amount of particle decoration had an influence on sensor response and resistance. The optimum amount of CuO nanoparticle decoration was 0.1 mmol. The response ($S=R_a/R_g$) and selectivity of CuO/SnO_2 based material toward the exposure of 75 ppm toluene has reached as high as 540 and 5, respectively. The effect of p-n heterojunction and metal-semiconductor contact on the gas sensing mechanism of p-type CuO/n-type SnO_2 was discussed. Furthermore, by decorating with CuO nanoparticles, CuO/SnO_2 morphology was well-maintained after gas sensing evaluation demonstrated its excellency for high temperature toluene gas sensor application.

Chapter 5 Described in detail regarding a facile preparation of CuO/ $Ti_3C_2T_x$ MXene hybrids *via* electrostatic self-assembly. The CuO nanoparticles (~7 nm) were uniformly dispersed on the surface and the interlayers of the $Ti_3C_2T_x$ MXene, forming hybrid heterostructures. The $CuO/Ti_3C_2T_x$ MXene exhibited the improved toluene gas sensing response (R_g/R_a) of 11.4, which

is nearly 5 times higher than that of the pristine CuO nanoparticles (2.3) to 50 ppm of toluene at 250 °C. Due to the different work function (Φ), the Schottky junction was established at the interface of CuO/Ti$_3$C$_2$T$_x$ MXene, acting as hole trapping region (HTR) at Ti$_3$C$_2$T$_x$ MXene side. Compared to other hybrid 2D materials such as MoS$_2$ and rGO, which have possessed a higher work function, the CuO/Ti$_3$C$_2$T$_x$ MXene maintained better toluene sensing performance. Thus, the work function is critical for designing a high sensing performance of hybrid metal oxides/2D materials. The hybridization of CuO with Ti$_3$C$_2$T$_x$ MXene improved not only enhancement of the response time but also the selectivity and the responses (270 s) and recovery times (10 s) compared with those of CuO, due to high conductivity of metallic phase in Ti$_3$C$_2$T$_x$ MXene. Such excellent performance showed the promising applications of metal oxides/2D hybrid materials for VOCs gas sensing.

To summarize, three points below are the main conclusion of the presented thesis:

1. The mixed solvents have a profound influence on surface charge and morphological feature on metal oxides

2. The opposed surface charges of metal oxides or 2D materials are beneficial for the wide particle distribution and intimate contact due to electrostatic self-assembly

3. Gas sensing properties of metal oxide can be enhanced by several simple approaches such as morphological and facet surface design, porosity, p-n heterojunction, and Schottky Junction

Although the surface charge of metal oxides can be tuned by organic molecular functionalization, its solely effect on gas sensing properties have been not well-understood. To prevent organic molecules evaporation, the metal oxides sensing material that can be operated at room temperature should be used to understand their influence. Last, the metal oxides/hybrid should be incorporated into the integrated gas sensor devices to investigate the performance in a real environmental exposure.

Publications

1. **A. Hermawan**, H.W. Son, Y. Asakura, T. Mori, and S.Yin. Synthesis of morphology controllable aluminum nitride by direct nitridation of γ-AlOOH in the presence of N_2H_4 and their sintering behavior. *J. Asian Ceram. Soc.*, 2018, **6**, 63-69. https://doi.org/10.1080/21870764.2018.1439611

2. **A. Hermawan**, Y. Asakura, M. Kobayashi, M. Kakihana and S.Yin. High temperature hydrogen gas sensing property of GaN prepared from α-GaOOH. *Sensors Actuators, B Chem.*, 2018, **276**, 388–396. https://doi.org/10.1016/j.snb.2018.08.021

3. **A. Hermawan**, A. Wibowo, L. A. T. W. Asri, S. Yin, and B. S. Purwasasmita. Improved ionic conductivity of porous $Li_4Ti_5O_{12}$ synthesized by sol-gel method using eggshell membrane as soft template. *Mater. Res. Express*, 2019, **6**, 075030. https://doi.org/10.1088/2053-1591/ab1298

4. **A. Hermawan**, Y. Asakura, M. Inada and S.Yin. One-step synthesis of micro-/mesoporous SnO_2 spheres by solvothermal method for toluene gas sensor. *Ceram. Int.*, 2019, **45**, 15435-15444. https://doi.org/10.1016/j.ceramint.2019.05.043

5. **A. Hermawan**, Y. Asakura, M. Inada, and S.Yin. A facile method for preparation of uniformly decorated-spherical SnO_2 by CuO nanoparticles for highly responsive toluene detection at high temperature. *J. Mater. Sci. Tech.* 2020, **51**, 119-129. https://doi.org/10.1016/j.jmst.2020.02.041

6. **A. Hermawan**, B. Zhang, T. Ardiansyah, Y. Asakura, T. Hasegawa, J. Zhu, P. Shi, and S. Yin. CuO Nanoparticles/$Ti_3C_2T_x$ MXene hybrid Nanocomposites for Detection of Toluene Gas. *ACS Appl. Nano Mater.* 2020, **3**, 4755-4766. https://doi.org/10.1021/acsanm.0c00749

7. **A. Hermawan**, Y. Asakura and S.Yin. Morphology control of aluminum nitride (AlN) for high temperature hydrogen sensor. *Int. J. Miner. Metall. Mater.*, 2020 (inpress), https://doi.org/10.1007/s12613-020-2143-8

8. Z. Wang, F. Wang, **A. Hermawan**, Y. Asakura, T. Hasegawa, H. Kumagai, H. Kato, M. Kakihana, J. Zhu and S. Yin, SnO-SnO_2 Modified Two-Dimensional MXene $Ti_3C_2T_x$ for Acetone Gas Sensor Working at Room Temperature. *J. Mater. Sci. Tech.* 2020 (inpress)

9. **A. Hermawan**, A.T. Hanindriyo, E. R. Ramadhan, Y. Asakura, T. Hasegawa, K. Hongo, M. Inada, R. Maezono, and S. Yin, Octahedral morphology of NiO with (111) facet synthesized from the transformation of NiOHCl for NO_x detection and degradation: Experiment and DFT calculation. *Inorg. Chem. Front.*, 2020 (inpress), https://doi.org/10.1039/D0QI00682C

Conferences

Oral Presentation

1. <u>A. HERMAWAN</u>*, Y. ASAKURA, and S.YIN, "Preparation of A Thick Film GaN for Hydrogen Gas Sensing Application" Japan Ceramic Society Annual Meeting 2018 (公益社団法人日本セラミックス協会 2018 年年会) Sendai, Japan [2018.3.15-17]

2. <u>A. HERMAWAN</u>*, Y. ASAKURA, and S.YIN, "Improvement of toluene gas sensing response of SnO_2 microspheres after CuO nanoparticles decoration" 137th Meeting of Society of Inorganic Materials Japan, Toyohashi, Japan [2018.11.15-17]

3. <u>A. HERMAWAN</u>*, Y. ASAKURA, M. INADA and S.YIN "Toluene gas sensing performance of micro-/mesoporous SnO_2 spheres synthesized in organic solvents" Japan Ceramic Society Annual Meeting 2019 (公益社団法人日本セラミックス協会 2019 年年会) Tokyo, Japan [2019.3.24-26]

4. B. ZHANG*, J. ZHU, Y.ASAKURA, <u>A. HERMAWAN</u>, and S.YIN "In Situ Topotactic Synthesis of 2D Layered Titanium Carbonitrides Derived from MXenes and Its Excellent H_2 Gas Sensing Performance" Japan Ceramic Society Annual Meeting 2019 (公益社団法人日本セラミックス協会 2019 年年会) Tokyo, Japan [2019.3.24-26]

5. <u>A. HERMAWAN</u>*, Y. ASAKURA, M. INADA and S.YIN, "Solvothermal synthesis of micro-/mesoporous SnO_2 spheres and their toluene gas sensing properties" 138th Meeting of Society of Inorganic Materials Japan, Tokyo, Japan [2019.6.6-7]

6. <u>A. HERMAWAN</u>*, B. ZHANG, Y. ASAKURA, and S. YIN, "Highly responsive toluene detection based on CuO nanoparticle/ $Ti_3C_2T_x$ sandwich structure", 21st International Symposium on Eco-Materials Processing and Design, Expo on Environment-friendly Surface Engineering Technologies (ISEPD2020), Yantai, China [2020.01.10-13]

Poster Presentation

1. <u>A. HERMAWAN</u>*, Y. ASAKURA, and S.YIN, "Hydrogen Gas Sensing Properties of AlN and GaN Prepared by Direct Nitridation," The 34th International Japan-Korea Seminar on Ceramics, Hamamatsu, Japan [2017.11.22-25]

2. <u>A. HERMAWAN</u>*, Y. ASAKURA, and S.YIN, "Synthesis of CuO decorated-SnO_2 microsphere for p-n junction type gas sensor application" 7 学会東北大会会, Akita, Japan [2018.9.15-16]

* = Main speaker

Awards

1. Encouragement Grants Award, Hatano Foundation in IMRAM, 簸野奨学金 多元研研究奨励賞 (2016). Total Grant: 200,000 JPY

2. Professional Master for Sustainable Environment (PMSE), Graduate School of Environmental Studies, Tohoku University (2017)

3. Best Poster Presentation Awards at the 34th International Japan-Korea Seminar on Ceramics, Hamamatsu, Japan (2017)

4. Best Oral Presentation Award at 137th Meeting of Inorganic Material Society of Japan, Toyohashi, Japan (2018)

5. Best Paper Award in J. Asian Ceram. Soc., (2018). Award: 100,000 JPY

6. Travel Grants from the Graduate School of Environmental Studies, Tohoku University, to attend ISEPD 2020 in China. Total Grant: 100,000 JPY

Postface Motivation

"Indeed, in the creation of the heavens and the earth and the alternation of the night and the day are signs for Ulul Albab"
(Holy Quran 3 :190)